
Automated Parametrization and Validation of Simplified Models of the Interatomic Interaction

Automatisierte Parametrisierung und
Validierung von vereinfachten Modellen
der interatomaren Wechselwirkung

DISSERTATION

zur Erlangung des Grades
eines Doktors der Naturwissenschaften
in der Fakultät für Physik und Astronomie
der Ruhr-Universität Bochum

Jan Jenke
aus
Gladbeck

Bochum, 2018

Eidesstattliche Versicherung

Hiermit versichere ich, dass ich meine Dissertation selbstständig und ohne unerlaubte fremde Hilfen angefertigt habe. Ich habe keine anderen als die angegebenen Hilfsmittel und Hilfen benutzt. Meine Dissertation habe ich in dieser oder ähnlicher Form noch bei keiner anderen Fakultät der Ruhr-Universität Bochum und bei keiner anderen Hochschule eingereicht.

Bochum, den _____

Jan Jenke

Erster Gutachter : Prof. Dr. Ralf Drautz
Zweiter Gutachter : Prof. Dr. Jörg Neugebauer
Tag der Disputation : 26.04.2019

Abstract

Materials properties are driven by a complex interplay of chemistry, atomic structure and microstructure. This interplay has to be accurately described to improve materials properties or to discover new materials by computer simulations. On the atomic level, this can be achieved in many cases with density-functional theory (DFT). However, the DFT method is limited to small systems due to the computational cost such that it is not possible to use it for simulations of representations of a material of more than a few hundred atoms and to investigate broad ranges of the chemical composition. Analytic bond-order potentials (BOPs) are based on the tight-binding (TB) approximation and are systematically derived from DFT. They are computationally very efficient and allow one to simulate much larger systems and composition ranges. However, a careful parametrization of the interatomic interaction is required to obtain accurate predictions. Only for a few systems, analytic BOP models have been parametrized so far because of the significant effort which is needed to obtain good parametrizations. Therefore, many questions in materials science cannot be investigated with the powerful analytic BOPs.

In this work, three new concepts are developed, which facilitate the parametrization process. Firstly, TB parametrizations across the periodic table are obtained for 1711 systems with respect to a consistent DFT reference. The parametrizations show clear chemical trends across the periodic table and provide a robust reference for refined models. Secondly, a map of local atomic environments is developed, which allows for an intuitive classification of the local atomic and electronic structure. Thirdly, an automated parametrization protocol for d -valent analytic BOPs is defined, which is initialized by the set of TB parametrizations across the periodic table and enables a systematic transferability optimization to reference structures which are selected from the map of local atomic environments. This generic protocol is applied to parametrize an analytic BOP for the element Re.

The developed concepts facilitate and accelerate the development of analytic BOP models and form a parametrization procedure that can be routinely applied. This paves the way to analyse complex systems with multiple elements with analytic BOPs.

Zusammenfassung

Die Eigenschaften von Materialien ergeben sich aus einem komplexen Zusammenspiel der Chemie, atomaren Struktur und Mikrostruktur. Dieses Zusammenspiel muss genau beschrieben werden, um mittels Computersimulationen Materialeigenschaften zu verbessern und neue Materialien zu entdecken. Dies kann in vielen Fällen mit Dichtefunktionaltheorie (DFT) auf atomarer Ebene erreicht werden. Allerdings ist die DFT Methode durch die Rechenzeit auf kleine Systeme beschränkt, sodass es nicht möglich ist, sie für Simulationen von Materialrepräsentationen von mehr als ein paar hundert Atomen zu nutzen und breite Bereiche der chemischen Zusammensetzung zu untersuchen. Analytische Bond-Order Potentiale (BOPs) basieren auf der Tight-Binding (TB) Näherung und sind systematisch von der DFT hergeleitet. Sie sind rechnerisch sehr effizient und erlauben, große Systeme und Zusammensetzungsbereiche zu simulieren. Allerdings ist eine sorgfältige Parametrisierung der interatomaren Wechselwirkung nötig, um genaue Vorhersagen zu erhalten. Bisher wurden wegen des signifikanten Aufwands nur für einige wenige Systeme analytische BOP Modelle parametrisiert. Daher können viele materialwissenschaftliche Fragestellungen nicht mit den leistungsfähigen analytischen BOPs untersucht werden.

In dieser Arbeit werden drei neue Konzepte entwickelt, die den Parametrierungsprozess vereinfachen. Als Erstes werden TB Parametrisierungen gegenüber einer konsistenten DFT Referenz über das Periodensystem für 1711 Systeme hergeleitet. Die Parametrisierungen zeigen klare chemische Trends über das Periodensystem und liefern eine stabile Referenz für weiterentwickelte Modelle. Als Zweites wird eine Karte der lokalen atomaren Umgebungen entwickelt, welche eine intuitive Klassifikation der lokalen atomaren und elektronischen Struktur ermöglicht. Als Drittes wird ein automatisiertes Parametrisierungsprotokoll für d -valente analytische BOPs definiert, welches durch den Satz der TB Parametrisierungen über das Periodensystem initialisiert wird und eine systematische Transferabilitätsoptimierung gegenüber Referenzstrukturen ermöglicht, die von der Karte der lokalen atomaren Umgebungen ausgewählt werden. Dieses allgemeine Protokoll wird zur Parametrierung eines analytischen BOP für das Element Re benutzt.

Die entwickelten Konzepte erleichtern und beschleunigen die Entwicklung analytischer BOP Modelle und bilden eine Parametrierungsprozedur, welche routinemäßig eingesetzt werden kann. Dies ebnet den Weg, komplexe Systeme mit mehreren Elementen mit analytischen BOPs zu untersuchen.

Danksagung

Zunächst möchte ich mich bei meinem Erstbetreuer Prof. Dr. Ralf Drautz dafür bedanken, dass ich an einem interessanten Promotionsthema arbeiten konnte. Seine ehrgeizigen Ziele haben meine Arbeit besonders geprägt und seine Erläuterungen haben mir geholfen, diese zu erreichen. Ebenso möchte ich Prof. Dr. Jörg Neugebauer dafür danken, dass er die Zweitbetreuung meiner Arbeit übernommen hat.

Von meinem Gruppenleiter Dr. Thomas Hammerschmidt konnte ich viel lernen und besonderer Dank gebührt ihm für seine inspirierenden Ideen, die mir bei meiner Promotion geholfen haben.

Bei Christa Hermichen und Denisa Voicu möchte ich mich für die Unterstützung bei allen administrativen Tätigkeiten bedanken.

Ohne die IT Abteilung (Lothar Merl, Niklas Caesar, Vladimir Lenz) und die von ihnen errichtete IT Infrastruktur wären meine numerischen Rechnungen unmöglich gewesen, sodass ihnen ebenfalls mein Dank gilt.

Den aktuellen und ehemaligen Mitgliedern am ICAMS möchte ich für die freundliche und offene Atmosphäre danken. Besonders hervorheben möchte ich Alvin Ladines, der mir alle technischen Details von BOPfox und BOPcat erklärt hat, und Aparna P. A. Subramanyam für die gute Zusammenarbeit bei dem letzten Projekt meiner Promotion.

Nicht zuletzt möchte ich meinen Eltern danken, die mich stets unterstützt haben, sowie meiner Frau, die mir immer Motivation gibt, meine Ziele zu erreichen.

Contents

1	Introduction	1
2	Theory of Electronic Structure Methods	5
2.1	Background	6
2.1.1	Many-Body Quantum Theory	6
2.1.2	Born-Oppenheimer Approximation	7
2.1.3	Rayleigh-Ritz Variational Principle	8
2.1.4	Approximate Solutions	9
2.2	Density-Functional Theory	11
2.2.1	Hohenberg-Kohn Theorems	11
2.2.2	Kohn-Sham Equations	12
2.2.3	Exchange Correlation Functionals	14
2.2.4	Crystal Periodicity	15
2.2.5	Pseudo-Potentials	16
2.2.6	Basis Sets	18
2.2.7	Implementations	20
2.3	Tight-Binding	20
2.3.1	Harris-Foulkes Functional and Expansion of Kohn-Sham Energy Functional	20
2.3.2	Tight-Binding Approximations	23
2.3.3	Matrix Elements	25
2.3.4	Two-Center Approximation	25
2.3.5	Tight-Binding Bond Model	26
2.3.6	Orthogonal Tight-Binding	31
2.3.7	Forces in the Tight-Binding Bond Model	32
2.3.8	Downfolding Procedure	33
2.3.9	Parametrization	35
2.3.10	Summary of Calculation Steps	36
2.4	Analytic Bond-Order Potentials	36
2.4.1	Moments of the Density of States	38
2.4.2	Moments Theorem	38
2.4.3	Recursion Coefficients	39
2.4.4	Continued Fraction Expansion of the Local Density of States	40

2.4.5	Constant Terminator	41
2.4.6	Moments Expansion of the Density of States	42
2.4.7	Termination of Moments Expansion	43
2.4.8	Terminators and Estimates of the Bandwidth	44
2.4.9	Strictly Positive Density of States	46
2.4.10	Bond Energy	47
2.4.11	Self-Consistency	47
2.4.12	Forces	48
2.4.13	Summary of Calculation Steps	48
2.4.14	Second and Fourth Moment Approximations	49
2.4.15	Computer Implementation of Analytic Bond-Order Potential and Tight-Binding Calculations: BOPfox	52
2.4.16	Estimation of Energy Differences	52
2.4.17	Illustration of Analytic Bond-Order Potentials	54
3	Tight-Binding Parametrization Across the Periodic Table	59
3.1	Background	59
3.1.1	Tight-Binding Description of Dimers	59
3.1.2	Reduced Tight-Binding	61
3.1.3	Canonical Tight-Binding	63
3.1.4	Rectangular d -Band Model	65
3.1.5	Explicit Tight-Binding Parametrizations for Groups of Elements	67
3.2	Tight-Binding Parametrizations from the Downfolding Procedure	68
3.2.1	Density-Functional Theory Reference	68
3.2.2	Application of Downfolding Procedure	69
3.2.3	Parametrization	70
3.3	Evaluation of Results from the Downfolding Procedure	73
3.3.1	Si as Example for sp -valent Elements	73
3.3.2	Mo as Example for d -valent Elements	74
3.3.3	Homoatomic Dimers	74
3.3.4	Heteroatomic Dimers	78
3.3.5	Energy Contributions	78
3.3.6	Comparison to Other Methods	80
4	Electronic Structure Based Map of Local Atomic Environments	87
4.1	Background	88
4.1.1	Moments Theorem and Structural Stability	88
4.1.2	Atomic Environments	91
4.1.3	Descriptors of Atomic Environments	95
4.2	Moments as Descriptors	96
4.3	Map of Local Atomic Environments	98

4.3.1	Simple Crystal Structures	98
4.3.2	Crystal Structures with Multiple Inequivalent Lattice Sites	101
4.3.3	Random Structures	103
4.4	Electronic Structure Interpretation of Map of Local Atomic Environments	103
4.4.1	Relation of Descriptors to Binding Energy	103
4.4.2	Trends of Structural Stability from Tight-Binding	105
4.4.3	Trends of Structural Stability from Density-Functional Theory	107
5	Automated Parametrization Strategy	111
5.1	Background	112
5.1.1	Model Parameter Optimization	112
5.1.2	Parametrization Strategies	113
5.2	Parametrization of Analytic Bond-Order Potentials for Transition-Metals	115
5.2.1	Computational Details	115
5.2.2	Parametrization Protocol	116
5.3	Transferability Assessment and Improvement	120
5.4	Parameterization of an Analytic Bond-Order Potential for Re	125
5.4.1	Reference Data	125
5.4.2	Construction of Fit Set	132
5.4.3	Transferability Adjustment	133
5.4.4	Pareto-Optimal Analytic BOP Model for Re	142
5.5	Correlation of Model Predictions	148
5.6	Influence of Model Complexity	150
 Conclusion		 153
 Outlook		 155
 Appendices		
A Trends of Homoatomic Dimers		158
B Trends of Heteroatomic Dimers		160
C Calculation of Elastic Constants for the Hexagonal Crystal Structure		175
 Bibliography		 179

1

Introduction

Materials properties are often determined by a complex interplay of the chemistry and the atomic structure of the material. Density-functional theory (DFT) allows for accurate quantum mechanical simulations of the interatomic interaction for most elements and atomic configurations and therefore became a standard tool in materials science. However, the computational effort of DFT calculations rises rapidly with system size. Therefore, simulations of structures with more than a few hundred atoms are practically impossible and systematic scanning for desired materials properties is limited to rather small subsets of the atomic structure and chemical composition.

For example, Ni-base superalloys are often processed with more than ten alloying elements. The composition determines the partitioning and segregation, which further determines the mechanical properties like the creep resistance by the energies related to structural changes. The high number of alloying elements makes a comprehensive screening of the space of chemical compositions within DFT impossible, e.g. to reduce the formation of brittle topologically close-packed phases. Moreover, many important structural changes like the movement of dislocations are hardly accessible with DFT due to the size of the corresponding atomic configurations.

Machine-learning approaches may be used to statistically predict physical quantities from a small set of data, which is accessible with experiments or with DFT, but they are not able to provide a detailed understanding of the underlying mechanisms.

Alternatively, DFT can be coarse grained in a second-order approximation to the tight-binding (TB) theory, which is computationally faster than DFT but has the same scaling behaviour with the system size. By a moments expansion, the TB theory can be further coarse grained to the linear scaling analytic

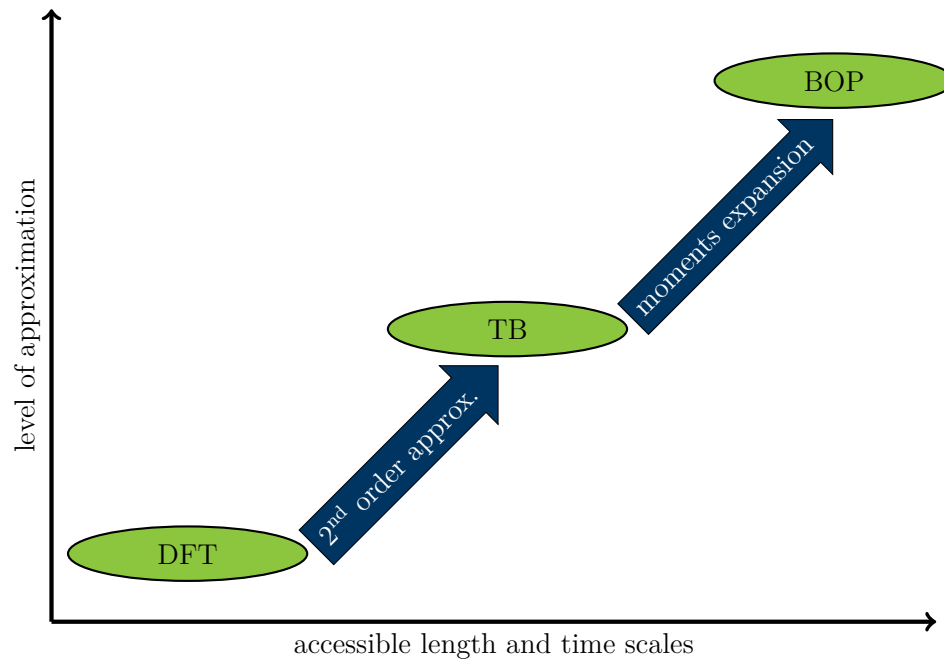


Figure 1.1.: Coarse graining of the electronic structure. While DFT allows in many cases for an accurate description of the electronic structure, the applications are limited to rather small length and time scales. By a second-order approximation, the TB theory is derived, which is further coarse grained in analytic BOPs by a moments expansion.

bond-order potentials (BOPs). The two coarse graining steps are illustrated in Fig. 1.1. The scaling behaviour of analytic BOPs enables simulations of large atomic structures and the overall decrease in computational time compared to DFT allows one to perform much more simulations in a given time. Thus, large sets of the chemical space can be scanned for desired materials properties and it can be used to investigate complex materials such as the mentioned Ni-base superalloys in detail. Especially with regard to the exponential increase of computational power, which is observed in the last decades and referred to as Moore's law, the gap between system sizes which can be investigated with the cubic scaling DFT method and the linear scaling analytic BOP method is continuously increasing. In contrast to DFT, the TB method and the analytic BOPs require a pairwise parametrization of the interatomic interaction. Compared to empirical potentials, the physical nature of the two methods guarantees a robust transferability across the space of atomic environments such that it is able to provide many qualitative predictions without much parametrization effort. However, if quantitative predictions are needed a careful parametrization of the interatomic interaction is required. The interatomic interaction can be obtained for a particular atomic configuration with a downfolding procedure from the DFT reference, but the model parameters have to be further optimized to increase the transferability of the model. This

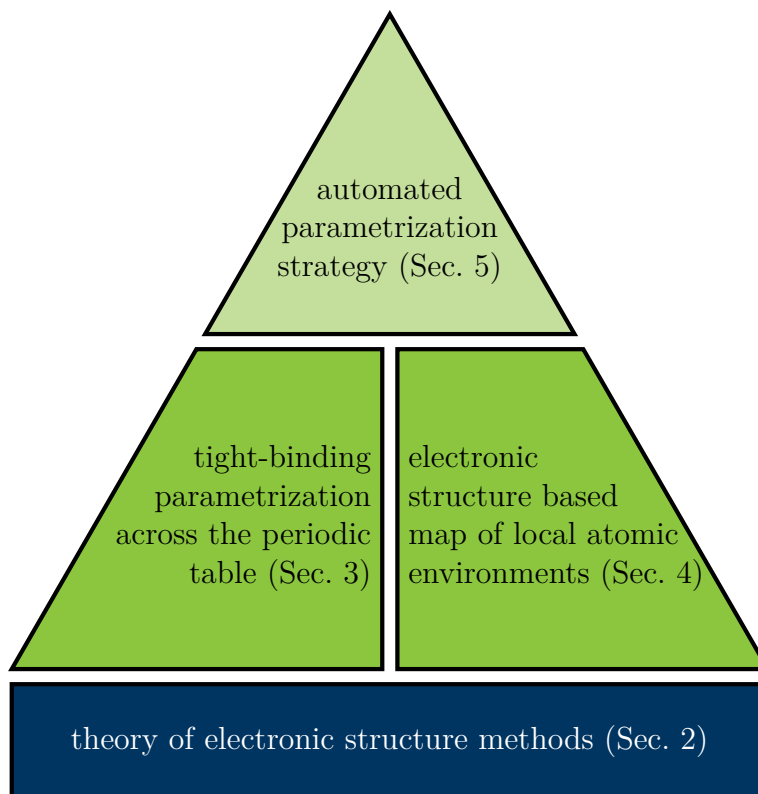


Figure 1.2.: Structure of the present work. In Sec. 2, the electronic structure methods employed in this work (DFT, TB, analytic BOPs) are introduced. Pairwise TB parametrizations across the periodic table are derived for a consistent reference in Sec. 3 and an electronic structure based map of local atomic environments is developed in Sec. 4, which provides intuitive insight into the similarity of the local atomic structure. The TB parametrizations across the periodic table and the information which is obtained from the map of local atomic environments are used in an automated parametrization strategy, which is developed in Sec. 5.

parametrization process turned out to be very time consuming. Therefore, only a few parametrizations have been developed and systematically tested. This hampers the analysis of a broader set of materials by the efficient analytic BOPs.

To allow for a fast parametrization of transferable analytic BOPs for quantitative predictions for arbitrary systems, three challenges have to be solved. An understanding of the electronic interaction across the periodic table, i.e. the chemical diversity, has to be developed in order to derive a TB reference for the models. Moreover, an intuitive insight into the large space of atomic environments, i.e. the geometrical diversity, is needed in order to understand which atomic environments are relevant for the model and to understand its transferability. Finally, these two aspects have to be combined in a general

and robust parametrization strategy that can be routinely applied.

A solution of these three challenges is developed in the present work, whose structure is illustrated in Fig. 1.2. Section 2 provides the basis for the following investigations and introduces the employed electronic structure methods, which are DFT, TB and analytic BOPs. Reference TB parametrizations across almost all combinations of elements of the first five periods of the periodic table are developed in Sec. 3. An understanding of the chemical diversity in term of the electronic interaction across the periodic table is obtained by the extraction of trends. In Sec. 4, the theory of analytic BOPs is employed to derive moments-descriptors, which are used to construct an electronic structure based map of local atomic environments. It is shown that the map enables an interpretation of atomic environments in terms of the atomic geometry and the electronic structure. Clear trends of structural stability are obtained in the map on the level of TB and DFT. These results indicate that the map of local atomic environments provides intuitive insight into the geometrical diversity. An automated parametrization strategy is developed in Sec. 5 which makes use of the obtained insight into the chemical and geometrical diversity by the TB parametrizations across the periodic table and the electronic structure based map of local atomic environments. This strategy is applied to parametrize a Pareto-optimal analytic BOP for Re.

2

Theory of Electronic Structure Methods

This work uses three electronic structure methods: Density-functional theory (DFT), tight-binding (TB) and analytic bond-order potentials (BOPs). In this section, the theory for the different electronic structure methods is summarized. Background information to many-body quantum theory is provided, which is necessary to derive the Hohenberg-Kohn equations, which are solved in DFT. Moreover, important concepts, which are used to solve these equations computationally, are discussed. The TB theory is introduced afterwards and connections of DFT and TB are presented. They are given by (i) an approximation to the DFT energy functional, which results in the TB bond model and (ii) a downfolding procedure, which allows one to approximate the DFT wave function by a TB basis. Afterwards, the analytic BOPs are discussed, which are derived as a systematic approximation to TB and are based on a moments expansion of the density of states (DOS).

The DFT method is applied in Secs. 3, 5. The connection between DFT and TB is relevant for Sec. 3. The interpretation of the moments of the BOPs is applied in Sec. 4 and the BOP formalism is used in Sec. 5.

This section partially summarizes textbooks and lecture notes (Refs. 1–9) and is complemented by publications which go beyond these references.

2.1. Background

2.1.1. Many-Body Quantum Theory

If relativistic effects are neglected, the Hamilton operator \hat{H} of a many-body system is written as a sum of operators, which define separate energy contributions,

$$\hat{H} = \hat{T}_n + \hat{T}_e + \hat{V}_{n-n} + \hat{V}_{e-e} + \hat{V}_{e-n} + \hat{V}_{\text{ext}}. \quad (2.1)$$

The kinetic energy operators of the nuclei and the electrons are given by \hat{T}_n and \hat{T}_e , separately. The operator \hat{V}_{n-n} defines the interaction of the nuclei and \hat{V}_{e-e} the interaction of the electrons. The interaction between the nuclei and the electrons is defined by \hat{V}_{e-n} and the interaction with external potentials is defined by \hat{V}_{ext} . The momentum operator of nucleus I with mass M_I is defined as $\hat{P}_I = -i\hbar \frac{\partial}{\partial \mathbf{R}_I}$ and the momentum operator of electron i with mass m as $\hat{p}_i = -i\hbar \frac{\partial}{\partial \mathbf{r}_i}$. With these definitions, the kinetic energy operators are given by

$$\hat{T}_n = \sum_{I=1}^{N_n} \frac{\hat{P}_I^2}{2M_I} \quad (2.2)$$

and

$$\hat{T}_e = \sum_{i=1}^{N_e} \frac{\hat{p}_i^2}{2m}, \quad (2.3)$$

where N_e is the number of electrons and N_n is the number of nuclei. In the following, it is assumed that electrons and nuclei interact only via the Coulomb interaction, i.e. magnetism is not considered. Therefore, the interaction operators are given by

$$\hat{V}_{n-n}(\{\mathbf{R}\}) = \frac{1}{2} \sum_{IJ, I \neq J} \frac{Z_I Z_J e^2}{|\mathbf{R}_I - \mathbf{R}_J|}, \quad (2.4)$$

$$\hat{V}_{e-e}(\{\mathbf{r}\}) = \frac{1}{2} \sum_{ij, i \neq j} \frac{e^2}{|\mathbf{r}_i - \mathbf{r}_j|} \quad (2.5)$$

and

$$\hat{V}_{e-n}(\{\mathbf{r}, \mathbf{R}\}) = - \sum_{iI} \frac{Z_I e^2}{|\mathbf{r}_i - \mathbf{R}_I|}, \quad (2.6)$$

where Z_I is the proton number of nucleus I . The time-independent Schrödinger equation for this problem is written as

$$\hat{H}\Psi_s(\{\mathbf{r}\}, \{\mathbf{R}\}) = E_s\Psi_s(\{\mathbf{r}\}, \{\mathbf{R}\}), \quad (2.7)$$

where the solution $\Psi_s(\{\mathbf{r}\}, \{\mathbf{R}\})$ depends on all electron positions $\{\mathbf{r}\}$ and all nuclei positions $\{\mathbf{R}\}$ and s labels the state.

It is useful to estimate the relative scale of the separate contributions to the Hamiltonian. Therefore, dimensionless position vectors are constructed by $\tilde{\mathbf{R}}_I = \mathbf{R}_I/a_0$, $\tilde{\mathbf{r}}_i = \mathbf{r}_i/a_0$, where $a_0 = \hbar^2/me^2$ is the Bohr radius. With these definitions, the Hamiltonian may be rewritten as

$$\begin{aligned} \frac{\hat{H}}{E_0} = & - \sum_{I=1}^{N_n} \frac{\partial^2}{\partial \tilde{\mathbf{R}}_I^2} - \sum_{i=1}^{N_e} \frac{m}{M_n} \frac{\partial^2}{\partial \tilde{\mathbf{r}}_i^2} \\ & + \frac{1}{2} \sum_{ij, i \neq j} \frac{e^2}{|\tilde{\mathbf{r}}_i - \tilde{\mathbf{r}}_j|} - \frac{1}{2} \sum_{iI} \frac{Z_I e^2}{|\tilde{\mathbf{r}}_i - \tilde{\mathbf{R}}_I|} + \frac{1}{2} \sum_{IJ, I \neq J} \frac{Z_I Z_J e^2}{|\tilde{\mathbf{R}}_I - \tilde{\mathbf{R}}_J|}, \end{aligned} \quad (2.8)$$

where $E_0 = me^4/\hbar^2 = 2\text{Ry}$. The parameter m/M_n is the ratio of the electron mass and the mass of the nuclei M_n , which is temporarily assumed to be constant for all nuclei. This ratio is a small parameter and setting it to zero corresponds to neglecting the motion of the nuclei. This is assumed in the Born-Oppenheimer approximation.

2.1.2. Born-Oppenheimer Approximation

The assumption of the Born-Oppenheimer approximation [10] is that the motion of the electrons can be decoupled from the motion of the nuclei. This may be justified by the assumption $M_n \gg m$ or equivalently that the motion of the electrons happens on a shorter time scale than those of the nuclei. Consequently, the nuclei positions $\{\mathbf{R}\}$ are taken as fixed parameters when solving the Schrödinger equation for the electrons.

The Hamiltonian of the coupled system of nuclei and electrons may be split into

$$\hat{H} = \hat{T}_n + \hat{H}_{\text{e,eff}}, \quad (2.9)$$

where

$$\hat{H}_{\text{e,eff}} = \hat{T}_e + \hat{V}_{\text{e-e}} + \hat{V}_{\text{e-n}} + \hat{V}_{\text{n-n}} + \hat{V}_{\text{ext}} \quad (2.10)$$

describes the effective Hamiltonian acting on the electrons for fixed nuclei positions and the classical interaction of the nuclei $\hat{V}_{\text{n-n}}$. Therefore, the electron-nucleus interaction $\hat{V}_{\text{e-n}}$ may be regarded as an external potential acting on the electrons. The external potential and the electron-nucleus interaction are summarized to

$$\hat{V}_{\text{ext,e-n}} = \hat{V}_{\text{ext}} + \hat{V}_{\text{e-n}}. \quad (2.11)$$

The eigenstates of the effective Hamiltonian $\psi_i(\{\mathbf{r}\}; \{\mathbf{R}\})$ are defined by

$$\hat{H}_{\text{e,eff}} \psi_i(\{\mathbf{r}\}; \{\mathbf{R}\}) = \epsilon_i \psi_i(\{\mathbf{r}\}; \{\mathbf{R}\}) \quad (2.12)$$

and have to be anti-symmetric due to the Pauli exclusion principle [11]. They may be used to expand the eigenstates of the coupled system,

$$\Psi_s(\{\mathbf{r}\}, \{\mathbf{R}\}) = \sum_i \chi_{si}(\{\mathbf{R}\}) \psi_i(\{\mathbf{r}\}; \{\mathbf{R}\}). \quad (2.13)$$

Applying this expression to the Schrödinger equation (Eq. 2.7) results in [5]

$$\left(\hat{T}_N + \epsilon_i\right) \chi_{si}(\{\mathbf{R}\}) + \sum_j A_{ji}(\{\mathbf{R}\}) \chi_{sj}(\{\mathbf{R}\}) = E_s \chi_{si}(\{\mathbf{R}\}), \quad (2.14)$$

where

$$\begin{aligned} A_{ji}(\{\mathbf{R}\}) = & - \sum_I \frac{\hbar^2}{2M_I} \int d\mathbf{r}_1 \dots d\mathbf{r}_{N_e} \left[\psi_i^*(\{\mathbf{r}\}; \{\mathbf{R}\}) \left(\frac{\partial^2}{\partial \mathbf{R}_I^2} \psi_j(\{\mathbf{r}\}; \{\mathbf{R}\}) \right) \right. \\ & \left. + 2\psi_i^*(\{\mathbf{r}\}; \{\mathbf{R}\}) \left(\frac{\partial}{\partial \mathbf{R}_I} \psi_j(\{\mathbf{r}\}; \{\mathbf{R}\}) \right) \frac{\partial}{\partial \mathbf{R}_I} \right]. \end{aligned} \quad (2.15)$$

The off-diagonal elements are neglected in the Born-Oppenheimer approximation and Eq. 2.14 reduces to

$$\left(\hat{T}_n + v_i(\{\mathbf{R}\})\right) \chi_{si}(\{\mathbf{R}\}) = E_s \chi_{si}(\{\mathbf{R}\}). \quad (2.16)$$

This equation may be interpreted as a Schrödinger equation for the nuclei in an effective potential $v_i(\{\mathbf{R}\})$.

2.1.3. Rayleigh-Ritz Variational Principle

The Rayleigh-Ritz variational principle [12, 13] in Dirac bra-ket notation is given by

$$E_0 \leq \frac{\langle \Psi | \hat{H} | \Psi \rangle}{\langle \Psi | \Psi \rangle}, \quad (2.17)$$

where E_0 is the ground state energy. It states that the possibly degenerate ground state minimizes $\langle \Psi | \hat{H} | \Psi \rangle$ under the constraint of normalized wave functions, $\langle \Psi | \Psi \rangle = 1$. It is readily proved by

$$\begin{aligned} \langle \Psi | \hat{H} | \Psi \rangle &= \sum_s \langle \Psi | \hat{H} | \Psi_s \rangle \langle \Psi_s | \Psi \rangle = \sum_s E_s \langle \Psi | \Psi_s \rangle \langle \Psi_s | \Psi \rangle \\ &\geq E_0 \sum_s \langle \Psi | \Psi_s \rangle \langle \Psi_s | \Psi \rangle = E_0 \langle \Psi | \Psi \rangle, \end{aligned} \quad (2.18)$$

where E_s and $|\Psi_s\rangle$ are the eigenenergies and eigenstates of \hat{H} , separately. The Rayleigh-Ritz variational principle (Eq. 2.17) may be rewritten as

$$E_0 = \min_{\Psi} E[\Psi], \quad (2.19)$$

where

$$E[\Psi] = \frac{\langle \Psi | \hat{H} | \Psi \rangle}{\langle \Psi | \Psi \rangle} \quad (2.20)$$

is a functional of the wave function Ψ . Therefore, the ground state of \hat{H} is found by minimizing the functional $E[\Psi]$ with respect to Ψ .

2.1.4. Approximate Solutions

The calculation of the ground state of the decoupled Schrödinger equation for the electrons (Eq. 2.12) depends on $3N_e$ parameters. The number of parameters for a computational energy minimization with the Rayleigh-Ritz variational principle can be roughly estimated to be p^{3N_e} , where p is the number of parameters per variable which is needed for a desired numerical accuracy [14]. Due to the exponential increase of parameters, a computational solution of this task is only tractable for a few electrons and completely intractable for typical problems in solid state physics. Approximate solutions can be found by making assumptions on the functional form of the ground state wave function.

The Hartree approximation [15] neglects the anti-symmetry of the wave function and assumes that the eigenstates of $\hat{H}_{e,\text{eff}}$ are given by

$$\psi^{\text{H}}(\{\mathbf{r}\}) = \psi_1(\mathbf{r}_1)\psi_2(\mathbf{r}_2) \dots \psi_{N_e}(\mathbf{r}_{N_e}), \quad (2.21)$$

where ψ_i is a one-particle wave function of electron i , which is normalized by

$$\int d\mathbf{r}_i \rho_i(\mathbf{r}_i) = 1, \quad (2.22)$$

where

$$\rho_i(\mathbf{r}_i) = \psi_i^*(\mathbf{r}_i)\psi_i(\mathbf{r}_i). \quad (2.23)$$

The application of the Rayleigh-Ritz variational principle leads to single particle equations,

$$\left[\hat{T}_{e,i} + \hat{V}_{\text{H},i} + \hat{V}_{\text{ext},e-n,i} \right] \psi_i(\mathbf{r}_i) = \epsilon_i \psi_i(\mathbf{r}_i), \quad (2.24)$$

where

$$\hat{T}_{e,i} = \frac{\hat{p}_i^2}{2m} \quad (2.25)$$

and

$$\hat{V}_{\text{H},i}(\mathbf{r}_i) = e^2 \sum_{j \neq i} \int d\mathbf{r}_j \frac{\rho_j(\mathbf{r}_j)}{|\mathbf{r}_i - \mathbf{r}_j|} \quad (2.26)$$

is the Hartree potential and describes the Coulomb repulsion of the electrons. The potential $\hat{V}_{\text{ext},e-n,i}$ contains the electron-nucleus interaction

$$\hat{V}_{e-n,i}(\{\mathbf{r}\}) = - \sum_I \frac{Z_n e^2}{|\mathbf{r}_i - \mathbf{R}_I|} \quad (2.27)$$

as well as possibly any other external potential.

The Hartree-Fock approximation [16] considers the anti-symmetry of the wave function and assumes that the eigenstates of $H_{e,\text{eff}}$ are given by Slater determinants

$$\psi^{\text{HF}}(\{\mathbf{r}\}) = \frac{1}{\sqrt{N_e!}} \begin{vmatrix} \psi_1(\mathbf{r}_1) & \psi_1(\mathbf{r}_2) & \dots & \psi_1(\mathbf{r}_{N_e}) \\ \psi_2(\mathbf{r}_1) & \psi_2(\mathbf{r}_2) & \dots & \psi_2(\mathbf{r}_{N_e}) \\ \vdots & \vdots & & \vdots \\ \psi_{N_e}(\mathbf{r}_1) & \psi_{N_e}(\mathbf{r}_2) & \dots & \psi_{N_e}(\mathbf{r}_{N_e}) \end{vmatrix}. \quad (2.28)$$

Compared to the Hartree approximation, the application of the Rayleigh-Ritz variational principle leads to an additional term in the single particle equations,

$$[\hat{T}_{e,i} + \hat{V}_{H,i} + \hat{V}_{X,i} + \hat{V}_{\text{ext},e-n,i}] \psi_i(\mathbf{r}_i) = \epsilon_i \psi_i(\mathbf{r}_i), \quad (2.29)$$

which is the exchange potential,

$$\hat{V}_{X,i}(\mathbf{r}_i) = e^2 \sum_{j \neq i} \int d\mathbf{r}_j \frac{\rho_j^X(\mathbf{r}_i, \mathbf{r}_j)}{|\mathbf{r}_i - \mathbf{r}_j|}, \quad (2.30)$$

where

$$\rho_j^X(\mathbf{r}_i, \mathbf{r}_j) = \sum_{j \neq i} \frac{\psi_i^*(\mathbf{r}_i) \psi_i(\mathbf{r}_j) \psi_j^*(\mathbf{r}_j) \psi_j(\mathbf{r}_i)}{\psi_i(\mathbf{r}_i) \psi_i^*(\mathbf{r}_i)} \quad (2.31)$$

is the single particle exchange density.

Both the Hartree and Hartree-Fock equations can be solved iteratively on a computer. The single particle wave functions have to be expanded in a basis. Possible basis sets can be found in Sec. 2.2.6. An initial guess for the atomic wave functions has to be made to calculate the Hartree potential and in case of the Hartree-Fock approximation also the Fock potential. New estimates for the single particle wave functions are calculated from the initial guess. This procedure is repeated until a convergence criteria is reached. The computational time of such an approach scales with N_e^3 due to the required diagonalisation procedure and is therefore only applicable to system sizes of a few atoms. However, the Hartree-Fock method includes the exchange potential but neglects the correlation of electrons. A method which has the same scaling behaviour but takes the correlation of electrons into account is DFT.

2.2. Density-Functional Theory

2.2.1. Hohenberg-Kohn Theorems

The two Hohenberg-Kohn theorems [17] highlight the relevance of the electron density

$$\rho(\mathbf{r}) = N_e \int d\mathbf{r}_2 \dots d\mathbf{r}_{N_e} |\psi(\mathbf{r}, \mathbf{r}_2, \dots, \mathbf{r}_{N_e})|^2 \quad (2.32)$$

for electronic structure theory. Hohenberg's and Kohn's first theorem shows that the ground state energy of the effective electron Hamiltonian (Eq. 2.10) is a unique functional of the electronic ground state density. The second theorem states that an energy functional $E[\rho]$ exists which is minimal for the electronic ground state density.

Theorem 1:

The decoupled Schrödinger equation for the electrons (Eq. 2.12) is rewritten as

$$\epsilon_n = \langle \psi_n | \hat{T}_e | \psi_n \rangle + \langle \psi_n | \hat{V}_{e-e} | \psi_n \rangle + \langle \psi_n | \hat{V}_{\text{ext},e-n} | \psi_n \rangle. \quad (2.33)$$

The interaction with the external potential and the nuclei is expressed in terms of the electron density (Eq. 2.32),

$$\langle \psi_n | \hat{V}_{\text{ext},e-n} | \psi_n \rangle = \int d\mathbf{r} \rho(\mathbf{r}) v_{\text{ext},e-n}(\mathbf{r}), \quad (2.34)$$

where $v_{\text{ext},e-n} = v_{\text{ext}} + v_{e-n}$ and

$$v_{e-n}(\mathbf{r}) = - \sum_I \frac{Z_I e^2}{|\mathbf{r} - \mathbf{R}_I|} \quad (2.35)$$

is the potential of the nuclei. The proof of the first theorem is conducted by assuming that a Hamiltonian $\hat{H}_{e,\text{eff}}$ with potential $v_{\text{ext},e-n}(\mathbf{r})$ has the ground state ψ_0 and ground state energy E_0 and another Hamiltonian $\hat{H}'_{e,\text{eff}}$ with potential $v'_{\text{ext}}(\mathbf{r})$ has the ground state ψ'_0 and ground state energy E'_0 . It is further assumed that both ground states have the same ground state density $\rho_0(\mathbf{r})$. It follows

$$E'_0 < E_0 + \int d\mathbf{r} [v'_{\text{ext},e-n}(\mathbf{r}) - v_{\text{ext},e-n}(\mathbf{r})] \rho_0(\mathbf{r}) \quad (2.36)$$

and

$$E_0 < E'_0 + \int d\mathbf{r} [v_{\text{ext},e-n}(\mathbf{r}) - v'_{\text{ext},e-n}(\mathbf{r})] \rho_0(\mathbf{r}), \quad (2.37)$$

leading to the contradiction $E + E' < E + E'$. It is therefore proven that the two ground states ψ and ψ' cannot have the same electronic ground state density. The electronic ground state density defines (upon a constant) $v_{\text{ext},e-n}$ and thus the Hamiltonian and the ground state.

Theorem 2:

From the first theorem, it is known that the ground state energy is a functional of the electronic ground state density. Therefore, an energy functional

$$E_{\text{HK}}[\rho(\mathbf{r})] = T[\rho(\mathbf{r})] + V_{\text{e-e}}[\rho(\mathbf{r})] + \int d\mathbf{r} \rho(\mathbf{r})v_{\text{ext,e-n}}(\mathbf{r}) + V_{\text{n-n}} \quad (2.38)$$

can be defined which takes the value of the ground state energy E_0 if $\rho(\mathbf{r}) = \rho_0(\mathbf{r})$. $V_{\text{n-n}}$ is the energy of the nucleus-nucleus interaction. It remains to show that $E_{\text{HK}}[\rho(\mathbf{r})]$ takes its minimum for $\rho_0(\mathbf{r})$. Assuming that $\rho_0(\mathbf{r})$ is the electronic ground state density of $\hat{H}_{\text{e,eff}}$ with ground state ψ_0 , a different electron density $\rho'(\mathbf{r})$ necessarily corresponds to a different state ψ' with energy E' . The inequality

$$E_{\text{HK}}[\rho_0(\mathbf{r})] = E_0 = \langle \psi_0 | \hat{H}_{\text{e,eff}} | \psi_0 \rangle < \langle \psi' | \hat{H}_{\text{e,eff}} | \psi' \rangle = E' = E_{\text{HK}}[\rho'(\mathbf{r})] \quad (2.39)$$

follows, which proves the second theorem.

The Hohenberg-Kohn theorems show that a functional $E_{\text{HK}}[\rho(\mathbf{r})]$ exists which only depends on the electron density $\rho(\mathbf{r})$. If the functionals $T[\rho(\mathbf{r})]$ and $V_{\text{e-e}}[\rho(\mathbf{r})]$ were known, a minimization procedure to find the energy and the electron density of the ground state could be constructed.

2.2.2. Kohn-Sham Equations

Kohn and Sham developed a procedure which iteratively minimizes Eq. 2.38 without knowledge of $T[\rho(\mathbf{r})]$, the functional of the kinetic energy [18]. They also provided approximations for the unknown part $V_{\text{e-e}}[\rho(\mathbf{r})]$ of the functional, which are discussed in Sec. 2.2.3.

The Hohenberg-Kohn energy functional (Eq. 2.38) is expressed as

$$E_{\text{KS}}[\rho(\mathbf{r})] = T[\rho(\mathbf{r})] + V_{\text{H}}[\rho(\mathbf{r})] + V_{\text{xc}}[\rho(\mathbf{r})] + \int d\mathbf{r} \rho(\mathbf{r})v_{\text{ext,e-n}}(\mathbf{r}) + V_{\text{n-n}}, \quad (2.40)$$

where

$$V_{\text{H}}[\rho(\mathbf{r})] = \frac{1}{2} \int d\mathbf{r} d\mathbf{r}' \frac{\rho(\mathbf{r})\rho(\mathbf{r}')}{|\mathbf{r} - \mathbf{r}'|} \quad (2.41)$$

defines the Hartree energy and the exchange correlation energy V_{xc} includes the energy functional of the electron-electron interaction $V_{\text{e-e}}$. This representation is referred to as Kohn-Sham energy functional. The variation with respect to the electron density under the condition that the electron number has to be preserved leads to

$$\frac{\delta E_{\text{KS}}}{\delta \rho} = \frac{\delta T}{\delta \rho} + v_{\text{H}}(\mathbf{r}) + v_{\text{xc}}(\mathbf{r}) + v_{\text{ext}}(\mathbf{r}) = \epsilon. \quad (2.42)$$

$$v_{\text{H}}(\mathbf{r}) = \int d\mathbf{r}' \frac{\rho(\mathbf{r}')}{|\mathbf{r} - \mathbf{r}'|} \quad (2.43)$$

is the Hartree potential,

$$v_{\text{xc}}(\mathbf{r}) = \frac{\delta V_{\text{xc}}[\rho]}{\delta \rho} \quad (2.44)$$

defines the exchange correlation potential and ϵ is a Lagrange multiplier. The potentials may be summarized to an effective potential

$$v_{\text{eff}}(\mathbf{r}) = v_{\text{H}}(\mathbf{r}) + v_{\text{xc}}(\mathbf{r}) + v_{\text{ext,e-n}}(\mathbf{r}) \quad (2.45)$$

and Eq. 2.42 can be written as

$$\frac{\delta T}{\delta \rho} + v_{\text{eff}}(\mathbf{r}) = \epsilon. \quad (2.46)$$

Exactly the same equation is obtained for non-interacting electrons moving in an external potential v_{eff} , where the energy functional is given as

$$E_{v_{\text{eff}}}[\tilde{\rho}(\mathbf{r})] = T[\tilde{\rho}(\mathbf{r})] + \int d\mathbf{r} \tilde{\rho}(\mathbf{r})v_{\text{eff}}(\mathbf{r}). \quad (2.47)$$

This problem reduces to the solution of the single particle equations

$$[\hat{T}_{e,n} + v_{\text{eff}}(\mathbf{r})] \psi_n(\mathbf{r}) = \epsilon_n \psi_n(\mathbf{r}) \quad (2.48)$$

and it follows that the electronic ground state density of the non-interacting particles in the external potential is the same as the electronic ground state density of the original many electron system, $\tilde{\rho}(\mathbf{r}) = \rho(\mathbf{r})$. The electronic ground state density is given by*

$$\rho(\mathbf{r}) = \sum_{n=1}^{N_e} |\psi_n(\mathbf{r})|^2 = \sum_{n=1} f_n |\psi_n(\mathbf{r})|^2, \quad (2.49)$$

where f_n is the occupation number, which is equal to two for occupied states and equal to zero for unoccupied states. The kinetic energy functional can be expressed as

$$T[\rho(\mathbf{r})] = \sum_n f_n \int d\mathbf{r} \psi_n(\mathbf{r}) \hat{T}_{e,n} \psi_n^*(\mathbf{r}). \quad (2.50)$$

The ground state energy is given by

$$E = \sum_n f_n \epsilon_n + V_{\text{xc}}[\rho(\mathbf{r})] - \int d\mathbf{r} \rho(\mathbf{r})v_{\text{xc}}(\mathbf{r}) - \frac{1}{2} \int d\mathbf{r} \rho(\mathbf{r})v_{\text{H}}(\mathbf{r}) \quad (2.51)$$

and reduces to the energy in the Hartree approximation if exchange and correlation effects are neglected. An iterative minimization of the Kohn-Sham

*This can be verified by substituting the Slater determinant (Eq. 2.28) into Eq. 2.32.

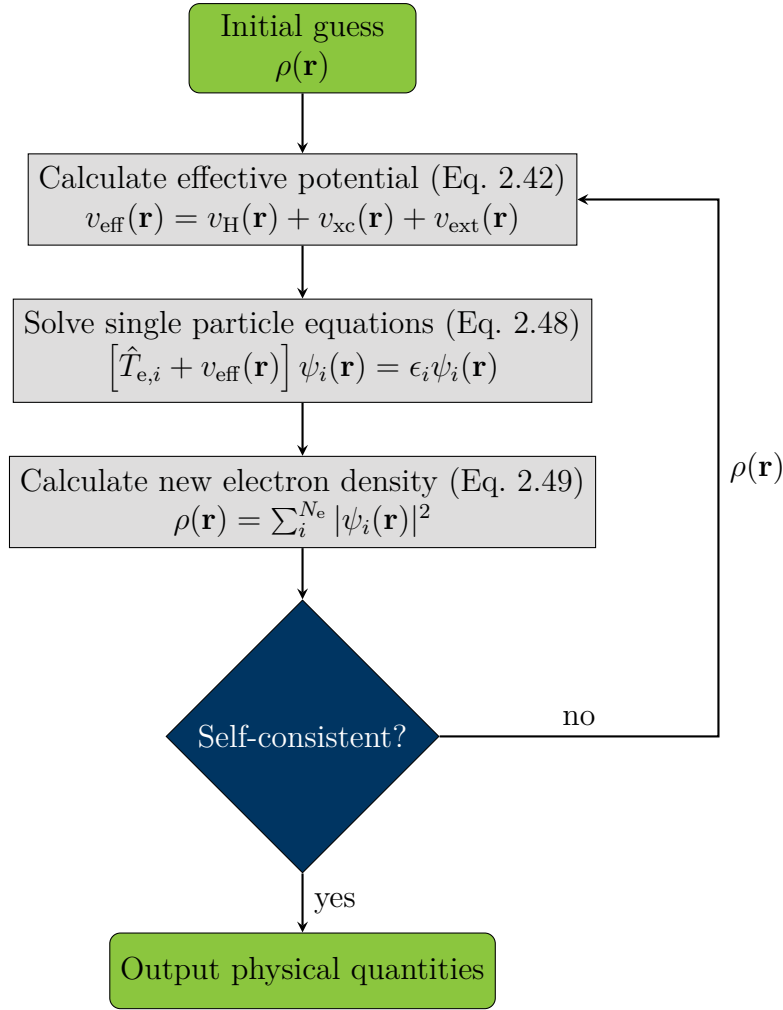


Figure 2.1.: Self-consistent solution of the Kohn-Sham equations.

energy functional is sketched in Fig. 2.1.

2.2.3. Exchange Correlation Functionals

$V_{xc}[\rho(\mathbf{r})]$ and $v_{xc}(\mathbf{r})$ have to be approximated for an application of the Kohn-Sham equations as they are unknown. The simplest approximation is the local density approximation (LDA). In this approximation, it is assumed that

$$V_{xc}^{\text{LDA}}[\rho(\mathbf{r})] = \int d\mathbf{r} \rho(\mathbf{r}) \epsilon_{xc}^{\text{LDA}}(\rho(\mathbf{r})), \quad (2.52)$$

where $\epsilon_{xc}^{\text{LDA}}$ takes the expression from the homogeneous electron gas, even though the electron density is not constant in space. The exchange part of the homogeneous electron gas was derived by Dirac [19] and the correlation part was estimated by Wigner [20] and later more accurately determined by

Monte Carlo methods [21, 22]. In the LDA, the electrons at position \mathbf{r} are considered as free electrons with an electron density $\rho(\mathbf{r})$. It seems to be evident that this approximation is only valid for electronic densities which slowly vary in space and was therefore introduced by Kohn and Sham for this regime. However, the LDA gave already very predictive results for many applications and the inclusion of gradients of the electron density provided by Kohn and Sham, known as gradient expansion approximation (GEA), gave disappointing and often less accurate results [23]. It was noticed afterwards that conditions for the exchange hole, a depletion of electron density around a given electron, can be derived, which are fulfilled in the LDA but not in the GEA [23]. These conditions are considered in the generalized gradient approximations (GGA), which can be expressed as

$$V_{\text{xc}}^{\text{GGA}}[\rho(\mathbf{r})] = \int d\mathbf{r} \rho(\mathbf{r}) \epsilon_{\text{xc}}^{\text{GGA}}(\rho(\mathbf{r}), \nabla\rho(\mathbf{r})). \quad (2.53)$$

A widely used GGA functional was developed by Perdew and Wang and is known as PW91 exchange correlation functional [24]. An improved version, which simplified the description of the exchange correlation was developed by Perdew, Burke and Ernzerhof and is known as PBE exchange correlation functional [25, 26].

Further improvements to the GGA functional have been developed. The class of meta-GGA functionals [27] additionally depends on the kinetic energy density and hybrid functionals [28] mix the exact exchange potential from the Hartree–Fock approximation (Eq. 2.30) with the results from the GGA functional. The development of exchange correlation potentials is still a field of ongoing research [29].

2.2.4. Crystal Periodicity

An ideal crystal is defined as a system where the atoms form a periodic arrangement. A lattice vector is given by

$$\mathbf{R} = n_1 \mathbf{a}_1 + n_2 \mathbf{a}_2 + n_3 \mathbf{a}_3, \quad (2.54)$$

where n_1, n_2, n_3 are integers and $\mathbf{a}_1, \mathbf{a}_2, \mathbf{a}_3$ are unit cell vectors. The electron-nucleus potential is periodic with respect to the lattice vectors,

$$v_{\text{e-n}}(\mathbf{r}) = v_{\text{e-n}}(\mathbf{r} + \mathbf{R}), \quad (2.55)$$

and thus also the electron density

$$\rho_{\text{e-n}}(\mathbf{r}) = \rho_{\text{e-n}}(\mathbf{r} + \mathbf{R}). \quad (2.56)$$

Bloch's theorem [30] states that the wave functions therefore fulfil

$$\psi(\mathbf{r} + \mathbf{R}) = \exp(i\mathbf{k}\mathbf{R})\psi(\mathbf{r}). \quad (2.57)$$

For this reason, the solutions of the stationary Schrödinger equation in a periodic potential can be written as Bloch functions

$$\psi_{\mathbf{k}}(\mathbf{r}) = \exp(i\mathbf{k}\mathbf{r})u_{\mathbf{k}}(\mathbf{r}), \quad (2.58)$$

where

$$u_{\mathbf{k}}(\mathbf{r}) = u_{\mathbf{k}}(\mathbf{r} + \mathbf{R}) \quad (2.59)$$

is a periodic function. The unit cell vectors in reciprocal space are defined as

$$\mathbf{b}_1 = \frac{2\pi}{V_{\text{cell}}}(\mathbf{a}_2 \times \mathbf{a}_3), \quad \mathbf{b}_2 = \frac{2\pi}{V_{\text{cell}}}(\mathbf{a}_3 \times \mathbf{a}_1), \quad \mathbf{b}_3 = \frac{2\pi}{V_{\text{cell}}}(\mathbf{a}_1 \times \mathbf{a}_2) \quad (2.60)$$

with

$$V_{\text{cell}} = \mathbf{a}_1 \cdot (\mathbf{a}_2 \times \mathbf{a}_3) \quad (2.61)$$

such that lattice vectors in reciprocal space are given by

$$\mathbf{G} = m_1\mathbf{b}_1 + m_2\mathbf{b}_2 + m_3\mathbf{b}_3. \quad (2.62)$$

Since

$$\psi_{\mathbf{k}}(\mathbf{r}) = \psi_{\mathbf{k}'}(\mathbf{r}) \quad (2.63)$$

for $\mathbf{k}' = \mathbf{k} + \mathbf{G}$, a solution for \mathbf{k}' is not required if $\psi_{\mathbf{k}}(\mathbf{r})$ is already known. For this reason, the first Brillouin zone is introduced, which is defined as the Wigner-Seitz cell [31] in reciprocal space. The eigenstates $\psi_{\mathbf{k}}$ have to be calculated only inside the first Brillouin zone as it contains all information.

The number of \mathbf{k} -points is infinite for an infinite large system. However, for practical calculations, the number of \mathbf{k} -points has to be set to a finite value to sample the first Brillouin zone. Schemes how to sample the \mathbf{k} -points of the first Brillouin zone were developed by Gilat and Raubenheimer [32], Chadi and Cohen [33] as well as Monkhorst and Pack [34]. After solving the Schrödinger equation for several \mathbf{k} -points, integration methods have to be applied to obtain e.g. the DOS. Frequently used integration methods were developed by Methfessel and Paxton [35] as well as Blöchl et al. [36].

2.2.5. Pseudo-Potentials

Bond formation is almost exclusively driven by valence electrons. However, the core electrons cannot be simply neglected in the solution of the Kohn-Sham equations (Eqs. 2.45, 2.48, 2.49) as they shield the attractive Coulomb interaction of the nuclei and repel valence electrons with the same angular momentum l and the magnetic quantum number m due to the Pauli exclusion

principle. Moreover, the electronic wave functions oscillate increasingly in the core region with increasing principal quantum number n as they have to be orthogonal to the wave functions with lower values for n . This increases the demands on the computational solution of the Kohn-Sham equations (Eqs. 2.45, 2.48, 2.49) as more basis functions are required to represent these features. An explicit treatment of the core electrons is therefore unwanted. A method to systematically remove the core electrons in electronic structure calculations are norm-conserving pseudo-potentials [37]. They replace the interaction of the nucleus and the core electrons with the valence electrons by a pseudopotential. As a consequence, the electronic wave functions oscillate less in the core region and the computational solution is simplified. An alternative is the linear augmented-plane-wave (LAPW) method [38]. A generalization of both methods is the projector augmented-wave (PAW) method [39]. It is a linear transformation between the pseudo wave functions $\tilde{\psi}_i(\mathbf{r})$ and the all-electron wave function $\psi_i(\mathbf{r})$,

$$\psi_i(\mathbf{r}) = \hat{\mathcal{T}}\tilde{\psi}_i(\mathbf{r}). \quad (2.64)$$

The transformation operator is given by

$$\hat{\mathcal{T}} = 1 + \sum_I \sum_{\alpha} (|\phi_I^{\alpha}\rangle - |\tilde{\phi}_I^{\alpha}\rangle) \langle \tilde{p}_I^{\alpha}|, \quad (2.65)$$

where I is the atom index and α the orbital index. The functions $\phi_I^{\alpha}(\mathbf{r})$ are the solutions of the all-electron Kohn-Sham equations (Eqs. 2.45, 2.48, 2.49) for a single atom (all-electron partial waves) and $\tilde{\phi}_I^{\alpha}(\mathbf{r})$ are the pseudo partial waves, which agree with the all-electron partial waves outside an augmentation region Ω_I and are a smooth continuation of the all-electron partial waves inside Ω_I . To achieve

$$\phi_I^{\alpha} = \hat{\mathcal{T}}\tilde{\phi}_I^{\alpha}, \quad (2.66)$$

the projector functions $\tilde{p}_I^{\alpha}(\mathbf{r})$ have to fulfil

$$\sum_{\alpha} |\tilde{\phi}_I^{\alpha}\rangle \langle \tilde{p}_I^{\alpha}| = 1 \quad (2.67)$$

within Ω_I . The radial functions of the $3p$ orbital of silicon, which were computed with the PBE-GGA functional (Sec. 2.2.3), are shown as an example in Fig. 2.2. The functions were computed by the program package GPAW (Sec. 2.2.7) and are accessible in Ref. 40. It can be noted that the all-electron partial wave function $\phi^{3p}(r)$ and the pseudo partial wave $\tilde{\phi}^{3p}(r)$ agree for distances larger than the augmentation sphere radius r_c^{3p} and differ inside the augmentation sphere, where the pseudo partial wave $\tilde{\phi}^{3p}(r)$ is smooth and the all-electron partial wave $\phi^{3p}(r)$ has to have a node to be orthogonal to the $2p$ all-electron partial wave. The projector function $\tilde{p}^{3p}(\mathbf{r})$ contributes only inside the augmentation sphere. The PAW method is usually combined with

the frozen core approximation, i.e. the core states are not modified from their atomic reference.

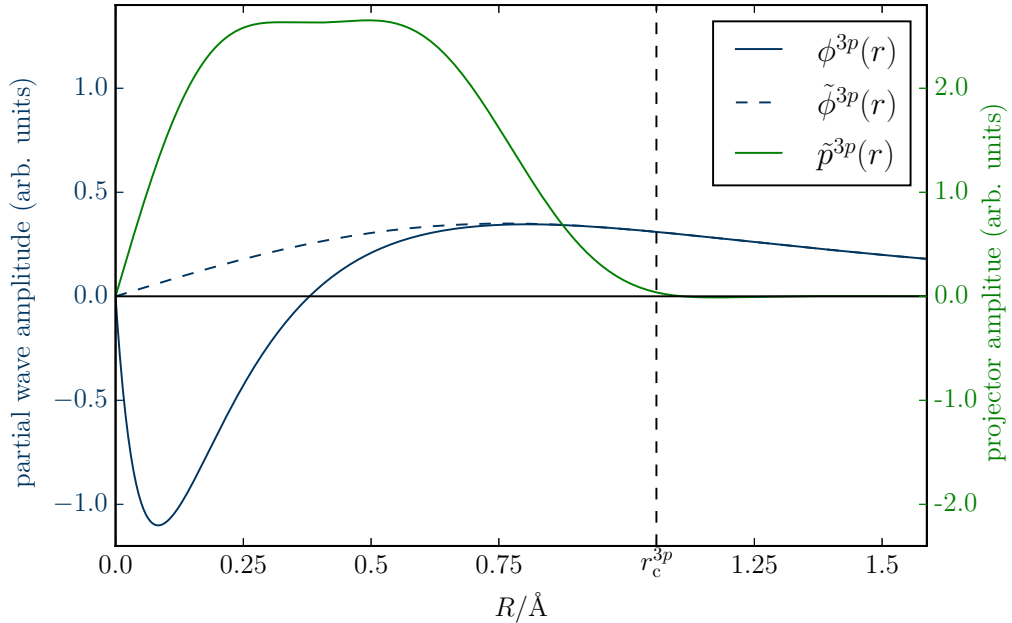


Figure 2.2.: Radial functions of the all-electron partial wave $\phi^{3p}(r)$, pseudo partial wave $\tilde{\phi}^{3p}(r)$ and projector function $\tilde{p}^{3p}(\mathbf{r})$ of the $3p$ orbital of Si computed with the PBE-GGA functional.

2.2.6. Basis Sets

The wave functions ψ_i have to be expanded in a basis for a practical calculation of the Kohn-Sham equations (Eqs. 2.45, 2.48, 2.49). Different basis sets are summarized in the following.

Plane-Wave Basis

A natural choice for the basis set are plane-waves in periodic systems. The basis functions have to be lattice periodic to expand the periodic Bloch function (Eq. 2.58). A complete set of lattice periodic plane-waves is given by $\{\exp(i\mathbf{G}\mathbf{r})\}$ such that

$$\psi_{\mathbf{k}}(\mathbf{r}) = \exp(i\mathbf{k}\mathbf{r}) \frac{1}{\sqrt{V_{\text{cell}}}} \sum_{\mathbf{G}} c_{\mathbf{k}+\mathbf{G}} \exp(i\mathbf{G}\mathbf{r}). \quad (2.68)$$

The set of lattice periodic plane-waves has to be truncated for practical implementations. This is done by defining an energy cut-off E_{cut} , which limits the

number of included reciprocal lattice vectors \mathbf{G} in the plane-wave expansion by

$$\frac{\hbar^2}{2m}|\mathbf{k} + \mathbf{G}|^2 \leq E_{\text{cut}}. \quad (2.69)$$

The choice of E_{cut} is a convergence parameter in plane-wave DFT calculations.

Atomic Orbital Basis

A chemistry motivated way to represent the wave functions is the expansion in a linear combination of atomic orbitals (LCAO). Atomic orbitals are written as [1]

$$\phi_{Ilm}(\mathbf{r}) = \phi_{Il}(r_I)Y_{lm}(\mathbf{r}_I), \quad (2.70)$$

where I labels the atom located at \mathbf{R}_I , n is the principal quantum number, l the angular momentum, m the magnetic quantum number and $\mathbf{r}_I = \mathbf{r} - \mathbf{R}_I$. The angular dependence is given by spherical harmonics $Y_{lm}(\mathbf{r}_I)$ and the radial dependence by $\phi_{Il}(r_I)$. The radial functions are expanded in a multiple- ζ basis, i.e.

$$\phi_{Il}(r_I) = \sum_z^{N_\zeta} k_{Ilz} R_{Ilz}(r_I). \quad (2.71)$$

A multiple- ζ basis consists of a finite set of N_ζ radial basis functions and is therefore incomplete. However, due to their chemistry motivated construction it is possible that less basis functions are required as compared to e.g. the plane-wave basis to obtain a desired accuracy [41]. A possible procedure to construct a multiple- ζ basis is the following [42, 43]: The single- ζ basis function is constructed by solving the Kohn-Sham equations (Eqs. 2.45, 2.48, 2.49) for an isolated atom. Afterwards, extra basis functions are created for the same angular momentum with the split-valence technique described in Ref. 42. The atomic orbitals (Eq. 2.70) can be applied to non-periodic systems. A basis which fulfils Bloch's theorem can be constructed by [30]

$$\phi_{\mathbf{k}Ilm}(\mathbf{r}) = \frac{1}{\sqrt{N}} \sum_{\mathbf{R}} \exp(i\mathbf{k}\mathbf{R}) \phi_{Ilm}(\mathbf{r} - \mathbf{R}_I - \mathbf{R}). \quad (2.72)$$

To neglect the core electrons in the atomic orbital basis, pseudo atomic orbitals (PAO) can be constructed according to Eq. 2.66. Moreover, the range of the orbitals can be constrained by a confinement potential. The onset of the confinement potential is controlled by the energy shift Δ_{PAO} of the confined orbital compared to the free electron orbital [43, 44].

Real-Space Grid

A different method is to abandon the usage of an explicit basis, and instead discretize the simulation cell such that all physical quantities are represented by numerical values at each grid point [45]. The number of grid points in each

Cartesian direction N_α determines the grid spacing vectors

$$\mathbf{h}_\alpha = \mathbf{a}_\alpha / N_\alpha. \quad (2.73)$$

2.2.7. Implementations

An assessment of the reliability of different DFT implementations can be found in Ref. 46. The authors conclude that most of the implementations agree very well. In the present work, the **GPAW** [43, 45, 47] and **VASP** [48–52] program packages are used, which give consistent results [46]. Both implementations are used with the PBE exchange correlation functional and the PAW method. The **GPAW** code supports all presented basis sets (plane-waves, atomic orbitals, real-space grid) and can therefore perform simulations on periodic and non-periodic systems. The **VASP** code only supports plane-waves and therefore only periodic systems can be simulated. The possibility of an expansion of the wave functions in an atomic orbital basis is essential for the downfolding procedure (Sec. 2.3.8) and was the criteria to use **GPAW** for this purpose. However, the stability and performance of the **VASP** program package was essential to perform high-throughput calculations (cf. Secs. 4.4, 5.4.1).

2.3. Tight-Binding

The TB method was developed before DFT and the assumption originally taken were purely empirical. However, the TB theory can be understood as an approximation to DFT. This section starts with an expansion of the DFT energy. Then, the atomic orbitals basis and the two-center approximation are introduced. Finally, the TB bond model is derived, which approximates the DFT energy by physical intuitive contributions.

2.3.1. Harris-Foulkes Functional and Expansion of Kohn-Sham Energy Functional

The Kohn-Sham energy functional (Eq. 2.40) can be expressed in shorthand notation as

$$E_{\text{KS}}[\rho] = \mathbf{T}\rho + \frac{1}{2}\mathbf{J}^{\text{H}}\rho\rho + V_{\text{xc}}[\rho] + \mathbf{V}^{\text{ext},e-n}\rho + V_{n-n}. \quad (2.74)$$

This is obtained by expanding the eigenstates in a non-orthogonal basis $\{\phi_i\}$,

$$\psi_n(\mathbf{r}) = \sum_i c_i^{(n)} \phi_i(\mathbf{r}), \quad (2.75)$$

where covariant and contravariant basis functions [53] are used, which are related by

$$\phi^j(\mathbf{r}) = \sum_i (S^{-1})_{ij} \phi_i(\mathbf{r}). \quad (2.76)$$

In this notation, the electron density is given by

$$\rho(\mathbf{r}) = \sum_{ij} \rho^{ij} \phi_i^*(\mathbf{r}) \phi_j(\mathbf{r}), \quad (2.77)$$

where

$$\rho_{ij} = \sum_n f_n c_i^{*(n)} c_j^{(n)} \quad (2.78)$$

is the electron density matrix. Equivalently, the electron density can also be written as

$$\rho(\mathbf{r}) = \sum_{ij} \rho_{ij} \phi^{*i}(\mathbf{r}) \phi^j(\mathbf{r}), \quad (2.79)$$

where the indices of the expansion coefficients are raised in the expression for the density matrix,

$$\rho^{ij} = \sum_n f_n c^{*(n)i} c^{(n)j}. \quad (2.80)$$

With these definitions, the kinetic energy functional (Eq. 2.50) is written in this notation as

$$\mathbf{T}\boldsymbol{\rho} = \sum_n f_n \langle \psi_n | \hat{T} | \psi_n \rangle = \sum_{ij} T_j^i \rho_i^j. \quad (2.81)$$

Similarly, the Hartree functional (Eq. 2.41) is written as

$$\frac{1}{2} \mathbf{J}^H \boldsymbol{\rho} \boldsymbol{\rho} = \sum_{ijkl} (J^H)_{ij}^{kl} \rho_l^j \rho_k^i \quad (2.82)$$

and the functional of the interaction with the external potential and the nuclei (Eq. 2.35) as

$$\mathbf{V}^{\text{ext,e-n}} \boldsymbol{\rho} = \sum_{ij} (V^{\text{ext,e-n}})_j^i \rho_i^j. \quad (2.83)$$

Only the exchange correlation functional is unknown and may formally be written as a series expansion

$$V_{\text{xc}}[\boldsymbol{\rho}] = \mathbf{V}^{\text{xc}} \boldsymbol{\rho} + \frac{1}{2} \mathbf{J}^{\text{xc}} \boldsymbol{\rho} \boldsymbol{\rho} + \frac{1}{6} \mathbf{K}^{\text{xc}} \boldsymbol{\rho} \boldsymbol{\rho} \boldsymbol{\rho} + \dots \quad (2.84)$$

Terms of the same order are grouped together and the Kohn-Sham energy functional can be written as

$$E_{\text{KS}}[\boldsymbol{\rho}] = V_{\text{n-n}} + (\mathbf{T} + \mathbf{V}^{\text{ext,e-n}}) \boldsymbol{\rho} + (\mathbf{J}^H + \mathbf{J}^{\text{xc}}) \boldsymbol{\rho} \boldsymbol{\rho} + \frac{1}{6} \mathbf{K}^{\text{xc}} \boldsymbol{\rho} \boldsymbol{\rho} \boldsymbol{\rho} + \dots \quad (2.85)$$

As discussed in Sec. 2.2.2, the Kohn-Sham equations (Eqs. 2.45, 2.48, 2.49) are solved recursively. Therefore, ρ may be regarded as an output electron density after one self-consistency cycle and ρ^0 is the corresponding input electron density. They are related by

$$\rho = \rho_0 + \delta\rho. \quad (2.86)$$

The Hamiltonian of the Kohn-Sham energy functional (Eq. 2.85) of the input electron density is given by

$$\mathbf{H}_0 = \frac{\partial E_{\text{KS}}}{\partial \rho} = \mathbf{T} + \mathbf{V}^{\text{ext},e-n} + (\mathbf{J}^{\text{H}} + \mathbf{J}^{\text{xc}})\rho_0 + \frac{1}{2}\mathbf{K}^{\text{xc}}\rho_0\rho_0 + \dots \quad (2.87)$$

With this definition, the energy functional may be rewritten as

$$\begin{aligned} E_{\text{KS}}[\rho] = & V_{n-n} + \mathbf{H}_0(\rho^0 + \delta\rho) + \frac{1}{2}(\mathbf{J}^{\text{H}} + \mathbf{J}^{\text{xc}})(-\rho^0\rho^0 + \delta\rho\delta\rho) + \\ & \frac{1}{6}\mathbf{K}^{\text{xc}}(-2\rho^0\rho^0\rho^0 + 3\rho^0\delta\rho\delta\rho + \delta\rho\delta\rho\delta\rho) + \dots \end{aligned} \quad (2.88)$$

The terms are collected again and the Kohn-Sham energy functional is written as

$$\begin{aligned} E_{\text{KS}}[\rho] = & V_{n-n} + \mathbf{H}_0\rho + V_{\text{xc}}[\rho_0(\mathbf{r})] - \int d\mathbf{r} \rho_0(\mathbf{r})v_{\text{xc}}(\mathbf{r}) - \\ & \frac{1}{2} \int d\mathbf{r} \rho_0(\mathbf{r})v_{\text{H}}(\mathbf{r}) + \mathcal{O}(\delta\rho^2), \end{aligned} \quad (2.89)$$

where all terms linear in $\delta\rho$ cancel out. This was noticed by Harris [54] and Foulkes [55] and is therefore named Harris-Foulkes functional

$$E_{\text{HF}}[\rho_0] = \sum_n f_n \epsilon_n + V_{\text{xc}}[\rho_0(\mathbf{r})] - \int d\mathbf{r} \rho_0(\mathbf{r})v_{\text{xc}}(\mathbf{r}) - \frac{1}{2} \int d\mathbf{r} \rho_0(\mathbf{r})v_{\text{H}}(\mathbf{r}) \quad (2.90)$$

with

$$\mathbf{H}_0\rho = \sum_n f_n \epsilon_n, \quad (2.91)$$

where ϵ_n are the eigenvalues of \mathbf{H}_0 .

During the self-consistency cycle, the Kohn-Sham energy functional (Eq. 2.85) is computed by

$$\begin{aligned} E_{\text{KS}}[\rho] = & V_{n-n} + \mathbf{H}_0\rho + \frac{1}{2}\mathbf{J}'\delta\rho\delta\rho + \frac{1}{6}\mathbf{K}'\delta\rho\delta\rho\delta\rho - \\ & \frac{1}{2}(\mathbf{J}^{\text{H}} + \mathbf{J}^{\text{xc}})\rho^0\rho^0 - \frac{1}{3}\mathbf{K}^{\text{xc}}\rho^0\rho^0\rho^0 + \dots \end{aligned} \quad (2.92)$$

and the Hamiltonian is updated by

$$\begin{aligned} \mathbf{H}_0 &= \mathbf{T} + \mathbf{V}^{\text{ext},e-n} + (\mathbf{J}^{\text{H}} + \mathbf{J}^{\text{xc}})\boldsymbol{\rho} + \frac{1}{2}\mathbf{K}^{\text{xc}}\boldsymbol{\rho}\boldsymbol{\rho} \\ &= \mathbf{H}_0 + \mathbf{J}'\delta\boldsymbol{\rho} + \frac{1}{2}\mathbf{K}'\delta\boldsymbol{\rho}\delta\boldsymbol{\rho} + \dots, \end{aligned} \quad (2.93)$$

where all terms which are proportional to $\delta\boldsymbol{\rho}$ are collected by \mathbf{J}' and all terms which are proportional to $\delta\boldsymbol{\rho}\delta\boldsymbol{\rho}$ by \mathbf{K}' .

The input electron density may be chosen as the overlap of spherical atomic-like electron densities,

$$\rho_0(\mathbf{r}) = \sum_I \rho_0^I(|\mathbf{r} - \mathbf{R}_I|) \quad (2.94)$$

and the Hartree potential (Eq. 2.43) can therefore be written like the electron-nucleus potential (Eq. 2.35) as sum of single particle potentials,

$$v_{\text{H}}^0(\mathbf{r}) = \sum_I v_{\text{H}}^I(\mathbf{r} - \mathbf{R}_I). \quad (2.95)$$

This is in general not possible for the exchange correlation potential since it includes higher order terms (Eq. 2.87). Therefore, the total effective potential (Eq. 2.45) can only be approximated as a sum of single particle potentials,

$$v_{\text{eff}}(\mathbf{r}) \approx \sum_I v_{\text{eff}}^I(\mathbf{r} - \mathbf{R}_I). \quad (2.96)$$

This approximation is used in Sec. 2.3.3.

2.3.2. Tight-Binding Approximations

Atomic Orbital Basis (Local Minimal Basis)

The atomic orbital basis was already introduced in Sec. 2.2.6 as a possible basis for the expansion of the DFT wave function. The TB method is based on the assumption that the electronic wave functions can be expressed as a linear combination of atomic orbitals (LCAO), where the basis functions are written according to Eq. 2.70 as

$$\phi_{Ilm}(\mathbf{r}) = \phi_{Il}(r_I)Y_{lm}(\hat{\mathbf{r}}_I). \quad (2.97)$$

The principal quantum number n is omitted, since in the TB theory typically only valence electrons are considered. In the TB method, the radial wave functions ϕ_{Il} are fixed, whereas they are calculated self-consistently in DFT. The spherical harmonics Y_{lm} are eigenstates of the angular momentum operator and they are in general complex. It is convenient to define real atomic orbitals from the real and imaginary part of the spherical harmonics for explicit calculations and for visualizations. These orbitals are named according

to their orientation in a three-dimensional Cartesian coordinate system. They are given by [56]

$$\begin{aligned}
 s &= Y_{00} & p_z &= Y_{10}, & d_{3z^2-r^2} &= Y_{20}, \\
 p_x &= \frac{Y_{1-1} - Y_{11}}{\sqrt{2}}, & d_{zx} &= \frac{Y_{2-1} - Y_{21}}{\sqrt{2}}, \\
 p_y &= \frac{Y_{1-1} + Y_{11}}{\sqrt{2}i}, & d_{yz} &= \frac{Y_{2-1} + Y_{21}}{\sqrt{2}i}, \\
 & & d_{x^2-y^2} &= \frac{Y_{2-2} + Y_{22}}{\sqrt{2}}, \\
 & & d_{xy} &= \frac{Y_{2-2} - Y_{22}}{\sqrt{2}i}
 \end{aligned}$$

for the first three values of the angular momentum l and are illustrated in Fig. 2.3.

Secular Equation

Expanding the wave function in LCAO Bloch states (Eq. 2.72),

$$\psi_{\mathbf{k}}(\mathbf{r}) = \sum_{l m n} c_{\mathbf{k}l m} \phi_{\mathbf{k}l m}(\mathbf{r}), \quad (2.98)$$

and applying it to the time-independent Schrödinger equation results in the secular equation[†]

$$\sum_{l' l' m'} (H_{l m, l' l' m'}(\mathbf{k}) - \epsilon_i(\mathbf{k}) S_{l m, l' l' m'}(\mathbf{k})) c_{\mathbf{k}l' l' m'} = 0, \quad (2.99)$$

where

$$H_{l m, l' l' m'}(\mathbf{k}) = \sum_{\mathbf{R}} H_{l m, l' l' m'}(\mathbf{R}) \exp(i\mathbf{k}\mathbf{R}) \quad (2.100)$$

with

$$H_{l m, l' l' m'}(\mathbf{R}) = \int d\mathbf{r} \phi_{l m}^*(\mathbf{r} - \mathbf{R}_I) \hat{H} \phi_{l' l' m'}(\mathbf{r} - (\mathbf{R}_{I'} + \mathbf{R})) \quad (2.101)$$

and

$$S_{l m, l' l' m'}(\mathbf{k}) = \sum_{\mathbf{R}} S_{l m, l' l' m'}(\mathbf{R}) \exp(i\mathbf{k}\mathbf{R}) \quad (2.102)$$

with

$$S_{l m, l' l' m'}(\mathbf{R}) = \int d\mathbf{r} \phi_{l m}^*(\mathbf{r} - \mathbf{R}_I) \phi_{l' l' m'}(\mathbf{r} - (\mathbf{R}_{I'} + \mathbf{R})). \quad (2.103)$$

[†]To show that the matrix elements are non-zero only for $\mathbf{k} = \mathbf{k}'$, one has to use translational invariance and $\sum_{\mathbf{R}} \exp(i\mathbf{R}(\mathbf{k} - \mathbf{k}')) \propto \delta(\mathbf{k} - \mathbf{k}')$.

The secular equation has to be solved for each value of \mathbf{k} and the \mathbf{k} -point sampling and integration methods which were introduced in Sec. 2.2.4 can be used.

2.3.3. Matrix Elements

As shown in Sec. 2.3.1, the Hamiltonian acting on the TB wave functions can be approximated as

$$\hat{H} = \hat{T}_e + \sum_I v_{\text{eff}}^I(\mathbf{r} - \mathbf{R}_I). \quad (2.104)$$

The overlap matrix elements (Eq. 2.103) are classified in one-center integrals and two-center integrals. The orbitals are at the same site ($\mathbf{R} = 0$ and $\mathbf{R}_I = \mathbf{R}_{I'}$) in one-center integrals and they are at different sites in two-center integrals. Similarly, the Hamiltonian matrix elements (Eq. 2.101) may be classified as one-, two- and three-center integrals. The two orbitals and the single particle potential $v_{\text{eff}}^I(\mathbf{r} - \mathbf{R}_I)$ are located at the same site I in one-center integrals. Two-center integrals are given by either two orbitals at different sites and a potential contribution from one of the two sites or by two orbitals at the same site and a potential contribution from a different site. In three-center integrals, the orbitals and the single particle potential are all located at different sites. The three-center integrals and the two-center integrals with both orbitals at the same site depend on the atomic structure. These integrals are neglected in the two-center approximation.

2.3.4. Two-Center Approximation

The number of two-center integrals is equal to $(2l + 1)^2$ for a pair of atoms where each atom has $2l + 1$ orbitals. However, Slater and Koster showed that the number of independent two-center integrals can be significantly reduced in the two-center approximation by taking into account the symmetry of the spherical harmonics [57]. In a coordinate system where the interatomic vector $\mathbf{R}_{IJ} = \mathbf{R}_I - \mathbf{R}_J$ is parallel to quantization axis \mathbf{e}_z (bond orientated coordinate system), only Hamiltonian and overlap matrix elements are non-zero whose magnetic quantum numbers m and m' are equal to each other. This can be geometrically verified by overlapping the atomic orbitals in Fig. 2.3. These non-vanishing matrix elements of the Hamiltonian matrix (overlap matrix) are referred to as bond integrals (overlap integrals). For example, it can be seen that the overlap of the p_x and p_y orbital with the s orbital form positive and negative contributions, which exactly cancel each other. However, the overlap of the s and p_z orbital is finite. The interatomic vector \mathbf{R}_{IJ} may be

expressed in terms of direction cosines

$$\begin{aligned}\alpha &= \frac{\mathbf{R}_{IJ} \cdot \mathbf{e}_x}{|\mathbf{R}_{IJ}|} \\ \beta &= \frac{\mathbf{R}_{IJ} \cdot \mathbf{e}_y}{|\mathbf{R}_{IJ}|} \\ \gamma &= \frac{\mathbf{R}_{IJ} \cdot \mathbf{e}_z}{|\mathbf{R}_{IJ}|}.\end{aligned}\tag{2.105}$$

and each orbital in the global coordinate system may be expanded as a linear combination of orbitals in the bond coordinate system. Consequently, all two-center matrix elements of the Hamiltonian matrix (overlap matrix) can be expanded in bond integrals (overlap integrals). Explicit formulas are given in Refs. 57, 58. The transformation from the bond coordinate system to the global coordinate system can also be performed with rotation matrices [56, 59],

$$H_{IJ} = R(\phi_{IJ}, \theta_{IJ}) H_{IJ}^{(b)} R(\phi_{IJ}, \theta_{IJ})^T,\tag{2.106}$$

where $H_{IJ}^{(b)}$ is the pairwise Hamiltonian matrix in the bond orientated coordinate system. The angles ϕ_{IJ} and θ_{IJ} measure the orientation of the vector \mathbf{R}_{IJ} with respect to the global coordinate system. The bond and overlap integrals are named according to the angular momentum quantum number (s , p , d , ...) and the absolute value of the common magnetic quantum number (σ , π , δ , ...) of the contributing orbitals. For example, one s orbital and one p orbital can only form an $sp\sigma$ bond integral and two p orbitals can form $pp\sigma$ and $pp\pi$ bond integrals.

2.3.5. Tight-Binding Bond Model

With the expansion of the wave function in terms of atomic orbitals, the electron density can be written as

$$\rho(\mathbf{r}) = \sum_{Ilm, I'l'm'} \rho_{I'l'm'}^{Ilm} \phi_{Ilm}(\mathbf{r}) \phi_{I'l'm'}^{I'l'm'}(\mathbf{r}),\tag{2.107}$$

where

$$\rho_{I'l'm'}^{Ilm} = \sum_n f_n (c_n^{*(n)})^{Ilm} (c_n^{(n)})_{I'l'm'}\tag{2.108}$$

is the electron density matrix, which can be obtained by \mathbf{k} -point integration (Sec. 2.2.4) for periodic systems. The total number of electrons is given by

$$N = \sum_n f_n \langle \psi_n | \psi_n \rangle = \sum_{Ilm} \rho_{Ilm}^{Ilm},\tag{2.109}$$

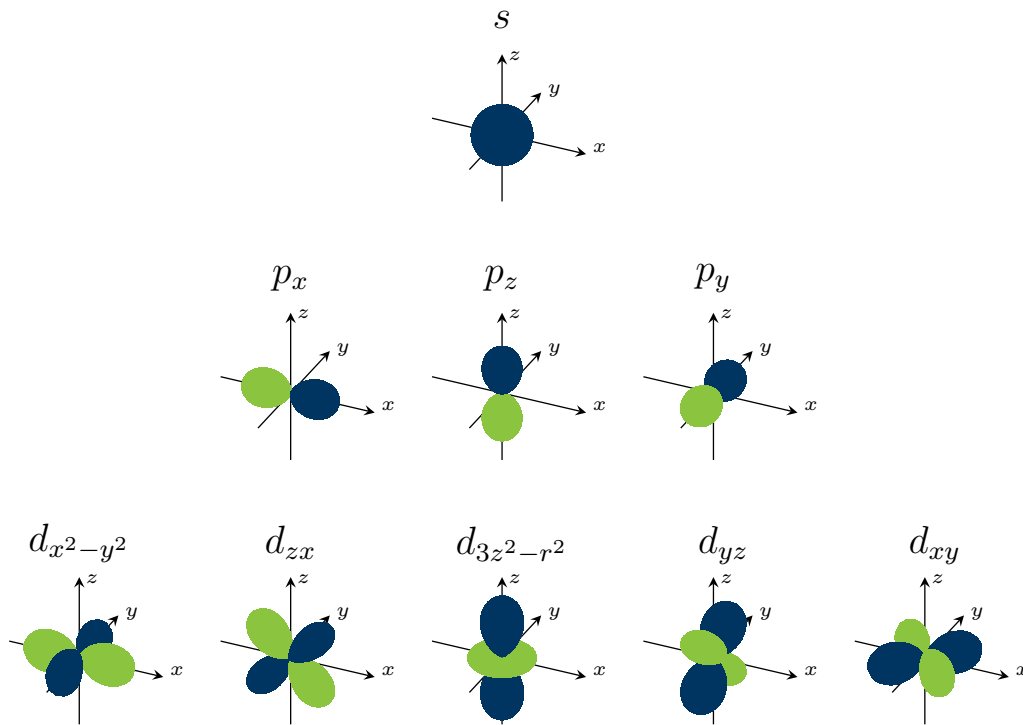


Figure 2.3.: Real atomic orbitals. Positive values are shown in blue, negative values in green.

where

$$N_{Ilm} = \rho_{Ilm}^{Ilm} = \sum_{I'l'm'} \rho^{IlmI'l'm'} S_{I'l'm'Ilm} \quad (2.110)$$

are the Mulliken charges, which may be interpreted as the charge on orbital Ilm .

In the TB bond model [60], the Kohn-Sham energy functional in representations of Eq. 2.92 is expanded up to second-order in $\delta\rho$. Moreover, the change in the electron density $\delta\rho$ is assumed to be only given by a change in the Mulliken charges (Eq. 2.110), i.e.

$$q_{Ilm} = \delta\rho_{Ilm}^{Ilm} = N_{Ilm} - N_{Ilm}^0. \quad (2.111)$$

Consequently, the Kohn-Sham energy functional is approximated by

$$\begin{aligned} U_{\text{TB}} = & \sum_{IlmI'l'm'} (H^0)_{I'l'm'}^{Ilm} \rho_{Ilm}^{I'l'm'} + \frac{1}{2} \sum_{IlmI'l'm'} J_{IlmI'l'm'} q_{Ilm} q_{I'l'm'} \\ & - \frac{1}{2} \sum_{IlmI'l'm'} J_{IlmI'l'm'} N_{Ilm}^0 N_{I'l'm'}^0 \end{aligned} \quad (2.112)$$

and the Hamiltonian matrix can be written as

$$H_{IlmI'l'm'} = H_{IlmI'l'm'}^0 + \sum_{I''l''m''} J_{IlmI''l''m''} S_{IlmI'l'm'} q_{I''l''m''}. \quad (2.113)$$

This equation reduces to

$$E_{Ilm} = E_{Ilm}^0 + \sum_{I''l''m''} J_{IlmI''l''m''} q_{I''l''m''} \quad (2.114)$$

for the diagonal elements of the Hamiltonian matrix (onsite levels) such that the change of the Hamiltonian matrix can be rationalized to a change of the onsite levels,

$$H_{IlmI'l'm'} = H_{IlmI'l'm'}^0 + (E_{Ilm} - E_{Ilm}^0) S_{IlmI'l'm'}. \quad (2.115)$$

During the self-consistency loop, the Mulliken charges may change. This induces a change of the onsite levels. The self-consistency criteria is met when the Mulliken charges or the onsite levels change less than a given tolerance. Alternatively, a different self-consistency procedure can be defined by directly varying the onsite levels such that

$$\frac{\partial U_{\text{TB}}}{\partial E_{Ilm}} = 0. \quad (2.116)$$

The TB bond model represents the energy expression (Eq. 2.112) as a sum of physically intuitive energy contributions, which is given by [61–63]

$$U_{\text{TB}} = U_{\text{bond}} + U_{\text{prom}} + U_{\text{rep}} + U_{\text{es}} + U_{\text{ion}} + U_{\text{atoms}}. \quad (2.117)$$

The binding (cohesive) energy is obtained by subtracting the energy of the free atoms U_{atoms} ,

$$U_{\text{B}} = U_{\text{bond}} + U_{\text{prom}} + U_{\text{rep}} + U_{\text{es}} + U_{\text{ion}}. \quad (2.118)$$

The bond energy is associated with the formation of bonds between different orbitals and is given by

$$U_{\text{bond}} = U_{\text{band}} - \sum_{Ilm} E_{Ilm}^0 N_{Ilm}, \quad (2.119)$$

where

$$U_{\text{band}} = \sum_{IlmI'l'm'} \left(H^0 \right)_{I'l'm'}^{Ilm} \rho_{Ilm}^{I'l'm'} = \sum_n f_n \epsilon_n \quad (2.120)$$

is the band energy, which is used in the TB band model [64, 65].

The density matrix is also sometimes written as

$$\rho_{Ilm}^{I'l'm'} = \Theta_{Ilm}^{I'l'm'} \quad (2.121)$$

and referred to as bond-order. It may be interpreted as the strength of a bond [66] as it is proportional to the difference of occupied bonding N_+ and antibonding states N_- ,

$$\Theta_{IlmI'l'm'} = \frac{1}{2}(N_+ - N_-), \quad (2.122)$$

where the bonding and antibonding states are given by

$$|\varphi_{\pm}\rangle = \frac{1}{\sqrt{2}} (|\varphi_{Ilm}\rangle \pm |\varphi_{I'l'm'}\rangle). \quad (2.123)$$

With the definition of the DOS,

$$n(E) = \sum_n \langle \psi_n | \psi_n \rangle \delta(\epsilon_n - E), \quad (2.124)$$

and the local DOS [67],

$$\begin{aligned} n(E) &= \sum_{Ilm} \sum_n \langle \psi_n | \varphi_{Ilm} \rangle \langle \varphi^{Ilm} | \psi_n \rangle \delta(\epsilon_n - E) \\ &= \sum_{Ilm} n_{Ilm}(E), \end{aligned} \quad (2.125)$$

the bond energy may also be written in the onsite representation,

$$U_{\text{bond}} = \sum_{lm} \int_{-\infty}^{E_F} dE (E - E_{lm}^0) n_{lm}(E), \quad (2.126)$$

where E_F is the Fermi energy.

The promotion energy is the energy which is needed for the repopulation of atomic levels. It is given by

$$U_{\text{prom}} = \sum_{lm} E_{lm}^0 (q_{lm} - \Delta q_{lm}). \quad (2.127)$$

The charge $\sum_{lm} \Delta q_{lm}$ is the additional charge on atom I due to interatomic charge transfer. The repulsive energy

$$U_{\text{rep}} = -\frac{1}{2} \sum_{lmI'l'm'}^{I \neq I'} J_{lmI'l'm'} N_{lm}^0 N_{I'l'm'}^0 + U_{\text{prep}} + U_{\text{n-n}} \quad (2.128)$$

summarizes the intraatomic elements of the double-counting second-order term. The preparation energy

$$U_{\text{prep}} = \sum_{lm} (E_{lm}^0 - E_{lm}^{\text{at}}) N_{lm}^0 \quad (2.129)$$

measures the energy change due to a change of the atomic onsite levels from the free atom value E_{lm}^{at} to E_{lm}^0 and the nucleus-nucleus interaction is labelled $U_{\text{n-n}}$.

In the TB bond model, it is assumed that only the total charge on each atom

$$q_I = \sum_{lm} q_{lm} \quad (2.130)$$

enters the second-order term, which is split into the electrostatic interaction

$$U_{\text{es}} = \frac{1}{2} \sum_{IJ}^{I \neq J} J_{IJ} q_I q_J \quad (2.131)$$

and the ionic onsite contribution

$$U_{\text{ion}} = \sum_I \bar{E}_I q_I + \sum_I J_{II} q_I^2, \quad (2.132)$$

where

$$\bar{E}_I = \sum_{lm} \frac{E_{lm}^{(0)} \Delta q_{lm}}{q_I} \quad (2.133)$$

is the electronegativity and J_{II} is related to the Hubbard parameter [68] U as it measures the resistance against charge transfer. The energy of the free

atoms is given by

$$U_{\text{atoms}} = \sum_{ilm} E_{ilm}^{\text{at}} N_{ilm}^0 - \frac{1}{2} \sum_{ilm'l'm'} J_{ilmI'l'm'} N_{ilm}^0 N_{I'l'm'}^0 \quad (2.134)$$

such that the binding energy (Eq. 2.118) is approximated by

$$\begin{aligned} U_B &= U_{\text{TB}} - U_{\text{atoms}} \\ &= \sum_{ilmI'l'm'} \left(H^0 \right)_{I'l'm'}^{ilm} \rho_{ilm}^{I'l'm'} - \sum_{ilm} E_{ilm}^{\text{at}} N_{ilm}^0 \\ &\quad - \frac{1}{2} \sum_{ilmI'l'm'}^{I \neq I'} J_{ilmI'l'm'} N_{ilm}^0 N_{I'l'm'}^0 + \frac{1}{2} \sum_{IJ} J_{IJ} q_I q_J \end{aligned} \quad (2.135)$$

in the TB bond model.

2.3.6. Orthogonal Tight-Binding

The atomic orbital basis used in TB (Sec. 2.3.2) is by definition non-orthogonal. However, an orthogonal basis can be constructed with a Löwdin transformation [69],

$$S^{1/2} |\phi_{ilm}\rangle = |\phi_{ilm}^{\text{orth}}\rangle, \quad (2.136)$$

such that the secular equation (Eq. 2.99) transforms to

$$\sum_{I'l'm'} \left(H_{ilm,I'l'm'}^{\text{orth}}(\mathbf{k}) - \epsilon_i(\mathbf{k}) \right) c_{\mathbf{k}I'l'm'}^{\text{orth}} = 0, \quad (2.137)$$

where

$$H^{\text{orth}} = S^{-1/2} H S^{-1/2}. \quad (2.138)$$

The energy expressions in the TB bond model (Sec. 2.3.5) remain unchanged, except that covariant and contravariant indices do not have to be distinguished anymore. With the definition

$$S^{-1/2} = 1 - \frac{1}{2} \mathfrak{S}, \quad (2.139)$$

the Löwdin transformed Hamiltonian matrix may also be expressed as

$$H^{\text{orth}} = H - \frac{1}{2} (\mathfrak{S}H + H\mathfrak{S}) + \frac{1}{4} \mathfrak{S}H\mathfrak{S}. \quad (2.140)$$

This formula may be used for an approximate Löwdin transformation [70] by setting

$$\mathfrak{S} \approx S - 1, \quad (2.141)$$

which corresponds to a truncated Taylor expansion of $S^{-1/2}$.

The energy contributions of the TB bond model (Eq. 2.117) are in general

different in the non-orthogonal and in the Löwdin orthogonalized representation. However, the band energy is invariant to the orthogonalization. The difference of the preparation energy in the orthogonal and non-orthogonal model is referred to as overlap repulsion and is given by

$$\begin{aligned}
 U_{\text{overlap}} &= U_{\text{prep}}^{\text{orth}} - U_{\text{prep}} \\
 &= -\frac{1}{2} \sum_{Ilm} \left[\sum_{I'l'm'} (H_{IlmI'l'm'} \mathfrak{S}_{I'l'm'Ilm} + \mathfrak{S}_{IlmI'l'm'} H_{I'l'm'Ilm}) \right. \\
 &\quad \left. - \frac{1}{2} \sum_{I''l''m''} \mathfrak{S}_{IlmI''l''m''} H_{I''l''m''I'l'm'} \mathfrak{S}_{I'l'm'Ilm} \right] N_{Ilm}^0.
 \end{aligned} \tag{2.142}$$

The overlap repulsion is added to the repulsive energy in the orthogonal TB model,

$$U_{\text{rep}}^{\text{orth}} = U_{\text{rep}} + U_{\text{overlap}}. \tag{2.143}$$

It may be interpreted as an additional repulsive contribution due to the orthogonalization of the atomic orbitals, which repel each other when they are brought together [71]. Due to the non-pairwise behaviour, it may dominate the repulsive energy contribution in an orthogonal TB model (Sec. 3.3.5).

2.3.7. Forces in the Tight-Binding Bond Model

The forces on atom K can be calculated by the negative gradient of the binding energy, $\mathbf{F}_K = -\nabla_K U_B$. Due to the Hellmann-Feynman theorem [72, 73], the gradient with respect to the band energy can be calculated from gradients of the Hamiltonian and overlap matrix elements only and is explicitly given by [6]

$$\begin{aligned}
 \nabla_K U_{\text{band}} &= \nabla_K \left(\sum_{IlmI'l'm'} (H^0)_{I'l'm'}^{Ilm} \rho_{Ilm}^{I'l'm'} \right) \\
 &= \sum_n \langle \psi_n | \hat{\rho} \nabla_K \hat{H} | \psi_n \rangle \\
 &= \sum_{IlmI'l'm'} (\nabla_K H^0)_{I'l'm'}^{Ilm} \rho_{Ilm}^{I'l'm'} \\
 &\quad - \sum_n \sum_{IlmI'l'm'} f_n(c^{*(n)})^{Ilm} (c^{(n)})_{I'l'm'} \nabla_K S_{Ilm}^{I'l'm'},
 \end{aligned} \tag{2.144}$$

where the last term vanishes in orthogonal TB models. If the onsite levels are self-consistent (Eq. 2.116), the forces in the orthogonal TB model are given by

$$\begin{aligned}
 \nabla_K U_B &= \sum_{IlmI'l'm'} \rho_{IlmI'l'm'} \nabla_K H_{IlmI'l'm'} \\
 &\quad + \frac{1}{2} \sum_{IlmI'l'm'} (\nabla_K J_{IlmI'l'm'}) q_{Ilm} q_{I'l'm'} + \nabla_K U_{\text{rep}}.
 \end{aligned} \tag{2.145}$$

The generalization to the non-orthogonal case is straightforward.

2.3.8. Downfolding Procedure

The most important ingredient for the TB bond model is the reference Hamiltonian matrix H^0 , from which the electron density matrix can be calculated. Downfolding methods for the construction of H^0 based on the results of DFT calculation have been developed [74, 75]. An alternative to downfolding methods is the reduced TB approximation, which is discussed in Sec. 3.1.2. It requires, however, much stronger approximations than the downfolding methods. In the following, the method of Ref. 74 is introduced:

Firstly, a DFT reference state has to be constructed. This can be done by the solution of the Kohn-Sham equations (Eqs. 2.45, 2.48, 2.49) in the Harris-Foulkes approximation (Eq. 2.90) for a particular reference system. The eigenstates may be expanded in a multiple- ζ LCAO basis (Eq. 2.70), where the number of radial functions per orbital controls the accuracy of the approximation,

$$\psi_n(\mathbf{r}) = \sum_{l m z} c_{l m z}^{(n)} \phi_{l m z}(\mathbf{r}). \quad (2.146)$$

However, in the TB approximation only one radial function per orbital is used (minimal basis). One may therefore formally write each TB minimal basis function as a linear combination of the multiple- ζ orbitals,

$$\varphi_{l m}(k) = \sum_z k_{l m z} \phi_{l m z}(\mathbf{r}). \quad (2.147)$$

The downfolding procedure maximizes the projection of the minimal basis onto the DFT eigenstates expanded in a multiple- ζ basis. The projection may be expressed as

$$P = \max_k \frac{1}{N_e} \sum_n f_n \langle \psi_n | \hat{P}(k) | \psi_n \rangle, \quad (2.148)$$

where

$$\hat{P}(k) = \sum_{l m} |\varphi_{l m}(k)\rangle \langle \varphi_{l m}(k)| \quad (2.149)$$

is the projection operator and f_n is the occupation of eigenstate ψ_n . The occupation number is determined by the Fermi distribution

$$f(E) = \frac{1}{\exp((E - \mu)/k_B T) + 1}, \quad (2.150)$$

where the temperature T is a parameter of the downfolding procedure which controls the relevance of eigenstates which are not occupied at 0 K. The coefficients $k_{l m z}$ are obtained by numerical optimization of the non-linear problem (Eq. 2.148).

From the optimized minimal basis, the TB overlap and Hamiltonian matrix can be constructed,

$$\begin{aligned} S_{IlmI'l'm'} &= \langle \varphi_{Ilm} | \varphi_{I'l'm'} \rangle, \\ H_{IlmI'l'm'} &= \langle \varphi_{Ilm} | \hat{H} | \varphi_{I'l'm'} \rangle. \end{aligned} \quad (2.151)$$

Extensions to the Downfolding Procedure

The downfolding procedure is able to construct an optimal minimal basis function for each orbital type considered in the LCAO basis set. However, the LCAO basis may include more orbital types than usually used in TB even if some of them are excluded by pseudopotentials or the PAW method (Sec. 2.2.5). A matrix minimization technique is developed in the present work to obtain TB models of reduced basis size that reproduce the relevant eigenvalues of the minimal basis Hamiltonian while keeping the change in the eigenstates minimal. The optimal minimal basis obtained from the downfolding procedure is divided into basis functions which should be included (TB) and which should not be included (TB-omit) in the TB model according to the selected chemical description of the elements,

$$\{|\varphi^{Ilm}\rangle\} = \left\{ \{|\varphi^{Ilm}\rangle^{\text{TB}}\}, \{|\varphi^{I'l'm'}\rangle^{\text{TB-omit}}\} \right\}. \quad (2.152)$$

The normalized eigenstates of the minimal basis system are then written as

$$|\psi_n\rangle^{(1-\zeta)} = \sum_{Ilm} c_{Ilm}^{(n),\text{ini}} |\varphi^{Ilm}\rangle^{\text{TB}} + \sum_{I'l'm'} c_{I'l'm'}^{(n),\text{ini}} |\varphi^{I'l'm'}\rangle^{\text{TB-omit}}, \quad (2.153)$$

where summation over co- and contravariant indices is used. An initial guess for the eigensystem of the TB part of the minimal basis system is constructed by removing the basis functions which should not be included (TB-omit) in the TB model and by normalization,

$$|\psi_n\rangle^{\text{ini}} = \sum_{Ilm} \frac{1}{\|\psi_n^{\text{ini}}\|^{1/2}} c_{Ilm}^{(n),\text{ini}} |\varphi^{Ilm}\rangle^{\text{TB}}. \quad (2.154)$$

In general, the initial guess for the eigensystem is not orthogonal. However, an initial guess for the TB Hamiltonian matrix with the desired eigenspectrum is constructed by

$$H_{IlmI'l'm'}^{\text{TB,ini}} = \sum_n \frac{1}{\|\psi_n^{\text{ini}}\|} c_{Ilm}^{(n),\text{ini}} c_{I'l'm'}^{(n),\text{ini}} \epsilon^{(n)}, \quad (2.155)$$

where $\epsilon^{(n)}$ is the eigenenergy corresponding to the minimal basis eigenstate $|\psi_n\rangle^{(1-\zeta)}$. The initial guess for TB Hamiltonian matrix is diagonalized and an

intermediate TB eigensystem is obtained,

$$|\psi_n\rangle^{\text{int}} = \sum_{Ilm} c_{Ilm}^{(n),\text{int}} |\varphi^{Ilm}\rangle^{\text{TB}}. \quad (2.156)$$

The eigensystem is now orthogonal. However, a rotation of the eigensystem does not change the eigenenergies. In order to remove this degree of freedom, the intermediate eigensystem is rotated,

$$|\psi_n\rangle^{\text{TB}} = \hat{R} |\psi_n\rangle^{\text{int}}, \quad (2.157)$$

such that it is closest to the minimal basis eigensystem. This is done by a numerical optimization which minimizes

$$\sum_{nn'} \left(\delta_{nn'} - {}^{\text{TB}} \langle \psi_n | \psi_{n'} \rangle^{\text{int}} \right)^2. \quad (2.158)$$

The optimum defines the optimal TB eigenstates

$$|\psi_n\rangle^{\text{TB}} = \hat{R} |\psi_n\rangle^{\text{int}} = \sum_{Ilm} c_{Ilm}^{(n),\text{TB}} |\varphi^{Ilm}\rangle^{\text{TB}}. \quad (2.159)$$

Similar to Eq. 2.155, the optimal TB Hamiltonian is constructed by

$$H_{IlmI'l'm'}^{\text{TB}} = \sum_n c_{Ilm}^{(n),\text{TB}} c_{I'l'm'}^{(n),\text{TB}} \epsilon^{(n)}. \quad (2.160)$$

An orthogonal TB model is created by a Löwdin transformation [69],

$$H^{\text{TB,orth}} = S^{-1/2} H^{\text{TB}} S^{-1/2}. \quad (2.161)$$

2.3.9. Parametrization

The downfolding procedure can be used to parameterize the matrix elements of the Hamiltonian matrix H and the overlap matrix S . For this purpose, the downfolding procedure may be applied on one or several structures and a distance-dependent function may be fitted to the individual values of each matrix element. Applications can be found in Refs. 63, 76–79. A common approximation is to use constant values for the onsite matrix elements of the Hamiltonian matrix $E_{Ilm} = H_{IlmIlm}$ in an orthogonal TB model. Moreover, the repulsive energy is often approximated by a simple pair potential

$$U_{\text{rep}}(R_{IJ}) = \frac{1}{2} \sum_I \sum_{J \neq I} V_{IJ}(R_{IJ}), \quad (2.162)$$

which is parametrized to reference values from DFT or experiment. Sometimes specific states are neglected in the electronic structure description and are compensated by explicit functions which depend on the atomic structure

of the material. Furthermore, the interaction range of different atoms has to be limited by a finite cut-off value r_{cut} for practical calculations. This can be achieved by multiplication of the bond integrals, overlap matrix elements and pair potentials with a cut-off function. The cosine function

$$f_{\text{cut}}(R_{IJ}) = \begin{cases} 1 & \text{if } R_{IJ} \leq (r_{\text{cut}} - d_{\text{cut}}) \\ 0 & \text{if } R_{IJ} > r_{\text{cut}} \\ \frac{1}{2} \left(\cos \left(\pi \left[\frac{R_{IJ} - (r_{\text{cut}} - d_{\text{cut}})}{d_{\text{cut}}} \right] \right) + 1 \right) & \text{else} \end{cases} \quad (2.163)$$

is a typical choice, which smoothly goes from 1 to 0 between $r_{\text{cut}} - d_{\text{cut}}$ and r_{cut} . The parametrization process of analytic BOPs (Sec. 2.4) is analogous to the parametrization process of TB models and is further developed and evaluated in Sec. 5 of this work.

2.3.10. Summary of Calculation Steps

A flowchart of a self-consistent TB calculation is shown in Fig. 2.4. The calculation is initialized with a distance-dependent description of the repulsive energy contribution and the intraatomic Hamiltonian and overlap matrix elements in the bond coordinate system. Initial onsite levels are guessed. Afterwards, the intraatomic Hamiltonian and overlap matrix elements in the global coordinate system are calculated. The matrices are transformed into reciprocal space and the density matrix is calculated by \mathbf{k} -point integration methods. From the change of the Mulliken charges, new onsite levels are calculated and the previous steps are repeated until the self-consistency criteria is reached. Finally, the separate energy contributions and the forces are calculated.

2.4. Analytic Bond-Order Potentials

Analytic BOPs provide a systematic moments expansion of the local DOS of a TB model and allow for energy and force calculations. The computational time of the method scales linearly with the system size and therefore enables calculations for system sizes which are not feasible to calculate with the TB method, which has a cubic scaling with the system size.

The moments itself are descriptors of the shape of the local DOS and can be related to the atomic surrounding of an atom via the moments theorem. This is discussed in the first part of this section and is important for Sec. 4. Afterwards, the moments expansion of the local DOS is conducted and methods to terminate the expansion are presented. Then, the calculation of energies and forces as well as the self-consistency procedure are discussed. Finally, the steps during a BOP calculation are summarized.

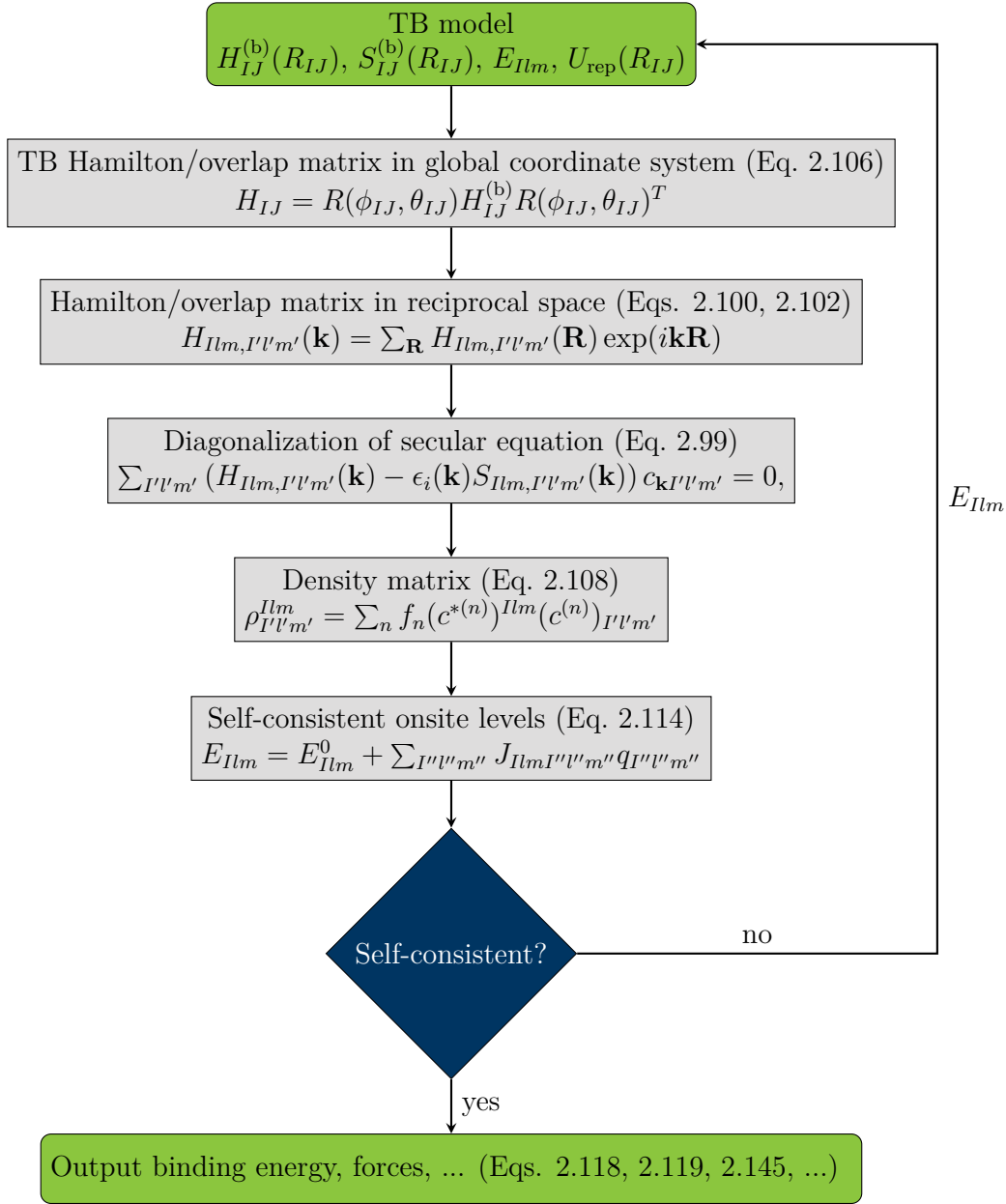


Figure 2.4.: Flowchart of a self-consistent TB calculation.

2.4.1. Moments of the Density of States

Moments are routinely used in statistics as shape parameters of probability distributions. Equivalently, they may be used to describe the (local) electronic DOS (Eqs. 2.124, 2.125). The moments of the local electronic DOS are defined as

$$\mu_{Ilm}^{(n)} = \int dE E^n n_{Ilm}(E) \quad (2.164)$$

and are referred to as local moments. The moments of the electronic DOS $\mu^{(n)}$ are obtained by averaging over all local moments. The first five moments may be interpreted as:

$$\begin{aligned} \mu^{(0)} &: \text{total number of states} \\ \hat{\mu}^{(1)} = \mu^{(1)}/\mu^{(0)} &: \text{center of gravity} \\ \hat{\mu}^{(2)} = \mu^{(2)}/\mu^{(0)} &: \text{mean square width} \\ \hat{\mu}^{(3)} = \mu^{(3)}/\mu^{(0)} &: \text{skewness} \\ \hat{\mu}^{(4)} = \mu^{(4)}/\mu^{(0)} &: \text{bimodality} \end{aligned}$$

The bimodality is rationalized by the dimensionless shape parameter [4]

$$s = \frac{\hat{\mu}^{(4)}}{(\hat{\mu}^{(2)})^2} - \frac{(\hat{\mu}^{(3)})^2}{(\hat{\mu}^{(2)})^3} - 1. \quad (2.165)$$

The DOS is bimodal for $s < 1$ and unimodal otherwise. The fourth moment is bounded below by [80]

$$\frac{\hat{\mu}^{(4)}}{(\hat{\mu}^{(2)})^2} \geq \frac{(\hat{\mu}^{(3)})^2}{(\hat{\mu}^{(2)})^3} + 1 \quad (2.166)$$

such that $\hat{\mu}^{(4)} \geq (\hat{\mu}^{(2)})^2$.

2.4.2. Moments Theorem

The moments theorem [81] expresses in an orthogonal TB model the moments of the local DOS as a product of Hamiltonian matrix elements,

$$\begin{aligned} \mu_{Ilm}^{(n)} &= \sum_{Ilm} \langle \varphi_{Ilm} | \hat{H}^n | \varphi_{Ilm} \rangle \\ &= \sum_{I'V'm'I''V''m''\dots} H_{IlmI'V'm'} H_{I'V'm'I''V''m''} H_{I''V''m''\dots} \dots H_{\dots Ilm}. \end{aligned} \quad (2.167)$$

All neighbouring matrix elements in the product of Eq. 2.167 have always a common orbital index and the first and last indices in the product are the same. The sum of the different orbital indices may therefore be interpreted as

sum of all possible hopping paths of length n starting and ending at orbital Ilm . The moments theorem therefore relates the electronic structure with the atomic structure.

As only onsite hops can result in hopping paths of length one, the first local moment which contains information of the atomic surrounding of an atom is the second local moment $\mu_{Ilm}^{(2)}$. It explicitly depends on the interatomic distances due to the distance dependence of the intersite matrix elements of the Hamiltonian matrix. The third and fourth local moments are constructed from all self-returning hopping paths of length three and four and therefore they depend on the atomic structure of the surrounding atoms, e.g. the crystal structure. The relationship of the moments of the DOS and to the crystal structure and to trends in the structural stability is discussed in Sec. 4.1.1.

2.4.3. Recursion Coefficients

The moments of the DOS are used in the method of moments [81, 82] for approximating the DOS without calculating the eigenvalues. A closely related procedure is the recursion method [83, 84], which tridiagonalizes the TB Hamiltonian matrix with the Lanczos algorithm [85]. A new basis is constructed by the recursive formula

$$b_{n+1}|u_{n+1}\rangle = (\hat{H} - a_n)|u_n\rangle - b_n|u_{n-1}\rangle, \quad (2.168)$$

where $|u_0\rangle$ may be chosen arbitrarily, e.g. $|u_0\rangle = |\varphi_{Ilm}\rangle$. The recursion coefficients a_n and b_n are chosen such that the recursively generated states are normalized and orthogonal to all previously generated states such that an orthonormal basis is generated. Consequently, the matrix elements of the Hamiltonian in the new basis are given by

$$\langle u_m|\hat{H}|u_n\rangle = \begin{cases} a_n & \text{if } m = n \\ b_n & \text{if } m = n - 1 \\ b_{n+1} & \text{if } m = n + 1 \\ 0 & \text{otherwise.} \end{cases} \quad (2.169)$$

The resulting Hamiltonian matrix has the tridiagonal form

$$H = \begin{pmatrix} a_0 & b_1 & & & & & & \\ b_1 & a_1 & b_2 & & & & & \\ & b_1 & a_2 & b_3 & & & & \\ & & b_3 & a_3 & b_4 & & & \\ & & & b_4 & a_4 & b_5 & & \\ & & & & & \ddots & \ddots & \ddots \\ & & & & & & \ddots & \ddots \end{pmatrix}, \quad (2.170)$$

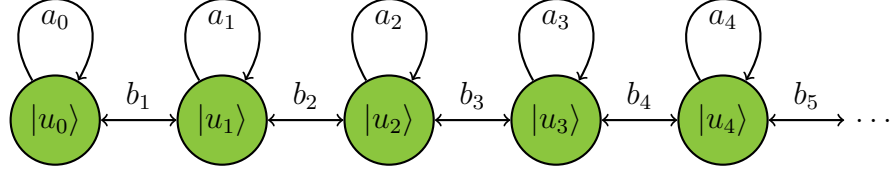


Figure 2.5.: Illustration of the semi-infinite Lanczos chain.

corresponding to a one-dimensional semi-infinite chain of orbitals which only interact with their nearest neighbours as illustrated in Fig. 2.5. With the specific choice $|u_0\rangle = |\varphi_{ilm}\rangle$, the n -th moment of the local DOS of orbital ilm can be computed from the recursion coefficients by summation over all self-returning hopping paths of length n in the semi-infinite chain,

$$\begin{aligned} \mu_{ilm}^{(n)} &= \langle \varphi_{ilm} | \hat{H}^n | \varphi_{ilm} \rangle = \langle u_0 | \hat{H}^n | u_0 \rangle \\ &= \sum_{i_1 \dots i_{n-1}} \langle u_0 | \hat{H} | u_{i_1} \rangle \langle u_{i_1} | \hat{H} | u_{i_2} \rangle \dots \langle u_{i_{n-1}} | \hat{H} | u_0 \rangle. \end{aligned} \quad (2.171)$$

The first five moments are given by [61]

$$\begin{aligned} \mu_{ilm}^{(0)} &= 1, \\ \mu_{ilm}^{(1)} &= a_0, \\ \mu_{ilm}^{(2)} &= a_0^2 + b_1^2, \\ \mu_{ilm}^{(3)} &= a_0^3 + 2a_0b_1^2 + a_1b_1^2, \\ \mu_{ilm}^{(4)} &= a_0^4 + 3a_0^2b_1^2 + 2a_0a_1b_1^2 + a_1^2b_1^2 + b_1^2b_1^2 + b_1^4. \end{aligned} \quad (2.172)$$

Recursive formulas to calculate the recursion coefficients from the moments are given in Refs. 61, 86.

2.4.4. Continued Fraction Expansion of the Local Density of States

Haydock developed a continued fraction expansion [84] based on the recursion coefficients, which allows for an approximate calculation of the local DOS and scales linearly with the system size. It is used in numerical BOPs and is relevant for Sec. 2.4.7. It is presented in the following:

The inverse of the one particle Green's function for the time independent Schrödinger equation is defined as [3]

$$\hat{G}^{-1} = E - \hat{H}. \quad (2.173)$$

With the identity

$$\delta(x) = -\frac{1}{\pi} \lim_{\eta \rightarrow 0} \text{Im} \left([x + i\eta]^{-1} \right), \quad (2.174)$$

the local DOS (Eq. 2.125) may be written as

$$n_{Ilm}(E) = -\frac{1}{\pi} \lim_{\eta \rightarrow 0} \text{Im} G_{IlmIlm}(x + i\eta). \quad (2.175)$$

With the choice $|u_0\rangle = |\varphi_{Ilm}\rangle$, the Green's function is given by the continued fraction [84]

$$G_{IlmIlm}(E) = \frac{1}{E - a_0 - \frac{b_1^2}{E - a_1 - \frac{b_2^2}{E - a_2 - \frac{b_3^2}{\ddots}}}}. \quad (2.176)$$

2.4.5. Constant Terminator

The continued fraction has an infinite number of fractions for an infinite or periodic system. Therefore, it is necessary for practical calculations to replace the recursion coefficients from a given recursion level n_{rec} onwards by approximate values. The simplest approximation is the constant terminator,

$$a_n = a_\infty, b_n = b_\infty, \text{ for } n > n_{\text{rec}}. \quad (2.177)$$

Other terminators are presented in Sec. 2.4.8. With the constant terminator, the remaining part of the continued fraction may be calculated analytically [84] and is given by

$$\begin{aligned} t_{IlmIlm}(E) &= \frac{1}{E - a_\infty - \frac{b_\infty^2}{E - a_\infty - \frac{b_\infty^2}{E - a_\infty - \frac{b_\infty^2}{\ddots}}}} \\ &= \frac{1}{b_\infty} \left[\frac{E - a_\infty}{2b_\infty} - i \sqrt{1 - \left(\frac{E - a_\infty}{2b_\infty} \right)^2} \right]. \end{aligned} \quad (2.178)$$

As E may take all possible values between the band edges, the values a_∞ and $4b_\infty$ may be interpreted as the band center and the bandwidth, separately. The terminator (Eq. 2.178) is referred to as square root terminator because of the functional form of the imaginary part, which is relevant for the DOS. The bond energy may be calculated in the onsite representation (Eq. 2.126)

by

$$U_{\text{bond}} = \sum_{l m} \int_{-\infty}^{E_F} dE (E - E_{l m}^0) \tilde{n}_{l m}(E), \quad (2.179)$$

where

$$\tilde{n}_{l m}(E) = -\frac{1}{\pi} \text{Im} \frac{1}{E - a_0 - \frac{b_1^2}{E - a_\infty - \frac{b_\infty^2 t_{l m l m}(E)}{\ddots}}} \quad (2.180)$$

approximates the local DOS. In numerical BOPs [61, 87–90], the integration of Eq. 2.179 is carried out numerically.

Pettifor and Oleinik [91–93] carried out the continued fraction expansion up to $n_{\text{rec}} = 2$ analytically and used the results for the modelling of semiconductors. They used $a_\infty = 0$ and $b_\infty = 0$ together with a choice of $|u_0\rangle$, which is related to the eigenstates of a dimer to take into account that semiconductors have covalent saturated bonds.

2.4.6. Moments Expansion of the Density of States

An alternative to numerical BOPs and analytic BOPs for semiconductors are valence-dependent analytic BOPs for transition-metals from Drautz and Pettifor [62, 74], which allow for an analytic integration of the local DOS but also a choice of the recursion level n_{max} to control the approximation to the TB reference. This approach is used in the present work and is explained in the following:

The first state in the Lanczos chain is chosen to be an atomic orbital $|u_0\rangle = |\varphi_{l m}\rangle$ to allow for a fast convergence when treating transition-metals.

The local DOS $n_{l m}(E)$ is expanded around a reference DOS $n_{l m}^0(E)$ which is chosen to be the result of the continued fraction expansion where all recursion coefficients take the constant values

$$a_n = a_\infty, b_n = b_\infty \quad \forall n. \quad (2.181)$$

It follows from Eqs. 2.175, 2.178 that the reference density may be expressed as

$$t_{l m l m}(E) = \frac{1}{2b_\infty} n_{l m}^0(\epsilon) \quad (2.182)$$

with

$$n_{l m}^0(\epsilon) = \frac{2}{\pi} \sqrt{1 - \epsilon^2}, \quad (2.183)$$

where

$$\epsilon = \frac{E - a_\infty}{2b_\infty} \quad (2.184)$$

scales the energy to an interval $[-1, 1]$. The local DOS may be written as the sum of the reference density and a perturbation $\delta n_{Ilm}(\epsilon)$,

$$n_{Ilm}(\epsilon) = n_{Ilm}^0(\epsilon) + \delta n_{Ilm}(\epsilon). \quad (2.185)$$

The orthonormality of the Chebyshev polynomials of the second kind [94]

$$P_n(\epsilon) = \sum_{m=0}^n p_{nm} \epsilon^m \quad (2.186)$$

with respect to the weight $n_{Ilm}^0(\epsilon)$,

$$\int_{-1}^1 d\epsilon P_k(\epsilon) P_l(\epsilon) n_{Ilm}^0(\epsilon) = \delta_{kl}, \quad (2.187)$$

is employed to expand the local DOS

$$n_{Ilm}(\epsilon) \approx n_{Ilm}^{n_{\max}}(\epsilon) = n_{Ilm}^0(\epsilon) \sum_{n=0}^{n_{\max}} \sigma_{Ilm}^{(n)} P_n(\epsilon), \quad (2.188)$$

where the reference density $n_{Ilm}^0(\epsilon)$ is absorbed into the sum for $k = 0$ as $P_0(\epsilon) = 1$ and the expansion is for practical calculations truncated at an expansion level $n_{\max} = 2n_{\text{rec}}$. The coefficients $\sigma_{Ilm}^{(n)}$ are referred to as expansion coefficients and are formally given by

$$\sigma_{Ilm}^{(n)} = \int_{-1}^1 d\epsilon P_n(\epsilon) n_{Ilm}(\epsilon). \quad (2.189)$$

Inserting Eq. 2.186 into Eq. 2.189 leads to

$$\sigma_{Ilm}^{(n)} = \sum_{k=0}^n p_{nk} \hat{\mu}_{Ilm}^{(k)}, \quad (2.190)$$

where

$$\hat{\mu}_{Ilm}^{(n)} = \frac{1}{2b_{\infty}} \sum_{k=0}^n \binom{n}{k} (-1)^k a_{\infty}^k \mu_{Ilm}^{(n-k)} \quad (2.191)$$

are the dimensionless moments.

2.4.7. Termination of Moments Expansion

In contrast to the continued fraction expansion of the local DOS (Eq. 2.180), where higher recursion coefficients are estimated by a terminator, the expansion of the local DOS in form of Eq. 2.188 is carried out up to an expansion level n_{\max} and contributions from higher moments are completely neglected. This drawback has been solved by Seiser et al. [95] and is discussed in the following.

The expansion coefficients $\sigma_{ilm}^{(n)}$ may be calculated from the recursion coefficients a_n, b_n . As the continued fraction expansion (Eq. 2.176) allows one to estimate higher recursion coefficients from terminators, higher expansion coefficients may consequently also be estimated. The DOS of the analytic BOPs (Eq. 2.188) is therefore extended to

$$n_{ilm}^{n_{\text{exp}}}(\epsilon) = n_{ilm}^0(\epsilon) \left(\sum_{n=0}^{n_{\text{max}}} \sigma_{ilm}^{(n)} P_n(\epsilon) + \sum_{n=n_{\text{max}}+1}^{n_{\text{exp}}} \sigma_{ilm}^{(n)} P_n(\epsilon) \right), \quad (2.192)$$

where the expansion coefficients for $n \in [n_{\text{max}} + 1, n_{\text{exp}}]$ are calculated from the corresponding estimated recursion coefficients.

The recursion coefficients are calculated exactly from the moments up to $n_{\text{rec}} = n_{\text{max}}/2$ by the procedure described in Refs. 61, 86 (Sec. 2.4.3). Higher recursion coefficients up to $n_{\text{exp}}/2$ are estimated from the terminators. The expansion coefficients may be calculated by the recursive formula

$$\zeta_k^{(n+1)} = 2 \left(\hat{a}_k \zeta_k^{(n)} + \hat{b}_k \zeta_{k-1}^{(n)} + \hat{b}_{k+1} \zeta_{k+1}^{(n)} \right) - \zeta_k^{(n-1)} \quad (2.193)$$

with

$$\hat{a}_k = \frac{a_k - a_\infty}{2b_\infty}, \quad (2.194)$$

$$\hat{b}_k = \frac{b_k}{2b_\infty}, \quad (2.195)$$

$$\zeta_k^{(n)} = \langle u_k | P_n(\hat{h}) | u_0 \rangle \quad (2.196)$$

and

$$\hat{h} = \frac{\hat{H} - a_\infty}{2b_\infty} \quad (2.197)$$

such that $\sigma_{ilm}^{(n)} = \zeta_0^{(n)}$. Equation 2.193 may be proven by using the recurrence relation of the Chebyshev polynomials of the second kind [94]

$$P_{n+1}(\epsilon) = 2\epsilon P_n(\epsilon) - P_{n-1}(\epsilon) \quad (2.198)$$

and by the recursive formula (Eq. 2.168). Note that the computation of Eq. 2.193 requires the evaluation of all recursion coefficients up to a_{n-1} and b_n .

The two different approaches to approximate the local DOS by either Eq. 2.188 or Eq. 2.192 are summarized and compared in Fig. 2.6.

2.4.8. Terminators and Estimates of the Bandwidth

The analytic BOP expansion around a reference DOS (Eq. 2.183) requires estimates for the band edges E_{top} and E_{bottom} , which are related to the asymptotic

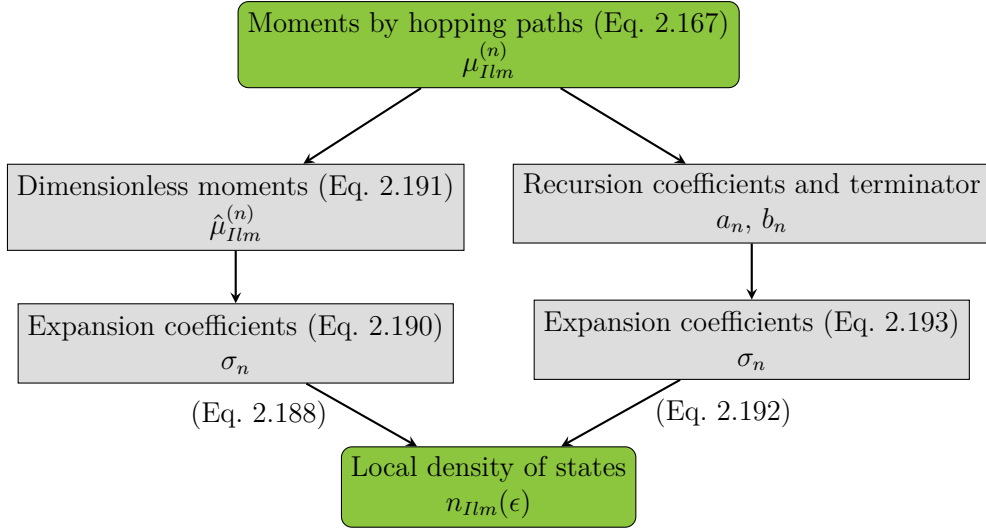


Figure 2.6.: Calculation of the local DOS in analytic BOPs. The left branch of the diagram illustrates the calculation procedure for Eq. 2.188, the right branch for the extended Eq. 2.192.

recursion coefficients by

$$b_\infty = \frac{E_{\text{top}} - E_{\text{bottom}}}{4} \quad (2.199)$$

and

$$a_\infty = \frac{E_{\text{top}} + E_{\text{bottom}}}{2} \quad (2.200)$$

and are responsible for the scaling of the energy by Eq. 2.184. Estimates have been developed by Beer and Pettifor [96] and by Haydock and Johannes [97]. A similar method to the one of Haydock and Johannes has been introduced by Ford et al. [98], which estimates the asymptotic recursion coefficients for the band edges from

$$a_\infty = \frac{1}{1 + n_{n_{\text{rec}}}} \sum_{n=0}^{n_{\text{rec}}} a_n \quad (2.201)$$

and

$$b_\infty = \sqrt{\frac{1}{n_{n_{\text{rec}}}} \sum_{n=1}^{n_{\text{rec}}} b_n^2}. \quad (2.202)$$

An underestimation of the bandwidth can result in undesired oscillations of the analytic BOP DOS [98]. Therefore, Seiser et al. [95] used Gerschgorin's circle theorem [99] and estimated lower and upper boundaries for the lower and upper band edges, which are given by

$$E_{\text{bottom}} = \min_n (a_n - b_n - b_{n+1}) \quad (2.203)$$

and

$$E_{\text{top}} = \max_n (a_n + b_n + b_{n+1}). \quad (2.204)$$

It was observed by Ford et al. that the constant terminators (Eq. 2.181), which are computed from the estimates of the band edges, are not necessarily an optimal choice to estimate the expansion coefficients for $n > n_{\text{max}}$. A smoother convergence with respect to the number of exactly calculated recursion coefficients n_{rec} could be obtained by estimating

$$a_{\infty} = \frac{\sum_{k=0}^{n_{\text{rec}}} w_k a^k}{\sum_{k=0}^{n_{\text{rec}}} w_k} \quad (2.205)$$

and

$$b_{\infty} = \frac{\sum_{k=0}^{n_{\text{rec}}} w_k b^k}{\sum_{k=0}^{n_{\text{rec}}} w_k}, \quad (2.206)$$

where the weight

$$w_k = \frac{1}{\alpha(n_{\text{rec}} - k) + 1} \quad (2.207)$$

depends on a parameter α , which controls the smoothness of the convergence and takes optimal values for $\alpha \geq 1$.

The recursion coefficients oscillate in systems with band gaps and the treatment of these systems therefore requires to estimate the recursion coefficients for $n > n_{\text{rec}}$ by oscillating functions [100]. The period length determines the number of band gaps, e.g. a period length equal to one is sufficient to model systems with a single band gap [95].

2.4.9. Strictly Positive Density of States

The expansion of the DOS in Chebyshev polynomials of the second kind (Eq. 2.188) can be transformed into a Fourier series expansion [95],

$$n_{llm}^{n_{\text{max}}}(\epsilon) = \sum_{n=0}^{n_{\text{max}}} \sigma_{llm}^{(n)} \sin((n+1)\phi), \quad (2.208)$$

where

$$\sin((n+1)\phi) = n_{llm}^0(\epsilon) P_n(\epsilon). \quad (2.209)$$

Therefore, the analytic BOP expansion is effected by Gibbs ringing, which can also cause non-physical negative values in the analytic BOP DOS. Similar to the kernel polynomial method [101] Seiser et al. introduced damping factors g_n for the expansion coefficients to avoid Gibbs ringing [95]. With this, the BOP expansion (Eq. 2.192) is written as

$$n_{llm}^{n_{\text{exp}}}(\epsilon) = n_{llm}^0(\epsilon) \left(\sum_{n=0}^{n_{\text{max}}} g_n \sigma_{llm}^{(n)} P_n(\epsilon) + \sum_{n=n_{\text{max}}+1}^{n_{\text{exp}}} g_n \sigma_{llm}^{(n)} P_n(\epsilon) \right). \quad (2.210)$$

2.4.10. Bond Energy

The expansion of the local DOS in analytic BOPs is used to calculate the bond energy analytically. For this purpose, the extended expansion of the local DOS in Chebyshev polynomials (Eq. 2.210) is inserted into the onsite representation of the bond energy (Eq. 2.126),

$$U_{\text{bond}}^{IIm, n_{\text{exp}}} = 2b_{\infty} \int_0^{\epsilon_{\text{F}}} d\epsilon \sum_{n=0}^{n_{\text{exp}}} n_{IIm}^0(\epsilon) g_n \sigma_{IIm}^{(n)} P_n(\epsilon) (\epsilon - \epsilon_{IIm}). \quad (2.211)$$

With a change of variables $\epsilon = \cos(\phi)$, the integration is readily carried out and the bond energy may be written as

$$U_{\text{bond}}^{IIm, n_{\text{exp}}} = 2b_{\infty} \sum_{n=0}^{n_{\text{exp}}} g_n \sigma_{IIm}^{(n)} [\hat{\chi}_{n+2}(\phi_{\text{F}}) - 2\epsilon_{IIm} \hat{\chi}_{n+1}(\phi_{\text{F}}) + \hat{\chi}_n(\phi_{\text{F}})], \quad (2.212)$$

where

$$\begin{aligned} \hat{\chi}_0(\phi_{\text{F}}) &= 0, \\ \hat{\chi}_1(\phi_{\text{F}}) &= 1 - \frac{\phi_{\text{F}}}{\pi} + \frac{1}{2\pi} \sin(2\phi_{\text{F}}), \\ \hat{\chi}_n(\phi_{\text{F}}) &= \frac{1}{\pi} \left(\frac{\sin((n+1)\phi_{\text{F}})}{n+1} - \frac{\sin((n-1)\phi_{\text{F}})}{n-1} \right) \end{aligned} \quad (2.213)$$

are the response functions [62, 87]. The response functions $\hat{\chi}_n(\phi_{\text{F}})$ with $n \geq 2$ are illustrated in Fig. 2.7. They are equal to zero for $\epsilon_{\text{F}} = \pm 1$ such that the bond energy is, as expected, also equal to zero for these values. In particular, the third-order response function $\hat{\chi}_3(\phi_{\text{F}})$ is positive for less than half full band and negative for more than half full band. The fourth-order response function $\hat{\chi}_4(\phi_{\text{F}})$ is negative at the band edges and positive at the band center.

2.4.11. Self-Consistency

In analytic BOPs, the eigenspectrum is an approximation to the exact TB eigenspectrum. Consequently, a self-consistent choice of the charges according to Eq. 2.114 does not result in a stationary point of the BOP energy. Instead, the energy has to be minimized with respect to the onsite levels. The resulting self-consistency criteria may be written as

$$\frac{\partial U_{\text{B}}}{\partial E_{IIm}} = \tilde{\Theta}_{IImIIm} - N_{IIm} = 0, \quad (2.214)$$

where the bond-order like term $\tilde{\Theta}$ is obtained from the derivative of the BOP energy expansion with respect to the Hamiltonian matrix elements. The derivation and the precise form of $\tilde{\Theta}$ is given in Ref. 102. The bond-order

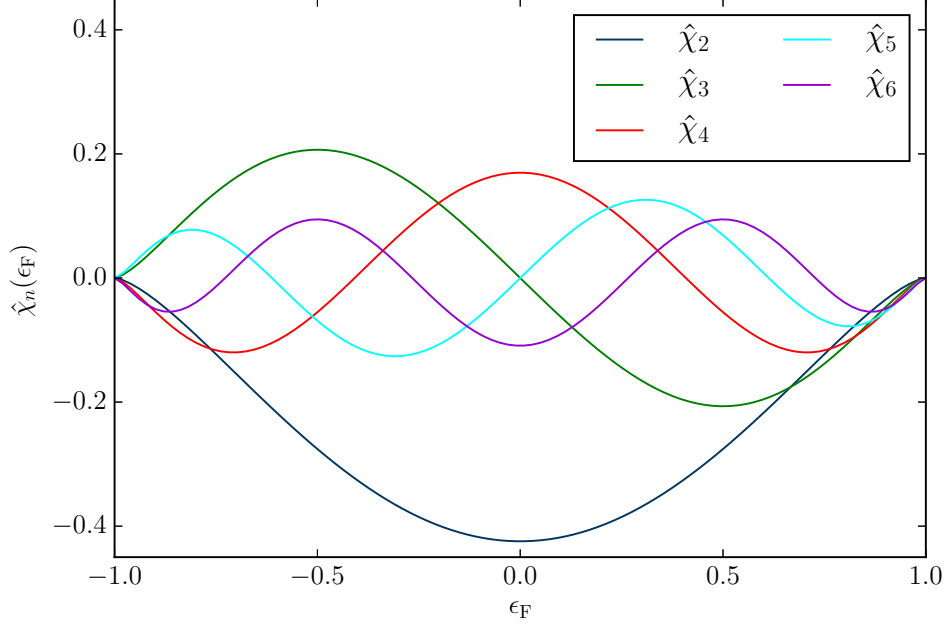


Figure 2.7.: Response functions for $n \in [2, 6]$ as a function of the normalized Fermi energy ϵ_F . The number of roots increases with n .

like term converges to the exact bond-order (Eq. 2.121) for $n_{\max} \rightarrow \infty$ and the TB self-consistency criteria (Eq. 2.116) is recovered.

2.4.12. Forces

In analytic BOPs, the forces are equivalent to TB, except that the exact bond-order has to be replaced by the bond-order like term $\tilde{\Theta}$ such that the gradient of the binding energy is given by

$$\begin{aligned} \nabla_K U_B = & \sum_{IlmI'l'm'} \tilde{\Theta}_{IlmI'l'm'} \nabla_K H_{IlmI'l'm'} \\ & + \frac{1}{2} \sum_{IlmI'l'm'} (\nabla_K J_{IlmI'l'm'}) q_{Ilm} q_{I'l'm'} + \nabla_K U_{\text{rep}}, \end{aligned} \quad (2.215)$$

which corresponds to Eq. 2.145 for $n_{\max} \rightarrow \infty$.

2.4.13. Summary of Calculation Steps

A flowchart of a self-consistent analytic BOP calculation is shown in Fig. 2.8. As in TB calculations (Sec. 2.3.10), the calculation is initialized with a distance-dependent description of the repulsive energy contribution and the intraatomic Hamiltonian matrix elements in the bond coordinate system. Initial onsite

levels are guessed. Afterwards, the intraatomic Hamiltonian and overlap matrix elements in the global coordinate system are calculated. Instead of a transformation of the matrices into reciprocal space, which is done in TB, the moments of the local DOS are calculated. They are used to calculate the exact recursion coefficients. Different possibilities can be chosen to estimate the band edges and the higher recursion coefficients. The expansion coefficients can be calculated from the exact and the estimated recursion coefficients. By usage of a kernel, a strictly positive analytic BOP expansion of the DOS is obtained. The previous steps are repeated until the self-consistency criteria is reached and afterwards the energy contributions and forces are calculated.

2.4.14. Second and Fourth Moment Approximations

The TB theory can be derived from a second-order approximation to DFT and the analytic BOPs are a systematic approximation to TB. However, many models of the interatomic interaction are empirically or semi-empirically derived (cf. Ref. 103 for a database of interatomic potentials). The functional form of some of them can be derived from approximations to the BOP formalism. Ackland et al. [104] proved that the bond energy (Eq. 2.126) can be written as

$$U_{\text{bond}} \propto -\sqrt{\mu^{(2)}} \quad (2.216)$$

under the assumption of local charge neutrality and the assumption that only the width of the DOS changes as a response to structural changes. The atomic second moments of the DOS of a system with only one orbital type

$$\mu_I^{(2)} = \frac{1}{2l+1} \sum_m \mu_{Ilm}^{(2)} \quad (2.217)$$

are obtained by averaging over the different magnetic quantum numbers and are rotationally invariant. They can therefore be written as sums of the squares of the bond integrals

$$\mu_I^{(2)} = \sum_{J\alpha} \beta_\alpha (R_{IJ})^2, \quad (2.218)$$

where β_α labels the different bond integrals. For a non-self-consistent TB model where the repulsive energy is parametrized as a pair potential (Eq. 2.162), the binding energy (Eq. 2.118) can be written for a charge neutral system as

$$U_{\text{FS}} = - \sum_I \sqrt{\sum_{J \neq I} \rho_{IJ}(R_{IJ})} + \frac{1}{2} \sum_I \sum_{J \neq I} V_{IJ}(R_{IJ}), \quad (2.219)$$

where

$$\rho_I = \sum_J \rho_{IJ}(R_{IJ}) = \sum_{J\alpha} \beta_\alpha (R_{IJ})^2 \quad (2.220)$$

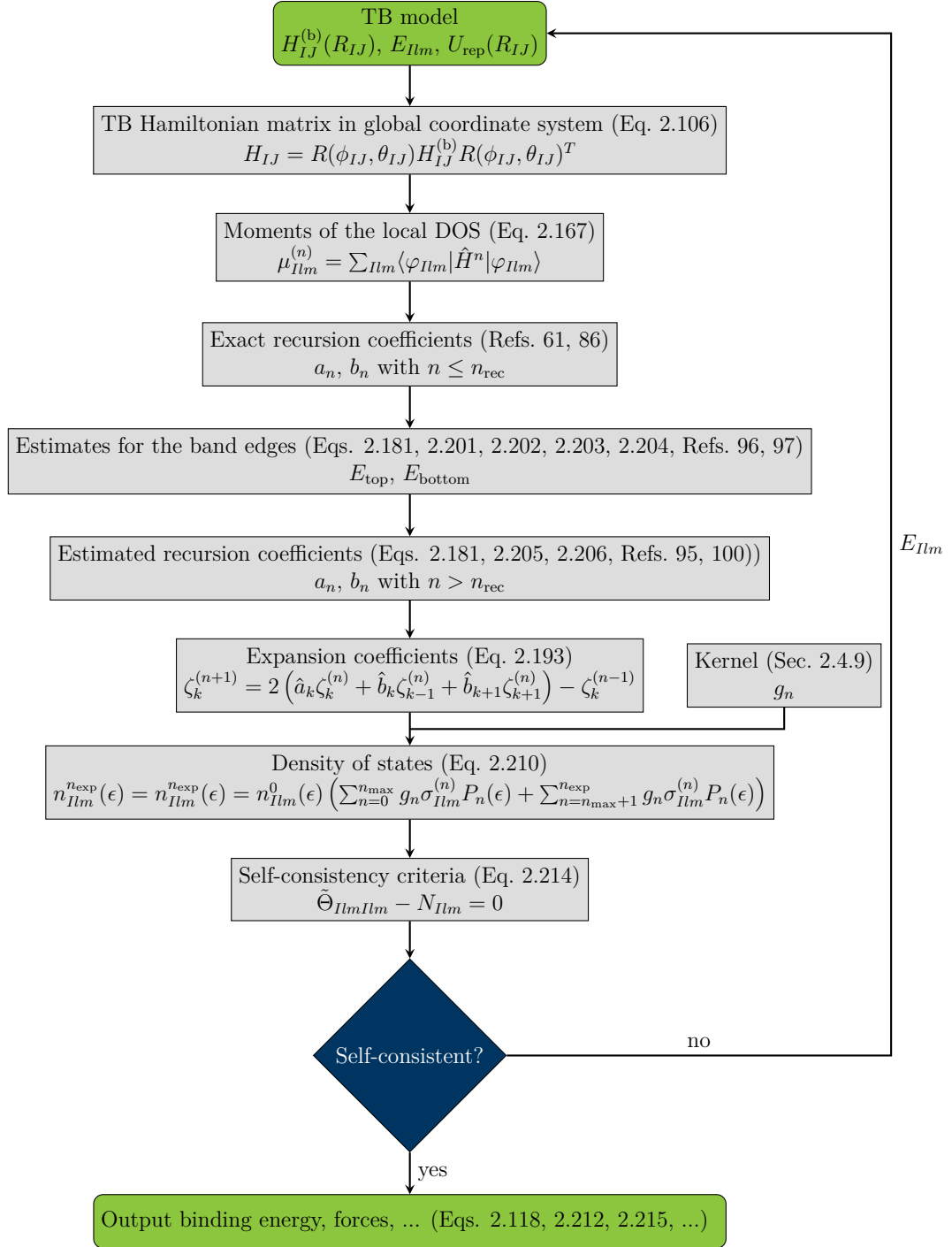


Figure 2.8.: Flowchart of a self-consistent analytic BOP calculation.

may be interpreted as an atomic site density. This functional form of the interatomic interaction corresponds to the potential of Finnis and Sinclair [105]. The original derivation of the square root dependence of the atomic density ρ_I was derived with a much stronger assumption of a Gaussian DOS [106, 107].

The class of potentials of the embedded atom method [108, 109] (EAM) and glue potentials [110] can be considered as a generalization of the Finnis-Sinclair potential as they parametrize the dependence on the atomic site density ρ_I by a general function $F_I(\rho_I)$. They are therefore given by

$$U_{\text{EAM}} = \sum_I F_I \left(\sum_{J \neq I} \rho_{IJ}(R_{IJ}) \right) + \frac{1}{2} \sum_I \sum_{J \neq I} V(R_{IJ}). \quad (2.221)$$

In case of the EAM and glue potentials, the functions ρ_{IJ} , V_{IJ} and F_I are obtained by parameter optimization of flexible functional forms to given sets of reference data.

The analytic BOP expression (Eq. 2.212) can be approximated to validate the Finnis-Sinclair model and models which also take contributions of the fourth moment [111–114] to the energy into account. As derived in Ref. 62, a symmetric ($\mu_{ilm}^{(3)} = 0$) fourth moment approximation to the bond energy is given by

$$U_{\text{bond}}^I \approx 10\sqrt{\mu_I^{(2)}} \left[\hat{\chi}_2(\phi_F) + (\hat{\chi}_4(\phi_F) + \hat{\chi}_6(\phi_F)) \left(\frac{\mu_I^{(4)}}{(\mu_I^{(2)})^2} \right) \right] \quad (2.222)$$

for a d -valent BOP model where the asymptotic recursion coefficients (Eq. 2.181) are chosen as

$$\begin{aligned} b_\infty &= b_1 = \sqrt{\mu_{ilm}^{(2)}}, \\ a_\infty &= a_1 = \frac{\mu_{ilm}^{(3)}}{\mu_{ilm}^{(2)}} = 0 \end{aligned} \quad (2.223)$$

and $a_0 = 0$ is obtained by a shift of all onsite levels to zero. This approximation does not only provide a band filling dependence of the second moment term of the Finnis Sinclair potential, it may also be regarded as an alternative derivation of the fourth moment models [111–114], from which the bond angle dependence of the Tersoff potential [115–117] can be derived [118].

As explained in Ref. 4, the structural trends of the central d -band transition-metals are driven by the d -electrons alone and the prediction of the energy difference between fcc and hcp (Sec. 4.1 for more details) requires at least 6 moments [4, 62, 119]. Therefore, it is sufficient to describe the s -electrons by a second-moment potential and to apply the analytic BOP expansion or the TB formalism only to the d -electrons for an accurate prediction

of the cohesive energies of these phases. With this argument, an embedding term, which describes only the s -electrons, has been parametrized in Refs. 63, 74, 76, 98, 120, 121 based on Ref. 122, which takes the form

$$U_{\text{emb},s} = - \sum_I \sqrt{\sum_{J \neq I} (a_{\text{emb}}^{IJ})^2 \exp(-b_{\text{emb}}^{IJ} R_{IJ}^2)}. \quad (2.224)$$

2.4.15. Computer Implementation of Analytic Bond-Order Potential and Tight-Binding Calculations: BOPfox

The program package **BOPfox** for analytic BOP and TB calculations has been developed and a summary of the implementation is available in Ref. 123. The program requires three input files: A file `models.bx` contains initial values for the onsite levels and the parameters for a distance dependant description of the bond integrals and overlap matrix elements (Sec. 2.3.4) as well as the parameters of further energy contributions as the repulsive pair potentials (Eq. 2.162) and energy contributions in form of the embedded atom potentials (Eq. 2.221). The atomic arrangement is defined in a file `structure.bx`. Calculation settings as the choice of the type of calculation (TB or analytic BOP) or calculation type specific settings as the number of \mathbf{k} -points in a TB calculation or the number of exactly evaluated moments n_{max} are provided in a file `infox.bx`. All parameters which specify details of the TB or analytic BOP calculation are provided in this file and a full list of options can be found in the **BOPfox** manual. The **BOPfox** implementation covers all computational details which are discussed in Sec. 2.3 and in the present section. **BOPfox** reads all settings from the input files and returns the values for the atomic and total energies and forces after a successful calculation. User specific output requests as e.g. the DOS, the values of the moments (Eq. 2.164) or the recursion coefficients (Eq. 2.169) are also handled by the `infox.bx` file.

The **BOPfox** program is implemented with focus on computational efficiency. The theoretical linear scaling of the computational time with respect to the system size has been verified in Ref. 124. By a benchmark of the program, it was obtained that the computational time scales as $n_{\text{max}}^{4.5}$ with increasing number of exactly evaluated moments n_{max} . This is in agreement with the results of a theoretical complexity analysis [124]. Efficient parallelization concepts, which enable a distribution of the computations on multiple computer cores, have been developed and implemented in **BOPfox** [125, 126].

2.4.16. Estimation of Energy Differences

It is possible to estimate energy differences by approximations to the BOP and TB theory. These approximations are introduced in the following. The structural energy difference theorem [127] can be used together with the Wolfsberg-

Helmholtz approximation [4] to estimate energy differences of equilibrium structures without explicit knowledge of the repulsive energy U_{rep} .

The structural energy difference theorem states that the energy difference between two structures is given to first-order by

$$\Delta U \approx [\Delta U_{\text{bond}}]_{\Delta U_{\text{rep}}=0}, \quad (2.225)$$

where $\Delta U_{\text{rep}} = 0$ indicates that the volumes of the individual structures are scaled such that their repulsive energy contributions are equal to each other. One can in many cases [4, 66, 128] assume that repulsive energy U_{rep} is dominated by the overlap repulsion (Eq. 2.142) for computing ΔU . In the Wolfsberg-Helmholtz approximation, it is further assumed that the overlap matrix elements are proportional to a common radial decay of the bond integrals such that U_{rep} can be approximated as

$$U_{\text{rep}} \propto \beta(R)^2 \propto \mu^{(2)}, \quad (2.226)$$

where the second proportionality follows from Eq. 2.218. Instead of scaling the volumes of the individual structures such that $\Delta U_{\text{rep}} = 0$, it is therefore a good approximation to scale them such that $\Delta \mu^{(2)} = 0$.

The assumption (Eq. 2.226) has its limitations and is not always valid. For example, the χ -phase structure (Sec. 4.1.2) of Mn is stabilized over close-packed hcp that is taken by the isoelectronic Tc or Re by a softer repulsion with an exponent that is smaller than 2 as Mn does not have d states in the core [121]. The same holds for carbon, where graphite is stabilized over the diamond structure by the same mechanism [4].

For evaluating the difference in the bond energy between two structures, one needs to take into account that the Fermi level of the two structures will in general be different. A first-order expansion of the bond energy difference between two structures with the same number of valence electrons N_e at identical first and second moment was derived [128, 129],

$$\Delta U_{\text{bond}} = 2(2l + 1)b^{(\infty)} \sum_{n=3}^{n_{\text{max}}} \Delta \sigma^{(n)} \hat{\chi}_n^{(1)}(\phi_{\text{F}}), \quad (2.227)$$

where $\Delta \sigma^{(n)}$ corresponds to the difference in the expansion coefficients,

$$\hat{\chi}_n^{(1)}(\phi_{\text{F}}) = \frac{1}{\pi} \left[\frac{2 \sin(n+1)\phi_{\text{F}}}{n(n+2)} - \frac{\sin(n+3)\phi_{\text{F}}}{(n+2)(n+3)} - \frac{\sin(n-1)\phi_{\text{F}}}{n(n-1)} \right] \quad (2.228)$$

are first-order response functions and ϕ_{F} depends on the number of valence electrons N_e .

2.4.17. Illustration of Analytic Bond-Order Potentials

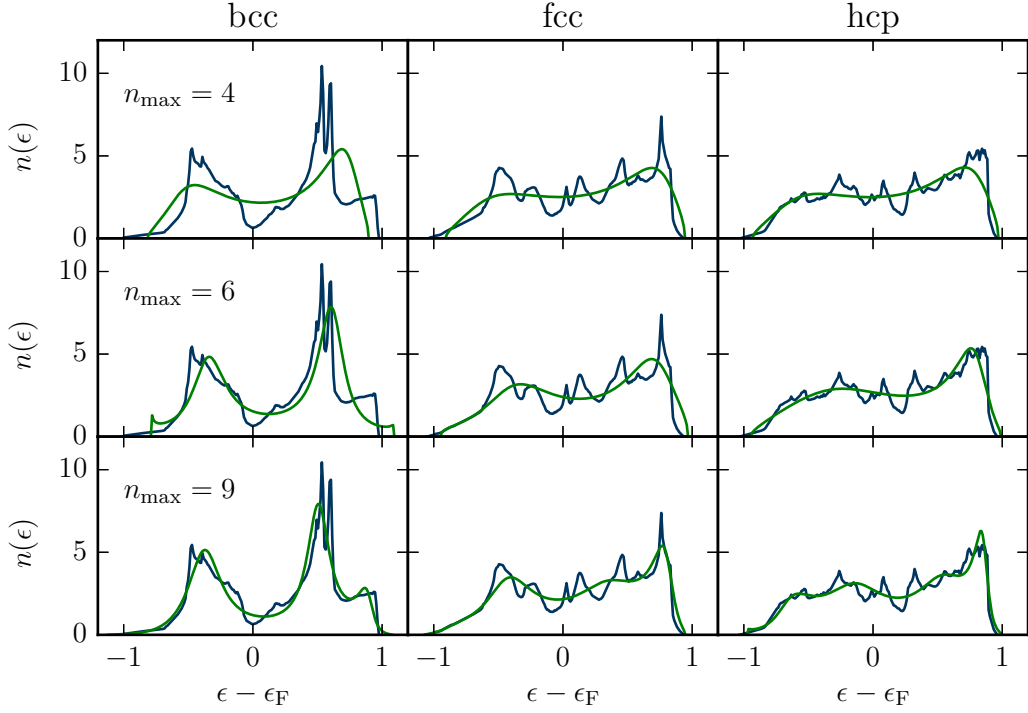


Figure 2.9.: Comparison of TB DOS (blue) and BOP DOS (green) for different numbers of exactly calculated moments n_{\max} calculated with a canonical d -valent TB model for bcc, fcc and hcp. The analytic BOP DOS converges to the TB DOS with increasing values for n_{\max} for all structures. $n_{\text{exp}} = 50$ is chosen for all calculations.

The analytic BOP approximation can be understood best by a comparison of the DOS and energies obtained by a \mathbf{k} -space TB calculation and by analytic BOP approximations for different numbers of exactly calculated moments n_{\max} . For this purpose, the energy difference theorem (Eq. 2.225) is used together with the Wolfsberg-Helmholtz approximation (Eq. 2.226) by scaling the volumes of all considered structures such that the second moment is equal to one, $\mu^{(2)} = 1$. The analytic BOP calculations were performed with a constant terminator (Eq. 2.181) and an estimation of the asymptotic recursion coefficients by Gerschgorin's circle theorem (Eqs. 2.203, 2.204). To approximately describe the transition-metals, a canonical d -valent TB model,

$$\left. \begin{array}{l} dd\sigma(R) \\ dd\pi(R) \\ dd\delta(R) \end{array} \right\} = \left. \begin{array}{l} -6 \\ 4 \\ -1 \end{array} \right\} \beta(R), \quad (2.229)$$

is chosen, which has the same radial decay of R^{-5} for all dd bond integrals,

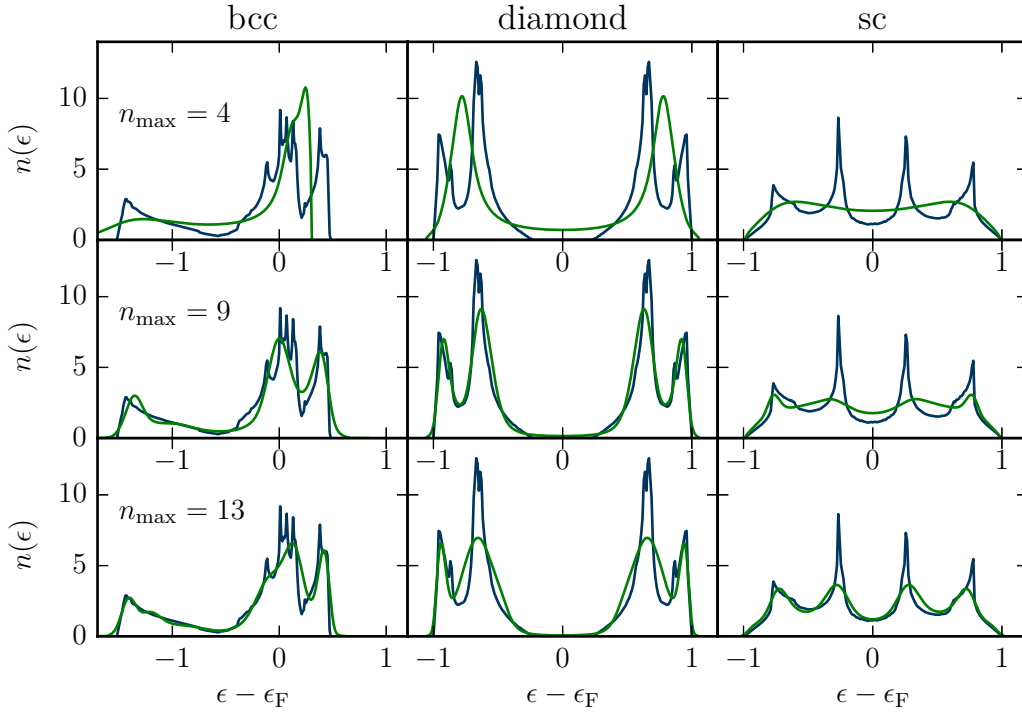


Figure 2.10.: Comparison of TB DOS (blue) and BOP DOS (green) for different numbers of exactly calculated moments n_{\max} calculated with a canonical sp -valent TB model for bcc, diamond and sc. The analytic BOP DOS converges to the TB DOS with increasing values for n_{\max} for all structures. $n_{\text{exp}} = 50$ is chosen for all calculations.

and is introduced in more detail in Sec. 3.1.3. In Fig. 2.9, the convergence of the analytic BOP DOS to the TB reference is illustrated for the example of the bcc, fcc and hcp crystal structures, which are taken by the d -valent transition-metals. The values r_{cut} and d_{cut} of the cut-off function (Eq. 2.163) were chosen such that the first and second nearest neighbours are included in bcc and only the first nearest neighbours are included in fcc and hcp.

It can be seen that the analytic BOP DOS systematically converges to the TB reference with increasing number of exactly calculated moments n_{\max} and that the DOS of fcc and hcp look almost identical for $n_{\max} = 4$. This can be understood from the similarity between the two structures and the relation of the moments of the DOS to the crystal structure by the moments theorem (Eq. 2.167).

An approximate description of the sp -valent elements is given by Cressoni's

and Pettifor's parametrization

$$\left. \begin{array}{l} s s \sigma \\ s p \sigma \\ p p \sigma \\ p p \pi \end{array} \right\} = \left. \begin{array}{l} -1.00 \\ 1.31 \\ 2.31 \\ -0.76 \end{array} \right\} \beta(R) \quad (2.230)$$

of the bond integrals, which is also introduced in more detail in Sec. 3.1.3. The difference of the onsite levels of the s and p orbitals is neglected as it is sufficient for qualitative predictions [66, 130]. Here, the radial decay is also set to R^{-5} . In Fig. 2.10, the convergence of the total DOS of the s and p orbitals is shown for bcc, diamond and sc. The cut-off function is again chosen such that in bcc the first and second nearest neighbours are included, while in diamond and sc only the first nearest neighbours are considered. The analytic BOP DOS again systematically converges to the TB reference, however, more moments are required to capture all features of the DOS compared to the previous calculations for the close-packed structures.

The differences in the bond energy can be used to estimate the differences in the total energy because the calculations were performed for normalized volumes with a scaled second moment. This was done for the results from the d -valent model in Fig. 2.11 and for the results from the sp -valent model in Fig. 2.12. As already expected from the DOS, it can be observed that in the d -valent TB model $n_{\max} \geq 6$ is required to reproduce the energy differences between fcc and hcp [62]. The shape of the DOS of the structures investigated with the sp -valent TB model are very different and their energy differences are much higher and can already be approximated with $n_{\max} = 4$.

In Sec. 4.1, the shape of the DOS and the sequence of stability of the different structures is related to the first moments of the DOS which are related to the crystal structure.

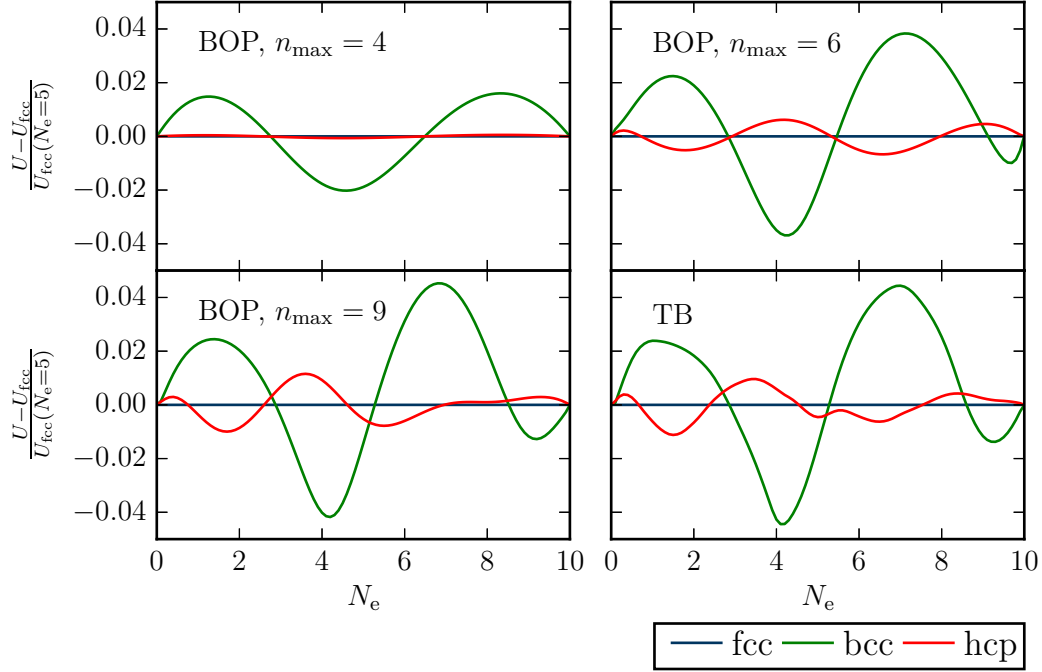


Figure 2.11.: Convergence of the energy differences between bcc, fcc and hcp with respect to the number of exactly calculated moments n_{\max} and comparison to the TB reference. The energies are calculated with the canonical d -valent TB model and normalized to the energy of fcc with a half filled d -band.

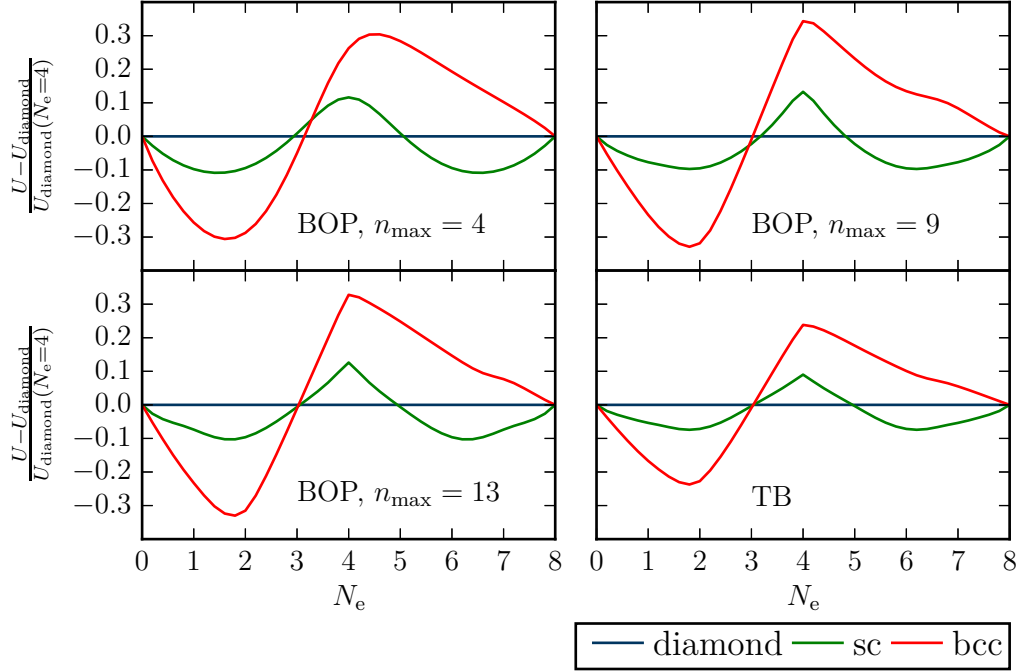


Figure 2.12.: Convergence of the energy differences between diamond, sc and bcc with respect to the number of exactly calculated moments n_{max} and comparison to the TB reference. The energies are calculated with the canonical sp -valent TB model and normalized to the energy of fcc with a half filled sp -band. The peaks in the curves at $N_e = 4$ due to the band gap of the diamond DOS are well reproduced with 9 and 13 exactly calculated moments.

3

Tight-Binding Parametrization Across the Periodic Table

The tight-binding (TB) method and the TB based analytic BOPs are computationally much faster than density-functional theory (DFT) and are based on a chemical intuitive description. They are therefore attractive for materials discovery and high-throughput calculations. However, the lack of available parametrizations and in part, the incompatibility of different parametrizations make DFT currently the only possible option. In this section, the first step to provide TB parametrizations across the periodic table is taken.

In Sec. 3.1, general TB parametrizations are introduced. For the purpose of the development of TB dimer parametrizations across the periodic table, the DFT reference is defined in Sec. 3.2.1, which is used in Sec. 3.2.2 by the downfolding procedure (Sec. 2.3.8) to obtain TB parameters in a consistent way. The data is parametrized in Sec. 3.2.3. This procedure is applied to virtually all combinations of elements from periods 1 to 6 and groups 3 to 18 of the periodic table. Thereby in total 1711 TB models are obtained. Selected models and trends across the periodic table are evaluated in Sec. 3.3.

3.1. Background

3.1.1. Tight-Binding Description of Dimers

A dimer is a molecule of two atoms. It is the only system, for which the two-center approximation is exact and it is therefore an important reference system for TB parametrizations. The Hamiltonian matrix of a dimer can be

valence	σ	π	δ
$s-s$	$\begin{pmatrix} E_1^s & ss\sigma \\ ss\sigma & E_2^s \end{pmatrix}$		
$s-sp$	$\begin{pmatrix} E_1^s & ss\sigma & sp\sigma \\ ss\sigma & E_2^s & E_2^{s,p_0} \\ sp\sigma & E_2^{s,p_0} & E_2^{p_0} \end{pmatrix}$	$\begin{pmatrix} E_2^{p\pm 1} \end{pmatrix}$	
$s-sd$	$\begin{pmatrix} E_1^s & ss\sigma & sd\sigma \\ ss\sigma & E_2^s & E_2^{s,d_0} \\ sd\sigma & E_2^{s,d_0} & E_2^{d_0} \end{pmatrix}$	$\begin{pmatrix} E_2^{p\pm 1} \end{pmatrix}$	$\begin{pmatrix} E_2^{d\pm 2} \end{pmatrix}$
$sp-sp$	$\begin{pmatrix} E_1^s & E_1^{s,p_0} & ss\sigma & sp\sigma \\ E_1^{s,p_0} & E_1^{p_0} & ps\sigma & pp\sigma \\ ss\sigma & ps\sigma & E_2^s & E_2^{s,p_0} \\ sp\sigma & pp\sigma & E_2^{s,p_0} & E_2^{p_0} \end{pmatrix}$	$\begin{pmatrix} E_1^{p\pm 1} & pp\pi \\ pp\pi & E_2^{p\pm 1} \end{pmatrix}$	
$sp-sd$	$\begin{pmatrix} E_1^s & E_1^{s,p_0} & ss\sigma & sd\sigma \\ E_1^{s,p_0} & E_1^{p_0} & ps\sigma & pd\sigma \\ ss\sigma & ps\sigma & E_2^s & E_2^{s,d_0} \\ sd\sigma & pd\sigma & E_2^{s,d_0} & E_2^{d_0} \end{pmatrix}$	$\begin{pmatrix} E_1^{p\pm 1} & pd\pi \\ pd\pi & E_2^{d\pm 1} \end{pmatrix}$	$\begin{pmatrix} E_2^{d\pm 2} \end{pmatrix}$
$sd-sd$	$\begin{pmatrix} E_1^s & E_1^{s,d_0} & ss\sigma & sd\sigma \\ E_1^{s,d_0} & E_1^{d_0} & ds\sigma & dd\sigma \\ ss\sigma & ds\sigma & E_2^s & E_2^{s,d_0} \\ sd\sigma & dd\sigma & E_2^{s,d_0} & E_2^{d_0} \end{pmatrix}$	$\begin{pmatrix} E_1^{d\pm 1} & dd\pi \\ dd\pi & E_2^{d\pm 1} \end{pmatrix}$	$\begin{pmatrix} E_1^{d\pm 2} & dd\delta \\ dd\delta & E_2^{d\pm 2} \end{pmatrix}$

Table 3.1.: σ -, π - and δ -block matrices of the dimer Hamiltonian matrix for different valences.

expressed as

$$H = \begin{pmatrix} \sigma_0 & 0 & 0 & 0 & 0 \\ 0 & \pi_{-1} & 0 & 0 & 0 \\ 0 & 0 & \pi_{+1} & 0 & 0 \\ 0 & 0 & 0 & \delta_{-2} & 0 \\ 0 & 0 & 0 & 0 & \delta_{+2} \end{pmatrix}, \quad (3.1)$$

where σ_0 , $\pi_{\pm 1}$ and $\delta_{\pm 2}$ are block matrices and are referred to as σ -block, π -block and δ -block. The index indicates the common magnetic quantum number of the contributing orbitals. The explicit form of the block matrices depend on the valence of the contributing elements and are summarized in Tab. 3.1. The onsite elements are on the diagonal of the block matrices and the bond integrals are on off-diagonal positions. Furthermore, the σ -blocks contain intraatomic parameters $E_{1/2}^{s,x_{1/2}}$, which are zero in case of free atoms and non-zero in the presence of a further atom [131]. The overlap matrix has an equivalent structure to the Hamiltonian matrix with values of one on the diagonal of the block matrices.

In Fig. 3.1, the equilibrium bond length R_{eq} of all homoatomic dimers is

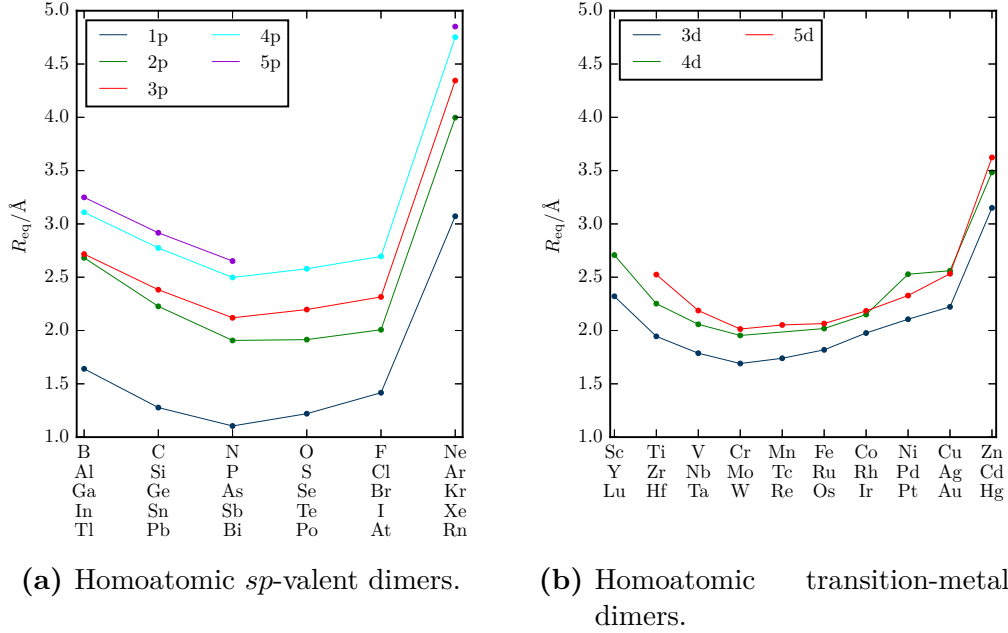


Figure 3.1.: Equilibrium distance R_{eq} of homoatomic sp -valent dimers (Fig. a) and sd -valent dimers (Fig. b).

self-consistently calculated with GPAW using a non-spin-polarized grid basis with $h = 0.15 \text{ \AA}$ (Sec. 2.2.6) in all Cartesian directions, the PBE exchange-correlation functional (Sec. 2.2.3) and the default PAW datasets (Sec. 2.2.5) of GPAW.

3.1.2. Reduced Tight-Binding

In the reduced TB approximation [91, 92], the number of independent Hamiltonian matrix elements is reduced by making approximations on the relation of the matrix elements. In case of a homoatomic sp - or sd -valent dimer, a reduction of the number of independent Hamiltonian matrix elements in an orthogonal TB model allows one to compute the matrix elements directly from a reference eigenspectrum.

The reduced TB approximation is discussed for a homoatomic sp -valent dimer. The LCAO secular equation (Eq. 2.99) for the π -block is given by

$$\det(\pi - E_{\pm 1}^{\pi} \mathbf{1}) = 0, \quad (3.2)$$

where π is defined in Tab. 3.1. The solutions of this equation are

$$E_p = \frac{E_+^{\pi} + E_-^{\pi}}{2} \quad (3.3)$$

and

$$pp\pi = \frac{E_+^\pi - E_-^\pi}{2}. \quad (3.4)$$

Neglecting the intraatomic parameters $E_{1/2}^{s,p}$ and making use of the cylindrical symmetry and the symmetry with respect to inversion, the secular equation for the σ -block can be split into

$$\det(\mathbf{H}_g - E_{+,-}^g \mathbf{1}) = 0 \quad (3.5)$$

and

$$\det(\mathbf{H}_u - E_{+,-}^u \mathbf{1}) = 0, \quad (3.6)$$

where

$$\mathbf{H}_g = \begin{pmatrix} E_s + ss\sigma & -sp\sigma \\ -sp\sigma & E_p - pp\sigma \end{pmatrix} \quad (3.7)$$

and

$$\mathbf{H}_u = \begin{pmatrix} E_s - ss\sigma & sp\sigma \\ sp\sigma & E_p + pp\sigma \end{pmatrix}. \quad (3.8)$$

From the two equations, the individual TB matrix elements can be expressed as

$$E_s = \frac{1}{2} (E_-^g + E_+^g + E_-^u + E_+^u) - E_p, \quad (3.9)$$

$$ss\sigma = \frac{1}{2(E_p - E_s)} (E_-^g E_+^g - E_-^u E_+^u - E_s (E_-^g + E_+^g - E_-^u - E_+^u)), \quad (3.10)$$

$$pp\sigma = \frac{1}{2(E_p - E_s)} (E_-^g E_+^g - E_-^u E_+^u - E_p (E_-^g + E_+^g - E_-^u - E_+^u)), \quad (3.11)$$

$$(sp\sigma)^2 = E_s E_p - ss\sigma \cdot pp\sigma - \frac{1}{2} (E_-^g E_+^g + E_-^u E_+^u). \quad (3.12)$$

Using the approximation [132]

$$(sp\sigma)^2 = -ss\sigma \cdot pp\sigma \quad (3.13)$$

only four independent matrix elements remain, which can be calculated from the four eigenenergies. From Eqs. 3.9, 3.12,

$$E_p = \frac{1}{4} (E_-^g + E_+^g - E_-^u - E_+^u) \pm \sqrt{\frac{1}{16} (E_-^g + E_+^g - E_-^u - E_+^u) - \frac{1}{2} (E_-^g E_+^g + E_-^u E_+^u)} \quad (3.14)$$

is obtained, which can be used to calculate the remaining matrix elements with Eqs. 3.9, 3.10, 3.11. Similar equations can be derived for a homoatomic sd -valent dimer. A generalized reduced TB approximation has been introduced in Ref. 133.

3.1.3. Canonical Tight-Binding

Two related TB parametrizations have been developed by Andersen et al. and Harrison et al., which provide general expressions for all bond integrals of s , p and d orbitals for all elements. They are constructed by only a very limited number of reference data and are successful in providing qualitative predictions.

Andersen considered the muffin-tin approximation [38], where only the effective potential of the single particle Schrödinger equation is retained inside atom-centred spheres. The potential in the interstitial region v_{int} of these spheres is assumed to be constant such that the potential energy surface of a two-dimensional layer of atoms has the shape of a muffin-tin. He used the Korringa–Kohn–Rostoker [134, 135] (KRR) formalism, where the wave functions are expanded with partial waves similar to the PAW method introduced in Sec. 2.2.5. He further applied the atomic-sphere approximation [136, 137] (ASA), where the potential is spherically symmetric inside spheres around the atom. Assuming $E - v_{\text{int}} = 0$ and neglecting two-center effects, he derived an orthogonal canonical TB model in which the radial dependence of the bond integrals depends only on the values of the angular quantum numbers of the orbitals and the amplitude on the common magnetic quantum numbers and the bandwidth [136]. The bond integrals are given by

$$\begin{aligned}
 ss\sigma &= -2(r_s/R)\Delta_s, \\
 sp\sigma &= -2\sqrt{3}(r_s/R)^2\sqrt{\Delta_s\Delta_p}, \\
 pp\{\sigma, \pi\} &= \{2, -1\} \times 6(r_s/R)^3\Delta_p, \\
 sd\sigma &= -2\sqrt{5}(r_s/R)^3\sqrt{\Delta_s\Delta_d}, \\
 pd\{\sigma, \pi\} &= \{-\sqrt{3}, 1\} \times 6\sqrt{5}(r_s/R)^4\sqrt{\Delta_p\Delta_d}, \\
 dd\{\sigma, \pi, \delta\} &= \{-6, 4, -1\} \times 10(r_s/R)^5\Delta_d,
 \end{aligned} \tag{3.15}$$

where R is the interatomic distance, $\Delta_{s,p,d}$ is a bandwidth parameter of the s , p , d band and

$$r_s = \sqrt[3]{\frac{3}{4\pi\rho}} \tag{3.16}$$

is the Wigner-Seitz radius, where ρ is the atomic density.

Another complete set of universal TB parametrizations for qualitative predictions has been summarized by Harrison in his solid state table of elements [138]. He parametrized distance-dependent functions [138, 139] for the $ss\sigma$, $sp\sigma$ and $pp\{\sigma, \pi\}$ bond integrals. They reproduce TB parameters for the elements C, Si and Ge [140] which were obtained by fitting to ab-initio results

[141]. The bond integrals are explicitly given by

$$\begin{aligned} ss\sigma &= -1.40 \hbar^2 / (mr_{\text{NN}}^2), \\ sp\sigma &= 1.84 \hbar^2 / (mr_{\text{NN}}^2), \\ pp\{\sigma, \pi\} &= \{3.24, -0.81\} \times \hbar^2 / (mr_{\text{NN}}^2), \end{aligned} \quad (3.17)$$

where r_{NN} is the nearest neighbour distance of the atoms in the solid and m is the mass of the electrons. He further used values for the onsite levels from Ref. 142. The same radial dependence of the bond integrals, but different structure-dependent pre factors were obtained by matching the TB band structure to the band structure obtained for free electrons [143].

Cressoni and Pettifor observed that it is necessary to increase the amplitude of $pp\pi$ by a factor of 1.3 in order to stabilize the close-packed structures with respect to the dimer for an sp -band filling equal to one [130]. Their parametrization has a ratio of

$$ss\sigma : sp\sigma : pp\sigma : pp\pi = -1 : 1.31 : 2.31 : -0.76. \quad (3.18)$$

for the bond integrals. Harrison and Froyen obtained the same radial dependence and canonical TB ratios as Andersen for the $dd\{\sigma, \pi, \delta\}$ bond integrals by applying the pseudopotential formalism to the muffin-tin potential. Their parametrization is explicitly given by[144]

$$dd\{\sigma, \pi, \delta\} = \left\{ -6\frac{7.5}{\pi}, 4\frac{7.5}{\pi}, -1\frac{7.5}{\pi} \right\} \times \frac{\hbar^2 r_d^3}{md^5}, \quad (3.19)$$

where r_d is the element specific d -state radius. The pre factors are modified to $\{-16.2, 8.75, 0\}$ to fit calculated energy bands and can be found in Harrisons solid state table of elements [138].

The combination of the s and p orbitals obtained from the free-electrons approach and d orbitals from the pseudopotential approach lead Harrison and Froyen to a parametrization of the hybrid bond integrals given by

$$\begin{aligned} sd\sigma &= -3.23 \frac{\hbar^2 r_d^{3/2}}{md^{7/2}}, \\ pd\sigma &= -5.02 \frac{\hbar^2 r_d^{3/2}}{md^{7/2}}, \\ pd\pi &= 2.90 \frac{\hbar^2 r_d^{3/2}}{md^{7/2}}. \end{aligned} \quad (3.20)$$

The pre factors are again modified in Harrisons solid state table of elements to $-3.16, -2.95$ and 1.36 in order to match calculated energy bands [138].

A further optimization of all pre factors of Harrisons solid state table is given in Ref. 145.

3.1.4. Rectangular d -Band Model

In the TB models presented in Sec. 3.1.3, the radial decay of the bond integrals depends only on the angular momentum quantum numbers of the contributing orbitals and is therefore the same for all elements of a specific period. Pettifor parametrized the bond integrals of the $4d$ transition-metal series to reference data for the d -bandwidth, the equilibrium distance and the bulk modulus

$$B = -V \frac{dP}{dV} = V \frac{d}{dV} \left(\frac{dU_B}{dV} \right), \quad (3.21)$$

where P is the pressure. He used the approximation of a rectangular density of states (DOS) of the d -electrons [4, 146, 147]. His results indicate that, opposite to the canonical TB model, the decay of the bond integrals depends on the number of valence electrons.

The DOS of the d -electrons is approximated by a rectangle of width W and height $10/W$,

$$n_d(E) = \begin{cases} 10/W & \text{if } E \in [E_d - \frac{W}{2}; E_d + \frac{W}{2}] \\ 0 & \text{else,} \end{cases} \quad (3.22)$$

where E_d is the band center. The bond energy contribution of the d -electrons (Eq. 2.126) is obtained by integration,

$$\begin{aligned} U_{\text{bond}}^d &= \int^{E_F} (E - E_d) n_d(E) dE \\ &= -\frac{W}{2} N_d (10 - N_d). \end{aligned} \quad (3.23)$$

The second moment of the rectangular DOS is given by

$$\mu^{(2)} = \frac{10}{W} \int_{-W/2}^{W/2} E^2 dE = \frac{10}{12} W^2. \quad (3.24)$$

It can also be expressed in terms of the bond integrals by

$$\mu^{(2)} = 10Z\beta^2, \quad (3.25)$$

where

$$\beta^2 = \frac{1}{5} (dd\sigma^2 + dd\pi^2 + dd\delta^2) \quad (3.26)$$

and Z is the number of nearest neighbours.

This allows one to relate the bandwidth to the bond integrals,

$$W = \sqrt{12Z}\beta(R). \quad (3.27)$$

The bond integrals are parametrized by

$$\beta(R) = bN_d \exp(-\lambda R) \quad (3.28)$$

and the pair repulsion is approximated within the Wolfsberg-Helmholtz approximation (Eq. 2.226) by

$$U_{\text{rep},IJ}(R) = aN_d^2 \exp(-2\lambda R). \quad (3.29)$$

The linear dependence of the bond integrals on N_d is motivated by their dependence on the electron density. According to the TB bond model, the binding energy (Eq. 2.118) is approximated by

$$U_B(R) = U_{\text{bond}}(R) + U_{\text{rep}}(R). \quad (3.30)$$

The equilibrium distance is obtained by setting the first derivative of U_B to zero and is given by

$$R_0 = \frac{1}{\lambda} \ln \left(\frac{10a\sqrt{Z}}{\sqrt{3}b(10 - N_d)} \right). \quad (3.31)$$

With this result, the bandwidth

$$W(R_0) = \frac{3b^2}{5a} N_d(10 - N_d) \quad (3.32)$$

and the binding energy

$$U_B(R_0) = \frac{1}{2} Z \beta(R_0) = \frac{3b^2}{200a} (N_d(10 - N_d))^2 \quad (3.33)$$

can be calculated at the equilibrium distance. The bulk modulus at the equilibrium distance is obtained by estimating the atomic equilibrium volume at $V_0 = R_0^3/\sqrt{2}$, which is exact for fcc and hcp and a good approximation for bcc. It is given by

$$B(R_0) = \frac{2\sqrt{2}\lambda^2}{9R_0} U_B(R_0). \quad (3.34)$$

The derived equations enable a calculation of the model parameters a , b and λ from reference data for the bandwidth W^{ref} , the equilibrium nearest neighbour distance R_0^{ref} and the bulk modulus B^{ref} .

Equation 3.32 can be rewritten as

$$\frac{b^2}{a} = \frac{5W}{3N_d(10 - N_d)}, \quad (3.35)$$

which allows for a calculation of the binding energy (Eq. 3.33). An equation for λ is obtained from the product of the bulk modulus and the equilibrium distance,

$$\lambda^2 = \frac{9B^{\text{ref}}R_0^{\text{ref}}}{2\sqrt{2}U_B}. \quad (3.36)$$

The ratio a/b is extracted from Eq. 3.31 and is used together with Eq. 3.35 to calculate a and b .

Pettifor obtained the values $a = 216$ eV and $b = 12$ eV from reference data for molybdenum and found that the other elements of the $4d$ row can be well described by a the linear interpolation*

$$\lambda = (0.966 + 0.142N_d)/\text{\AA} \quad (3.37)$$

of the decay parameter of the bond integrals and constant values for a and b .

3.1.5. Explicit Tight-Binding Parametrizations for Groups of Elements

In order to obtain more accurate TB parametrizations than the canonical TB models with its modifications (Sec. 3.1.3) and the rectangular d -band model (Sec. 3.1.4), a single system is considered and a TB model is parametrized such that it reproduces system specific reference data. However, attempts to follow one approach consistently for groups of elements are rare.

A distance-dependent parametrization of the bond integrals for all homoatomic systems of the d -block [148] as well as a parametrization of ground state structures across the periodic table [149] has been obtained by Papaconstantopoulos and co-workers within the NRL-TB formalism [150], in which the repulsive energy (Eq. 2.162) is replaced by a shift of the one-electron eigenvalues. These parametrizations have been obtained by direct fitting of the Hamiltonian matrix elements to DFT reference data, which may include total energies and band structures [151].

In density-functional tight-binding (DFTB) [152, 153], pseudoatomic wave functions are defined via a confinement potential. The Hamiltonian matrix elements are computed in the two-center approximation from pseudoatomic wave functions, which essentially corresponds to calculating the TB matrix elements by application of the pseudoatomic wave functions to the Hamiltonian of a dimer. The parameters of the confinement potential are optimized to construct those Hamiltonian matrix elements which best reproduce selected reference data. A DFTB parametrization across the periodic table has been obtained in Ref. 154 by fitting the model parameters to unary bulk structures. The performance of the model parameters was tested to a few binary

*The units of the parameters are transformed to \AA and the number of d -electrons N_d of Mo is changed from five to four compared to the original reference.

systems. A similar work was performed by Grimme et al. to parametrise the GFN-xTB Hamiltonian across the periodic table [155].

3.2. Tight-Binding Parametrizations from the Downfolding Procedure

The canonical TB models with its modifications (Sec. 3.1.3) and the rectangular d -band model (Sec. 3.1.4) indicate that the shape of the bond integrals vary across the periodic table. However, these parametrizations only provide qualitative predictions. On the other hand, the approaches of Sec. 3.1.5 are able to accurately reproduce the given reference data and are robust and general enough to be applied to different systems, but trends of the model parameters as existing in the rectangular d -band model (Sec. 3.1.4) have not been published. This means that the strategies of creating TB parametrizations for many systems can be divided into two extremes. On one hand the canonical TB models with its modifications and the rectangular d -band model parametrize the bond integrals as by assuming of specific trends across the periodic table. On the other hand accurate parametrizations with respect to reference data exist for large sets of elements in the periodic table, but their model parameters do not necessarily show trends.

It is therefore of interest to develop TB parametrizations from reference data without implying any trends of the parameters and to extract trends from the model parameters afterwards. This would enable an evaluation of existing TB parametrizations and would also provide a starting point for refined TB parametrizations. An alternative way to arrive at TB parameters are downfolding procedures which are presented in Sec. 2.3.8. This direct parametrization of the TB matrix elements is particularly attractive for high-throughput parametrization across the periodic table. The application of this method to virtually all combinations of elements from periods 1 to 6 and groups 3 to 18 is discussed in this section.

The reduced TB approximation (Sec. 3.1.2) can also be applied across the periodic table instead of the downfolding procedure. However, the approximations of this method could not be tested without comparing the results to more accurate methods and the findings in Sec. 3.3.6 indicate that the approximations are not generally valid. Moreover, with this method only orthogonal TB parametrizations can be obtained.

3.2.1. Density-Functional Theory Reference

TB calculations are usually carried out in the two-center approximation, in which all three-center integrals, i.e. the contributions to the interatomic matrix elements $H_{IIm,I'Im'}$ from the effective potential of atoms at a third site $v_{eff}^K(\mathbf{r} - \mathbf{R}_K)$ with $K \neq I, J$ are neglected (Sec. 2.3.4). This approximation

is exact for a dimer (cf. Sec. 3.1.1). In the downfolding procedure, the projection of a minimal basis onto the DFT reference eigenstates is optimized (Eq. 2.148) and by this three-center effects would be attributed to the TB Hamiltonian in the two-center approximation. This needs to be avoided as it would bias the TB matrix elements in the two-center approximation towards an incorrect compensation of the system-dependent three-center effects.

Furthermore, the second-order TB approximation to the Kohn-Sham energy functional (Eq. 2.112) is based on the Hamiltonian \hat{H}_0 constructed from the input electron density (Eq. 2.87). Therefore, the eigenstates obtained from the Harris-Foulkes approximation (Eq. 2.90) should be taken as the reference eigenstates in the downfolding procedure. Otherwise effects which are obtained from the self-consistent solution of the Kohn-Sham equations would be mixed into the initial TB Hamiltonian. However, these effects should be taken into account by the self-consistent variation of the TB Hamiltonian (Eq. 2.115). Taking the self-consistently determined DFT eigenstates as reference would again bias the TB matrix elements towards a particular system with a given self-consistently determined charge density. The best DFT reference for an application of the downfolding procedure across the periodic table is therefore the set of eigenstates of a dimer obtained in the Harris-Foulkes approximation (Eq. 2.90).

Harris-Foulkes-DFT reference states are created for interatomic distances from $\min(3/4R_{\text{eq}}, 3\text{\AA})$ to 8\AA in steps of 0.05\AA and the downfolding procedure is applied to them individually. The equilibrium bond length R_{eq} of all homoatomic dimers is taken from Fig. 3.1. The bond length R_{eq} is estimated by averaging the values of R_{eq} of the homoatomic dimers for the heteroatomic dimers.

3.2.2. Application of Downfolding Procedure

The calculation of the Harris-Foulkes-DFT reference states is carried out by **GPAW** with a non-spin-polarized 3- ζ basis (Sec. 2.2.6) and the PBE exchange-correlation functional (Sec. 2.2.3). The use of a 3- ζ basis is based on previous applications of the downfolding procedure [74], which indicate that the results obtained with three radial functions per orbital are already converged accurately enough with respect to the basis set size. The 3- ζ basis is generated with a value of the energy shift ΔE_{PAO} , which ensures that the onset of the confinement potential is larger than all considered interatomic dimer distances. The default PAW datasets (Sec. 2.2.5) of **GPAW** are used. The temperature parameter T of the downfolding procedure (Eq. 2.150) was adjusted to $k_{\text{B}}T = 1$ to obtain smooth results. By the application of the downfolding procedure, a minimal basis is constructed which includes all orbitals which were not excluded by the PAW method. These are, however, still more than usually considered in a TB description. An extension to the downfolding procedure to remove these orbitals was introduced in Sec. 2.3.8.

In this work, all elements from groups 3 to 18 and periods 1 to 6 are considered except for Po, At, Tc and Lu for which no PAW datasets are available in GPAW. These are in total 1711 inequivalent dimers. The elements in groups 3 to 11 are treated as *sp*-valent and the elements in groups 12 to 18 as *sd*-valent. Exceptions are Hydrogen and Helium, which are considered as *s*-valent.

3.2.3. Parametrization

Similar to the three-center effects, the two-center intraatomic parameters $E_{1/2}^{s,p/d}$ are determined by the local surrounding of the atom. In fact, they are typically neglected in TB and therefore also not parametrized in this work.

From an analysis of all bond integrals of all considered combinations of elements, it was found that the asymptotic behaviour can be well described by an exponential decay. However, the bond integrals differ from their asymptotic trend for shorter interatomic distances and may even change the sign of their slope. Therefore, a function which can parametrize all bond integrals has to be flexible enough to capture this behaviour. It should furthermore be systematically extendable to allow for the inclusion of additional values for shorter interatomic distances in the fit, which may result in a more complex radial dependence. This requires a flexible function with a variable number of fitting parameters.

Based on these requirements, the choice for a distance-dependent parametrization of the bond integrals is

$$\beta(R) = \sum_{i=0}^{i_{\max}} c_i \exp(-\lambda_i R^{n_i}) = \sum_{i=0}^{i_{\max}} f_i(R) \quad (3.38)$$

with $n_0 = 1$. The onsite matrix elements are parametrized by the same functional form,

$$E(R) = \sum_{i=0}^{i_{\max}} c_i \exp(-\lambda_i R^{n_i}) = \sum_{i=0}^{i_{\max}} f_i(R) \quad (3.39)$$

with $\lambda_0 = 0$, which sets the first term to a constant value. The parametrization procedure is the following:

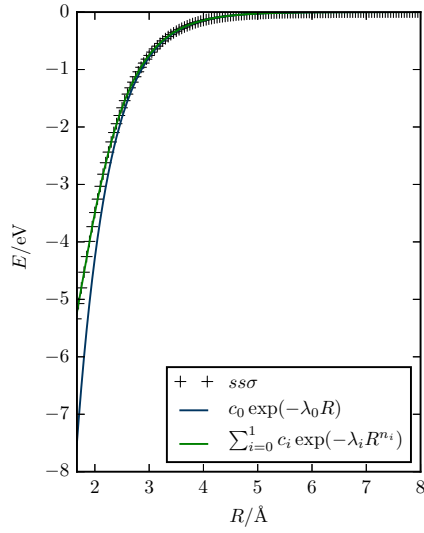
- Define a threshold Δ which is equal to the largest allowed quadratic difference between the fit and the raw data.
- Find the smallest interatomic distance to which $f_0(R)$ can describe the raw data without exceeding the threshold Δ .
- Subtract $f_0(R)$ from the raw data and fit the remaining data with $f_1(R)$ up to the smallest interatomic distance for which the threshold Δ is not exceeded.

- Continue by increasing i to i_{\max} until the fit $\sum_i f_i(R)$ can accurately describe all data points up to $\min(3/4R_{\text{eq}}, 3\text{\AA})$.

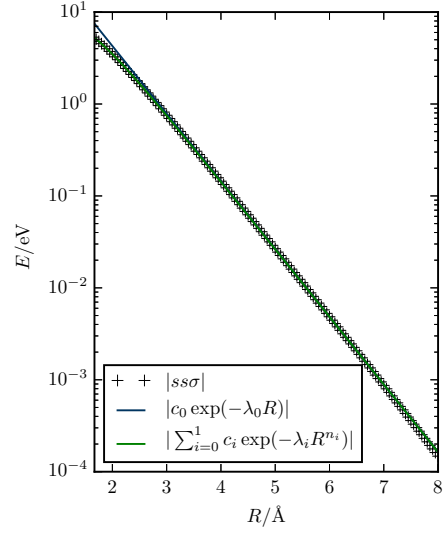
This parametrization scheme leads to terms which are responsible for particular interatomic distances such that the number of required parameters depends on the range of relevant interatomic distances.

The presented parametrization strategy is illustrated in Fig. 3.2 for the $ss\sigma$ matrix element of the Löwdin orthogonalized Hamiltonian matrix of the Si-Si dimer. In Fig. 3.2a, a pure exponential decay is fitted to the data points obtained from the downfolding procedure, which can describe the radial decay accurately enough for interatomic distances larger than approximately 3 Å. This is confirmed by the logarithmic plot in Fig. 3.2b, which shows a linear behaviour for interatomic distances below 3 Å that is well reproduced by the exponential fit. The difference of the data points obtained from the downfolding procedure and the exponential fit is calculated in Fig. 3.2c. It is parametrized by a generalized exponential decay of the form $c_1 \exp(-\lambda_1 R^{n_1})$. The sum of the exponential decay ($i = 0$) and the generalized exponential decay ($i = 1$) can already describe all data points accurately enough as verified in Figs. 3.2a, 3.2b and Fig. 3.2d, the latter showing the difference of the total fit and the raw data. The difference between the raw data and the fit is smaller than 1 meV for all considered interatomic distances. This value is much smaller than the accuracy in the eigenspectrum obtained by the downfolding procedure. It may be required to add further generalized exponential decay functions to parametrize all considered interatomic distances accurately enough for other matrix elements and other systems.

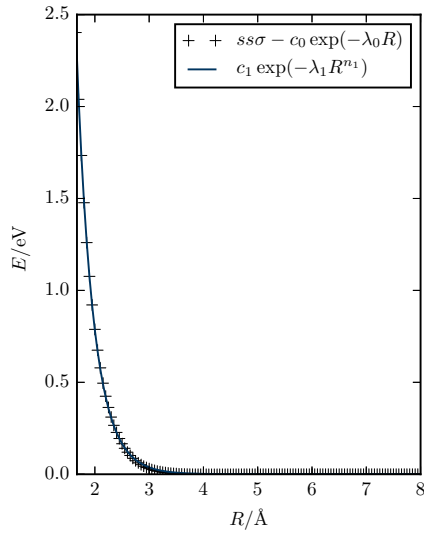
The parametrization procedure is applied to the orthogonal TB Hamiltonian matrix, the non-orthogonal TB Hamiltonian matrix and the overlap matrix of the 1711 inequivalent dimers. This requires the parametrization of 8476 interatomic matrix elements for each TB matrix and additionally 11310 on-site matrix elements for both, the orthogonal and non-orthogonal TB Hamiltonian matrix. Therefore, in total 48048 inequivalent matrix elements are parametrized. This shows that the functional form of the matrix elements (Eqs. 3.38, 3.39) is flexible enough to capture all possible features of the matrix elements. Moreover, this flexibility of the functional form is crucial for Sec. 5, in which the matrix elements are optimized to sets of DFT reference data by a numerical optimization method initialized by the parametrizations obtained for the dimers. The results are discussed in Secs. 3.3.1, 3.3.2 for the example of the homoatomic Si-Si and Mo-Mo dimers. All 1711 parametrizations are available as supplemental material on the attached CD.



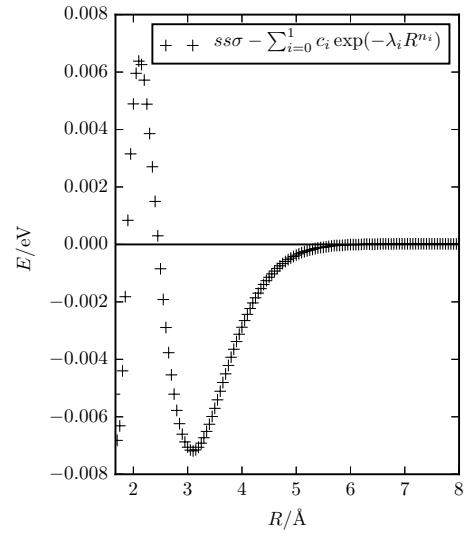
(a) $ss\sigma$ bond integral.



(b) $ss\sigma$ bond integral (logarithmic).



(c) Second term in the parametrization procedure of $ss\sigma$.



(d) Difference between raw data and fit.

Figure 3.2.: Illustration of the distance-dependent parametrization procedure of the TB Hamiltonian matrix elements for the example of the $ss\sigma$ matrix element of the Löwdin orthogonalized Hamiltonian matrix of the Si-Si dimer.

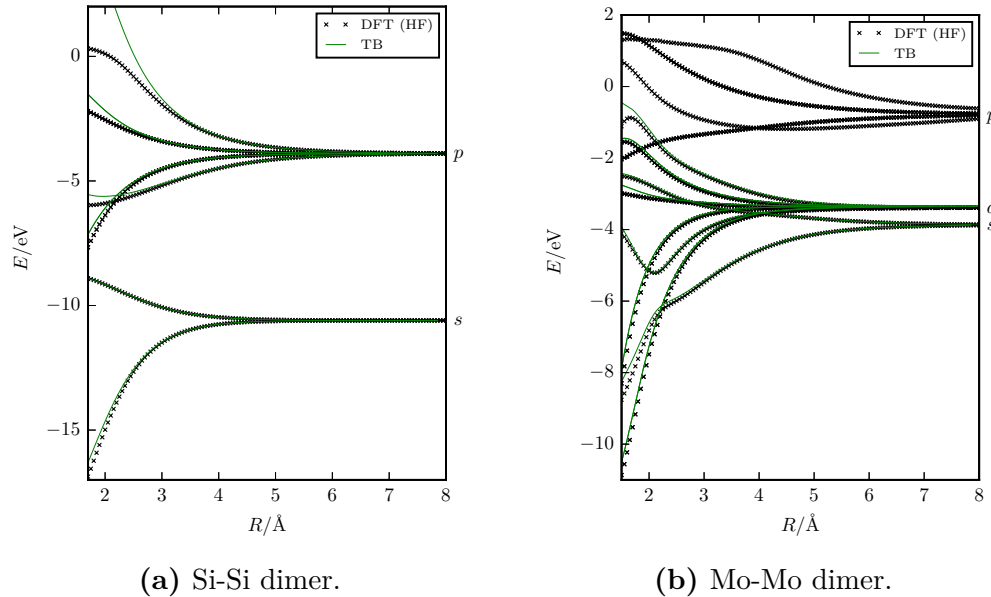


Figure 3.3.: Comparison of the eigenspectra of TB and the Harris-Foulkes (HF) approximation to DFT for the Si-Si and Mo-Mo dimer. The labels on the right y -axis indicate the character of the eigenvalues.

3.3. Evaluation of Results from the Downfolding Procedure

3.3.1. Si as Example for sp -valent Elements

The eigenspectrum of the homoatomic sp -valent Si-Si dimer as a representative sp -valent system is shown in Fig. 3.3a. The two s -states are lower in energy than the six p -states for all investigated interatomic distances. The states of the π -blocks are two-fold degenerated and therefore four different p -eigenenergies exist. The TB eigenenergies, obtained from the parametrized TB Hamiltonian matrix, and the Harris-Foulkes-DFT eigenenergies agree well for large interatomic distances, where the atomic orbitals are similar to those of free atoms. The agreement remains good for the states with a high occupation number f_n , which is defined by the Fermi distribution in Eq. 2.150. The agreement is worse for the states with a small occupation number for shorter interatomic distances. In general, the optimized minimal basis cannot reproduce all states exactly. The Fermi distributions causes that the states which are occupied at 0 K are well reproduced while a compromised description of the unoccupied states is tolerated. An exact agreement of the TB and Harris-Foulkes-DFT eigenenergies could be obtained by using the Harris-Foulkes-DFT eigenenergies in Eqs. 2.155, 2.160 of the extensions to the downfolding procedure. This would, however, not necessarily result in a more accurate TB basis, which is modified in the extensions to the downfold-

ing procedure. Therefore, this approach is not taken in this work.

The matrix elements of the TB Hamiltonian matrix, the overlap matrix and the Löwdin orthogonalized TB Hamiltonian matrix are shown in Fig. 3.4a. The individual data points show a monotonic trend with respect to the interatomic distance R . They have been parametrized with the functional forms of Eqs. 3.38, 3.39. Due to the monotonic behaviour of the matrix elements of the Si-Si dimer, all matrix elements can be parametrized by using only three functions $f_i(R)$ (i.e. $i_{\max} \leq 0, 1, 2$).

3.3.2. Mo as Example for d -valent Elements

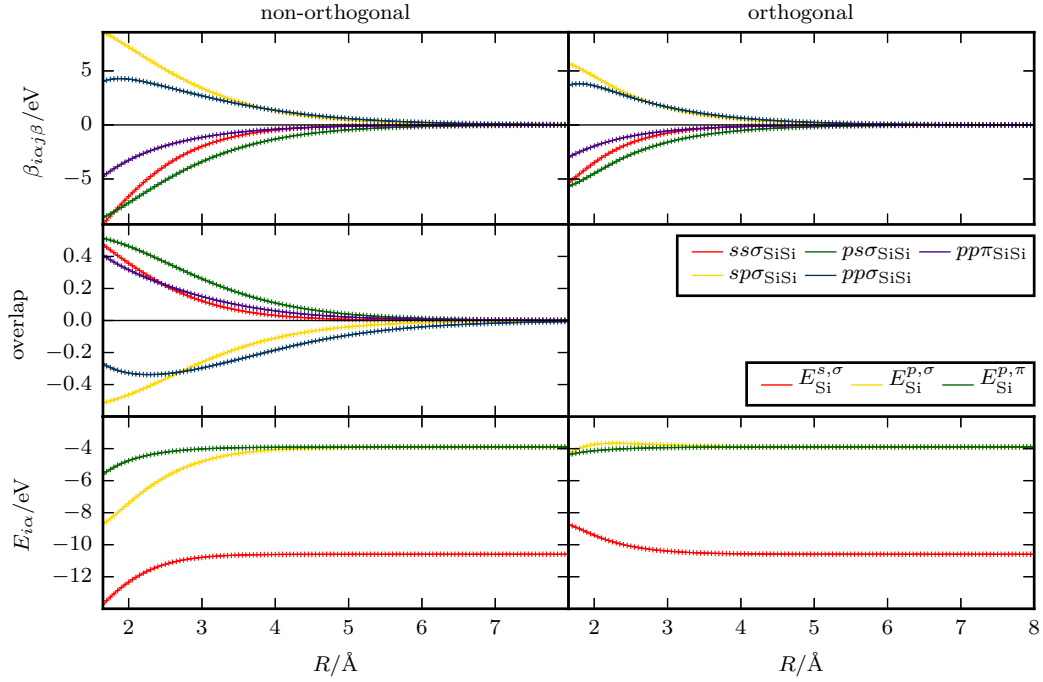
The Mo-Mo dimer is chosen as a representative sd -valent system. The comparison of the Harris-Foulkes-DFT and the TB eigenspectrum is compiled in Fig. 3.3b and the distance-dependent TB matrix elements are shown in Fig. 3.4b. The spectrum has more features than in the case of the Si-Si dimer due to the four additional two-fold degenerated δ -states in the TB spectrum. The two s -states are lower in energy than the d -states for large interatomic distances, however, the energy difference of the two valence states is much smaller compared to the Si-Si dimer. For smaller interatomic distances, the s - and d -eigenenergies even cross. It can be observed that the TB spectrum reproduces all relevant features of the Harris-Foulkes-DFT spectrum.

As already expected from the eigenspectrum, the matrix elements have in general more features in the region of short interatomic distances compared to the Si-Si dimer. This explains that the parametrization procedure requires more terms in Eqs. 3.38, 3.39 to reproduce the matrix elements for all considered interatomic distances. The distance dependence of $sd\sigma$ ($= ds\sigma$) of the TB Hamiltonian of the non-orthogonal model requires six terms and more parametrization steps than all other bond integrals. This might be already expected as this bond integral even changes its sign with distance.

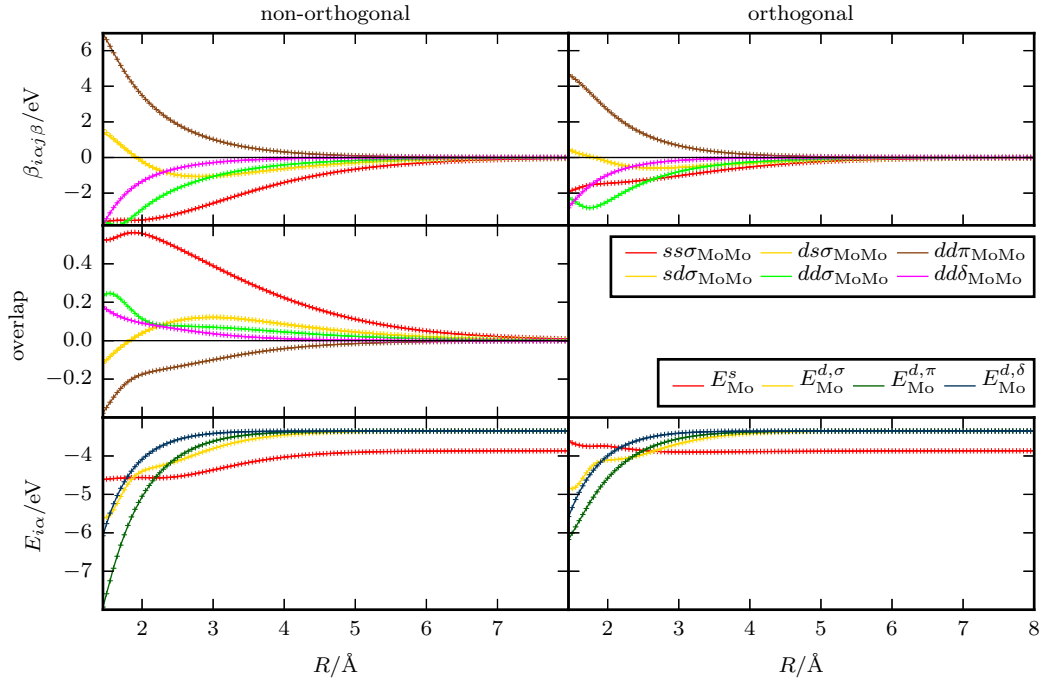
The variation of the matrix elements of the orthogonal TB model with respect to the interatomic distance is smaller compared to the non-orthogonal model for the Si-Si dimer and the Mo-Mo dimer. Opposite to the Si-Si dimer, the $ss\sigma$ bond integral of Mo is longer ranged than the other bond integrals. The presented parametrizations are longer ranged than existing parametrizations for Si [152] and Mo [148]. This can be understood as a screening effect of the surrounding atoms in a cluster or bulk material and is discussed in more detail in the following Sec. 3.3.3.

3.3.3. Homoatomic Dimers

In order to analyse chemical trends of the TB parametrizations, the $ss\sigma$ matrix element of the orthogonalized Hamiltonian is plotted for all homoatomic dimers from periods $2p$ and $4d$, which include Si and Mo. The results are summarized in Fig. 3.5. As shown in Fig. 3.5a, the bond integrals from



(a) Si-Si dimer.



(b) Mo-Mo dimer.

Figure 3.4.: TB matrix elements of the Si-Si (Fig. a) and the Mo-Mo (Fig. b) dimer. Crosses are the data points obtained by the downfolding procedure and the solid lines are the distance-dependent parametrizations in form of Eqs. 3.38, 3.39.

period $2p$ decrease in amplitude and in decay length with increasing electron count. This decrease in amplitude is very pronounced and larger than one order of magnitude between Al and Ar. The overall behaviour is similar for the homoatomic dimers from period $4d$. However, the effect is much less pronounced and the bond integrals even cross.

It is also notable that the $4d$ - $ss\sigma$ bond integrals are overall longer ranged than the $2p$ - $ss\sigma$ bond integrals. A measure of the range of the bond integrals is directly given by the coefficient λ_0 of the parametrization function (Eq. 3.38), which is an inverse decay length [146]. The trend of λ_0 across the different periods is visualized for the $ss\sigma$ bond integral of the orthogonalized Hamiltonian in Fig. 3.6. The trend of λ_0 is compiled in Sec. A of the appendix for the other bond integrals of the sp -valent (Fig. A.1) and sd -valent (Fig. A.2) dimers. A linear dependency of λ_0 of the homoatomic bond integrals across the different periods is clearly visible. It is well described by a linear relationship,

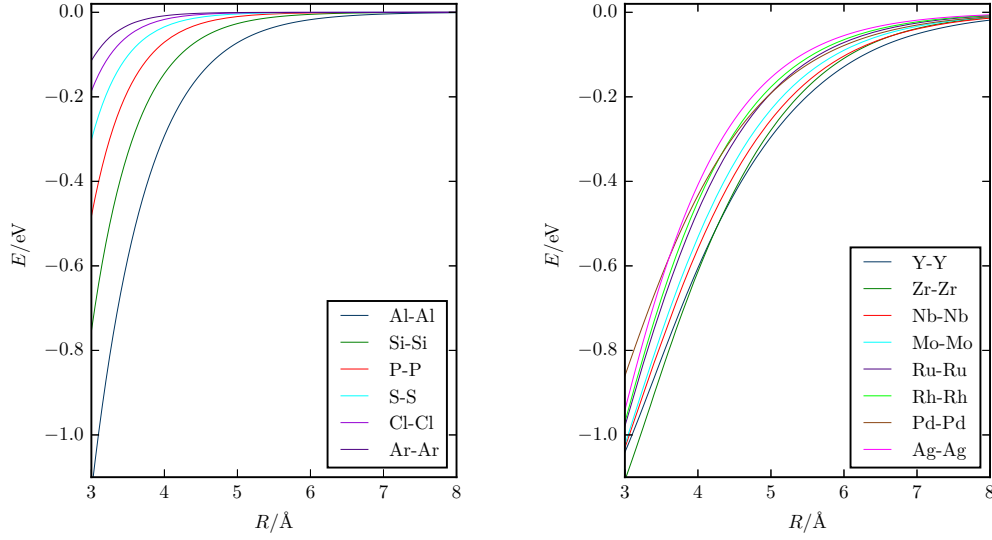
$$\tilde{\lambda}_0 = b_0 + m_0 N_{p/d}, \quad (3.40)$$

where $N_{p/d}$ is the average number of p/d electrons of the free atoms. Cr and Cu ($3d$ period) and Zr and Pd ($4d$ period) are excluded from the linear regression because they are clear outliers. Their irregular behaviour is related to the asymptotic behaviour of the employed GPAW datasets as it occurs not only for the homoatomic dimer but for all combinations with other elements as shown in Fig. 3.7, which is discussed later. This irregular behaviour of Cr, Cu, Zr and Pt is observable across all TB matrix elements. The values of the linear regression of λ_0 (Eq. 3.40) for all bond integrals of H^{orth} are summarized in Tab. 3.2. The slope parameter m_0 of $ss\sigma$ is at least five times higher for the sp -elements than for the sd -elements, indicating that the $ss\sigma$ bond integrals of sp -valent dimers decay faster. Also the pp bond integrals decay faster than the dd bond integrals. The pp bond integrals of sp -valent dimers are longest ranged, whereas the $ss\sigma$ bond integrals of sd -valent dimers are longest ranged.

Table 3.2 also shows that the parameters b_0 and m_0 are very similar for all dd bond integrals of one period. This validates the assumption of a common value for b_0 and m_0 for $dd\sigma$, $dd\pi$ and $dd\delta$, which is taken in the rectangular d -band model (Sec. 3.1.4). In the rectangular d -band model, the values of the linear relationship of the decay parameter are given by

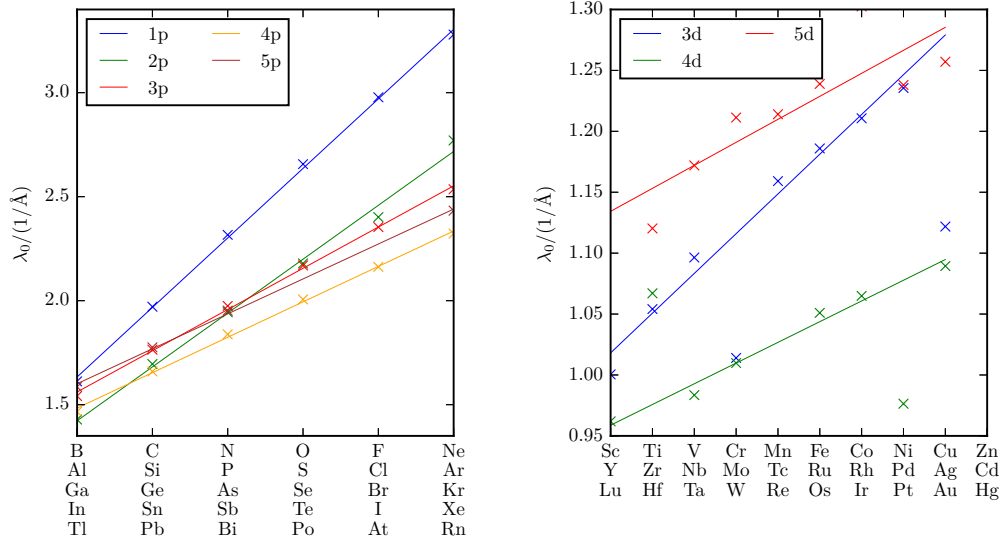
$$\begin{aligned} m_{0,d\text{-band}} &= 0.142/\text{\AA}, \\ b_{0,d\text{-band}} &= 0.966/\text{\AA}. \end{aligned} \quad (3.41)$$

They are slightly higher than the values obtained from the downfolding procedure for the $4d$ -period. Besides the strong approximations of the rectangular d -band model, this may be already expected as the two-center bond integrals are screened in the bulk crystal by the neighbouring atoms [71, 77, 156, 157].


 (a) Homoatomic $2p$ -dimers.

 (b) Homoatomic $4d$ -dimers.

Figure 3.5.: Matrix element $ss\sigma$ of H^{orth} of (a) periods $2p$ and (b) $4d$. Comparison shows a more pronounced shrinking of the bond integrals for the sp dimers than for the $4d$ dimers with increasing group number.


 (a) Homoatomic sp -valent dimers.

 (b) Homoatomic sd -valent dimers.

Figure 3.6.: Trend of the decay parameter λ_0 of the $ss\sigma$ matrix element of H^{orth} across different periods of the sp - and sd -valent homoatomic dimers. The linear trend and the outliers are discussed in Sec. 3.3.3.

period	$m_0/(1/\text{Å})$					$b_0/(1/\text{Å})$				
	$ss\sigma$	$sd\sigma$	$dd\sigma$	$dd\pi$	$dd\delta$	$ss\sigma$	$sd\sigma$	$dd\sigma$	$dd\pi$	$dd\delta$
3d	0.033	0.057	0.112	0.107	0.123	0.985	0.927	0.882	1.094	1.257
4d	0.017	0.041	0.101	0.099	0.105	0.942	0.854	0.684	0.877	1.044
5d	0.019	0.049	0.087	0.090	0.092	1.115	0.961	0.823	0.997	1.176
	$ss\sigma$	$sp\sigma$	$pp\sigma$	$pp\pi$		$ss\sigma$	$sp\sigma$	$pp\sigma$	$pp\pi$	
1p	0.334	0.261	0.207	0.222		1.299	0.859	0.843	1.032	
2p	0.259	0.221	0.179	0.191		1.164	0.697	0.700	0.864	
3p	0.198	0.196	0.163	0.170		1.363	0.740	0.696	0.868	
4p	0.170	0.146	0.145	0.148		1.313	0.801	0.689	0.866	
5p	0.168	0.136	0.138	0.139		1.433	0.781	0.668	0.847	

Table 3.2.: Slope parameter m_0 and intercept b_0 of the linear regressions of the decay parameter λ_0 of the bond integrals of H^{orth} according to Eq. 3.40.

3.3.4. Heteroatomic Dimers

In the previous subsection, the decay parameter λ_0 was used to analyse the range of the homoatomic bond integrals. In Fig. 3.7, the value of λ_0 of the $ss\sigma$ bond integral of H^{orth} is plotted across all considered heteroatomic dimers from periods 2 to 6. As already predicted from the results of the previous Sec. 3.3.3, a clear gap between the values for the sp - and sd -valent dimers is visible. The $ss\sigma$ bond integrals of the heterovalent sp - sd dimers are also relatively short ranged and take values for λ_0 , which are slightly larger than those of the sd - sd dimers. The value of λ_0 is determined by both the period and the number of the valence electrons of both atoms. The number of valence electrons of each atom is of the same importance for the sp - sp and the sd - sd bond integrals, whereas for the sp - sd bond integrals the value of the decay parameter is dominated by the number of valence electrons of the sd -element. As already mentioned above, the values for the dimers which include either Cr, Cu, Zr or Pd appear as clear outliers. The values of λ_0 of the other bond integrals of H^{orth} are compiled in Sec. B of the appendix for the sp -valent (Figs. B.1-B.4), sd -valent (Figs. B.5-B.9) and heterovalent dimers (Figs. B.10-B.14). The trends are more pronounced for the sp -valent elements than for the sd -valent elements. This is in agreement with the results for the homoatomic dimers (Sec. 3.3.3).

3.3.5. Energy Contributions

The TB bond model divides the binding energy U_B into intuitive contributions (cf. Sec. 2.3.5). The energy contributions differ in a non-orthogonal TB model and a Löwdin transformed orthogonal TB model. In Fig. 3.8, the energy contributions are summarized for an orthogonal and a non-orthogonal TB model for the Si-Si and the Mo-Mo dimer. The binding energy is calculated self-consistently with DFT as described in Sec. 3.1.1. The bond energy

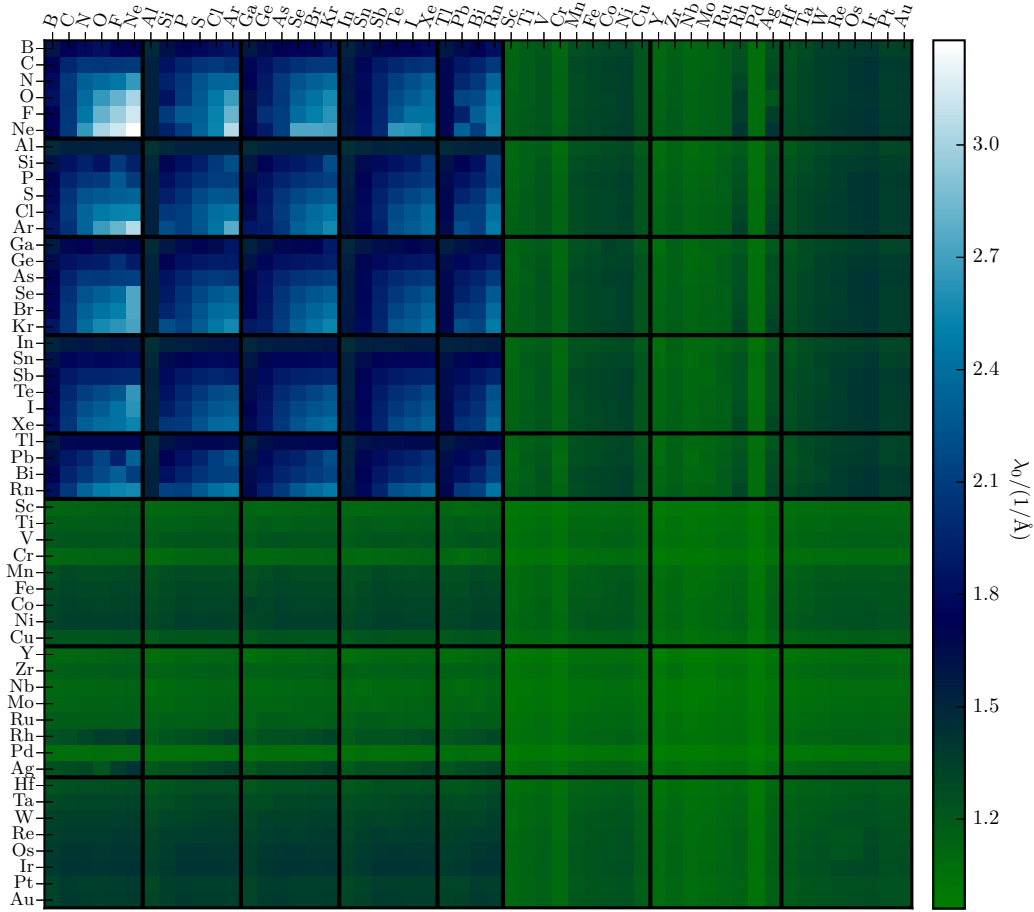


Figure 3.7.: Values of the parameter λ_0 describing the inverse decay length of the bond integrals for $ss\sigma$ of H^{orth} across all dimers.

U_{bond} (Eq. 2.119) and promotion energy U_{prom} (Eq. 2.127) are calculated from the TB matrix elements obtained in Sec. 3.2.2. The repulsive energy U_{rep} is obtained by subtracting these contributions from the binding energy. In the orthogonal TB models, the repulsive energy is positive and the bond energy is negative. The promotion energy is positive for both dimers at large interatomic distances. However, in case of the Mo-Mo dimer, it changes its sign at shorter interatomic distances. In the non-orthogonal models, the repulsive energy partially takes negative values and the bond energy is not monotonic in case of the Si-Si dimer. The difference in the energies of the orthogonal and non-orthogonal TB model is given by the overlap repulsion (Eq. 2.142), which defines the difference of the preparation energies (Eq. 2.129) of the orthogonal and non-orthogonal model and may be interpreted as an additional repulsion due to the orthogonalization of the orbitals. Adding it to the repulsive energy of the non-orthogonal TB model results in the repulsive energy of the orthogonal TB model. The different repulsive energy contributions and the overlap

repulsion are illustrated in Fig. 3.9 for the Si-Si and the Mo-Mo dimer. It shows that the overlap repulsion has a significant contribution to the repulsive energy in the orthogonal TB model and in case of the Si-Si dimer, it even dominates.

3.3.6. Comparison to Other Methods

Reduced Tight-Binding

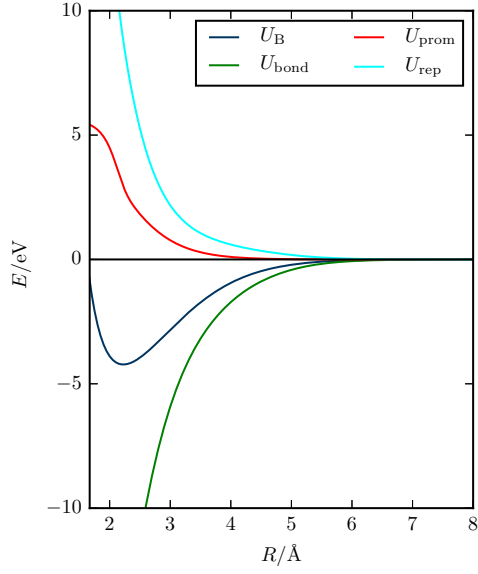
The assumption of the reduced TB approximation (cf. Sec. 3.1.2), $sp\sigma = \sqrt{|ss\sigma| \cdot pp\sigma}$, is compared to the results obtained from the downfolding procedure for the homoatomic sp -valent dimers in Fig. 3.10. As shown in Fig. 3.10a for the example of the homoatomic Si-Si dimer, the quality of the approximation depends on the interatomic distance. However, for a fixed interatomic distance of $R = 2.5 \text{ \AA}$, it can be seen in Fig. 3.10b that the ratio $sp\sigma / \sqrt{|ss\sigma| \cdot pp\sigma}$ is almost constant such that the approximation $sp\sigma \approx 1.5 \sqrt{|ss\sigma| \cdot pp\sigma}$ is more accurate. Only the elements from period 1p do not show a constant ratio. This is related to the fact that those bond integrals have the shortest range (cf. Fig. 3.6a).

Canonical Tight-Binding

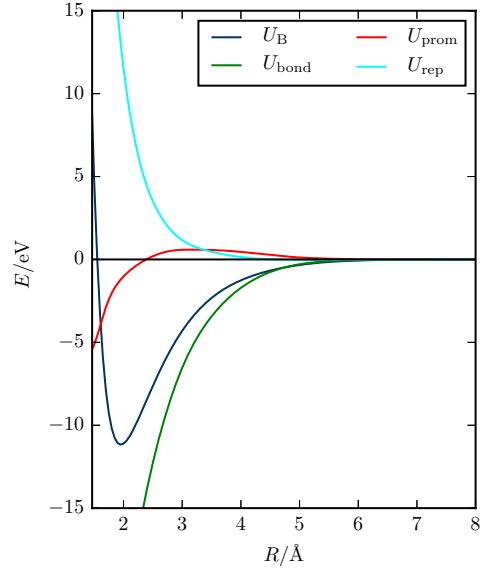
The ratios of the canonical TB parametrizations are compared to those which are obtained by the downfolding procedure. As shown in Sec. 3.3.3, the radial decay differs across the different periods and has a dependence on the number of valence electrons. However, the ratios of the bond integrals can be calculated for a particular interatomic distance, which is selected to be 4 \AA . Derivations from the pure exponential decay do not usually occur at this distance and the interatomic matrix elements are significantly different from zero. The TB model of Cressoni and Pettifor (Eq. 3.18) is chosen for a comparison as it was proven to describe the structural trends across the sp -valent materials qualitatively correct and has the same radial decay for all sp bond integrals. The ratios for the dd bond integrals are compared with the corresponding values of the original canonical TB model (Eq. 3.15). The results are summarized in Fig. 3.11.

In Fig. 3.11a, the value of the $pp\sigma$ matrix element of H^{orth} is fixed to match the value of 2.31 of Cressoni and Pettifor and the resulting ratios of the other matrix elements are calculated. A substantial effect of the number of valence electrons on the ratios is visible. The effect of the period number is much less pronounced and less systematic. The agreement of the ratios with the reference decreases for $ss\sigma$ and $pp\pi$ with increasing number of valence electrons but increases in case of $sp\sigma$.

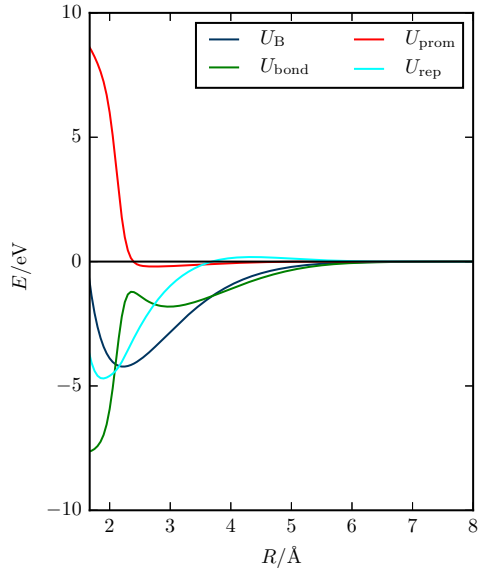
The ratios for the dd matrix elements of H^{orth} are compared to those of the canonical TB model in Fig. 3.11b by fixing the value of the $dd\sigma$ bond integral



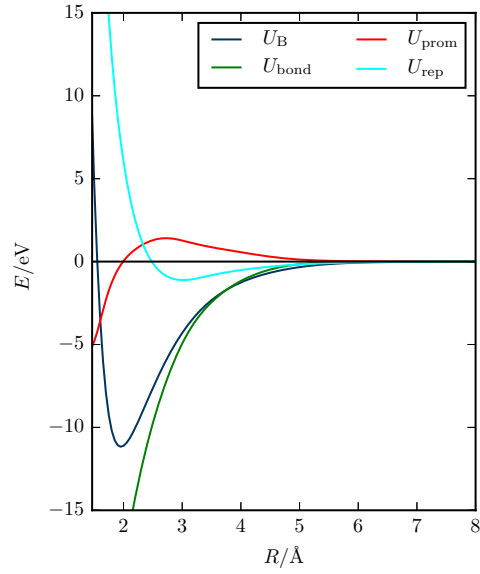
(a) Si-Si dimer, orthogonal TB.



(b) Mo-Mo dimer, orthogonal TB.



(c) Si-Si dimer, non-orthogonal TB.



(d) Mo-Mo dimer, non-orthogonal TB.

Figure 3.8.: TB energy contributions to the binding energy of the homoatomic Si-Si and Mo-Mo dimers in case of an orthogonal (Figs. a, b) and a non-orthogonal (Figs. c, d) TB model.

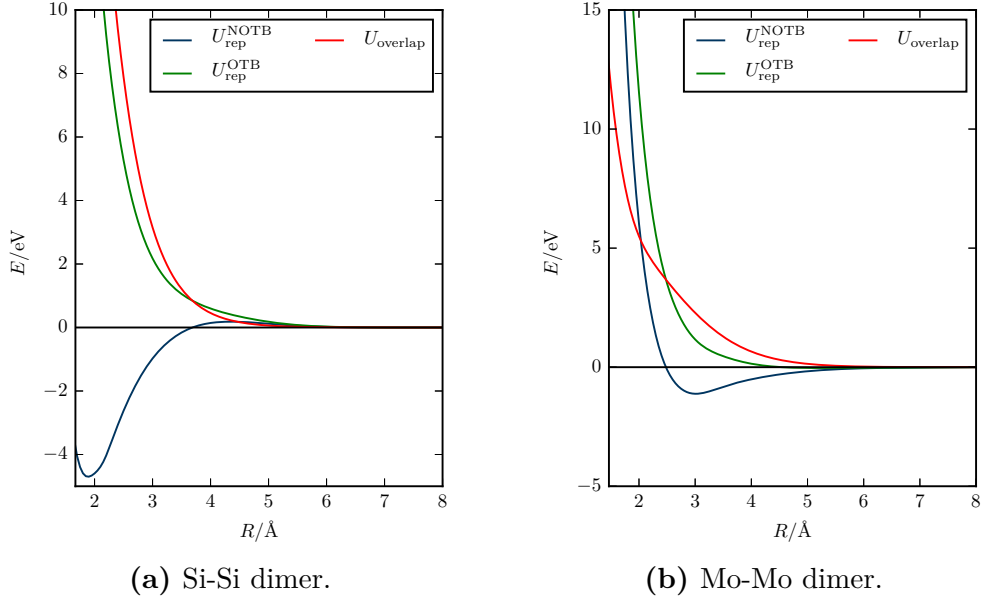


Figure 3.9.: Repulsive energy and overlap repulsion of the homoatomic Si-Si and Mo-Mo dimers.

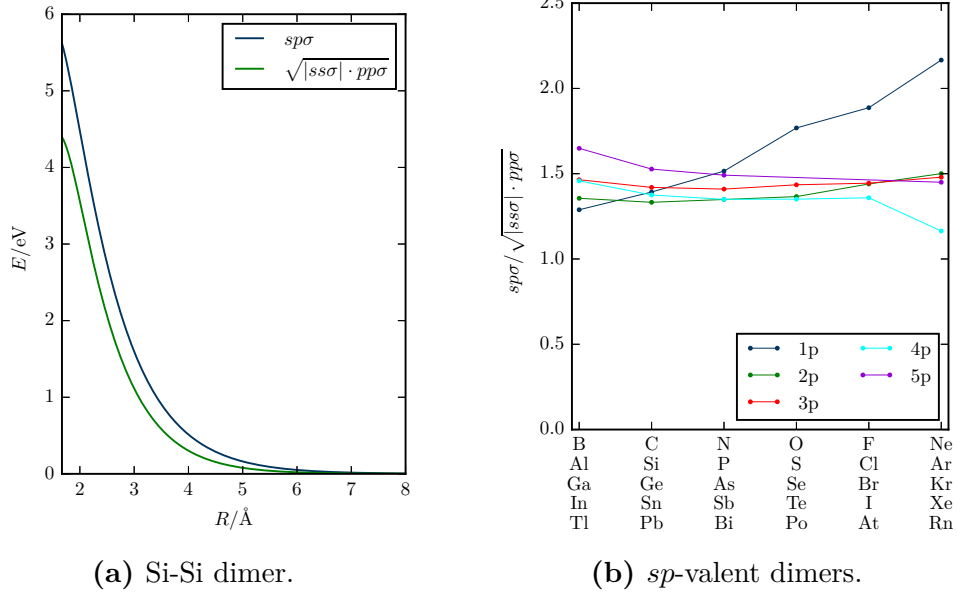


Figure 3.10.: Comparison of the $sp\sigma$ bond integral obtained from the downfolding procedure with the reduced TB approximation $sp\sigma = \sqrt{|ss\sigma|} \cdot pp\sigma$ for the orthogonalized TB Hamiltonian matrix. In Fig. a, the comparison is performed for the homoatomic Si-Si dimer and in Fig. b across the homoatomic sp -valent dimers at a fixed interatomic distance of $R = 2.5 \text{ \AA}$.

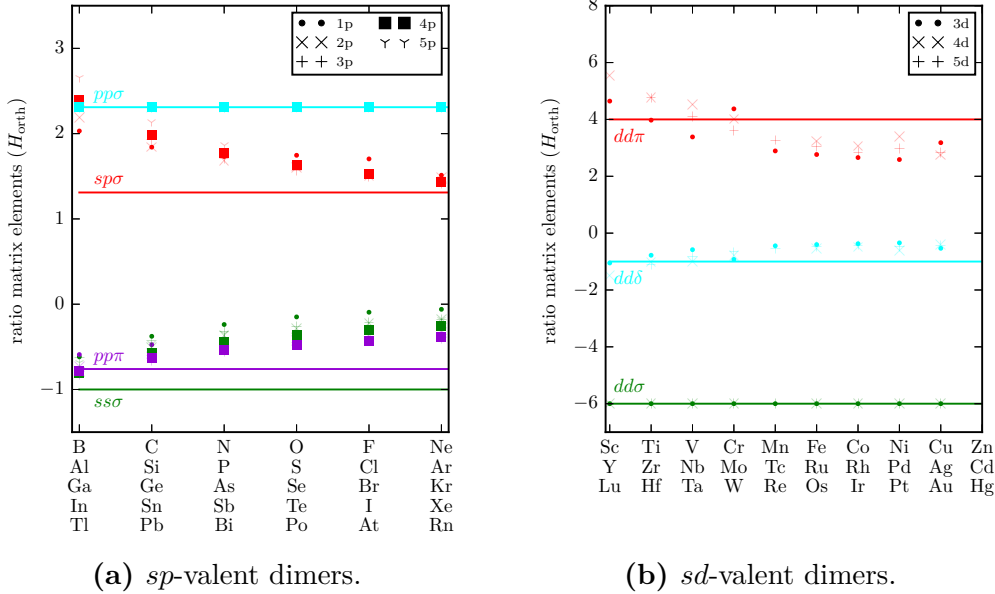


Figure 3.11.: Comparison of the ratios of the interatomic matrix elements of H^{orth} of the homoatomic dimers at an interatomic distance of 4 Å obtained from the downfolding procedure to those of the TB model of Cresoni and Pettifor (Eq. 3.18) in Fig. a and to the canonical TB model (Eq. 3.15) in Fig. b.

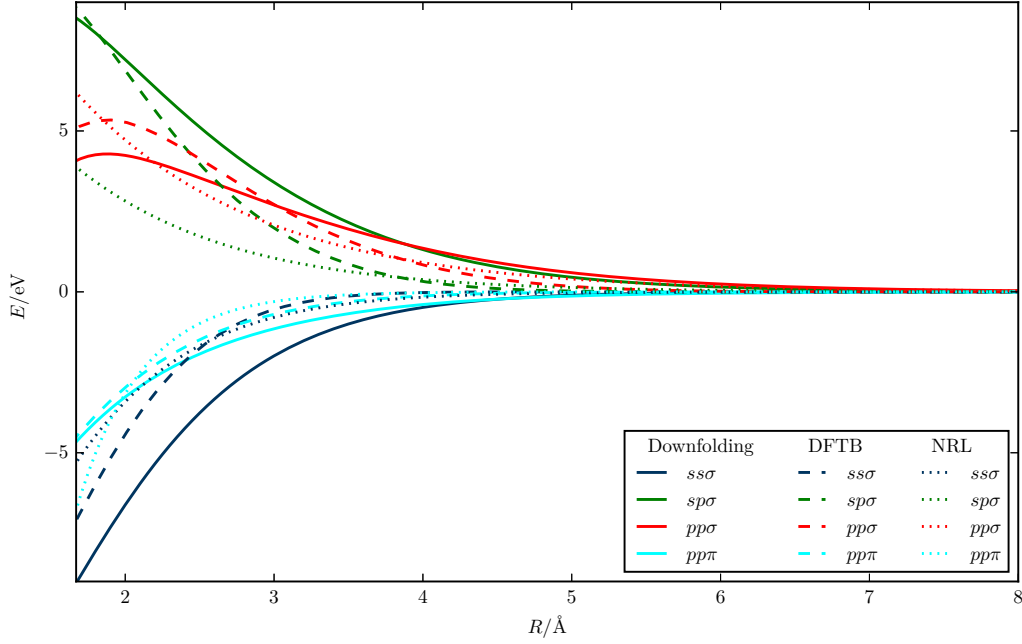
to 6. The effect of the numbers of valence electrons on the ratios is much less pronounced than for the *sp*-valent dimers and the effect of the period number is again lower. The ratios of the canonical TB model are astonishingly well reproduced, which is in agreement to the findings in Ref. 74 in case of Fe. It also explains that the canonical TB model is able to reproduce the DFT energy differences of the topologically close-packed phases for different band fillings [128].

DFTB and NRL-TB

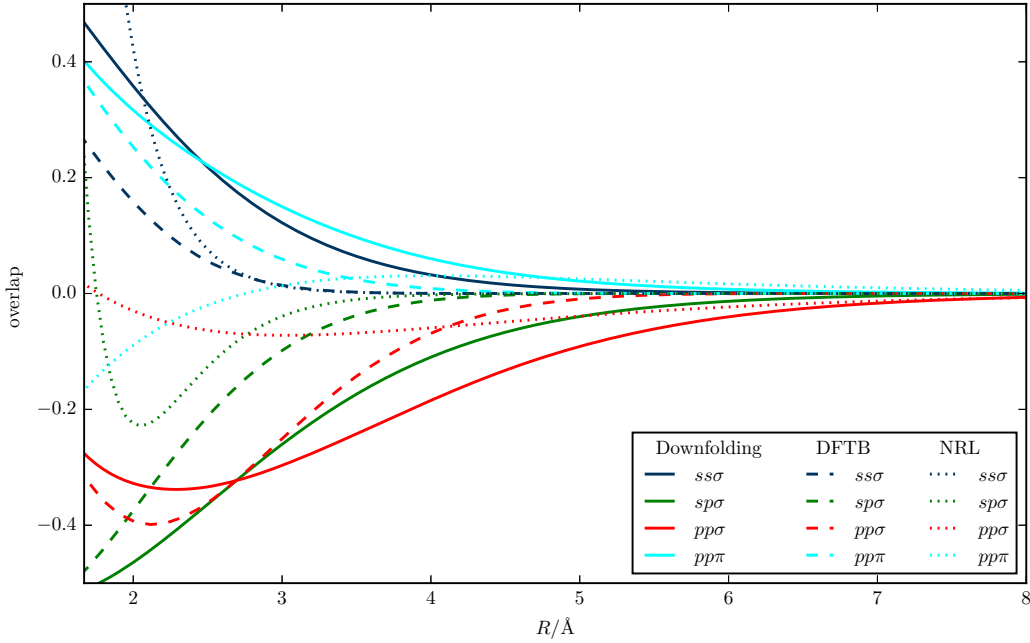
The example of the Si-Si dimer (Sec. 3.3.1) is well suited for a comparison to the DFTB and NRL-TB method, which are applied to a large set of the periodic table (Sec. 3.1.5). In case of DFTB, different parametrizations for Si are available [158]. The latest parametrization [159, 160] is used for comparison because it was reoptimized to experimental values for the band structure of bulk Si. The NRL-TB parameters for Si [161] are chosen to reproduce both the band structure and the total energy of different crystal structures.

A comparison of the parametrizations of the two methods to the results of the downfolding procedure applied to the Si-Si dimer is visualized in Fig. 3.12. The matrix elements used in DFTB and NRL-TB drop off faster with increasing interatomic distance R than those of the downfolding procedure. This may be understood as an effect of neighbouring atoms taken into account in the

other methods, which may lead to a contraction of the atomic orbitals. Especially in DFTB, the matrix elements are determined by an optimization of the parameters of a confinement potential, which should lead to a better representation of the orbitals in a solid. The results of the three methods agree well at interatomic distances between 2 Å and 3 Å for the Hamiltonian matrix elements. However, the overlap matrix elements in NRL-TB differ qualitatively in their radial behaviour from those of the other methods but also among themselves.



(a) Interatomic matrix elements of the TB Hamiltonian matrix H .



(b) Interatomic matrix elements of the TB overlap matrix S .

Figure 3.12.: Comparison of TB matrix elements obtained from downfolding procedure (Sec. 3.2.2) to DFTB [158–160] and NRL-TB [161]. The signs of the $sp\sigma$ matrix elements of the DFTB method are changed for a better comparison to the results of the other methods.

4

Electronic Structure Based Map of Local Atomic Environments

A quantitative descriptor of local atomic environments is often required for the analysis of atomistic data. Descriptors of the local atomic environment ideally provide physically and chemically intuitive insight. This requires descriptors that are low-dimensional representations of the interplay between atomic geometry and electronic bond formation. The moments of the local density of states (DOS) relate the atomic structure to the electronic structure and bond chemistry. The lowest moments, calculated from the closest atomic neighbourhood, carry the largest contributions to the local bond energy. This makes it possible to construct electronic structure based descriptors of the local atomic environment that have an immediate relation to the binding energy.

In Sec. 4.1, the relation between the moments of the DOS and structural stability is discussed. Different atomic environments are introduced and descriptors of atomic environments are presented. Descriptors based on the moments of the local DOS are constructed in Sec. 4.2 and used in Sec. 4.3 to project the space of local atomic environments onto a 2-D map. The separation of various atomic environments and their connections in the map are discussed in detail. The immediate relation of the map to the binding energy is discussed and illustrated in Sec. 4.4. The distances in the map are related to energy differences between local atomic environments as shown by analytic considerations based on analytic bond-order potentials (BOP) and by numerical assessment using TB and density-functional theory (DFT) calculations.

4.1. Background

4.1.1. Moments Theorem and Structural Stability

In Sec. 2.4.17, the convergence of the analytic BOPs towards the tight-binding (TB) reference was discussed and in Figs. 2.11, 2.12 the energy differences of different crystal structures were calculated in the TB and analytic BOP approximation. This section explains the energetic order and why some energy differences can be reproduced with four exactly calculated moments ($n_{\max} = 4$), while other crystal structures require at least six exactly calculated moments ($n_{\max} = 6$). Therefore, the moments of the local DOS are related to the crystal structure by the moments theorem (Eq. 2.167), which states that the moments of the DOS can be calculated by summation over self-returning hopping paths. In Fig. 4.1, the investigated crystal structures are illustrated together with selected self-returning hopping paths of length three and four, which contribute to the third and fourth moment, separately. In Tab. 4.1, the moments and the dimensionless shape parameter s (Eq. 2.165) are given for the densities of states which are illustrated in Figs. 2.9, 2.10.

In Fig. 2.11, it is shown that for low d -band fillings the energy of the bcc structure is higher than the energy of the fcc and hcp structure. This can already be reproduced with $n_{\max} = 4$. The reason is that fcc and hcp have a lower negative third moment than bcc (Tab. 4.1). As explained in Sec. 2.4.1, this corresponds to a more skewed DOS of fcc and hcp. Thus, for fcc and hcp more states of low energy are available than for bcc. This is related to the crystal structure by the moments theorem (Eq. 2.167). The fcc and hcp crystal structures are built by sequences of two-dimensional hexagonal close-packed layers, which consist of equilateral triangles as illustrated by the green self-returning hopping paths in Figs. 4.1b - 4.1d. The self-returning hopping paths of length three of the bcc structure (Fig. 4.1a) consist of nearest and next nearest neighbours and lead to a lower third moment.

The bcc structure has a lower energy than fcc and hcp for d -band fillings between approximately three and six. This is related to a more bimodal DOS, i.e. a smaller shape parameter s (Eq. 2.165), due to different self-returning hopping paths of length four, which form planar rings [4, 162]. The value of the fourth moment varies with the bond angle θ and is larger for fcc and hcp, where $\theta = 90^\circ$, and smaller for bcc, where $\theta = 70.5^\circ, 109.5^\circ$. Within the fourth moment approximation fcc and hcp are again lower in energy compared to bcc for large band fillings. This can also be understood from the shape parameter s , indicating that their DOS is more unimodal (less bimodal) than the bcc DOS.

Energy differences between fcc and hcp are mainly given by energy contributions from the sixth moment or higher. The moments of the two structures are identical up to the third moment and the fourth moments differ only by a tiny difference. This difference is given by the hopping paths of length four,

<i>d</i> -valent model					
structure	$\mu^{(3)}$	$\mu^{(4)}$	$\mu^{(5)}$	$\mu^{(6)}$	s
bcc	-0.231	1.678	-0.807	3.796	0.625
fcc	-0.24	1.827	-1.142	4.451	0.769
hcp	-0.24	1.822	-1.142	4.332	0.765
<i>sp</i> -valent model					
structure	$\mu^{(3)}$	$\mu^{(4)}$	$\mu^{(5)}$	$\mu^{(6)}$	s
bcc	-0.938	2.476	-3.883	8.094	0.597
diamond	0.0	1.201	0.0	1.637	0.201
sc	0.0	1.751	0.0	3.698	0.751

Table 4.1.: Moments and dimensionless shape parameter (Eq. 2.165) of the DOS evaluated in Figs. 2.9, 2.10.

which are related to the three-atom fourth moment contributions illustrated in red in Figs. 4.1c, 4.1d. This path starts in fcc e.g. at an atom of the A layer, reaches the C layer and finally the B layer and returns in the opposite direction. The hcp structure has an ABA stacking sequence instead of the ABC stacking sequence in fcc. Therefore, the corresponding path in hcp starts at layer A, continues to layer B and reaches again an A layer before it returns in the opposite direction. The difference in bond angles of these paths lead to a tiny difference in the fourth moment contribution from the *d* orbitals. The fifth moments of fcc and hcp are again identical (Tab. 4.1).

The energy differences of the bcc, diamond and sc structures are mainly given by the third and fourth moment of the *sp*-valent TB model. The diamond and sc structure do not have self-returning hopping paths of length three in the employed model. Therefore, their third moments are equal to zero, whereas the third moment of bcc takes a finite negative value. Thus, bcc is lowest in energy for small values of band filling. The energy of the diamond structure is lowest for intermediate band fillings between approximately three and five. This is in agreement with a much smaller value of the shape parameter s , indicating a much more bimodal DOS of the diamond structure. This can be explained by the bond angles of the three-atom fourth moment contribution in the diamond structure illustrated in red in Fig. 4.1f. In Ref. 130, it is evaluated for the employed model that the bond angle in the diamond structure ($\theta = 109.5^\circ$) is close to the position of the minimum of the fourth moment with respect to θ . The sc structure has a less bimodal DOS, which is also reflected by a larger value for the shape parameter s . It is therefore lowest in energy for high band fillings.

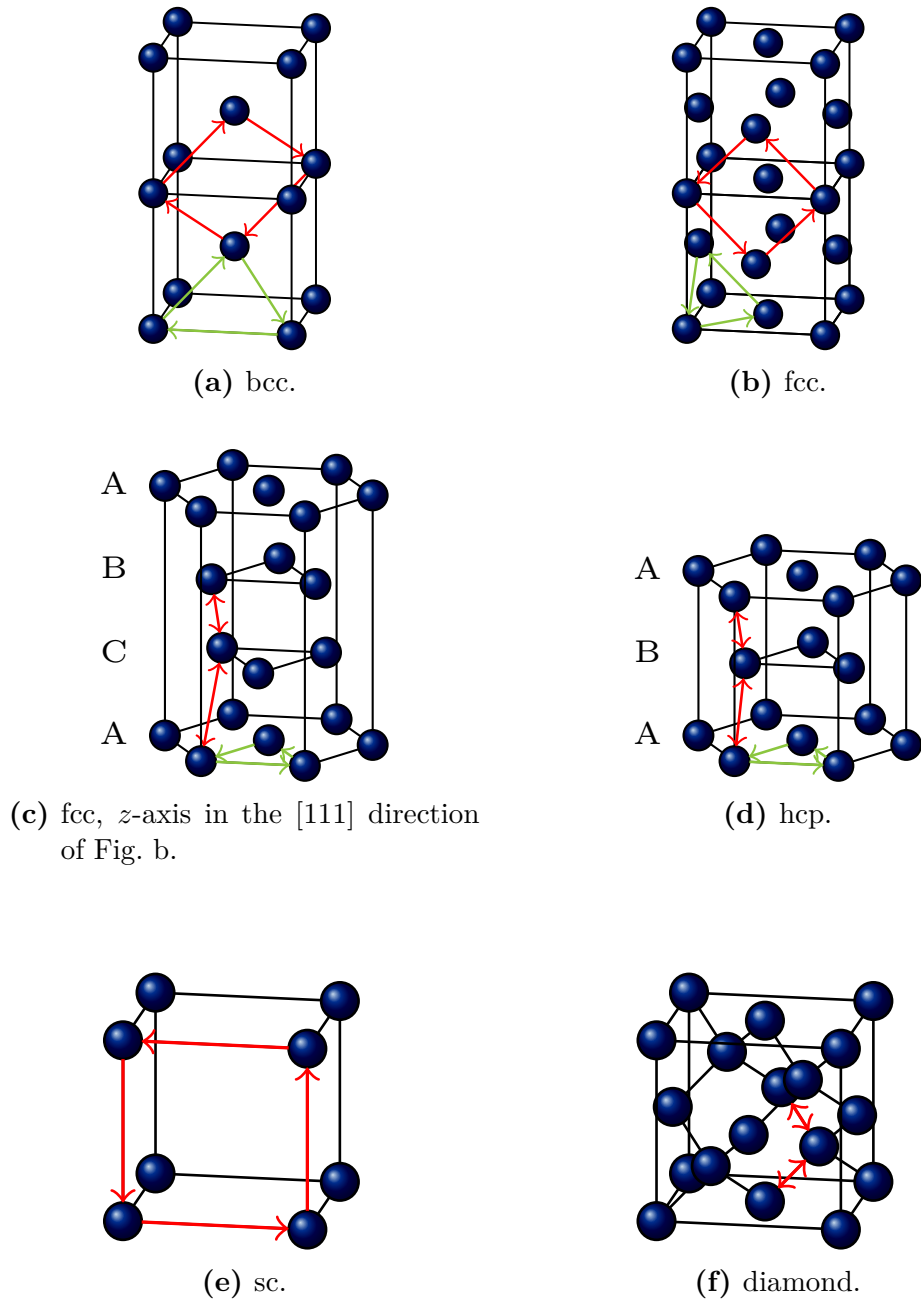


Figure 4.1.: bcc, fcc, hcp, sc and diamond crystal structure. Green and red arrows form selected hopping paths of length three and four, which are discussed in Sec. 4.1.1. In Fig. b, fcc is represented by a cubic unit cell, whereas it is represented by a hexagonal unit cell in Fig. c to allow for a comparison of the stacking sequence of the two-dimensional close-packed planes with hcp.

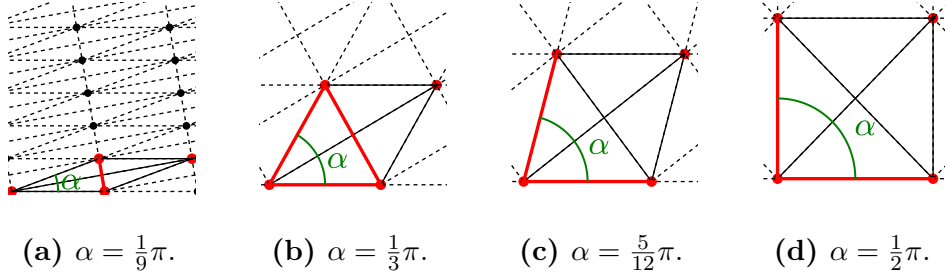


Figure 4.2.: Transformation path connecting the linear chain with the square lattice passing the hexagonal lattice. The shortest bond length is marked in red.

4.1.2. Atomic Environments

In Sec.4.2, the moments of the DOS are used to construct descriptors of atomic environments. These descriptors are used in Sec. 4.3 to construct a map of local atomic environments. In this section, different atomic environments are introduced, which are used in the following to assess the moments descriptors and the map of local atomic environments.

Transformation Paths

Transformation paths are continuous deformations of one crystal structure into another. All transformation paths presented in this work are described by one parameter p changing one structure continuously into the other. Here, transformation paths that are commonly used to test interatomic potentials (tetragonal, orthorhombic, trigonal, hexagonal) [163–166] as well as transformation paths (lin.-hex.-sq., lin.-sq., sq.-sc) that were found to correspond to envelopes of the map of local atomic environments, are selected. The tetragonal transformation path, also called the Bain path [167], connects bcc with fcc. On further continuation it connects fcc with a special body centred tetragonal (bct) structure which is also reached by other transformation paths. This is done by elongating the bcc cell in the [001] direction and compressing it in the [100] and [010] directions to keep the volume fixed.

The primitive cell along the path is given by

$$\begin{aligned} \mathbf{a}_1 &= a(4p)^{-1/3} \begin{pmatrix} -1 & 1 & p \end{pmatrix}^T, \\ \mathbf{a}_2 &= a(4p)^{-1/3} \begin{pmatrix} 1 & -1 & p \end{pmatrix}^T, \\ \mathbf{a}_3 &= a(4p)^{-1/3} \begin{pmatrix} 1 & 1 & -p \end{pmatrix}^T \end{aligned}$$

and the atom is located at

$$\mathbf{P}_1 = (0, 0, 0)$$

for all values of p . bcc is taken for $p = 1$, fcc for $p = \sqrt{2}$ and bct for $p = 2^{3/4}$. The orthorhombic transformation path connects bcc with the same special bct structure which is reached by the Bain path [168]. Further continuation of the orthorhombic transformation path leads back to bcc. This is also achieved by an elongation in the [001] direction, however, simultaneously a compression in the [110] direction is applied. The primitive cell vectors are therefore

$$\begin{aligned}\mathbf{a}_1 &= 4^{-1/3}a \left(-1, 1, p^{1/2}\right)^T, \\ \mathbf{a}_2 &= 4^{-1/3}a \left(1, -1, p^{1/2}\right)^T, \\ \mathbf{a}_3 &= 4^{-1/3}a \left(p^{-1/2}, p^{-1/2}, -p^{1/2}\right)^T\end{aligned}$$

and the atom is located at

$$\mathbf{P}_1 = (0, 0, 0)$$

for all values of p . bcc is taken for $p = 1$, the special bct structure for $p = \sqrt{2}$ and bcc for $p = 2$.

The trigonal transformation path connects bcc over sc with fcc. Further continuation of the trigonal transformation path connects fcc with the two-dimensional hexagonal lattice if a finite cut-off value is chosen and the nearest neighbour distance is scaled. This is obtained by an elongation in the [111] direction and a compression in perpendicular directions. The primitive cell is given by

$$\begin{aligned}\mathbf{a}_1 &= f \left(p - 3, p + 2, p + 2\right)^T, \\ \mathbf{a}_2 &= f \left(p + 2, p - 3, p + 2\right)^T, \\ \mathbf{a}_3 &= f \left(p + 2, p + 2, p - 3\right)^T\end{aligned}$$

with $f = a(25(3p + 1))^{-1/3}$. The atom remains at

$$\mathbf{P}_1 = (0, 0, 0).$$

The bcc structure is taken for $p = 1$, sc for $p = 2$, fcc for $p = 4$ and the two-dimensional hexagonal lattice for $p \rightarrow \infty$.

The bcc to hcp transformation cannot be obtained by a simple deformation of the cell, however, the atoms also have to change their relative positions [165, 169]. The hexagonal transformation path deforms bcc simultaneously in

the $[\bar{1}10]$, $[110]$ and $[001]$ directions. The cell vectors are explicitly given by

$$\begin{aligned}\mathbf{a}_1 &= 2^{-1/3} a f_1 (-1, 1, 0)^T, \\ \mathbf{a}_2 &= 2^{-1/3} a f_2 (0, 0, 1)^T, \\ \mathbf{a}_3 &= 2^{-1/3} a (f_1 f_2)^{-1} (1, 1, 0)^T\end{aligned}$$

with

$$\begin{aligned}f_1 &= 1 + \alpha_1(1 - p), \\ f_2 &= 1 + \alpha_2(1 - p)\end{aligned}$$

and

$$\begin{aligned}\alpha_1 &= (1 - 2^{1/6} \sqrt{1.5}) / (\sqrt{2} - 1), \\ \alpha_2 &= (1 - 2^{1/6}) / (\sqrt{2} - 1).\end{aligned}$$

Together with this deformation alternate (110) planes have to be shuffled in the $\pm[\bar{1}10]$ direction. The choice of Ref. 165 is taken and

$$s = \frac{2^{-1/6}(p-1)}{4\sqrt{6}(\sqrt{2}-1)f_1}$$

is chosen as the shuffling factor. The atomic positions in the direct coordinate system are given by

$$\begin{aligned}\mathbf{P}_1 &= (s, 0, 0), \\ \mathbf{P}_2 &= (1/2 + s, 1/2, 0), \\ \mathbf{P}_3 &= (-s, 1/2, 1/2), \\ \mathbf{P}_4 &= (1/2 - s, 0, 1/2).\end{aligned}$$

bcc is taken for $p = 1$ and hcp for $p = \sqrt{2}$.

With a finite cut-off value and a scaling of the nearest neighbour distance, the linear chain can be connected with the square lattice passing the hexagonal lattice as illustrated in Fig. 4.2. (lin.-hex.-sq.) The cell vectors of the two-dimensional cell are given by

$$\begin{aligned}\mathbf{a}_1 &= a \cos(p)^{-1/2} (1, 0)^T, \\ \mathbf{a}_2 &= a \cos(p)^{-1/2} (\cos(p), \sin(p))^T.\end{aligned}$$

The atom remains at position

$$\mathbf{P}_1 = (0, 0)$$

for all values of p . The square lattice is taken for $p = \pi/2$, the two-dimensional hexagonal lattice for $p = \pi/3$ and the linear chain for $p \rightarrow 0$.

With a finite cut-off value and a scaling of the nearest neighbour distance, the linear chain can also be directly connected with the two-dimensional square lattice by bringing linear chains from infinite separations together until the linear chains are separated by a distance equal to the nearest neighbour distance of the linear chain. (lin.-sq.)

Similarly, the two-dimensional square lattice can be connected with the simple-cubic structure by approaching square lattices from infinite separations until the square lattices are separated by a distance equal to the nearest neighbour distance of the square lattice. (sq.-sc)

Topologically Close-Packed Phases

Topologically close-packed (TCP) phases consist of coordination polyhedra which have only triangular faces [170]. The atoms in the TCP phases have coordination numbers 12, 14, 15 or 16. The number of atoms with inequivalent Wyckoff positions are listed in Tab. 4.2 for a selection of common TCP phases. As in previous works [128, 171], the χ phase is included in the comparison, although it is not a regular TCP phase in the crystallographic sense due to atoms with coordination number 13.

	CN12	CN13	CN14	CN15	CN16	$\langle \text{CN} \rangle$
χ	12	12	-	-	1,4	13.10
C14	2, 6	-	-	-	4	13.33
C15	4	-	-	-	2	13.33
C36	4, 6, 6	-	-	-	4, 4	13.33
μ	1,6	-	2	2	2	13.38
M	4, 4, 4, 8, 8	-	4, 4	4, 4	4, 4	13.38
R	1, 2, 6, 6, 6, 6	-	6, 6	6	2, 6	13.40
δ	4, 4, 4, 4, 4, 4	-	4, 4, 4, 4, 4	4, 4	4	13.43
P	4, 4, 4, 4, 8	-	4, 4, 4, 8	4, 4	4	13.43
Z	3	-	2	2	-	13.43
σ	2, 8	-	8, 8	4	-	13.47
A15	2	-	6	-	-	13.50

Table 4.2.: Selection of common TCP phases and χ phase ordered by increasing average coordination number (CN). A list with the number of inequivalent Wyckoff sites is provided for each CN.

Random Structures

Structures that are generated by randomly choosing a primitive cell and atomic positions in the primitive cell are referred to as random structures in this work. The primitive cell is described by the lattice vectors $\mathbf{a} = a\mathbf{e}_a$, $\mathbf{b} = b\mathbf{e}_b$, $\mathbf{c} = c\mathbf{e}_c$. The angle between \mathbf{b} and \mathbf{c} is named α , the angle between \mathbf{a} and \mathbf{c} is named β and the angle between \mathbf{a} and \mathbf{b} is named γ .

The structure generation is done as follows and was developed in collaboration with Aparna P. A. Subramanyam (AMS, ICAMS, RUB) [172]:

1. Randomly generate three values $a \leq b \leq c$, with $b/a \leq 3$ and $c/a \leq 3$.
2. Randomly generate angles α, β, γ in a range between 0 and π under the condition that the volume is larger than zero [173].
3. Place the first atom at the origin and place further atoms randomly in the primitive cell.
4. Even though the generated primitive cells have a finite volume, they may be effectively two-dimensional due to the finite number of bonds, which are obtained due to the choice of a cut-off distance r_{cut} of the interatomic Hamiltonian matrix elements. Exclude those structures.

As discussed in Sec. 4.3 and visualized with the map of local atomic environments in Fig. 4.4b, it is very unlikely to generate structures that are similar to highly symmetric structures with this method. However, it ensures that the random structures are not biased towards any reference structure.

4.1.3. Descriptors of Atomic Environments

The discussion of the relation of structural stability of the moments of the DOS and their relation to the atomic structure in Sec. 4.1 indicates that the moments of the DOS may be used to construct descriptors of the atomic environment. These descriptors may then be used to measure the similarity of different atomic environments and to identify relevant reference data for the parametrization of interatomic potentials, e.g. TB models (Sec. 2.3), analytic BOP models (Sec. 2.4) or empirical models (Sec. 2.4.14). They may also be used to analyse the transferability of interatomic potentials. A map of local atomic environments is developed in Sec. 4.3 for these purposes.

However, possible applications of descriptors of the atomic environment also include structure identification, e.g. during molecular dynamics simulations or machine learning applications in which physical quantities are predicted from the atomic structure. Steinhardt-parameters [174] and the related averaged local bond order parameters [175] are used for structure identification. Machine learned interatomic potentials utilize the bispectrum [176], smooth overlaps of atomic positions [177] or atom-centred symmetry functions [178–180]. Direct

machine learning of the atomic structure for the prediction of molecular properties is based on the Coulomb matrix [181], Fourier series of atomic radial distribution functions [182] and the bag of bonds method [183]. Materials properties are evaluated from combinations of atomic quantities [184–186], partial radial distribution functions [187] or structural and electronic fingerprints [188]. Descriptors are further constructed to classify structural properties in structure maps [184, 189] and property maps [185, 186, 188]. Some of the above descriptors are based on an expansion of the atomic density [174–177], whereas others are defined ad-hoc [178–183, 187], however, none of the descriptors provide a link between the atomic structure and the electronic structure similar to the moments of the DOS.

4.2. Moments as Descriptors

In a TB or DFT calculation, the electronic DOS is obtained by diagonalizing the Hamiltonian \hat{H} . The Hamiltonian thereby contains the complete information required for characterizing the electronic structure of a material and depends in particular on the positions of the atoms as well as their chemistry. Therefore, the moments of the DOS incorporate information on the atomic structure as well as the chemistry of a material. The moments of the DOS are explicitly linked to the crystal structure and chemistry through the moments theorem (Eq. 2.167). Therefore, the moments do not have to be obtained from the eigenspectrum of the TB problem after a computationally expensive diagonalization, but they can be easily computed with the BOPfox program (Sec. 2.4.15) via hopping paths along the crystal structure.

The moments μ_{llm} are not rotationally invariant. However, rotational invariance is required for a straightforward descriptor. This can be achieved by averaging the moments as

$$\mu_{ll}^{(N)} = \frac{1}{2l+1} \sum_{m=-l}^{+l} \mu_{llm}^{(N)}. \quad (4.1)$$

The resulting atomic moments are by construction also invariant with respect to reflection, translation of the atomic structure and to permutation of atoms of the same species. Therefore, they fulfil the basic requirements for an atomic scale descriptor [177, 178].

As the DOS is strictly positive, the zeroth moment may be normalized to 1, $\mu_{ll}^{(0)} = 1$. The first moment corresponds to the center of gravity of the DOS (Sec. 2.4.1),

$$\mu_{ll}^{(1)} = E_{ll}. \quad (4.2)$$

By an appropriate shift $E \rightarrow E - E_{ll}$ of the energy scale, $\mu_{ll}^{(1)} = 0$ is achieved. The second moment, the root mean square width of the local DOS, is the

lowest moment that depends on the atomic environment,

$$\mu_{ll}^{(2)} = \frac{1}{2l+1} \sum_{m'l'm'} \langle llm | \hat{H} | l'l'm' \rangle \times \langle l'l'm' | \hat{H} | llm \rangle. \quad (4.3)$$

Through the dependence of the second moment on the Hamiltonian matrix, the second moment depends explicitly on the interatomic distances. As the focus is a characterization of local atomic environments without an explicit scaling length or density dependence, the distance dependence needs to be removed from the second moment. This is achieved by scaling interatomic distances such that

$$\mu_{ll}^{(2)} = 1. \quad (4.4)$$

With the above scalings, the third and fourth moments $\mu_{ll}^{(3)}$ and $\mu_{ll}^{(4)}$ (that contribute information on the skewness and bimodality of the local DOS) are the two lowest moments that depend explicitly on the local atomic structure. The moments are rewritten in the form of recursion coefficients (Eq. 2.169) to suppress the implicit dependence between the third and fourth moments, which follows from Eq. 2.166 and is given by

$$\mu_{ll}^{(4)} \geq \left(\mu_{ll}^{(3)}\right)^2 + 1. \quad (4.5)$$

With the normalization $\mu_{ll}^{(0)} = 1$, $\mu_{ll}^{(1)} = 0$ and $\mu_{ll}^{(2)} = 1$, they are given by

$$a^{(1)} = \mu_{ll}^{(3)}, \quad (4.6)$$

$$b^{(2)} = \sqrt{\mu_{ll}^{(4)} - \left(\mu_{ll}^{(3)}\right)^2} - 1. \quad (4.7)$$

The recursion coefficients $a^{(1)}$ and $b^{(2)}$ are the two descriptors that are used to span the map of local atomic environments in Sec. 4.3. With this normalization, the recursion coefficient $a^{(1)}$ measures the skewness of the local DOS and the recursion coefficient $b^{(2)}$ corresponds to a dimensionless shape parameter (Eq. 2.165), which is smaller than one for a bimodal local DOS and larger than one for a unimodal DOS.

The electronic structure is approximately described by the dd bond integrals of the canonical TB model (Eq. 3.15) for d -valent systems and by the ratios of Cressoni's and Pettifor's TB model for sp -valent systems (Eq. 3.18) together with the same radial decay of the dd bond integrals of R^{-5} .

The pure d -model [62, 74–76, 128, 171, 190] is often sufficient to describe the elements of the d -block and captures structural trends across the $4d$ and $5d$ transition-metal series [62, 128, 171, 190]. In agreement with Ref. 66, the sp -model disregards the splitting of the onsite elements.

The bond integrals are smoothly forced to zero at $R = r_{\text{cut}}$ by the cut-off

function (Eq. 2.163). Constant values of r_{cut} and d_{cut} are chosen. With a normalized second moment (Eq. 4.4), they include second nearest neighbours within the cut-off sphere for the bcc structure, where the second nearest neighbour distance is close to the first nearest neighbour distance, and just exclude second nearest neighbours for the simple cubic structure. This is achieved by choosing $r_{\text{cut}} \approx 1.25r_{\text{nn,fcc}}$ and $d_{\text{cut}} \approx 0.13r_{\text{nn,fcc}}$, where $r_{\text{nn,fcc}}$ is the nearest neighbour distance of fcc with a normalized second moment according to Eq. 4.4. The exclusion of second nearest neighbours results in a zero third moment for the simple cubic structure but not for the fcc and hcp structure.

4.3. Map of Local Atomic Environments

In this section, it is shown that the moments-descriptor space can be low-dimensional as the lowest moments, calculated from the closest atomic neighbourhood, carry the largest contributions to the local bond energy. This allows one to construct a map of local atomic environments that is spanned by the two descriptors $a^{(1)}$ and $b^{(2)}$, which is shown in Fig. 4.3. This is different to two-dimensional representations, which are obtained from a higher-dimensional descriptors space by dimension-reduction algorithms applied to datasets of high dimensional features [191, 192]. These low dimensional representations depend on the considered set of atomic environments unlike the map of local atomic environments of this work. In this section, the position of several groups of atomic environments in the map is discussed, which include simple crystal structures, crystal structures with multiple inequivalent lattice sites and random structures. An electronic structure interpretation of the map of local atomic environments follows in Sec. 4.4.

4.3.1. Simple Crystal Structures

Atomic environments in different crystal structures are marked by specific symbols in the map of local atomic environments (Fig. 4.3). The red filled circles correspond to crystal structures with only one atomic environment. Other symbols indicate the different atomic environments in more complex crystal structures. Furthermore, existence regions for structures with one, two or more inequivalent atoms are marked while transformation paths between different structures are shown as lines. The envelopes of the existence regions are estimated from the positions of a large set of random structures (Sec. 4.3.3).

First, the map of local atomic environments provides a clear separation of simple crystal structures with only one atomic environment (filled red circles). No self returning hopping paths of length three are available for the linear chain, the two-dimensional square lattice (square 2-D), the simple cubic (sc) structure, graphene and diamond. They are therefore placed on the

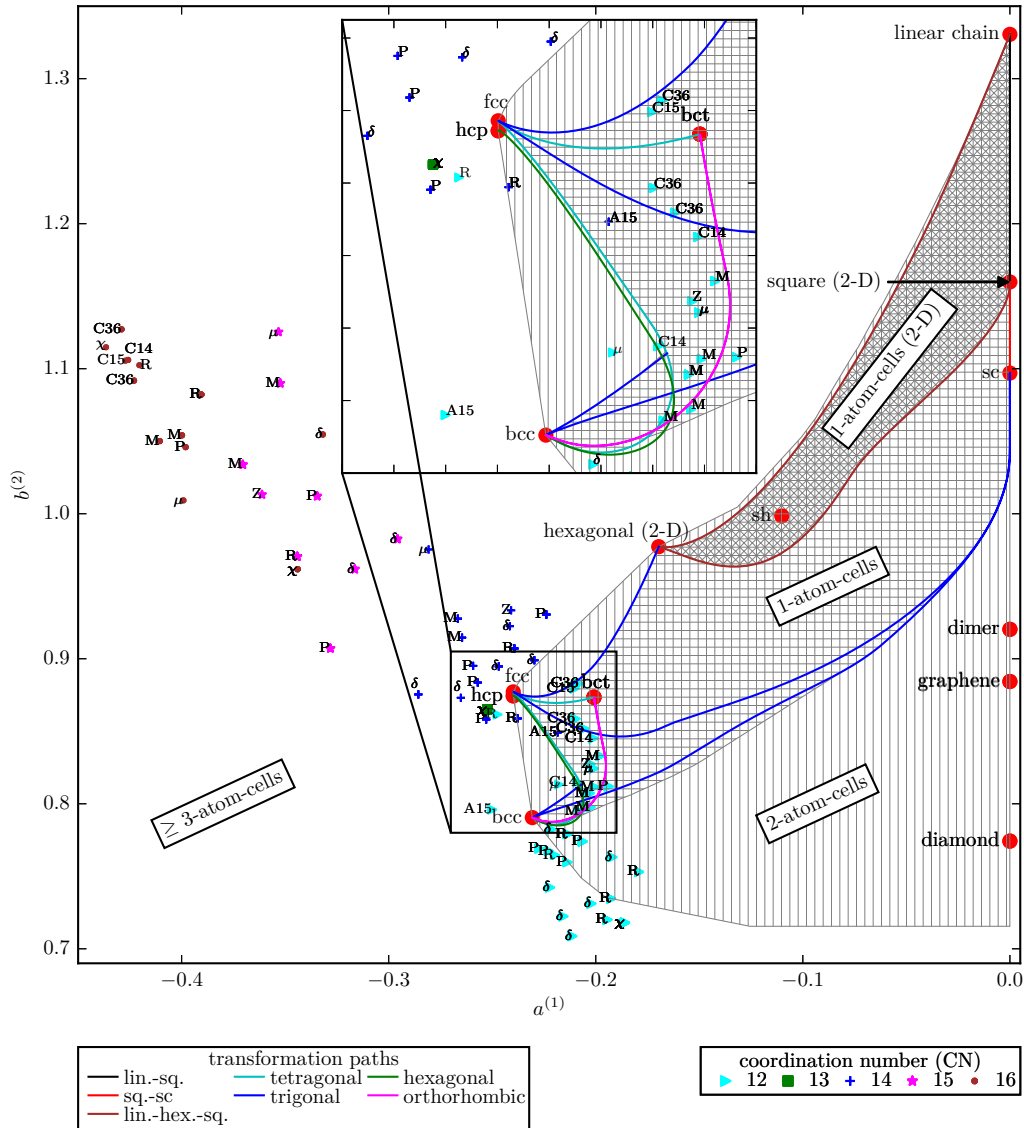


Figure 4.3.: Map of local atomic environments for a d -valent Hamiltonian including different crystal structures, transformation paths and estimated envelopes of the existence regions of crystal structures with one, two or more inequivalent atoms. Red filled circles correspond to simple crystal structures with only one atomic environment. Further symbols indicate the position of differently coordinated atoms of TCP phases. The common names of the phases are given next to the symbols. A square pattern shows the existence region of structures with one atom in the primitive cell. The region of 2-D 1-atom structures is further marked by diagonal lines. The existence region of crystal structures that contain a maximum of two atoms in the primitive cell is indicated by vertical lines. Transformation paths between different crystal structures are shown using coloured lines. The region around the close-packed phases (bcc, fcc, hcp) is magnified.

line $a^{(1)} = 0$ on the right of the map of local atomic environments. The linear chain (linear), the two-dimensional square lattice and the simple cubic structure are ordered according to their dimensionality. They are followed by the dimer, graphene and diamond. The dimer, graphene and diamond have characteristically lower values of $b^{(2)}$, which leads to a stabilization for specific values for the band filling, as discussed in Sec. 4.1 and further analysed in Sec. 4.4.2.

Towards the left of the map of local atomic environments, the close-packed structures face-centred-cubic (fcc), hexagonal-close-packed (hcp) and body-centred-cubic (bcc) can be found. The map of local atomic environments places fcc and hcp almost on top of each other, the values of the descriptors differ only due to their small fourth moment contributions (Sec. 4.1). As expected, the map of local atomic environments places the two structures that are closely related with respect to atomic environment and typically have a very similar cohesive energy very close to each other.*

Among the simple structures, the map places the bcc structure next to fcc and hcp. This is intuitive as the three structures are realized in transition-metal elements. The special body-centred-tetragonal (bct) structure is close to the close-packed structures. Between the close-packed structures and the open structures with $a^{(1)} = 0$ are the simple hexagonal and body-centred tetragonal structure as well as the two-dimensional close-packed hexagonal lattice (2-D hexagonal). The positions in the map may be related to the local DOS of the different crystal structures: the linear chain, the two-dimensional square lattice, the simple cubic structure, the dimer, graphene and diamond all have a symmetric DOS ($\mu^{(3)} = 0$) as can be partially seen in Fig. 2.10. The dimer, which has a perfect bimodal DOS ($b^{(2)} = 0$) for s orbitals, shows a finite value of $b^{(2)}$ for d orbitals, and the DOS of graphene and diamond are even more bimodal. The two-dimensional hexagonal lattice has the most skewed DOS among the two-dimensional structures with one atom in the primitive cell. The bcc structure is more bimodal and less skewed than fcc and hcp.

Some of these simple crystal structures are related by structural transformation paths that can readily be included in the map of local atomic environments (cf. Fig. 4.3). All transformation paths starting from the close-packed structures initially go to the right in the map of local atomic environments. The two transformation paths lin.-sq. and lin.-hex.-sq. form a closed area. This area is in agreement with the estimated envelope of the two-dimensional structures with one atom in the primitive cell. The trigonal transformation path connects bcc with the simple cubic structures. The tetragonal transfor-

*A map of local atomic environments that is able to differentiate between fcc and hcp can easily be set up by using higher recursion coefficients for the axes, such as $a^{(2)}$ and $b^{(3)}$. However, such a map then lacks explicit information about the lowest moment contributions that $a^{(1)}$ and $b^{(2)}$ that are most important for a general structural differentiation such that higher dimensions are required [171], which hampers the visual clarity of a two-dimensional map.

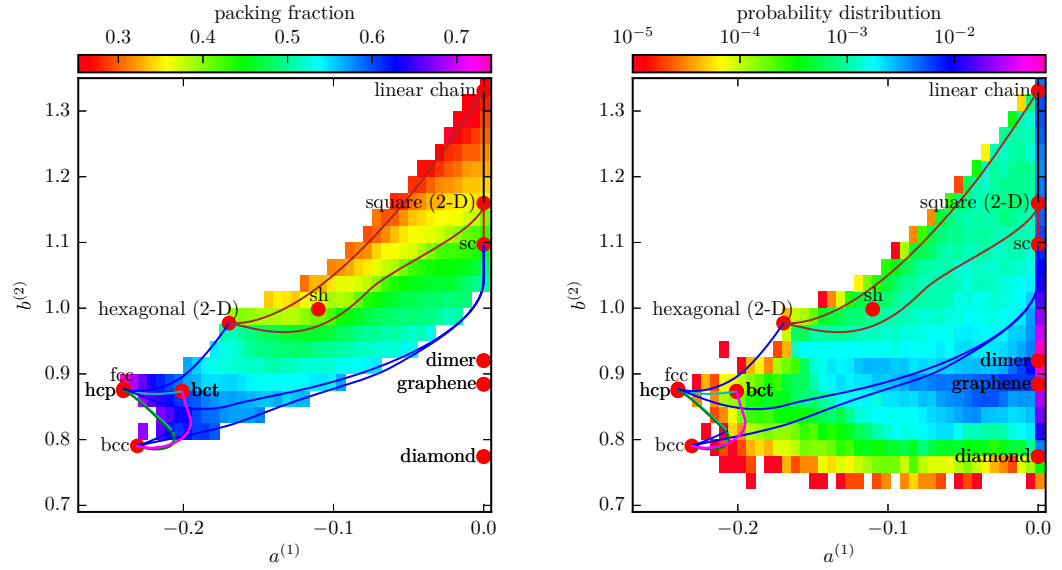
mation path from bcc to fcc is almost on top of the hexagonal transformation from bcc to hcp indicating that the intermediate structures along both paths are similar to each other. After approaching fcc, the tetragonal transformation path abruptly changes its direction towards the special bct structure. This structure is also reached by the orthorhombic transformation. As the transformation is continued, the orthorhombic path returns from bct to bcc along the same path as from bcc to bct. The trigonal path, the tetragonal path and the lin.-hex. path also form parts of the envelope for three-dimensional structures with one atom in the primitive cell.

4.3.2. Crystal Structures with Multiple Inequivalent Lattice Sites

A symbol is displayed in the map for each atomic environment for structures with several inequivalent atomic environments. As an example, the different atomic environments of TCP phases are shown. The moments of the DOS have been applied successfully to measure the similarity of different TCP phases and to identify trends of the local moments with coordination number [128, 171, 190]. The 12-fold coordinated atoms are close to the fcc and hcp structures in the map. The absolute values of $a^{(1)}$ and $b^{(2)}$ increase for atoms with higher coordination. The sublattices of the χ phase also follow this trend, the 13-fold coordinated site is close to the hcp structure.

A clear trend of coordination can be observed in the map of local atomic environments (cf. Fig. 4.3): Atoms with similar coordination polyhedra are close to each other, but they still can be distinguished in the map of local atomic environments. Atoms with high coordination leave the region of simple structures, indicating that these atomic environments only occur in combination with lattice sites of lower coordination.

In addition, randomly generated structures are used to evaluate domains in the map of local atomic environments that may be covered by structures with 1, 2 or 3 atoms in the unit cell. The domain of structures with 1-atom cells is surprisingly small. It covers the region from the linear chain and the simple cubic lattice at $a^{(1)} = 0$ to the close-packed bcc, fcc and hcp phases. A significant area of the domain corresponds to 2-D structures. The 1-atom domain is expanded significantly to lower values of $b^{(2)}$ for two atoms in the unit cell and comprises the dimer, graphene and diamond structures. Crystal structures with three atoms in the cell can in principle reach any point in the map. Figure 4.3 also shows that the continuous transformation paths between simple structures provide envelopes of two-dimensional and three-dimensional structures with one atom in the unit cell.



(a) Average packing fraction of 1-atom random structures.

(b) Probability distribution of 2-atom random structures.

Figure 4.4.: Random structures with one or two atoms in the primitive cell in a d -valent map of local atomic environments. The left figure shows the average packing fraction of the 3-D random structures with one atom in the primitive cell. The right figure shows the probability distribution of the 3-D random structures with two atoms in the primitive cell. Lines correspond to transformation paths introduced in Fig. 4.3.

4.3.3. Random Structures

In order to fill the phase space in the map of local atomic environments in between the simple structures of Sec. 4.3.1, large sets of random structures with one or two atoms in the unit cell are constructed. This construction is based on random choices of lattice vectors and atomic positions as described in detail in Sec. 4.1.2. A set of 50000 1-atom random structures and a set of 90000 2-atom random structures is constructed and used to estimate the envelopes in the map of local atomic environments in Fig. 4.3.

The filled region in Fig. 4.4a contains approximately 50000 random structures with one atom in the unit cell and is characterized in terms of the packing fraction, which is locally averaged in the map. It has a smooth trend across the map of local atomic environments. The boundaries of the set of 1-atom random structures are in agreement with the corresponding envelope in Fig. 4.3. The packing fraction is lowest for those (three-dimensional) structures that are close to the linear chain in the map. The averaged packing fraction increases towards the bottom and the left of the map of local atomic environments and takes its maximum value close to fcc and hcp, which have the highest possible value [193].

In order to assess the procedure for generating random structures, the probability to generate a structure with given values of $a^{(1)}$ and $b^{(2)}$ is estimated. Using the set of 2-atom random structures a smooth variation of the locally averaged probability with $a^{(1)}$ and $b^{(2)}$ is obtained in the d -valent map of local atomic environments as shown in Fig. 4.4b with maximum values for $a^{(1)} = 0$ and minimum values towards the close-packed structures bcc, fcc and hcp.

4.4. Electronic Structure Interpretation of Map of Local Atomic Environments

4.4.1. Relation of Descriptors to Binding Energy

The structural stability across the map of local atomic environments is rationalized by a TB model (Eq. 2.117) that does not take into account charge transfer between atoms or between different orbitals within an atom (i.e. the promotion energy) or magnetism. With these approximations, the binding energy (Eq. 2.118) is written as

$$U_B = U_{\text{bond}} + U_{\text{rep}}. \quad (4.8)$$

With the structural energy difference theorem (Eq. 2.225) and the Wolfsberg-Helmholtz approximation (Eq. 2.226), it is possible to estimate the energy difference between two structures without explicit parametrization of the repulsive contribution. By requiring that all structures have identical second

moments (Eq. 4.4), the map of local atomic environments therefore enables estimating the energy difference between two structures from the bond energy difference ΔU_{bond} .

Due to the restriction to only the four lowest moments of the DOS, the map of local atomic environments is not invertible, which would be required for an exact calculation of observables from the descriptors [182]. Nevertheless, it provides access to an intuitive understanding of the trends of structural stability that is discussed in the following.

To discuss trends in crystal structure stability, the simplest possible fourth moment expansion with $n_{\text{max}} = 4$, $a^{(\infty)} = a^{(0)} = 0$ and $b^{(\infty)} = b^{(1)} = 1$ is taken for making contact with the map of local atomic environments. The expansion of the bond energy (Eq. 2.212) may be applied to discuss trends in crystal structure stability. With the used approximations, the contribution of the response functions to the n -th expansion level is given by $\hat{\chi}_n(\phi_F) + \hat{\chi}_{n+2}(\phi_F)$ and the expansion coefficients reduce to $\sigma^{(1)} = \sigma^{(2)} = 0$, $\sigma^{(3)} = a^{(1)}$ and $\sigma^{(4)} = (a^{(1)})^2 + (b^{(2)})^2 - 1$. When an expansion coefficient $\sigma^{(n)}$ is negative, a large positive value of the response functions will lower the energy and vice versa. At less than half full band the simple metals take the close-packed structures bcc, hcp and fcc. These are stabilized over competing structures by large negative values of $a^{(1)}$ and small values of $b^{(2)}$. The details of the ordering from bcc Na over hcp Mg and fcc Al cannot be resolved within the map of local atomic environments as one cannot expect the simple, nearly-free electron metals to be described well within a simple TB approximation. At half full band the response function $\hat{\chi}_3$ is zero while $\hat{\chi}_4$ is at its maximum (Fig. 2.7) and therefore a small value of $b^{(2)}$ is favourable and helps to stabilize the diamond structure. The subtle competition between graphite and the diamond lattice in carbon is not covered by this arguments the comparison of the two structures at identical second moment is not adequate (Sec. 2.4.16). Still, graphene is close in the d - and sp -map. The dimer, which is stabilized for hydrogen with its half full s orbitals, takes the minimum of $b^{(2)} = 0$ in an s -valent map.

The transition-metals all take close-packed structures due to the attraction provided by the s -electrons, while the d -electrons determine the details of the crystal structure. In a map that only takes into account the d -valence, it may therefore not be expected to find the transition-metal structures at extreme boundaries of the map. Still, the map places them at large absolute values of $a^{(1)}$ and small values of $b^{(2)}$. As expected, the bcc structure, which is stabilized by the response function $\hat{\chi}_4$ at the center of the d -band, has a smaller value of $b^{(2)}$ than fcc or hcp, while hcp and fcc show a slightly more negative values for $a^{(1)}$.

The discussion of the stability of the TCP phases is more involved and it has been discussed in detail in Refs. 128, 189. The TCP phases are stabilized by a combination of average band filling and atomic size mismatch. The two factors have a different relevance in the different TCP phases. As the

atoms in the different coordination polyhedra have different second moments, a direct discussion of the stability of the TCP phases based on the map of local atomic environments alone is not possible. It can be noted that the TCP phases show small values of $b^{(2)}$ for the 12-fold coordinated sites, some of them even smaller than bcc, while the sites with higher coordination show large negative values of $a^{(1)}$.

The difference in energy between two structures can be approximated from Eq. 2.227 as

$$\Delta U_{\text{bond}} = 2(2l + 1) \left[\hat{\chi}_3(\phi_F) \Delta a^{(1)} + \hat{\chi}_4(\phi_F) \left(\Delta (b^{(2)})^2 + \Delta (a^{(1)})^2 \right) \right] \quad (4.9)$$

for $n_{\text{max}} = 4$, where $b^{(\infty)} = b^{(1)} = 1$ and $a^{(\infty)} = a^{(1)} = 0$ are estimated as before. The difference between two structures in the map of local atomic environments is approximated by a contribution $\Delta a^{(1)}$ that corresponds to the distance between the structures projected onto the x -axis and a second contribution that corresponds to the square of the distance between two structures in the map of local atomic environments. The relevance of the two contributions for the energy difference is determined by the number of valence electrons through the first-order response functions (Eq. 2.228). Independent of the number of valence electrons, this implies in general that it may be expected that the energy difference between pairs of structures increases with the distance of the structures in the map.

4.4.2. Trends of Structural Stability from Tight-Binding

The bond energy within the TB approximation is evaluated for the set of random structures in Fig. 4.4b. The canonical d -valent TB model (Eq. 2.229) is chosen with a band filling of 4, which is close to the maximum bcc stability (cf. Fig. 2.11). The locally averaged bond energy is shown in Fig. 4.5a. The bond energy has a smooth trend and is largest at the linear chain and decreases towards bcc, which has the smallest bond energy among all structures. The trend verifies the result of Sec. 4.4.1 that energy differences are to first-order proportional to smooth functions of the differences of the coordinates of the map of local atomic environments. The standard error of the bond energy of different random structures at given location in the map of local atomic environments is displayed in Fig. 4.5b. It is much lower than the range of energy values in the map of local atomic environments. This indicates that the descriptors of the map of local atomic environments are good predictors for structural stability. This direct consequence of the relation between geometric environment and electronic structure given by the moments theorem (Eq. 2.167) rules indeed the moments descriptors distinct from purely geometrical descriptors. The standard error is in correlation with the probability

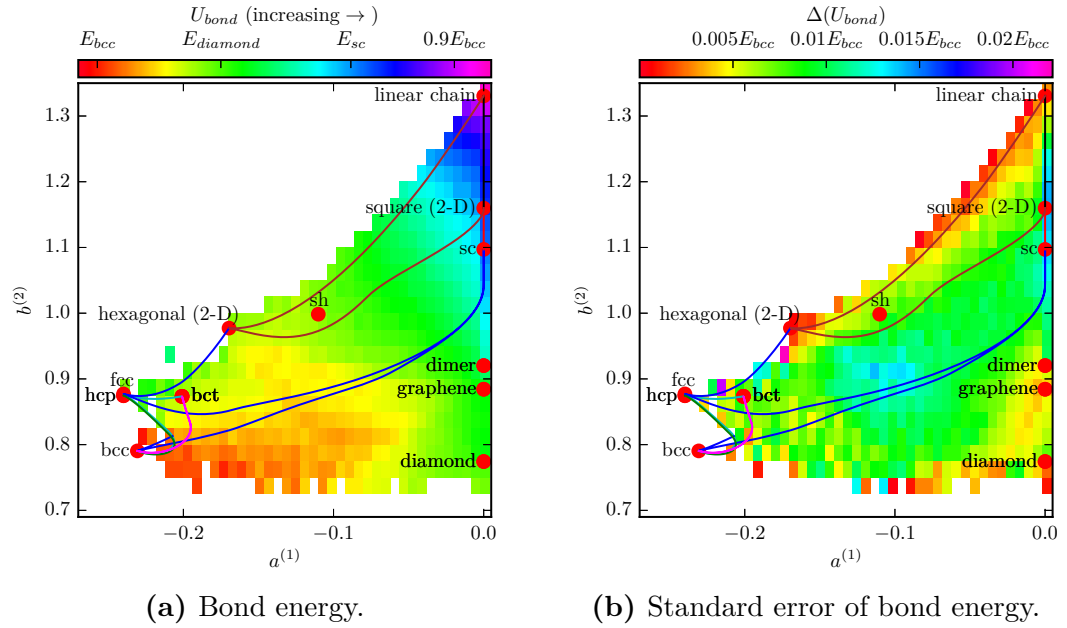


Figure 4.5.: Analysis of bond energy (Eq. 2.119) of two atom random structures from canonical d -valent TB model evaluated for a bandfilling of $N_e = 4$. The left figure shows the averaged bond energy and the right figure the related standard error that is calculated from different random structures at the same position of the map. Lines correspond to transformation paths introduced in Fig. 4.3.

function of the randomly generated structures (cf. Fig. 4.4b). This means that those regions where more structures are mapped to have a broader range of possible energy values.

The average bond energy for sp -valent TB model (Eq. 2.230) with different band fillings is shown in Fig. 4.6. The values of the atomic recursion coefficients differ from those obtained for the d -valent TB model, however, many features of the d -valent map of local atomic environment are still present in the sp -valent map. As the dimer configuration may be a stable configuration for sp -elements [130], it is an important feature of the sp -valent map that it positions the dimer apart from the other crystal structures. A smooth energy surfaces is obtained for all band fillings. As expected, at half full band the diamond structure has the lowest bond energy and for low band fillings the stability is shifted towards the close-packed phases (cf. Fig. 2.12).

4.4.3. Trends of Structural Stability from Density-Functional Theory

The bandfilling of $N_e = 4$ in the TB calculations of Sec. 4.4.2 corresponds to the transition-metals Mo ($4d$) and W ($5d$). This can be seen, e.g., in DFT-TB-BOP comparisons of structural trends in $4d$ and $5d$ d -valent transition-metals [128] and was employed in BOP parametrizations for Mo and W [163]. An evaluation of the approximately 90000 structures that are evaluated for TB is computationally too demanding.

It is expected that the atomic volume V_{norm} of each atom with normalized second moment to $\mu^{(2)} = 1$ correlates with the atomic equilibrium volume V_0 as the normalized volume may be interpreted as a measure for the homogeneity of its atomic surrounding. A small normalized volume indicates a homogeneous atomic surrounding with equidistant bond lengths. Therefore, also a positive correlation of the normalized volume V_{norm} and the equilibrium energy E_0 is expected. In Ref. 194, a random set of structures which samples the map of local atomic environments uniformly was taken and DFT calculations of these structures were performed with VASP (Sec. 2.2.7). The projector augmented-wave method (PAW) method (Sec. 2.2.5) was used with fourteen valence electrons (Mo_sv) for Mo and the generalized gradient approximations (GGA) (Sec. 2.2.3) to the PBE exchange correlation potential was employed. High accuracy of the calculations was obtained by a plane-wave cut-off energy of 500 eV and Monkhorst-Pack (Sec. 2.2.4) \mathbf{k} -point meshes with linear density not more than 0.1 \AA^{-1} . The equilibrium energy E_0 , volume V_0 and bulk modulus B_0 were obtained by fitting energy-volume curves with volume scalings of $\pm 10\%$ to the Birch-Murnaghan equation of stateMurnaghan244, PhysRev.71.809. The correlation of the normalized volume V_{norm} and the DFT equilibrium volume V_0 and energy E_0 is illustrated in Fig. 4.7. The smallest normalized volume V_{norm} corresponds to the smallest value V_0 and E_0 .

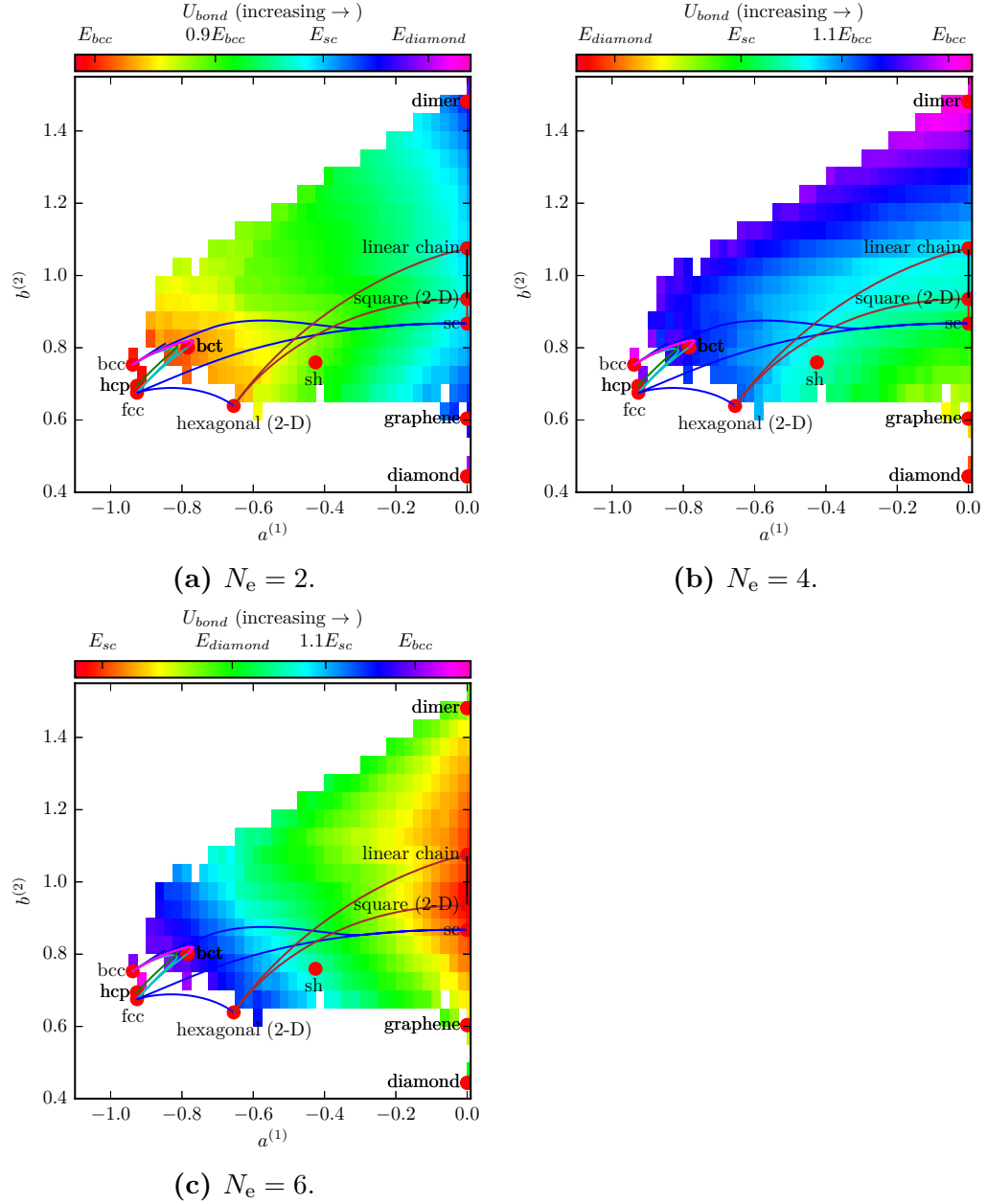


Figure 4.6.: Bond energy (Eq. 2.119) in the sp -valent map of local atomic environments as obtained from the canonical sp -valent TB model for different band fillings. Lines correspond to transformation paths introduced in Fig. 4.3.

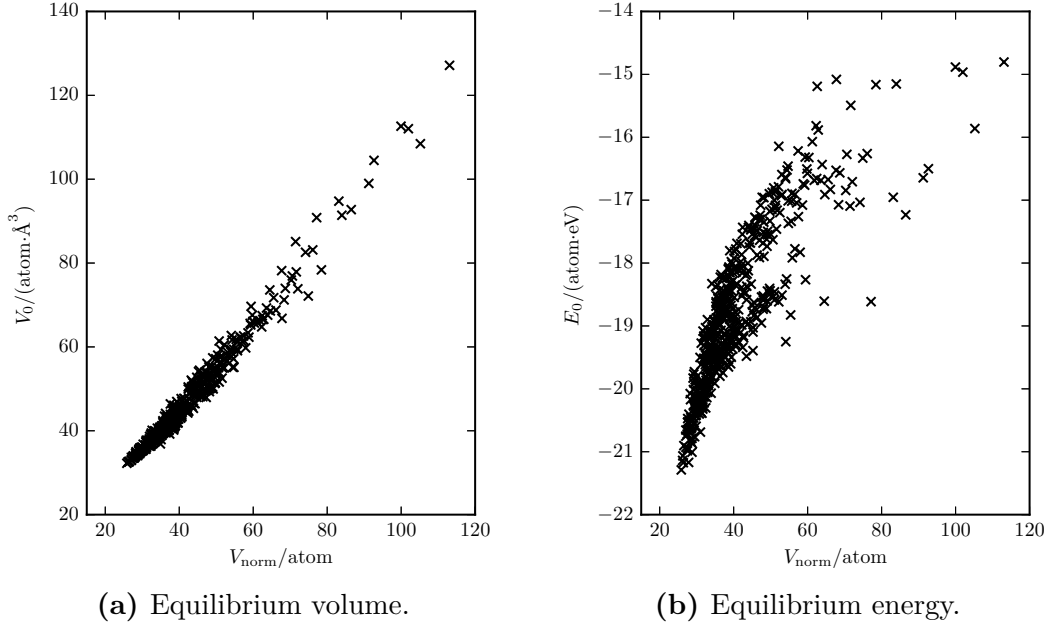


Figure 4.7.: Correlation of the atomic volume V_{norm} after normalizing the second moment to the atomic equilibrium volume V_0 (Fig. a) and the atomic equilibrium energy E_0 (Fig. b) calculated with DFT. Structures are randomly chosen and cover the region of 2-atom cells in the map of local atomic environment uniformly (cf. Fig. 4.3).

To approximate to the lowest-energy and smallest-volume surface in the map of local atomic environments, 521 two atom random structures with smallest normalized volumes that homogeneously cover the map are selected.

The results for the equilibrium energy per atom, the equilibrium volume per atom and the bulk modulus were calculated with the same DFT settings as above in Ref. 194 and are shown in Figs. 4.8.

The overall trend of the DFT equilibrium energy for Mo (Fig. 4.8a) is qualitatively captured by the bond energy of the corresponding TB calculations at $N_e = 4$ (Fig. 4.5a). The energy is lowest for bcc and increases with distance in the map of local atomic environment. The bcc structure also takes the smallest equilibrium volume. The bulk modulus is smooth across the map of local atomic environment and largest for bcc. The uncertainty of the results near the envelopes of the map is caused by a smaller number of random structures (cf. Fig. 4.4b).

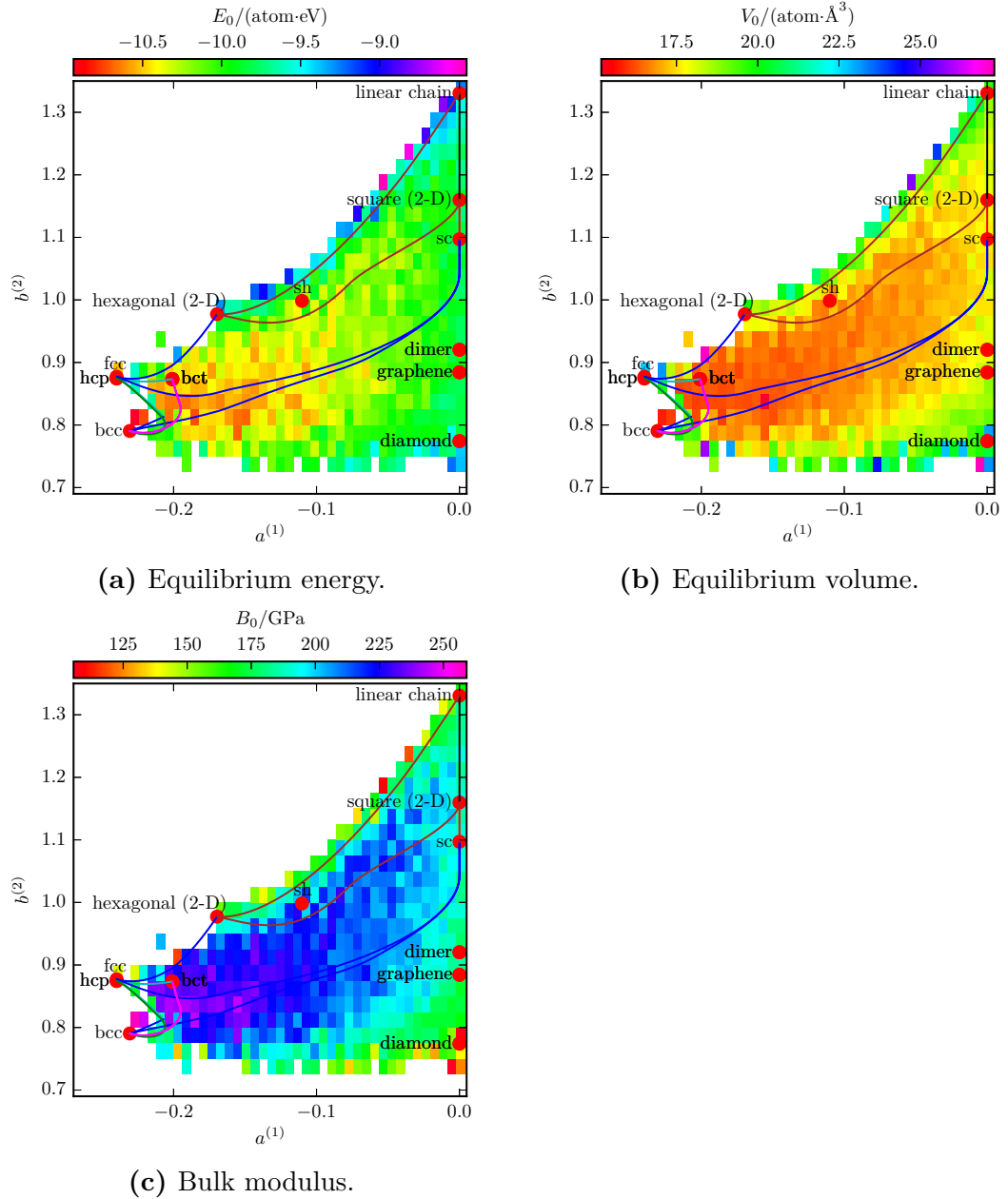


Figure 4.8.: DFT calculations of equilibrium energy (Fig. a), volume (Fig. b) and bulk modulus (Fig. c) for a set of random structures with two atomic sites, both occupied by Mo atoms. Lines correspond to transformation paths introduced in Fig. 4.3. The set was chosen to cover the area of 2-atom random structures homogeneously and to exhibit the smallest normalized volume among all randomly generated structures within one grid box of the map of local atomic environments. The trend of equilibrium energy for Mo obtained by DFT (left) is captured by the bond energy of the corresponding TB calculations at $N_e = 4$ (Fig. 4.5a).

5

Automated Parametrization Strategy

Density-functional theory (DFT) calculations can be applied to systems with elements across the periodic table. However, the computational effort of DFT calculations, which increases cubically with the system size, limits the applicability of the method to typically a few hundred atoms. Interatomic potentials like analytic bond-order potentials (BOPs), which have a linear scaling of the computational time with the system size, can be applied to much larger systems. However, they require a pairwise parametrization of the interaction of atoms of different species. An automated parametrization strategy is needed to enable accurate calculations with interatomic potentials of arbitrary systems. In this work, this is divided into three challenges: Firstly, a framework has to be implemented which automatically performs simulations for different model parameter sets, measures the accuracy with respect to reference data and interacts with an optimization algorithm which tunes the accuracy by changing the model parameters. Secondly, a general and robust protocol has to be defined, which determines the optimization steps towards an optimal set of model parameters. Thirdly, an understanding of the transferability of the model has to be obtained.

Existing optimization frameworks and strategies are discussed in Sec. 5.1. A new parametrization protocol for analytic BOPs, which is initialized by the tight-binding (TB) parametrization across the periodic table (Sec. 3), is introduced in Sec. 5.2. It optimizes the model parameters to DFT reference data. The map of local atomic environments (Sec. 4) is applied in Sec. 5.3 to systematically analyse and improve the transferability. In Sec. 5.4, the parametrization protocol is used to parametrize an analytic BOP for the element

Re in collaboration with Aparna P. A. Subramanyam (AMS, ICAMS, RUB), who defined the requirements on the potential for a successful application and who provided all DFT reference data, if not stated otherwise. The reference data and the applications of the potential are covered in more detail in Ref. 172. For a given model complexity, a Pareto front for the analytic BOP model for Re is mapped out by a systematic variation of a weight parameter. The optimal Re model for the given model complexity is selected from the Pareto front by a sequence of tests. Further applications of the developed parametrization strategy are given in the outlook.

5.1. Background

5.1.1. Model Parameter Optimization

In order to optimize an interatomic potential to reference data, a cost function needs to be defined which measures the discrepancy between the predictions of the potential and the reference data. A natural choice is the root-mean-square (RMS) cost function given by

$$c(\boldsymbol{\theta}) = \sqrt{\frac{\sum_n^{N_{\text{ref}}} w_n^2 e_n^2}{N_{\text{ref}}}}, \quad (5.1)$$

where

$$e_n = (E_{\text{pred},n}(s_n; \boldsymbol{\theta}) - E_{\text{ref},n}(s_n)). \quad (5.2)$$

Here, N_{ref} is the number of reference data points, $\boldsymbol{\theta}$ is a vector of model parameters, $E_{\text{pred},n}(s_n; \boldsymbol{\theta})$ is the model prediction for structure s_n for given model parameters, $E_{\text{ref},n}$ is the corresponding reference and w_n is a factor which may scale the summands to a common unit or may further weight them. Multiple predictions and reference data points may exist for a given structure s_n , e.g. energies and atomic forces. The approach to include atomic forces in the set of reference data is referred to as force-matching method [195].

Optimization methods are used to minimize the cost function $c(\boldsymbol{\theta})$ by automatically varying $\boldsymbol{\theta}$ and approaching the vector of parameters

$$\boldsymbol{\theta}^{\text{opt}} = \operatorname{argmin}_{\{\boldsymbol{\theta}\}} (c(\boldsymbol{\theta})), \quad (5.3)$$

which minimizes the cost function. While global minimization procedures are designed to find the global minimum, local minimization procedures converge to a local minimum, which is not necessarily the global minimum. A local minimization procedure, which is used in the automated parametrization protocol (Sec. 5.2), is the Levenberg-Marquardt algorithm [196, 197] in its specific form described in Ref. 198. In order to find a local minimum of Eq. 5.1, it has to be initialized by a vector of parameters $\boldsymbol{\theta}_0$. The parameters

are updated in iteration step $i + 1$ by

$$\boldsymbol{\theta}_{i+1} = \boldsymbol{\theta}_i - \left(\mathbf{J}_i^T \mathbf{J}_i + \lambda_i \mathbf{D}_i^T \mathbf{D}_i \right) \mathbf{J}_i^T \mathbf{e}_i, \quad (5.4)$$

where \mathbf{J}_i is the Jacobian of the cost function (Eq. 5.1) and λ_i and the diagonal matrix \mathbf{D}_i are adaptively computed to adjust and scale the steps. This adaptive choice makes the Levenberg-Marquardt algorithm fast and robust and is therefore preferred to the Gauss-Newton algorithm and gradient descent algorithm.

Parametrization interfaces like Potfit [199], GARFfield [200], MEAMfit [201], aenet [202], the MEAM parameter calibration tool [203], Atomicrex [204] and also an automated parametrization interface for DFTB using particle swarm optimization [205] have been developed. These interfaces read in reference data, automatically perform simulations for a given vector of model parameters $\boldsymbol{\theta}$ and optimize it according to an optimization method. In order to use such methods with analytic BOPs, the BOPcat (BOP construction, assessment and testing) program has been developed [206]. It interacts with BOPfox and allows for an optimization of the cost function for TB models and analytic BOPs. It gives complete freedom to the user to define a parametrization protocol. The parametrization of analytic BOPs is not solved with the development of parametrization interfaces, but a strategy to ensure physical model parameters, accurate reproduction of reference data and reasonable transferability needs to be developed. BOPcat allows the user to define optimization steps for all possible combinations of parameters and allows one to link individual optimization steps and is therefore perfectly suited to implement a parametrization protocol.

5.1.2. Parametrization Strategies

While most of the mentioned parametrization interfaces allow for an optimization to a set of given reference data, only a few of them provide a guideline for a protocol to parametrize interatomic potentials.

Artificial Neural Network Potentials

In case of the aenet code [202], which can parametrize artificial neural network potentials [207], an initial set of reference structures is used and the model parameters are fitted to the corresponding reference data. Afterwards, new structures are generated by molecular dynamics simulations. Reference values are calculated for testing the potential for the newly generated structures. If the potential predictions agree with the reference, the parametrization procedure ends. Otherwise the set of reference data is increased and the model parameters are optimized again. This procedure is required as artificial neural network potentials are not derived from physical considerations and have

a very large number of parameters. Therefore, many reference structures are needed such that the potential is optimized to interpolate between the reference values.

MEAM Potentials

The MEAM parameter calibration tool [203] for the parametrization of modified embedded atom method (MEAM) potentials provides recommended sequences of optimization steps in which additional data is added to the reference data and specific parameters are optimized in each step [208].

NRL-TB Potentials

In Refs. 151, 209, a similar parametrization strategy to that of the MEAM potentials is used to parametrize NRL-TB models (Sec. 3.1.5). Based on the assumption that it is likely to converge to a non-physical local minimum in a high dimensional parameter space, a subset of the data is initially taken and the model parameters are optimized. The reference data set is increased in a stepwise procedure and the Levenberg-Marquardt algorithm (Eq. 5.4) is used to reoptimize the parameters to a local minimum. This procedure ensures that a local minimum with physically meaningful parameters is obtained.

TB Bond Model Based Potentials

Stepwise and local optimization procedures have been employed for the parametrization of interatomic potentials which are based on an orthogonal TB bond model (Eq. 2.117). All parametrization strategies are customized. However, two approaches may be identified, which differ in their sets of reference data and parametrizations of the binding energy (Eq. 2.118).

In Refs. 163, 166, 210, the elastic properties, the equilibrium energy and volume of the ground state are fitted for a selection of *sd*-valent systems. In the parametrization process, the TB Hamiltonian matrix elements are not modified. Since the parametrization of a simple pair potential (Eq. 2.162) is not sufficient to reproduce the desired elastic properties an environment-dependent repulsion U_{env} is added. In Refs. 163, 210, the bond integrals are obtained from linear muffin-tin orbitals (Sec. 3.1.3) and the environmental term is parametrized in the form of Ref. 211,

$$U_{\text{env}} = \frac{1}{2} \sum_{I,J \neq I} \frac{B}{R_{IJ}} \exp\left(-(\lambda_I + \lambda_J) \frac{R_{IJ} - 2R_{\text{core}}}{2}\right), \quad (5.5)$$

where

$$\lambda_I = \lambda_0 + \left(\sum_{K \neq J} C \exp(-\nu R_{IK}) \right)^{1/m}. \quad (5.6)$$

In Ref. 166, the bond integrals are obtained by a downfolding procedure (Sec. 2.3.8) and a modified version of the environment-dependent repulsion of Ref. 212 is used, which is given by

$$U_{\text{env}} = \frac{1}{2} \sum_{I,J \neq I} B \exp(-\mu R_{IJ}) \exp(-(\lambda_I + \lambda_J)(R_{IJ} - 2R_{\text{core}})), \quad (5.7)$$

where λ_I is defined by Eq. 5.6 with $\lambda_0 = 0$ and $m = 1$. In this approach, the s -electrons are neglected and their contribution to the bond energy is attributed to a decrease of the pair repulsion.

Complementary to this approach, the parametrizations of sd -valent systems in Refs. 74, 76, 121 explicitly describe the energy contribution from the s -electrons by an embedding term in form of Eq. 2.224. The bond integrals are obtained by a downfolding procedure and are not modified. The parameters of the pair repulsion and the embedding contribution are optimized to reproduce DFT energy-volume curves of different phases. However, the elastic properties are either not at all (Refs. 74, 121) or only qualitatively (Ref. 76) considered in the parametrization process.

While the first approach leads to models which reproduce elastic properties well, the second approach leads to a better transferability across different phases. A compromise of the two regimes is made in Ref. 78, where an orthogonal sp -valent TB model for Si is parametrized. The repulsive energy is parametrized by a pair potential only and a modification of the embedding term (Eq. 2.224) is used to describe energy contributions from higher neighbour shells as both, the s - and p -electrons, are explicitly considered for short interatomic distances only. DFT energies of elastic deformations of the ground state phase and energy-volume curves of different phases are considered in the parametrization process by also optimizing the interatomic Hamiltonian matrix elements.

5.2. Parametrization of Analytic Bond-Order Potentials for Transition-Metals

5.2.1. Computational Details

All DFT calculations which are used in this section are performed non-spin-polarized with VASP (Sec. 2.2.7). The projector augmented-wave method (PAW) method is used (Sec. 2.2.5) with thirteen electrons (Re_pv) for rhenium and the generalized gradient approximations (GGA) (Sec. 2.2.3) to the PBE exchange correlation potential is employed. High accuracy of the calculations is obtained by a plane-wave cut-off energy of 400 eV and Monkhorst-Pack (Sec. 2.2.4) \mathbf{k} -point meshes with linear density not more than 0.125 \AA^{-1} .

If not mentioned otherwise, all analytic BOP calculations are performed with

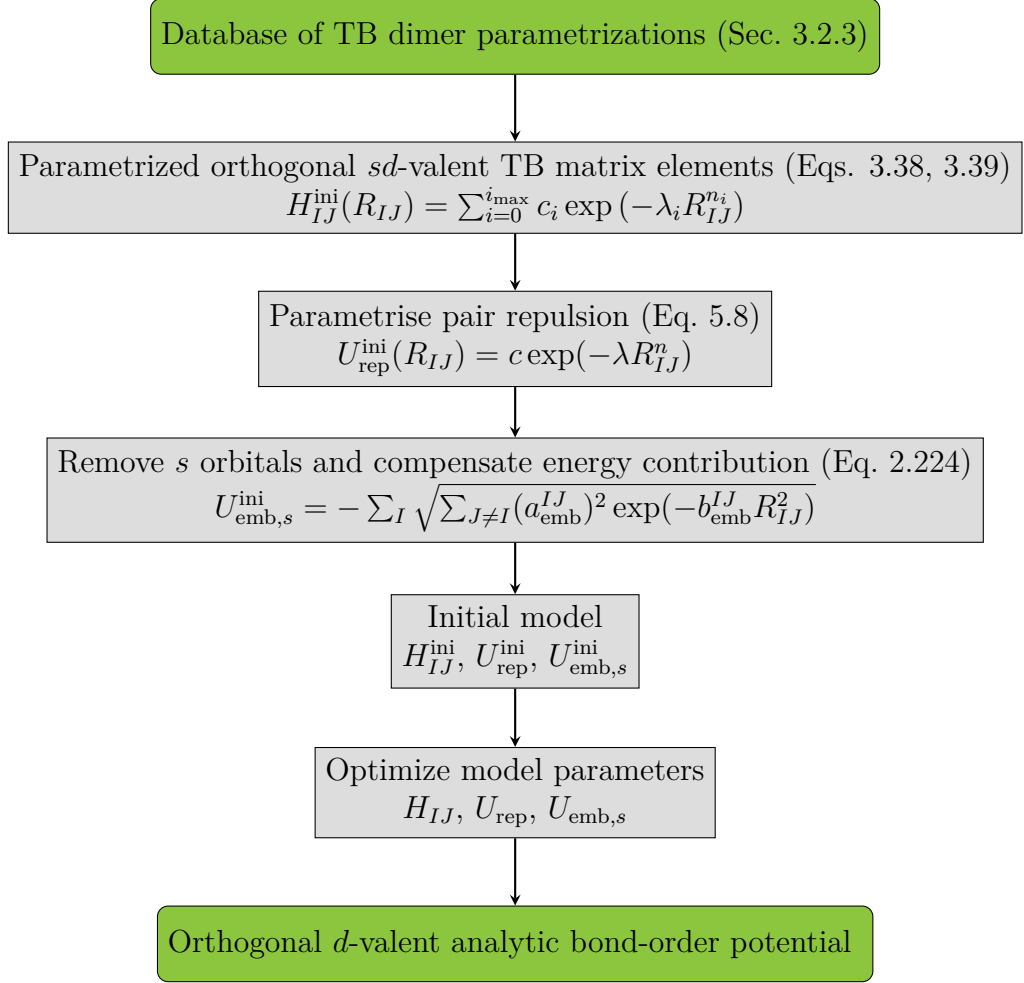


Figure 5.1.: Parametrization protocol of analytic BOPs for sd -valent systems.

$n_{\max} = 9$ exactly calculated moments, which has been found to be a good compromise between efficiency and accuracy [163, 166, 210]. Higher moments are estimated up to $n_{\text{exp}} = 100$ with a constant terminator (Eq. 2.181) and damping factors g_n ensure a strictly positive density of states (DOS) (Sec. 2.4.9). A value of $J_{II} = 10$ eV is used to describe the resistance against charge transfer (Eq. 2.132), which was found to allow for a qualitative correct treatment of the investigated stacking faults of Sec. 5.4.

5.2.2. Parametrization Protocol

The comprehensive set of TB parametrizations for dimers across the periodic table obtained in Sec. 3 is used in this section to construct a robust parametrization protocol for analytic BOPs for d -valent transition-metal systems.

The choice of reference data and the optimization of the transferability of the potentials is discussed in Sec. 5.3.

Local optimization procedures are used in the parameter optimization of interatomic potentials to facilitate the convergence to a physically meaningful minimum of the cost function (Eq. 5.1). This requires, however, an initialization of the model parameters in the vicinity of the desired minimum. For this purpose, the comprehensive set of TB parameters across the periodic table of Sec. 3 is particularly attractive as it provides TB parameters of the Hamiltonian matrix for 1711 different combinations of elements obtained by a consistent methodology. This is supported by the results of Refs. 74, 76, 121, 132, which indicate that interatomic Hamiltonian matrix elements have a good transferability to other phases. Therefore, the set of TB parameters across the periodic table should be a good initialization for a further local optimization. It was found in previous parametrization strategies that the s -electrons of central d -band transition-metals do not have to be explicitly described in the TB formalism, which is in agreement with the investigations in Refs. 62, 128, 171, 190.

Since the corresponding interatomic matrix elements are particularly long ranged (Sec. 3.3.3), and therefore require the evaluation of many hopping paths (Eq. 2.167) in the analytic BOP formalism, it is from a computational point of view attractive to replace their energy contribution by a simple embedding term (Eq. 2.224). With an explicit treatment of the s -electrons, it is expected that the pair repulsion can be described by a simple functional form. For this purpose, the first term of the flexible functional form used to parametrize the TB Hamiltonian matrix elements (Eqs. 3.38, 3.39) is taken and the pair repulsion is parametrized by

$$U_{\text{rep}}(R_{IJ}) = c \exp(-\lambda R_{IJ}^n). \quad (5.8)$$

While an initial parametrization of the Löwdin orthogonalized Hamiltonian matrix $H_{IJ}^{\text{ini}}(R_{IJ})$ is obtained from the set of TB dimer parametrizations (Sec. 3.2.3), initial parameters for the pair repulsion and the embedding term still have to be found. This is done in two initial optimization steps. All model parameters are optimized in a final optimization step.

- Firstly, the orthogonal sd -valent TB Hamiltonian matrix elements are used and an initial parametrization of the repulsive energy $U_{\text{rep}}^{\text{ini}}$ is obtained by an optimization of the cost function (Eq. 5.1) with respect to the three parameters of the pair repulsion (Eq. 5.8) for a (sub)set of binding energy reference data.
- Secondly, the s orbitals are removed from the model, the number of valence electrons is adjusted and the missing energy contribution is compensated as far as possible by another optimization step. An initial parametrization of the embedding term $U_{\text{emb}}^{\text{ini}}$ is obtained by an opti-

mization of the cost function with respect to the two parameters of the embedding term. The same (sub)set of binding energy reference data is used.

- Finally, all parameters of H_{IJ}^{ini} , $U_{\text{rep}}^{\text{ini}}$, $U_{\text{emb}}^{\text{ini}}$ are optimized to the complete fit set and an orthogonal d -valent analytic BOP is obtained.

The optimization steps are illustrated in Fig. 5.1 and performed with the BOPcat program [206] and the Levenberg-Marquardt algorithm (Eq. 5.4). The parametrization procedure is illustrated in Fig. 5.2 and explained in the following for a small set of DFT binding energy reference data for Re. The reference data consists of energy-volume curves for hcp with an optimised c/a -ratio as well as for fcc and bcc. The equilibrium volume is estimated with a fifth-order polynomial fit to the equation of state and volume scalings of $\pm 20\%$ are used. In Fig. 5.2a, the DFT energy reference data is illustrated by squares and the energy contribution from the initial Löwdin orthogonalized Hamiltonian matrix elements $H_{IJ}^{\text{ini},sd}$, which is given by the bond energy, is illustrated by solid lines. The interatomic matrix elements are described by the distance-dependent parametrization obtained in Sec. 3.2.3 and the onsite matrix elements are taken from the values of the free atom, which are taken from the dimer parametrizations for large interatomic distances (cf. Fig. 3.4). The range of the bond integrals is limited by a cut-off function (Eq. 2.163) with values of $r_{\text{cut}} = 6 \text{ \AA}$ and $d_{\text{cut}} = 0.5 \text{ \AA}$. The number of s -electrons is estimated by numerical integration of the projected DOS from DFT to 0.77 and the number of d -electrons to 5.3. The number of d -electrons is empirically adjusted to 5.7 to obtain better accuracy. Therefore, the total number of valence electrons is equal to $N_e = 6.47$.

In Fig. 5.2b, the electronic description is not modified, however, the pair repulsion (Eq. 5.8) is added to the model. It can be seen that the three different phases are already correctly ordered and that the variation of the energies with the volume are in a correct range. The energy differences are, however, not correctly described. By the exclusion of the s -electrons, the reduction of the cut-off sphere of the bond integrals to $r_{\text{cut}} = 4.45 \text{ \AA}$ and $d_{\text{cut}} = 1.35 \text{ \AA}$, the adjustment of the number of valence electrons to $N_e = 5.7$ and the introduction of the embedding term $U_{\text{emb}}^{\text{ini}}$, the quality of the model does not change as shown in Fig. 5.2c. However, a good agreement of the model with the DFT reference data is obtained by the optimization of all parameters of U_{rep} and U_{emb} and c_0 and c_1 of the parametrization of the bond integrals (Eq. 3.38) $dd\sigma$, $dd\pi$ and $dd\delta$ as shown in Fig. 5.2d. The change of the bond integrals and the repulsive energy during the last optimization step with respect to their initial values is illustrated in Fig. 5.3. The bond integrals change their values only slightly and for $dd\sigma$ the change is not even visible. The decrease of the range of the bond integrals corresponds to the screening effect which is discussed in Sec. 3.3.3. The initial pairwise repulsion is also close to the optimized parametrization. The tiny modifications of the parametrization leads

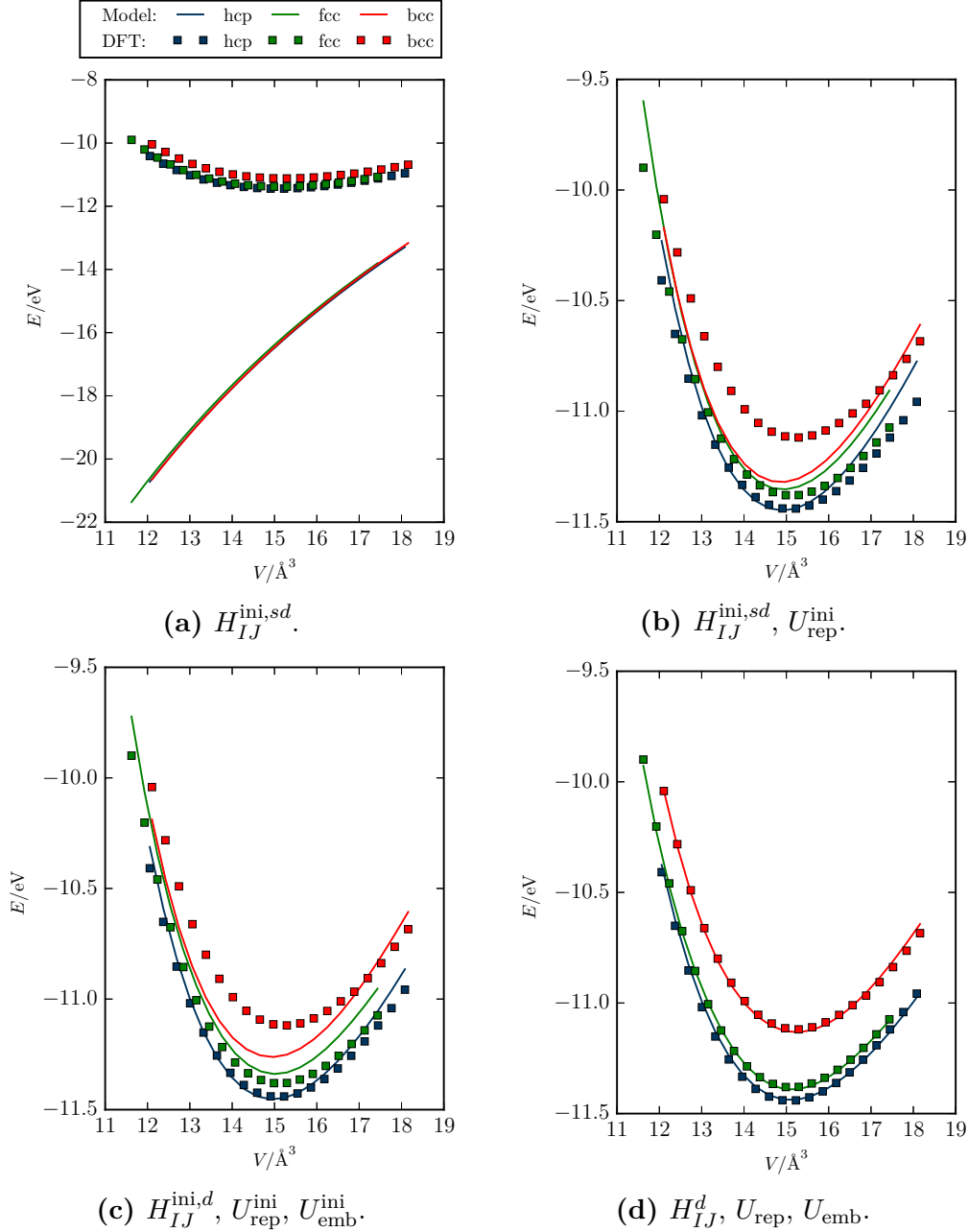


Figure 5.2.: Parametrization procedure of the orthogonal d -valent analytic BOP for Re with DFT energy-volume curves as reference data. The model predictions for the binding energy are compared to the DFT reference in each parametrization step. In Fig. 5.2a, the model is given only by $H_{IJ}^{ini, sd}$, the orthogonal TB parametrization of the Hamiltonian matrix obtained for dimers in Sec. 3.2.3. A pairwise repulsion U_{rep}^{ini} is added in Fig. 5.2b and in Fig. 5.2c the energy contribution of the s -electrons is replaced by an embedding term U_{emb}^{ini} . Fig. 5.2d shows the model with optimized parameters which define H_{IJ}^d , U_{rep} and U_{emb} .

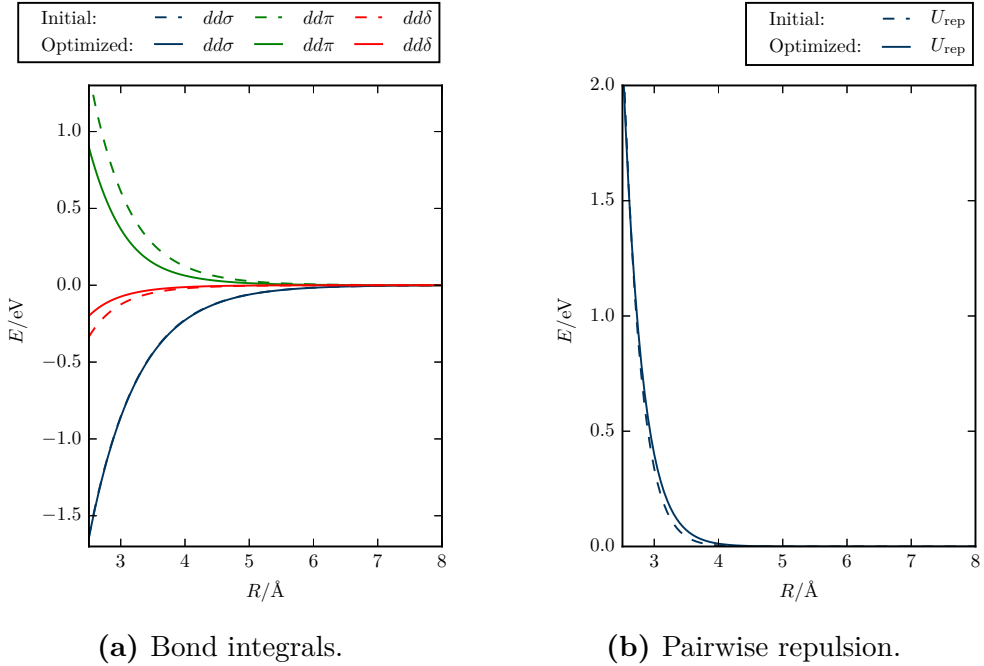


Figure 5.3.: Comparison of initial and optimized bond integrals of Re. The parametrization procedure of Fig. 5.2 was used with energy-volume DFT reference data for hcp with an optimised c/a -ratio, fcc and bcc.

to a significant improvement of the accuracy of the model, which indicates the relevance of an optimization of the model parameters and underlines the good quality of the initialization.

5.3. Transferability Assessment and Improvement

In Sec. 5.2, a parametrization protocol for d -valent orthogonal analytic BOPs was established. While it is able to parametrize a model which reproduces the provided reference data accurately it is unclear how transferable the obtained model is, i.e. how accurate its predictions are for structures which were not included in the parametrization process. A common approach is to split the reference data into a fit set and a test set. The model is optimized to the fit set and afterwards tested to the test set. This gives an impression for the transferability, which depends on the construction of the test set. In Fig. 5.4, this approach is conducted for a test set of 300 1-atom random structures (Sec. 4.1.2), which homogeneously covers the corresponding part of the map of local atomic environments (cf. Fig. 4.3) and therefore represents a large variety of atomic environments. The DFT calculations were performed by

Thomas Hammerschmidt (AMS, ICAMS, RUB) with the settings introduced in the beginning of Sec. 5. The equilibrium volume is estimated with a fifth-order polynomial fit to the equation of state and volume scalings of $\pm 10\%$ are used. While in the figure different structures share the same color, a correspondence of the model to the DFT reference can be clearly observed. The qualitative trend of the DFT reference is well reproduced by the model over a large range of volumes and energies. However, a detailed understanding of the transferability of the potential requires further analysis. More insight is obtained by a comparison of the predictions of the model for the equilibrium volumes and energies for the different phases in Figs. 5.5a, 5.5b. The figure shows that structures with small values for the equilibrium energy E_0 and volume V_0 are best reproduced among the structures.

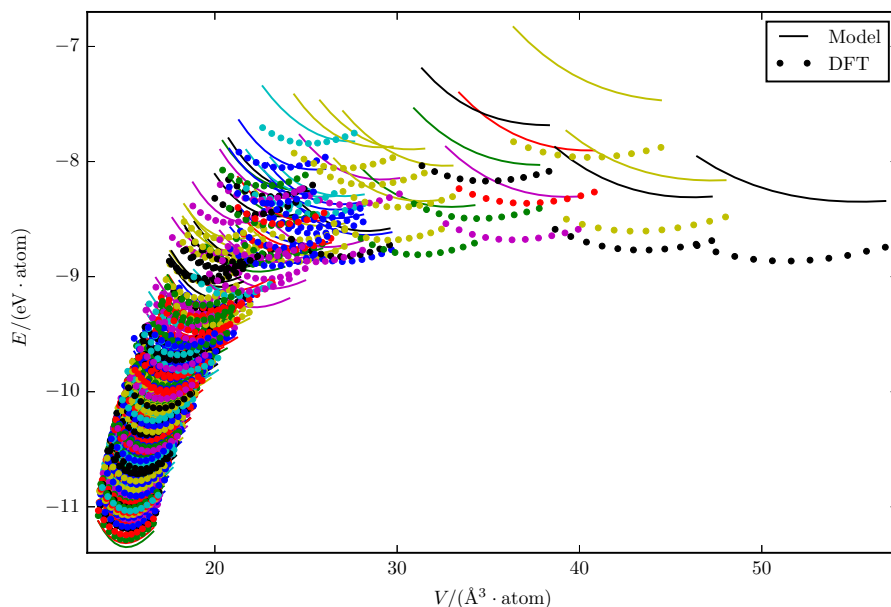


Figure 5.4.: Performance on 1-atom random structures of analytic BOP for Re optimized to hcp with an optimised c/a -ratio, fcc and bcc.

This is related to the choice of the fit set in this regime (indicated with black points in the figures). An approach to increase the transferability is to distribute the fit set over the range of possible DFT values for the equilibrium volume or energy. This approach has, however, the disadvantage that these values have to be calculated by computationally expensive DFT calculations a priori. Furthermore, this approach selects structures according to a value related to the total structure and not to the individual local atomic environments, which have to be correctly described by the model.

An alternative approach to increase the transferability, which became possible by the analysis of Sec. 4, is to select the reference structures for the

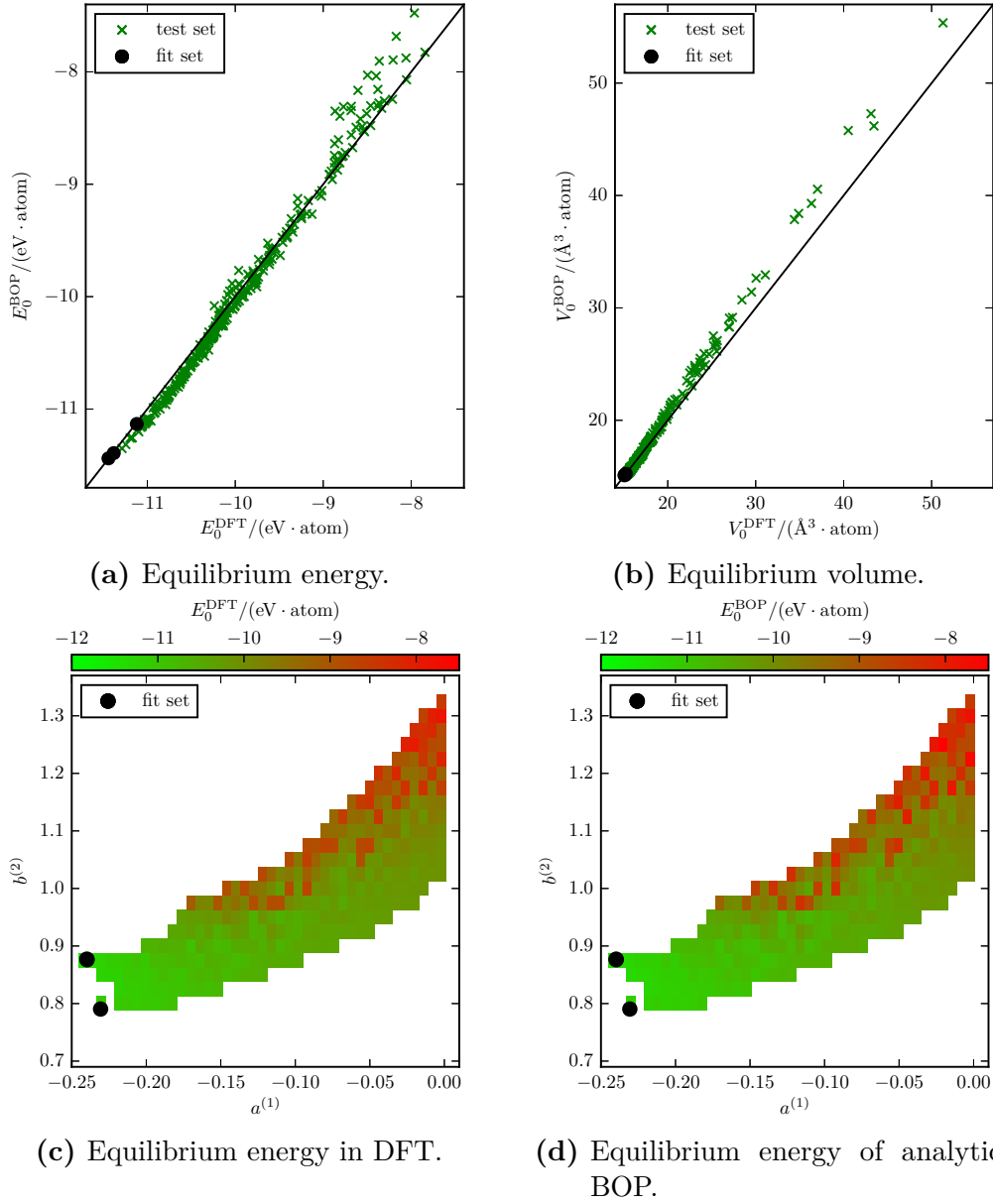


Figure 5.5.: Transferability analysis on 1-atom random structures of analytic BOP for Re optimized to hcp with an optimized c/a -ratio, fcc and bcc. The model predictions for the equilibrium energy and volume are compared to the DFT reference (Figs. a, b). A more detailed understanding for the transferability is obtained by a comparison of the equilibrium energy calculated with DFT and with the analytic BOP in the map of local atomic environments. The good agreement shows the intrinsic transferability of the analytic BOP (Figs. c, d).

parametrization process by their position in the map of local atomic environments. The map of local atomic environments allows for an intuitive, extensive and homogeneous sampling of reference structures according to their local atomic environments and thereby reduced the number of required DFT calculations significantly. In Figs. 5.5c, 5.5d, the values for the equilibrium energy obtained from DFT and from the model, which is obtained by the parametrization procedure of Fig. 5.2, are plotted in the map of local atomic environments. Even though the fit set is located at the border of the filled region of 1-atom random structures, the model reproduces the trend of the DFT results across the map, which indicates that the model has an intrinsic transferability. The intrinsic transferability of the analytic BOP is attributed to the physical coarse graining procedure, from which it is derived (Sec. 2.4) and the initial model parameters which are derived from DFT (Sec. 5.2). Such an intrinsic transferability can hardly be expected for interatomic potentials which are not derived from physical considerations, e.g. artificial neural network potentials. In Fig. 5.6a, the corresponding RMS error is evaluated in the map of local atomic environments. In general, the transferability decreases with increasing distance to the fit set. This results from the fact that the map of local atomic environments places larger differences in energy and atomic structure further apart (Sec. 4.4).

In Figs. 5.6b, 5.6c, the fit set is increased to a homogeneous distribution of 20 and 40 structures across the region of 1-atom structures and the related values of the RMS error are evaluated across the map. By this, the transferability is significantly increased. Figure 5.6d shows a learning curve of the RMS error in the energies of the fit set and the total set of structures with respect to the number of structures included the fit. The fit set represents a homogeneous distribution of structures in the map of local atomic environments. It shows that 40 structures in the fit set are already enough to have a good representation of all atomic environments because the error in the energies of the fit set and the total set of structures are almost converged. The unusual behaviour of a crossing of the two curves and a higher RMS error in the fit set than in the total set of structures can be explained as an artefact of the special choice of the fit set. The fit set is increased by adding those structures which have the largest distance to all other structures in the fit set, i.e. always the most difficult fit set is constructed. The learning curve converges to an RMS error of 65 meV which corresponds to 1.8% of the range of the equilibrium energies of the investigated structures. This indicates a good transferability of the model in the considered range of atomic environments.

This example indicates that it is possible to use an iterative transferability optimization procedure, which is illustrated in Fig. 5.7. It is initialized with an initial model, which is obtained by the parametrization protocol of Fig. 5.1 and a (weighted) fit set. A weighting of the reference data by weighting factors w_n in Eq. 5.2 may be used to further balance the transferability in different regimes and is used in Sec. 5.4. The model parameters are optimized to the

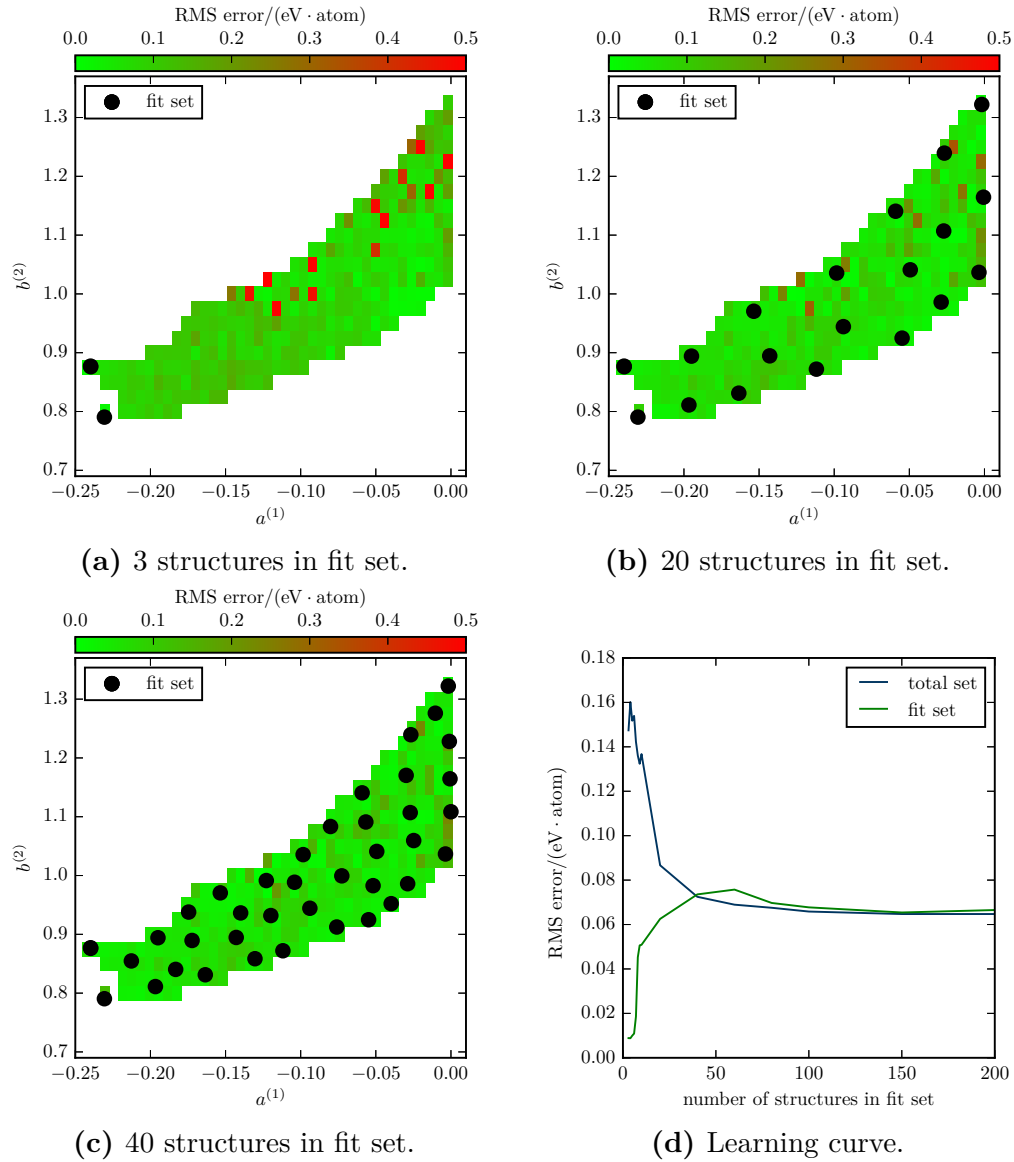


Figure 5.6.: Transferability improvement of analytic BOP for Re on 1-atom random structures. The RMS error of the analytic BOP optimized to hcp with an optimised c/a -ratio, fcc and bcc is evaluated in the map of local atomic environments (Fig. a). The transferability can be improved by using 20 and 40 structures in the fit set which are homogeneously distributed in the map of local atomic environments (Figs. b, c). A learning curve of the RMS error in the energies of the total set of structures and of the fit set is evaluated for different sizes of the fit set (Fig. d).

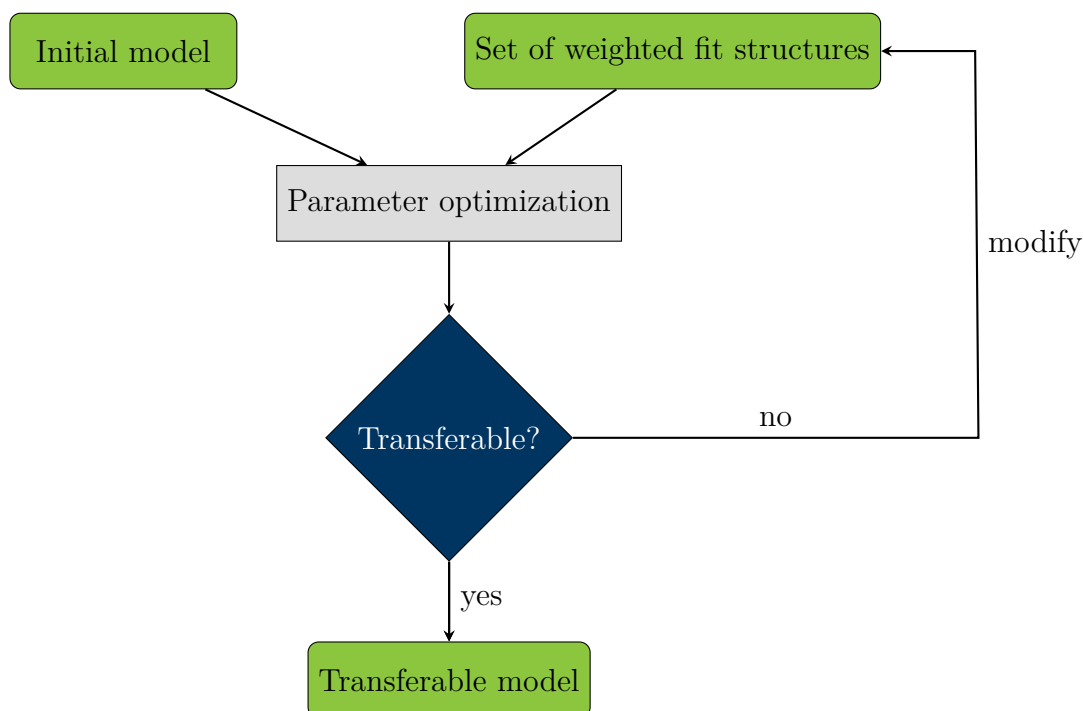


Figure 5.7.: Iterative approach to improve the transferability. Starting from an initial model and a set of weighted fit structures the model parameters are optimized. The map of local atomic environments can be used to analyse the transferability and the fit set may be modified until a transferable model is obtained.

fit set and the transferability is analysed and estimated with the map of local atomic environments. If the transferability is unsatisfactory, the fit set is modified and the parameter optimization is performed again. This is done iteratively until a transferable model is found.

5.4. Parameterization of an Analytic Bond-Order Potential for Re

The parametrization protocol (Fig. 5.1) and the transferability optimization procedure (Fig. 5.6) are used to parametrize an analytic BOP for Re. Its predictions are compared with a variety of reference data to verify its accuracy and transferability.

5.4.1. Reference Data

The reference data was selected by Aparna P. A. Subramanyam (AMS, ICAMS, RUB) based on knowledge of materials properties defining key quantities. It

includes different crystallographic phases, point defects, stacking faults (SFs), elastic properties and phonons. The corresponding reference structures are illustrated in Figs. 5.8, 5.9 in the map of local atomic environments. Figure 5.8 covers the same range of the moments-descriptors $a^{(1)}$ and $b^{(1)}$ as the map of local atomic environments in Fig. 4.3 and includes the envelopes of the 1-atom-cells and 2-atom cells, the crystal structures hcp, fcc and bcc, a selection of DFT relaxed topologically close-packed (TCP) phases, the tetragonal, trigonal, hexagonal and orthorhombic transformation paths, two vacancy diffusion paths, and DFT relaxed cells with point defects which include a vacancy and several self-interstitials. The map marks the region around hcp, fcc and bcc with a black solid line. This part of the map is magnified in Fig. 5.9a. The individual atoms of the point defects are not shown in this figure for a better visual interpretation. In this part of the map, a small region around hcp and fcc is again marked with a black solid line, which is magnified in Fig. 5.9b. The hcp structure with the c/a -ratio of Re predicted by DFT and the relaxed dhcp structure are added to this part of the map. Its elastic deformations and the individual atomic environments of the DFT relaxed basal intrinsic and basal extrinsic stacking faults are also visible. Moreover, the local atomic environments which are used to calculate the phonon spectrum are added to the map. The reference data is described in the following and split into a fit and a test set in Sec. 5.4.2.

Different Phases

It was shown in Sec. 5.3 that a homogeneous sampling of atomic environments by random structures in the existence regions of 1-atom cells or 2-atom cells is useful to analyse the transferability of an interatomic potential. The region of 1-atom cells has fcc at its left border and does not reach hcp, the ground state structure of Re, which is at the left border of the existence regions of the 2-atom cells.

Different transformation paths are presented in Sec. 4.1.2. The hexagonal transformation path deforms hcp into bcc. The tetragonal and trigonal transformation paths deform fcc, which is close to hcp in the map of local atomic environments, into bcc. The orthorhombic transformation path connects bcc with a special bct structure (Sec. 4.1.2) and is used to analyse the transferability to this part of the map of local atomic environments.

In Ni-base superalloys, Re is often used as a solid solution strengthener [213]. However, for a set of Re compounds TCP phases (Sec. 4.1.2) are found to be stable [214], which precipitate at high temperatures and stresses in Ni-base superalloys. This leads to a decrease of the strengthening effect and may cause fracture [213]. Therefore, an accurate description of the TCP phases is important if the potential is later extended to multi-component systems. The χ , C14, C15, C35, A15 and σ structure are selected as representative TCP phases to evaluate the accuracy of the description of TCP phases. The DFT

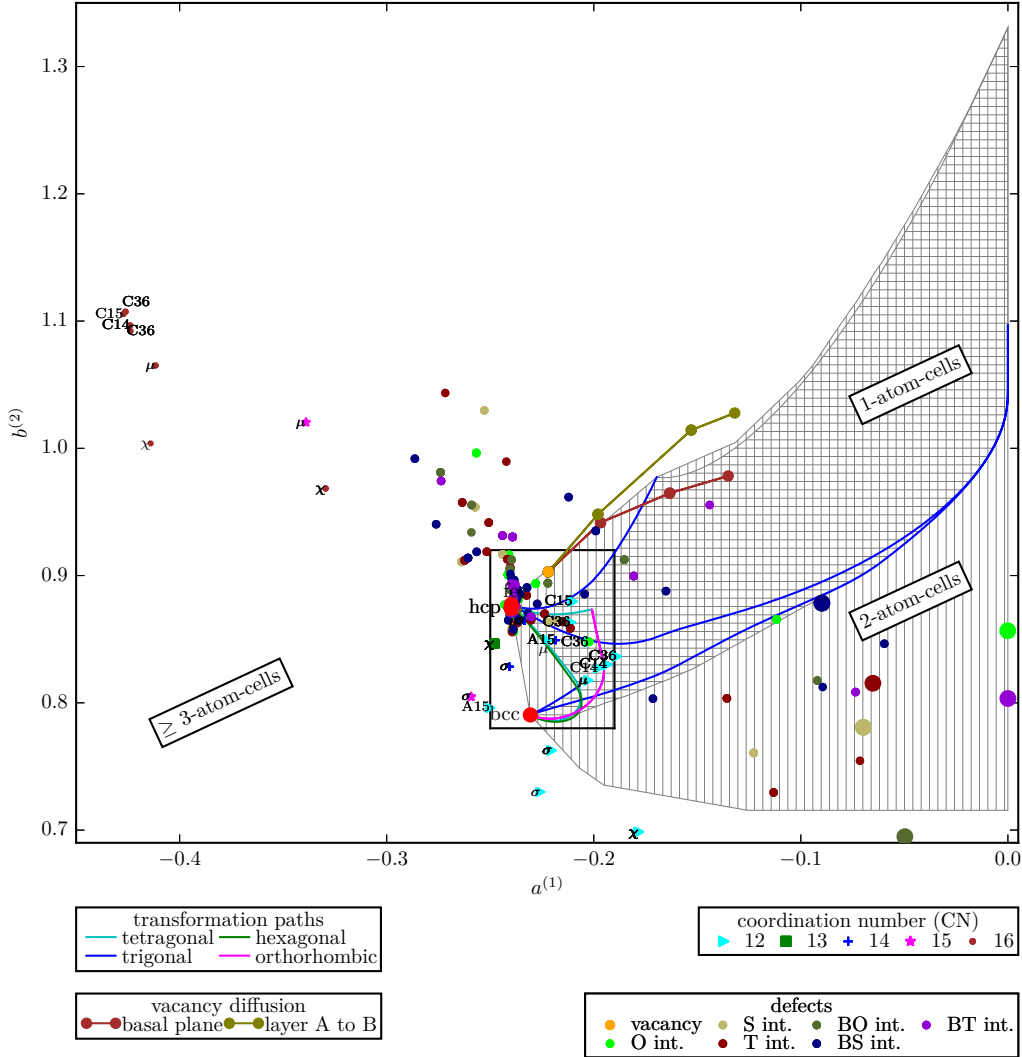
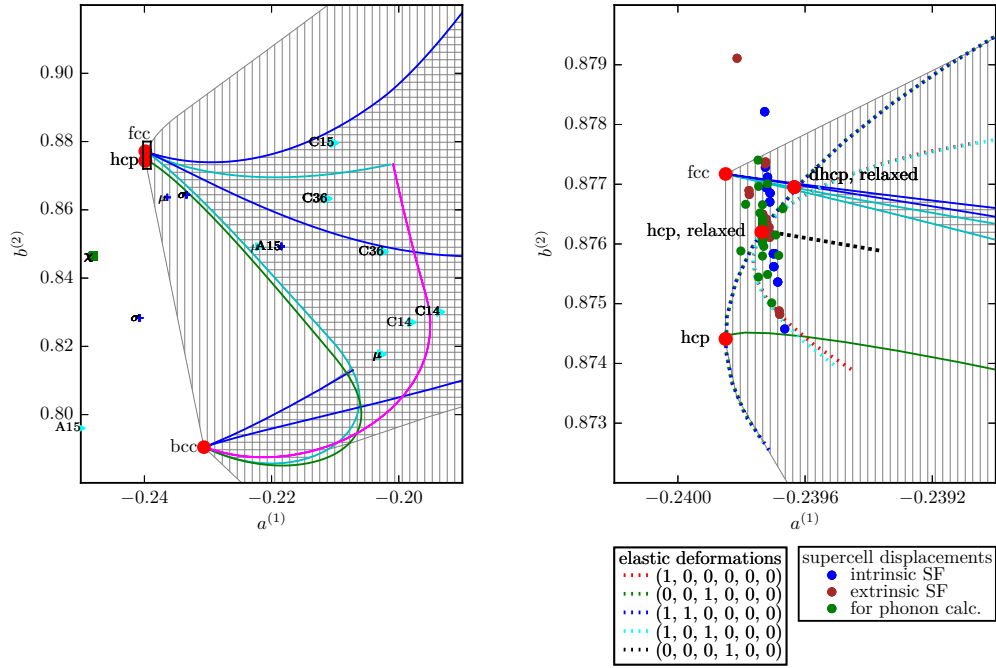


Figure 5.8.: Map of local atomic environments for d -valent Hamiltonian containing the reference data used for the parametrization of the analytic BOP for Re. The map shows the estimated envelopes for the existence regions of 3-D cells with one and two atoms in the primitive cell and the tetragonal, trigonal, hexagonal and orthorhombic transformation paths (cf. Fig. 4.3). The crystal structures hcp, fcc and bcc are marked by red filled circles and the further symbols indicate the different coordination polyhedra of the DFT relaxed TCP phases with the common name given next to the symbol. Vacancy diffusion paths calculated in DFT with the cNEB method are shown by solid lines and filled circles which represent the individual images. The DFT relaxed self-interstitial atom (SIA) structures from Fig. 5.10 are also shown by filled circles. The SIAs are highlighted by circles with a larger radius. The BC SIA structure relaxes to the BO structure and is therefore not explicitly shown. The marked region around the close-packed phases (bcc, fcc, hcp) is magnified in Fig. 5.9a.



(a) Magnified region around hcp, fcc and bcc.

(b) Magnified region around hcp and fcc.

Figure 5.9.: Magnified regions of the map of local atomic environments of Fig. 5.8.

The individual atomic environments of the structures with the point defects are not shown. Figure a shows the region around hcp, fcc and bcc. The marked region around hcp and fcc is further magnified in Fig. b. Additional red filled circles show the hcp structure with the DFT relaxed c/a -ratio and the relaxed dhcp structure. Dashed lines show the elastic deformations applied for the calculation of the elastic constants (Tab. C.1). The individual atomic environments of the DFT relaxed basal intrinsic and basal extrinsic SFs (Fig. 5.11) and the atomic environments which are used to calculate the phonon spectrum are shown by filled circles.

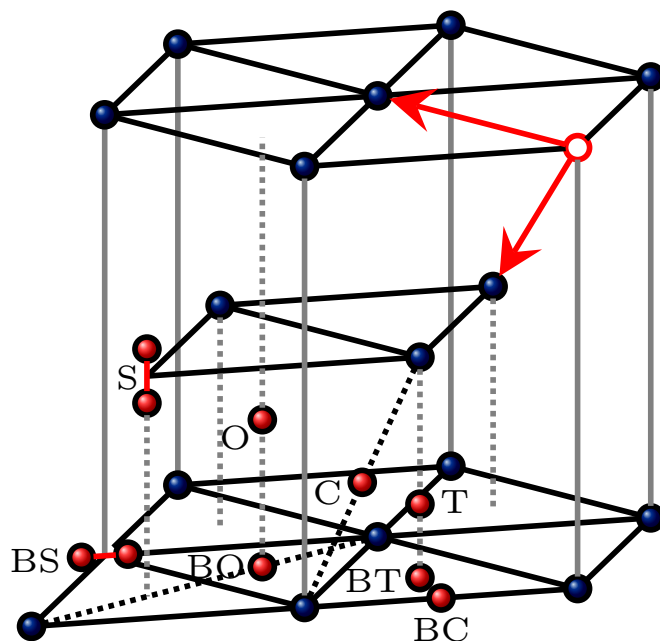


Figure 5.10.: Point defects in an hcp cell. SIAs are shown in red. They summarize crowdion (C), octahedral (O), split dumbbell (S), tetrahedral (T), basal crowdion (BC), basal octahedral (BO), basal split dumbbell (BS) and basal tetrahedral (BT) SIAs. A vacancy is marked by a red circle and the nearest neighbour diffusion in the basal plane and between two planes are illustrated by red arrows. Adapted from Ref. 215.

relaxed atomic environments of these structures are also added to the map. As for the prototype structures, which are used in Fig. 4.3, the distance of the hcp structure to the relaxed 12-, 13- and 14-fold coordination polyhedra is small in the map of local atomic environments and larger to the higher 15-, and 16-fold coordination polyhedra. This indicates that the higher coordination polyhedra are very different to the local atomic environment of hcp. Due to the large distances of the ground state structure hcp to the different phases in the map of local atomic environments, a transferability to them is referred to as global transferability in the following.

Point Defects

The concentration of vacancies and SIAs in a material depends on the temperature. Moreover, they are formed by plastic deformations and high-energy

particle irradiation [216]. For example, in magnetic-confinement fusion devices, tungsten is an attractive candidate as a plasma-facing material and under neutron irradiation, it may transmute to Re and a cascade produces different point defects (cf. Ref. 215, and references therein). Therefore, an accurate description of point defects by the interatomic potential is of relevance. The considered point defects include a vacancy and several SIAs. The different SIAs are illustrated and described in Fig. 5.10. The crowdion SIA is missing in the following analysis because of technical difficulties during the relaxation in DFT. The DFT relaxed structures with SIAs which do not relax to another configuration are added to the map of local atomic environments in Fig. 5.8. All atoms of a cell with a SIA share the same color and the SIAs are highlighted by circles with a larger radius. The SIAs have special environments and are located far from the hcp structure.

Vacancy diffusion between nearest neighbours in the basal plane and between two nearest neighbours in different planes is considered at the level of the climbing nudged elastic band (cNEB) method with an improved tangent definition [217, 218]. The diffusion paths are also added to Fig. 5.10.

Stacking Faults

In hcp crystals, SFs can have an important effect on the plasticity of crystals [216] and their energies are related to the preferred slip direction [219]. Therefore, it is important for an interatomic potential for Re to describe SFs correctly. The considered basal intrinsic and basal extrinsic SFs are shown in Fig. 5.11. The considered basal intrinsic SF has the lowest SF energy [219] and is constructed by a partial change of the stacking sequence ABAB to ACAC. The basal extrinsic SF is created by inserting an extra C plane in an hcp crystal with an ABAB stacking sequence. The individual local atomic environments of the DFT relaxed SF structures are shown in the map of local atomic environments in Fig. 5.9b. Each structure is constructed by 40 layers of atoms with two SFs in the cell. Due to the atomic relaxation, almost a continuous set of atomic environments in the region of hcp and fcc is formed and opposite to the unrelaxed case, none of the atomic environments of the intrinsic SF coincides with the position of the DFT relaxed dhcp structure.

Elastic Properties

The elastic properties of a material influence its thermodynamic properties, equation of state, phonon spectrum and structural stability. Therefore, it is important that an interatomic potential describes the behaviour of the material under elastic deformations accurately. The calculation of the elastic constants with DFT and with interatomic potentials for the hexagonal crystal structure is summarized in Sec. C of the appendix. The elastic deformations used in this work, the corresponding physical strain tensor and second deriva-

tive of the total energy are summarized in Tab. C.1. The physical strain ϵ is varied around $\pm 2\%$ and a polynomial of order two is fitted to the total energies to compute the elastic constants.

The related deformation paths of the DFT relaxed hcp structure of Re are visualized in the map of local atomic environments in Fig. 5.9b. The structures with the employed values of η are in the vicinity of the reference structure. A local transferability of the potential is therefore related to accurate elastic constants. The map of local atomic environments places the deformations $(0, 0, 1, 0, 0, 0)$ and $(1, 1, 0, 0, 0, 0)$ on top of each other because they differ only by a scaling of the volume, which is removed by the applied normalization of the second moment (Eq. 4.4). The deformations $(1, 0, 0, 0, 0, 0)$ and $(1, 0, 1, 0, 0, 0)$ are close to each other while the shear deformation $(0, 0, 0, 1, 0, 0)$ differs significantly from the other deformations.

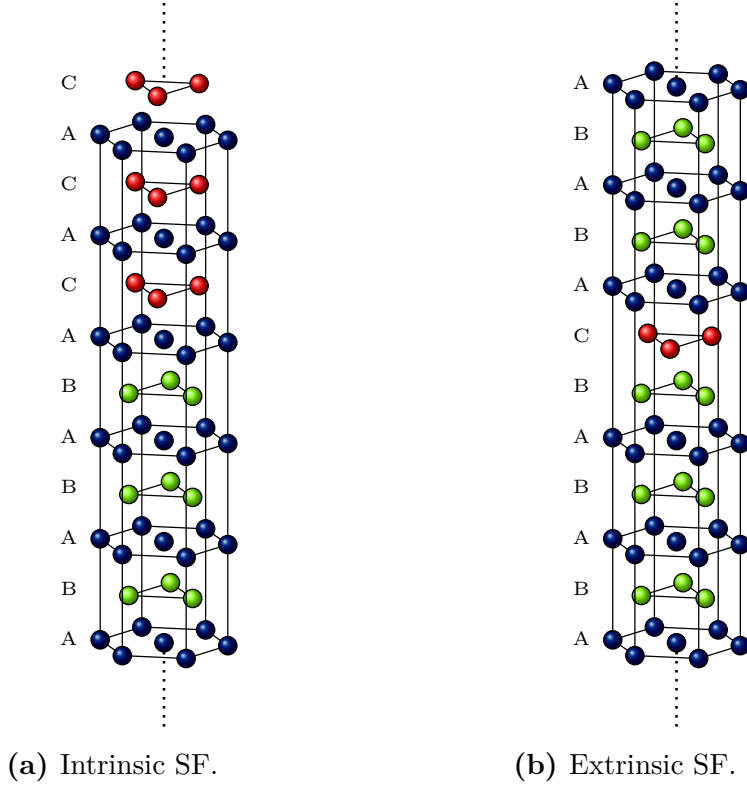


Figure 5.11.: Visualization of the change in the stacking sequence for the basal intrinsic and basal extrinsic SF.

Phonons

In a harmonic approximation, the phonons are calculated by solving the eigenvalue problem of the dynamical matrix, which is computed from the second-order force constant matrix. This can be calculated by DFT or interatomic

potentials with the finite displacement method. An implementation is provided in the program code `phonopy` (Ref. 222). The lattice vibrations have an important contribution to the free energy and thus play an important role for phase transitions and for thermal properties like the heat capacity. Moreover, imaginary phonon frequencies indicate dynamical instability of the system. The accuracy in the description of lattice vibrations of the potential can be estimated by the comparison of the phonon spectrum and the phonon DOS to the DFT reference.

A $4 \times 4 \times 3$ supercell of the primitive hcp cell is used for the calculation of the force constant matrix with an atomic displacement of one atom of 0.01 \AA in $[1, 0, 1]$ direction. The individual local atomic environments are added to the map of local atomic environments in Fig. 5.9b.

5.4.2. Construction of Fit Set

The reference data has to be divided into a fit set and a test set. The fit set should include the most relevant data as the accuracy of the potential is optimized to it. However, as the optimization process requires many iterations over the model parameters it should include only data which can be computed efficiently and should not include redundant information. In this work, only total energies per atom obtained from DFT are used as reference data. As discussed in Sec. 5.4.1, both the transferability to different phases and also the elastic properties of the ground state structure are important for the interatomic Re potential. The phases hcp, fcc, bcc, A15, C15 and σ phase are considered in the fit by total energies for 20 volume scalings of $\pm 20\%$ around their equilibrium volume estimated from a fifth-order polynomial fit to the equation of state. These structures have a moderate size and they include 12-, 14-, 15- and 16-fold coordination polyhedra such that a variety of different local atomic environments is considered. The elastic properties of the material are considered by taking into account the energies of the elastic deformations which are summarized in Tab. C.1 by 14 structures for each deformation with strain rates η up to $\pm 2\%$.

The cost function (Eq. 5.1) which is minimized by an optimization method summarizes all individual errors. The model parameters which minimize the error e_n of a quantity n will not in general minimize the error e_m of another quantity m . For example, the model parameters which minimize the RMS error in the energy-volume curve of one crystal structure will not minimize it for another crystal structure. Similarly, the model parameters which minimize the RMS error in the energies of the elastic deformations of the ground state will not correspond to those which minimize the RMS error in the energy-volume curves of the different crystal structures. In order to control the accuracy of the individual target properties, the errors e_n of the different target properties are weighted by weights w_n .

The relevance of the individual phases (hcp, fcc, A15, C15 and the σ phase)

depends on the energy difference to the ground state. This is considered by weighting the structures according to their equilibrium energy $E_{\text{struc}}^{(0)}$ by the function

$$w_{\text{struc}} = \exp\left(-\frac{(E_{\text{struc}}^{(0)} - E_{\text{hcp}}^{(0)})}{0.1\text{eV}}\right), \quad (5.9)$$

where the energies are normalized per atom and the value of 0.1 eV is empirically adjusted. This value corresponds to a temperature of 1160 K. By this choice, the hcp structure has a weight of 1 and the fcc structure, which is also low in energy, has a weight of approximately 0.55. The bcc structure, which is higher in energy than all other phases in the fit set, has a weight of approximately 0.04. The weights are adjusted such that a good transferability to the structures which are low in energy and a robust description of the structures which are higher in energy is expected.

While the energy-volume curves cover energy changes of around 1 eV/atom, the change in energy for the elastic deformations is not more than about 40 meV/atom. With equal weighting of the structures, the relative importance of the energy-volume curves would be higher than of the elastic deformations in the optimization process. In order to balance the two regimes, the error in energies of the elastic deformations is weighted against those of the energy-volume curves. This is done by a weighting factor for the RMS error in the energies of the elastic deformations

$$w_{\text{ela}} = a_{\text{ela}} \frac{\Delta E^{\text{struc}}}{\Delta E^{\text{ela}}}, \quad (5.10)$$

where ΔE^{struc} is the largest energy difference of the energy-volume curves in the fit set and ΔE^{ela} is the largest energy difference of the elastic deformations in the fit set. With the definitions of w_{struc} and w_{ela} , the choice of the different weights reduces to an adjustment of the parameter a_{ela} , which controls the balance between the local transferability to the elastic deformations of the hcp structure and the global transferability to the individual bulk structures.

5.4.3. Transferability Adjustment

It is not known a priori how a_{ela} should be chosen to obtain a desired accuracy in the two regimes. In order to measure the accuracy in the elastic deformations, the RMS error of the energies of each elastic deformation

$$c_{\text{ela}}(\boldsymbol{\theta}) = \sqrt{\frac{\sum_n^{N_{\text{ela}}} (E_{\text{pred},n}(s_n; \boldsymbol{\theta}) - E_{\text{ref},n}(s_n))^2}{N_{\text{ela}}}} \quad (5.11)$$

is averaged to define a cost function for the elastic deformations. Here, N_{ela} is the number of generated structures for each elastic deformation. Equivalently, a cost function which measures the accuracy in the description of the different

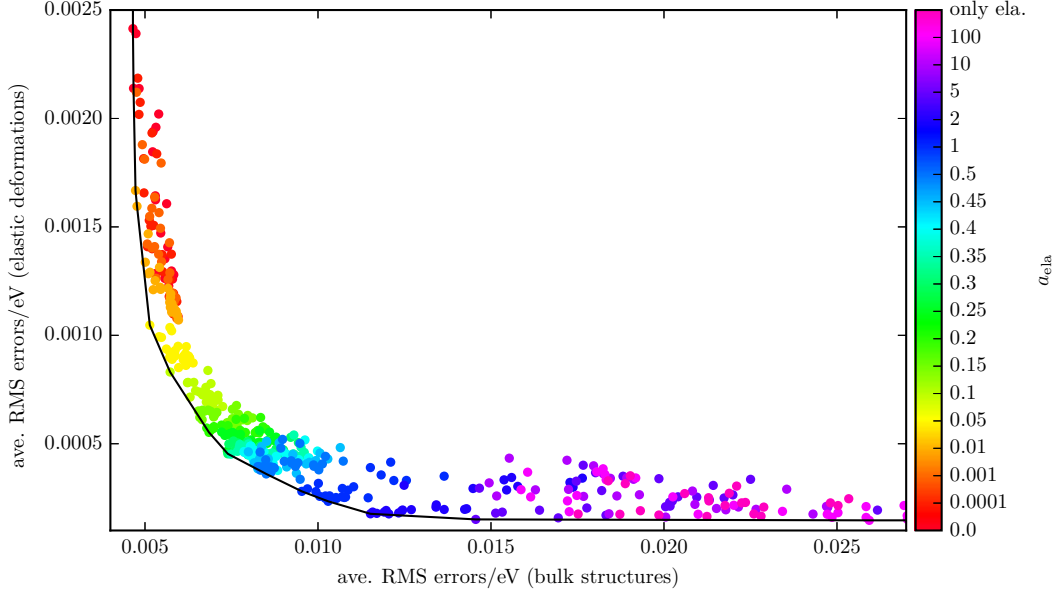


Figure 5.12.: Cost function of energies of the elastic deformations versus the cost function of the energies of the bulk structures obtained from optimized models initialized by random variations of the initial model and by varying the weight parameter a_{ela} of Eq. 5.10. The lower boundary of the points forms a Pareto front.

phases is defined by averaging the RMS error of the energy-volume curves

$$c_{\text{struc}}(\boldsymbol{\theta}) = \sqrt{\frac{\sum_n^{N_{\text{struc}}} w_{\text{struc}}^2 (E_{\text{pred},n}(s_n; \boldsymbol{\theta}) - E_{\text{ref},n}(s_n))^2}{N_{\text{struc}}}}, \quad (5.12)$$

where the different phases are weighed by w_{struc} according to Eq. 5.9. With the definition of a cost function for the elastic deformations and a cost function for the accuracy in the description of the different phases, the parameter a_{ela} is adjusted by an analysis based on Pareto fronts. Model parameters belong to the Pareto front if it is impossible to minimize one cost function without increasing another cost function [223]. Depending on the required accuracy in all cost functions, the best model for a specific application can be selected from the Pareto front.

A systematic sampling of the Pareto front is obtained by varying a_{ela} (Eq. 5.10) between 0 and 100 and optimizing the model only to the energies of the elastic deformations. The parametrizations are initialized by the parameters of the initial model ($H_{IJ}^{\text{ini}}, U_{\text{rep}}^{\text{ini}}, U_{\text{emb},s}^{\text{ini}}$) obtained from the parametrization protocol of Fig. 5.1. Thirty further initializations are generated for each value of a_{ela} by randomly changing the initial model parameters within a Gaussian distribution with a width of 5% of the reference value. The cost function for the energies of the elastic deformations (Eq. 5.10) versus the cost function for

the energies of the bulk structures (Eq. 5.9) is plotted in Fig. 5.12. A lower boundary is estimated from the data and plotted as a solid line. This curve is an estimate of the Pareto front. High values of a_{ela} lead to low errors in the energies of the elastic deformations but to high errors in the energies of the bulk structures. By decreasing a_{ela} , the errors in the energies of the bulk structures decreases in general but the errors in the energies of the elastic deformations increases.

It can be seen that the two cost functions do not become very high even when they are not considered in the optimization. This is in agreement with the results of Fig. 5.5 and is attributed to the physical coarse graining procedure, which is used to derive the analytic BOPs from DFT and to the initial model parameters, which are derived from DFT by the downfolding procedure (Sec. 3.2.3). The moderate errors in Fig. 5.12 show that the analytic BOPs have an intrinsic transferability.

In Fig. 5.13, several tests are evaluated for the different models and plotted with respect to the RMS errors in the energies of the elastic deformations and bulk structures. The tests summarize

- the error in the energy differences of hcp and dhcp at their equilibrium volume $\Delta_{\text{hcp-dhcp}}$,
- the error in the vacancy formation energy $E_{\text{F,vac}}$,
- the average absolute error in the energy barriers E_{barrier} of the two considered vacancy diffusion paths,
- the average absolute error in the elastic constants C_{ij} ,
- the average absolute error in the energies of the considered bulk structures E_{bulk} at their equilibrium volume excluding the dhcp structure,
- the error in the c/a -ratio of the hcp structure,
- the average absolute error in the two considered SF formation energies E_{SF} and
- the average absolute error in the considered self-interstitial formation energies E_{SIA} . To simplify these calculations, the atomic relaxation is initialized by the results from the DFT reference.

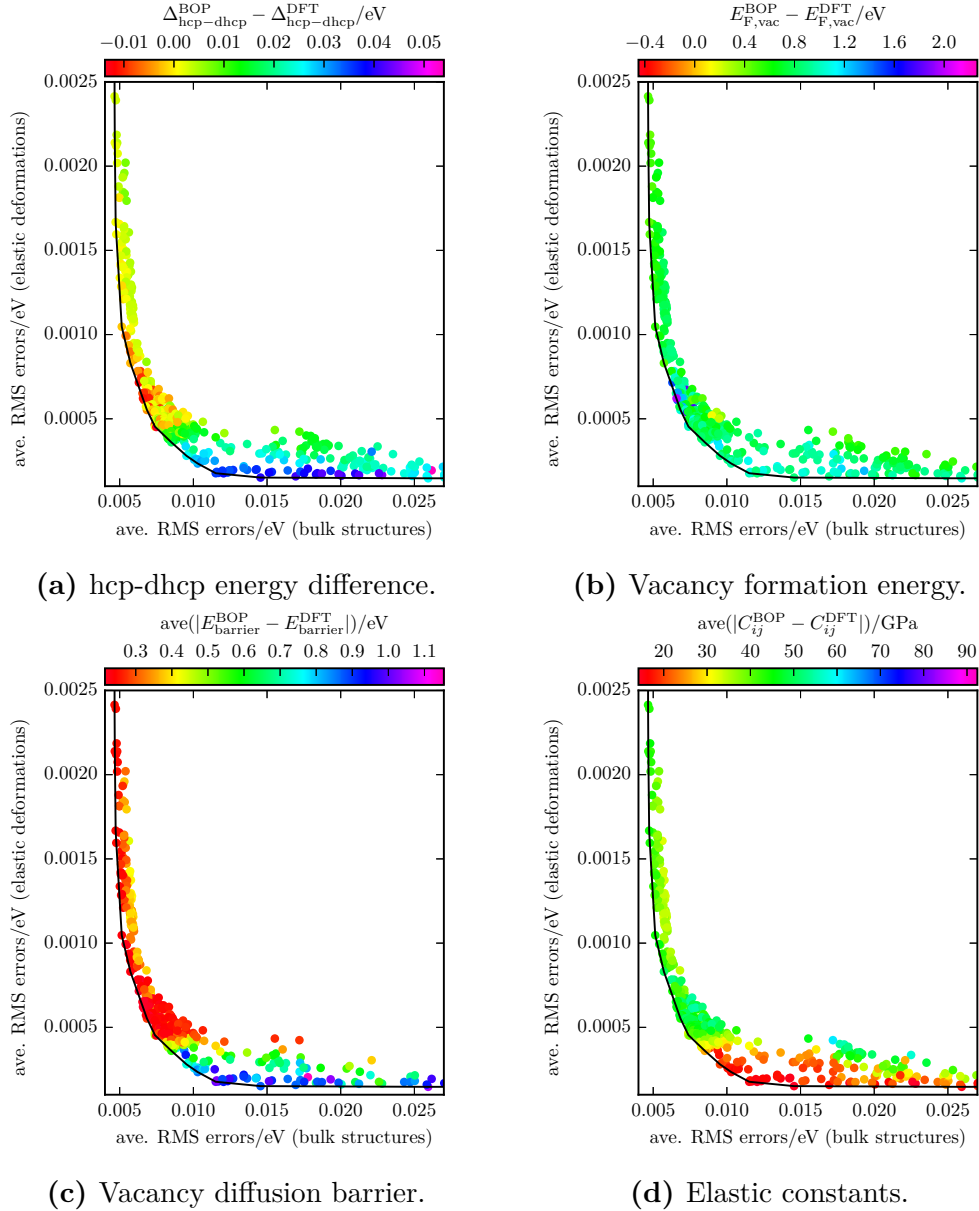
The energy differences of hcp and dhcp at their equilibrium volume is positive for a large fraction of models especially for those with a high weight on the RMS error in the energies of the elastic deformations. This qualitatively wrong behaviour of the models is related to the small DFT energy difference of the two structures which is equal to 1.76 meV. By using high weights for the RMS error in the energies of the elastic deformations of the ground state, other phases are not sufficiently considered by the cost function such

that the ordering of the phases may not be correctly described by the model (Fig. 5.13a).

The vacancy formation energy does not show much variation across the different models except for a set of similar models which overestimate the energy significantly (Fig. 5.13b).

Even though no atomic environments of the bulk phases are similar to those of the vacancy diffusion paths (see Fig. 5.8), the vacancy diffusion is better described by higher weights on the RMS error in the energies of the bulk phases (Fig. 5.13c).

As expected, the average absolute error in the energies of the elastic constants is lowest for those models which are optimized with a high weight on the RMS



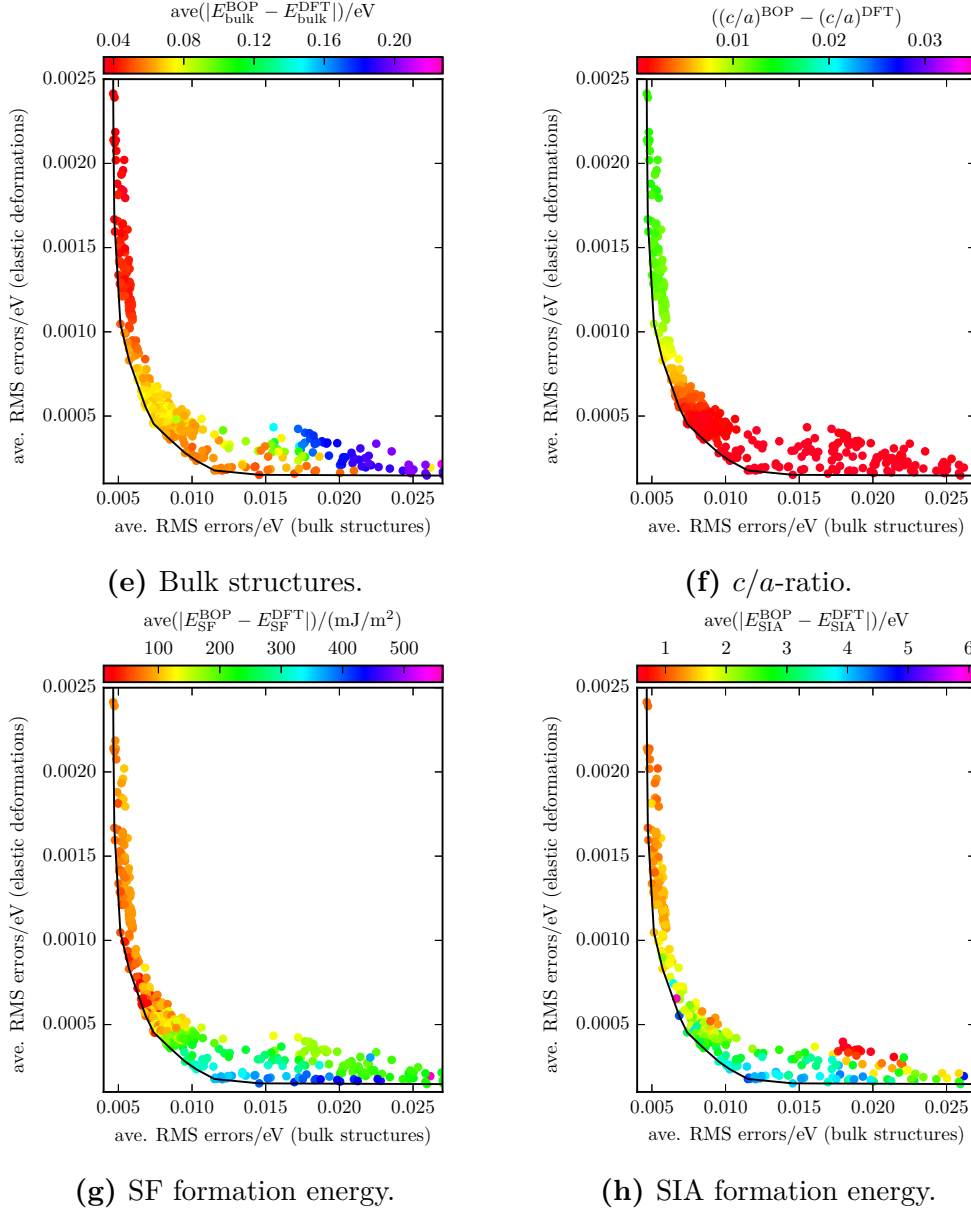


Figure 5.13.: A series of quantitative tests (Figs. a-h) is executed for the optimized models. The cost function of the energies of the elastic deformations is plotted versus the cost function of the energies of the bulk structures and the color indicates the difference of the prediction of the model to the DFT reference. A detailed description of the qualitative tests is provided in the text.

error in the energies of the elastic deformations (Fig. 5.13d).

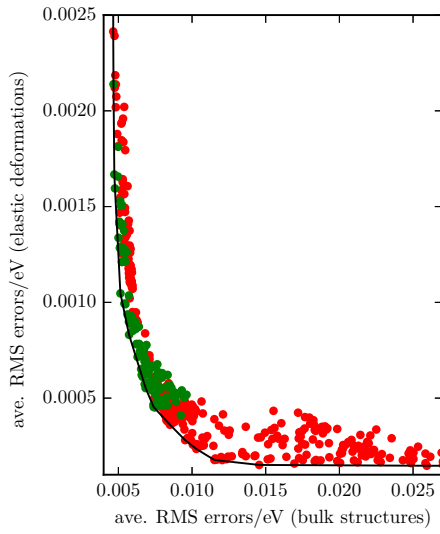
Similarly, the average absolute error in the energies of the considered bulk structures at their equilibrium volume decreases with increasing weight on the RMS error in the energies of the bulk structures (Fig. 5.13e).

The c/a -ratio of hcp is better described by high weights on the elastic deformations as it is related to the energies of the elastic deformation $(0, 0, 1, 0, 0, 0)$, which are considered in the fit set (Fig. 5.13f).

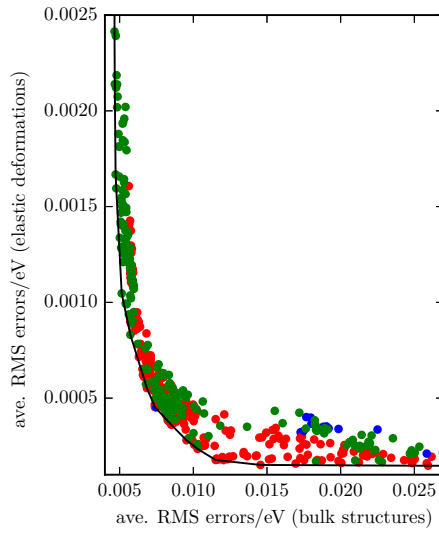
Similar to the error in the energies of the vacancy diffusion barriers, the average absolute errors in the considered SF and SIA formation energies decreases with increasing weight on the RMS error in the energies of the bulk structures (Figs. 5.13f, 5.13g). A negative formation energy for the dhcp structure may also cause a negative formation energy for the intrinsic SF because it includes local atomic environments which correspond to dhcp. A set of models with high weights on the RMS error in the energies of the elastic deformations does not follow the general trend and shows small errors in the SIA formation energies. The trends of the errors are often complex and in different directions with respect to the two RMS errors which define the Pareto front. Therefore, qualitative tests for the models are defined in order to exclude models if they do not reproduce test quantities accurately enough. In Figs. 5.14a-5.14h, the models which passed the test are shown in green and which did not pass the test in red in plots of the cost function of the energies of the elastic deformations versus the cost function of the energies of the bulk structures. A few points are marked in blue, which correspond to calculations which exceeded a maximal runtime. The qualitative tests are summarized in the following:

- The hcp structure at its equilibrium volume is lower in energy than the dhcp structure at its equilibrium volume (Fig. 5.14a).
- The error in the vacancy formation energy is lower than 0.8 eV (Fig. 5.14b).
- The errors in the considered vacancy diffusion barriers are both lower than 0.5 eV (Fig. 5.14c).
- The error in all elastic constants are lower than 90 GPa (Fig. 5.14d).
- The errors in the energies of the considered bulk structures at their equilibrium volume are lower than 0.05 eV or their energy difference to hcp are within a tolerance of $\pm 40\%$ (Fig. 5.14e).
- The error in the c/a -ratio of hcp is lower than 0.01.
- The SF energies are larger than 20 mJ/m² (Fig. 5.14f).
- The error in the SIA formation energies is lower than 2.2 eV (Fig. 5.14g).

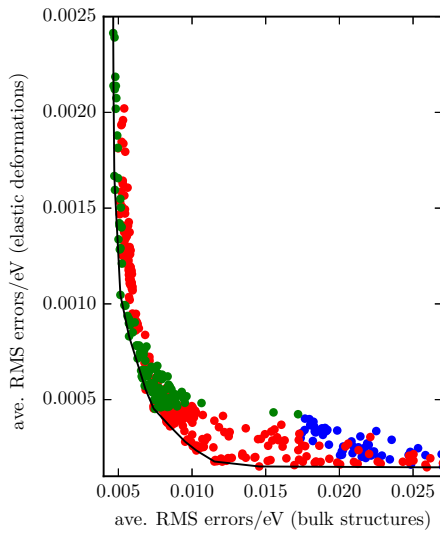
The tests for dhcp, the vacancy diffusion barriers, the bulk phases and the SIAs (Figs. 5.14a, 5.14c, 5.14e, 5.14h) are mainly passed by models which are obtained with a high weight on the RMS error in the energies of the bulk structures. Contrary, the test for the c/a -ratio (Fig. 5.14f) is passed mainly by models which are obtained with high weight on the RMS error in the energies of the elastic deformations and the test for the SFs (Fig. 5.14g) is



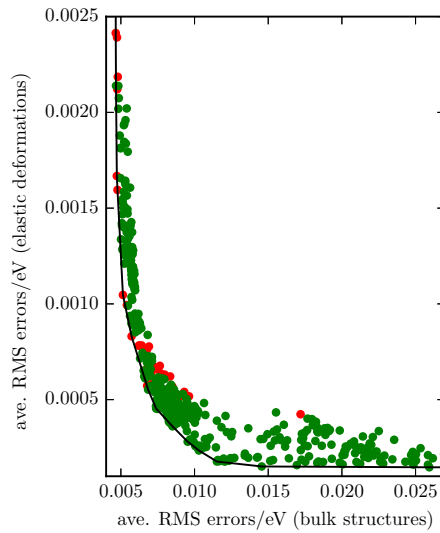
(a) hcp-dhcp energy difference.



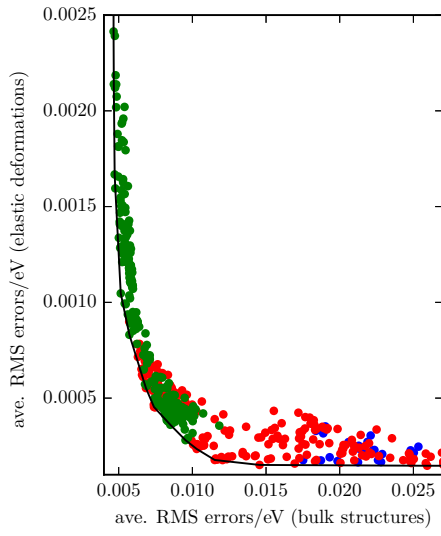
(b) Vacancy formation energy.



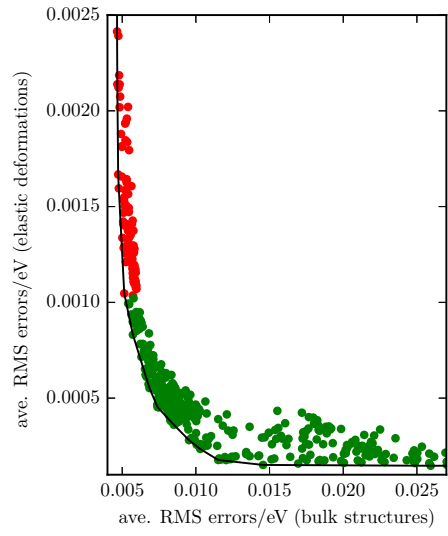
(c) Vacancy diffusion barrier.



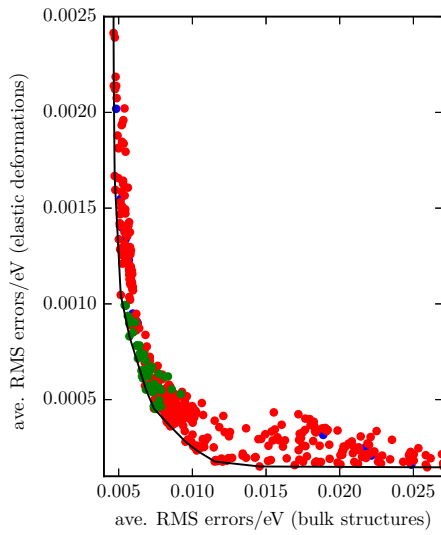
(d) Elastic constants.



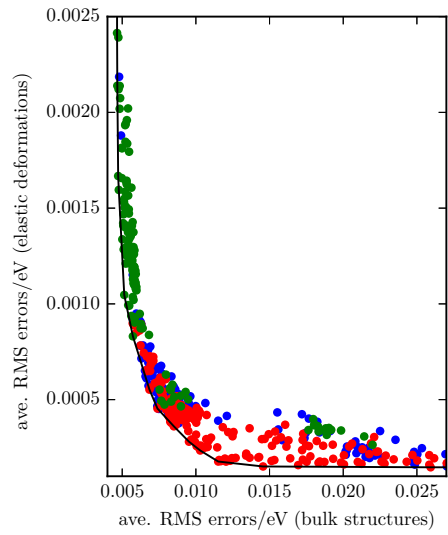
(e) Bulk structures.



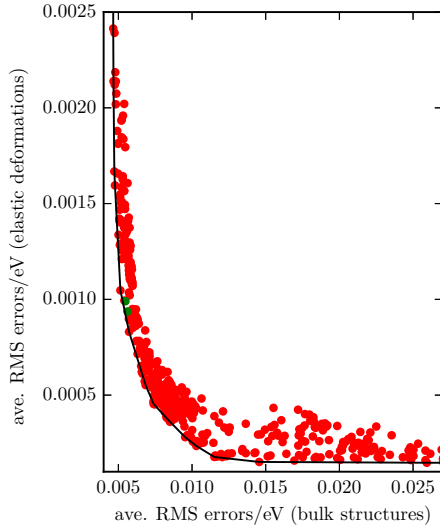
(f) c/a -ratio.



(g) SF formation energy.



(h) SIA formation energy.



(i) All tests.

Figure 5.14.: A series of qualitative tests (Figs. a-h) is executed for the optimized models. Models which passed the test are shown in green and models which did not pass it are shown in red in a plot of the cost function of the energies of the elastic deformations versus the cost function of the energies of the bulk structures. Only two models passed all tests as shown in Fig. i. A detailed description of the quantitative tests is provided in the text.

Bond integrals	c_0	λ_0	n_0	c_1	λ_1	n_1
$dd\sigma$	-25.6844	1.2112	0.9128	-0.0545	0.0022	5.8615
$dd\pi$	45.9185	1.5209	1.0781	1.3012	0.1368	2.8634
$dd\delta$	-11.8617	1.5604	0.9133	-9.7242	1.2671	1.7076
Pair repulsion	c_0	λ_0	n_0			
U_{rep}	65538.0909	4.7264	0.8625			
Embedding term	a_{emb}	b_{emb}				
$U_{\text{emb},s}$	2.4338	0.1382				

Table 5.1.: Parameters of Pareto-optimal analytic BOP for Re.

passed for intermediate weights. In Fig. 5.14i, it can be seen that only two models passed all tests which differ marginally. From the two models, the model with the smaller cost function of the energies of the bulk structures has been selected as the final Pareto-optimal analytic BOP model for Re.

5.4.4. Pareto-Optimal Analytic BOP Model for Re

Model Parameters

The parameters of the bond integrals, the embedding term for the s -electrons and the pairwise repulsive energy are summarized in Tab. 5.1. The bond integrals and the pairwise repulsive energy are visualized and compared to the initial model in Fig. 5.15. After the optimization the bond integrals are still close to the initialization and the pairwise repulsion did not change visually. This indicates again that the TB parametrizations across the periodic table which are obtained in Sec. 3 are a robust initialization.

Description of Bulk Structures

The prediction for the energy-volume curves of the considered bulk phases in the fit set and the test set are compared to their DFT reference in Fig. 5.16. It can be seen that in the fit set the energies of the hcp, fcc, A15 and σ phases are well reproduced. The bcc and C15 phase which have higher equilibrium energies were optimized with a very low weight according to Eq. 5.9. Therefore, their description is not good. As shown in Fig. 5.2, a much better description of the bcc phase is possible. However, such an accurate description is not possible with the given model complexity if a robust description of the elastic properties and good transferability to the TCP phases with a low energy has to be preserved. The χ phase which has an equilibrium energy which is close to the one of the fcc phase is well reproduced. The energies of the other phases in the fit set are slightly overestimated, but their energy differences are also well reproduced.

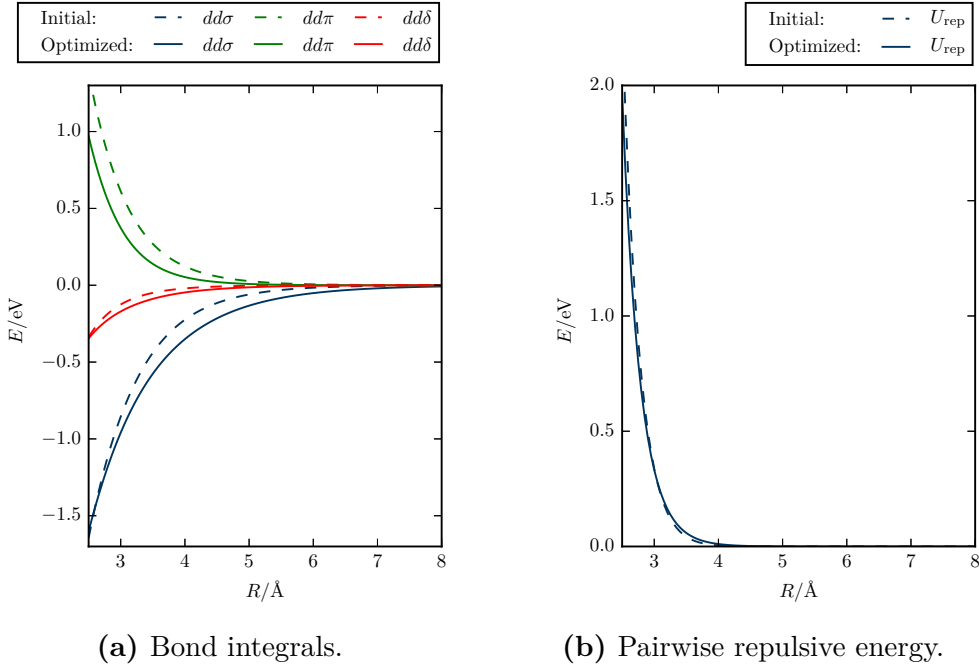


Figure 5.15.: Comparison of the bond integrals and the pairwise repulsive energy of the initial model and the Pareto-optimal model.

Description of Random Structures and Transformation Paths

The transferability to the 1-atom random structures is analysed in Fig. 5.17. In Fig. 5.17a, the RMS error is plotted in the map of local atomic environments, which also shows the tetragonal, trigonal, hexagonal and orthorhombic transformation paths. The region around hcp, fcc and bcc is magnified in Fig. 5.17b. The RMS error has a smooth behaviour in the map of local atomic environments and shows a clear minimum towards the hcp structure. The transferability is worse at the right of the filled region of the map where open atomic environments are located. However, the model still captures the qualitative trend of the equilibrium energy from the left to the right of the filled region in the map, as can be seen by a comparison of the model's prediction in Fig. 5.17c to the DFT reference in Fig. 5.5c.

The predictions of the model for the energies of the tetragonal, trigonal, hexagonal and orthorhombic transformation paths are compared to the DFT reference in Fig. 5.18. The predictions of the model qualitatively agree with the DFT reference for the tetragonal transformation path (Fig. 5.18a). A decrease of the transferability of the model during the deformation of fcc to bcc is already expected from Fig. 5.16 and is in agreement with the decrease of transferability of the random structures which lie close to this transformation in the map of local atomic environments (cf. Fig. 5.17b). The transferability is better for the other direction of the tetragonal transformation path, where fcc is transformed to the special bct structure. The difference of the predic-

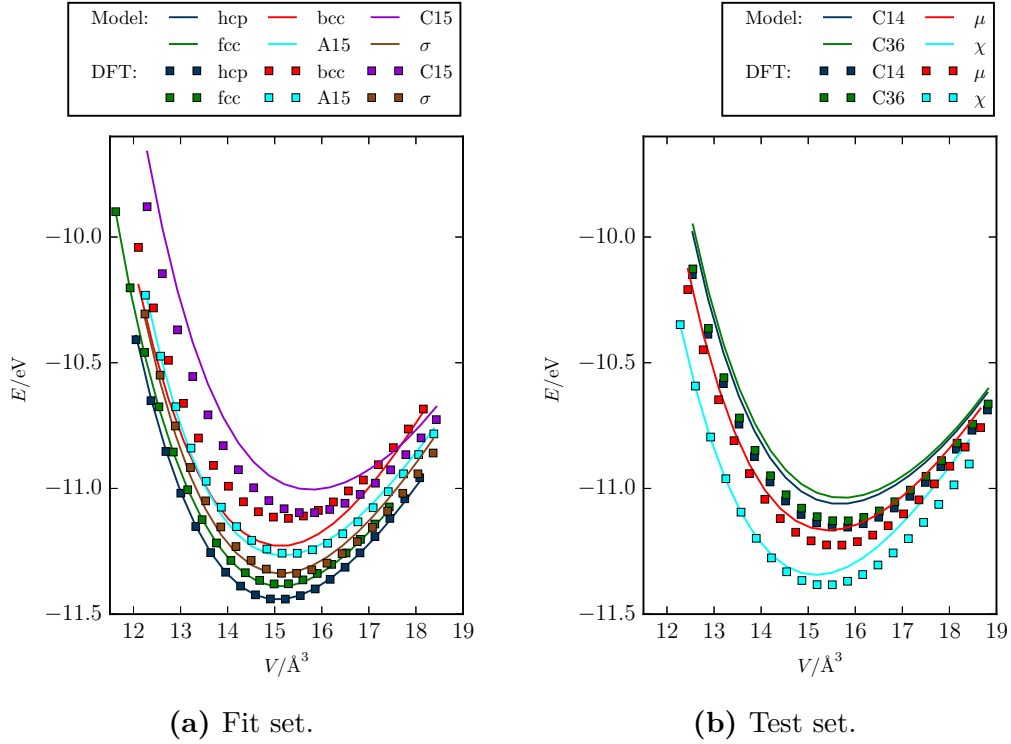
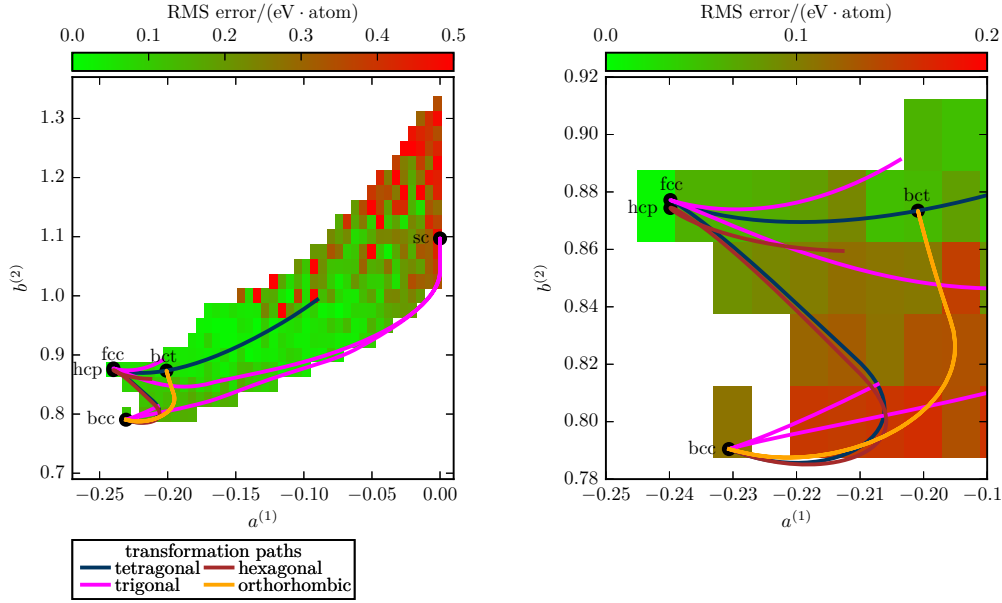


Figure 5.16.: Performance of Pareto-optimal analytic BOP on the bulk structures in the fit set and the test set.

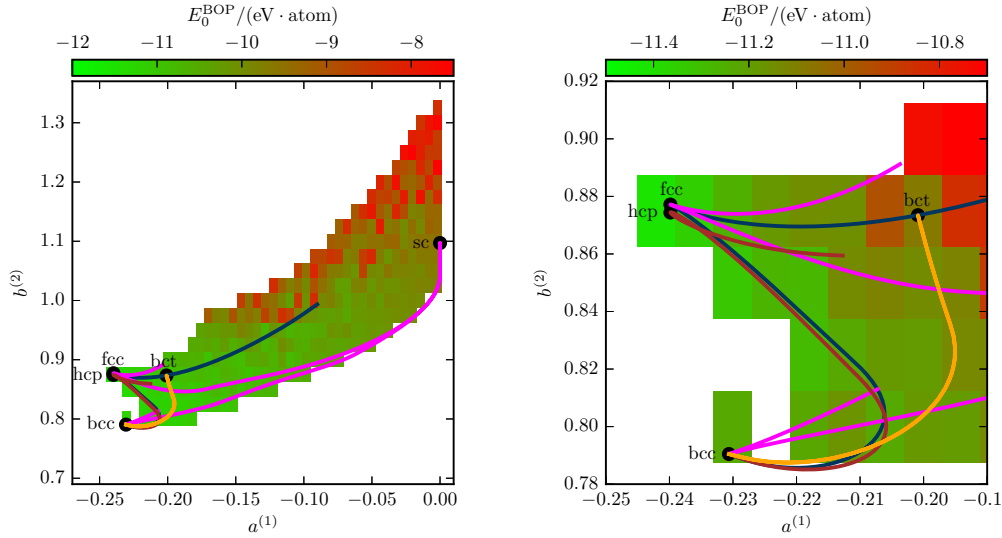
tion of the model to the DFT reference remains almost constant for a broad range of total energies. Again this is in agreement with the behaviour of the random structures which are located close to this part of the transformation path in the map of local atomic environments (cf. Fig. 5.17a). Similarly, the energies of the trigonal transformation path are qualitatively reproduced (Fig. 5.18b) and a significant overestimation of the total energy for the sc phase can be observed. Consistently, the RMS errors in the energies of the random structures which are close to the sc phase in the map of local atomic environments are also high. The energies for a continuation of the trigonal transformation path from the fcc phase are well reproduced by the model. As shown by the map, similar structures are created for the tetragonal deformation of fcc to bcc and the hexagonal deformation of hcp to fcc. Therefore, the energies of these deformations are also similar (Fig. 5.18c). The energies for the deformation of hcp in the other direction of the path agree well with the DFT reference. This is similar to the results for trigonal transformation path. The qualitative form of the energy profile of the orthorhombic transformation path is not reproduced by the model (cf. Fig. 5.18d) but also not relevant for the hcp-structure of Re. As also shown by the magnified part of the map of local atomic environments, the agreement of the energies of structures which are located close to bct is better than for structures which are located close

to bcc.



(a) RMS error in the energies of 1-atom random structures.

(b) Magnified region around hcp, fcc and bcc of Fig. a.



(c) Equilibrium energy of 1-atom random structures.

(d) Magnified region around hcp, fcc and bcc of Fig. c.

Figure 5.17.: Performance of the Pareto-optimal analytic BOP on the energies of a homogeneous sampling of 1-atom random structures in the map of local atomic environments.

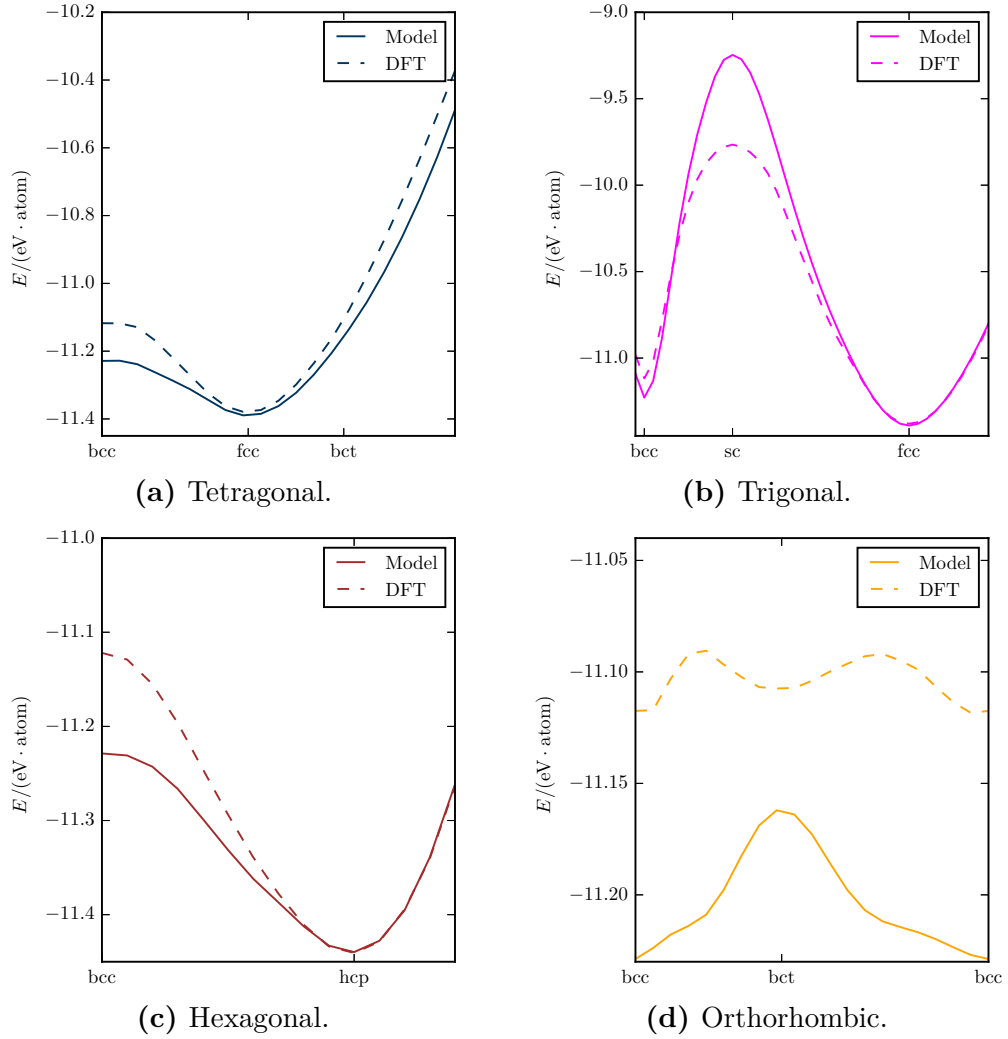


Figure 5.18.: Performance of the Pareto-optimal analytic BOP on the energies of the tetragonal, trigonal, hexagonal and orthorhombic transformation paths.

Description of Defects, Elastic Constants and Phonons

In Tab. 5.2, the predictions of the elastic constants, the energies for the SFs, properties of the ground state phase hcp and the formation energies of point defects are compared to the DFT reference.

The formation energies of the point defects are all overestimated, but the ordering of the energies is well reproduced except for a different ordering for the basal split dumbbell and basal tetrahedral SIAs, which both have a high formation energy.

The formation energies of the intrinsic and extrinsic SF are underestimated by the model but are still of the correct order. The basal intrinsic SF energy is related to the energy difference of hcp and dhcp. Still, the model predicts

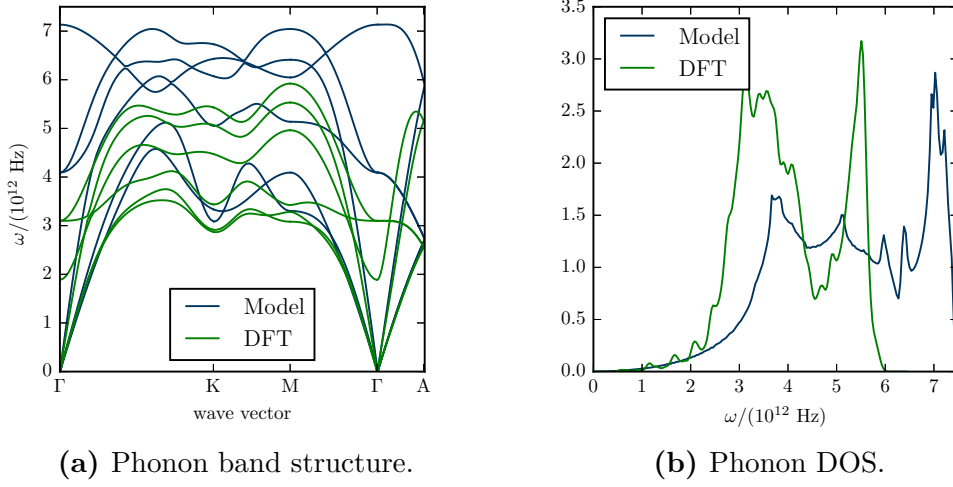


Figure 5.19.: Comparison of the predictions of the Pareto-optimal analytic BOP for the phonon band structure and phonon DOS to the DFT reference.

a value of -4.80 meV which is however higher than the DFT reference of -1.76 meV.

The values of the elastic constants C_{11} , C_{13} , C_{44} and C_{66} are well reproduced, however, the values of C_{12} and C_{33} are not accurate. This is again related to the limited model complexity and the requirement of a robust description of the other phases. It can be seen in Fig. 5.13d that much better elastic constants can be obtained with higher values of a_{ela} . As the c/a -ratio is related to the elastic deformation C_{33} , the model does not predict it correctly. The phonon spectra and the phonon DOS from the model and the DFT reference are compared in Fig. 5.19. The predictions of the model are in good agreement with the DFT reference for low frequencies as the slope of the acoustical phonon branches are similar close to the Γ -point. The agreement is much worse for higher frequencies. The optical phonon branches are not well reproduced and the phonon DOS is shifted to higher frequencies. Not much variation in the quality of the description of the phonons can be observed across all investigated models of Fig. 5.12. Therefore, a better description can probably only be obtained by less approximations to the analytic BOP. For example, an environment-dependent parametrization of the bond integrals or the repulsive energy contribution (Sec. 5.1.2) may improve the description of the phonons. It may also be possible that the s -electrons have to be explicitly described by the analytic BOP formalism.

Elastic constants (GPa)	DFT	Model
C_{11}	625	627
C_{12}	232	303
C_{13}	213	240
C_{33}	677	592
C_{44}	170	142
C_{66}	196	162
Stacking faults (mJ/m ²)	DFT	Model
intrinsic	55	21
extrinsic	349	278
Ground state phase	DFT	Model
c/a -ratio	1.617	1.608
$E_{\text{hcp}}^{(0)} - E_{\text{dhcp}}^{(0)}$ (meV)	-1.76	-4.80
Point defects (eV)	DFT	Model
vacancy	3.22	3.91
vacancy diffusion barrier (basal plane)	2.02	2.02
vacancy diffusion barrier (layer A to B)	1.71	2.17
octahedral interstitial	8.16	9.46
split dumbbell interstitial	6.78	8.96
tetrahedral interstitial	6.76	8.93
basal crowdion interstitial	BT	BT
basal split dumbbell	9.41	10.97
basal tetrahedral	10.17	10.44

Table 5.2.: Comparison of the predictions of the Pareto-optimal analytic BOP for the elastic constants, SF energies, c/a -ratio, hcp-dhcp energy difference and energies of point defects to the DFT reference. The basal crowdion SIA relaxes to the basal tetrahedral (BT) SIA.

5.5. Correlation of Model Predictions

In Sec. 5.4.3, the analytic BOP potential for Re is selected from the Pareto front by a series of tests which the model has to pass. Figure 5.13 shows that the test quantities often have trends with respect to the RMS errors in the energies of the elastic deformations and of the bulk structures. This indicates that the different test quantities are correlated for the employed fit set and functional form of the model. In Fig. 5.20, the Spearman's rank correlation coefficients ρ_S of the absolute values of all test quantities are evaluated for the different analytic BOPs with $n_{\text{max}} = 9$. A statistically significant correlation exists for the majority of pairs of test quantities. Test quantities which have a positive correlation coefficient can be improved at the same time. However, a negative correlation coefficient shows that an improvement of one test quantity corresponds to a compromise of the other test quantity. This shows

that the selected analytic BOP potential for Re cannot be optimal in all test quantities at the same time. The test quantities with the largest and smallest

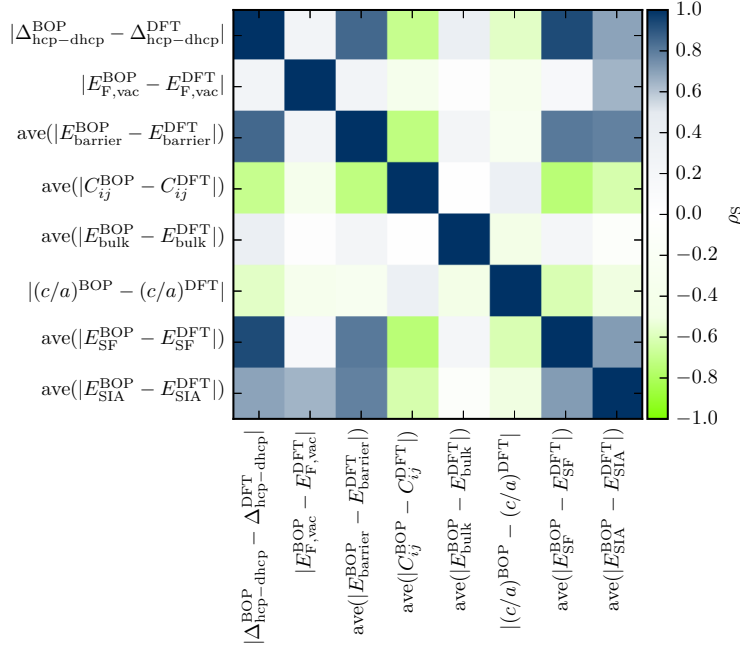
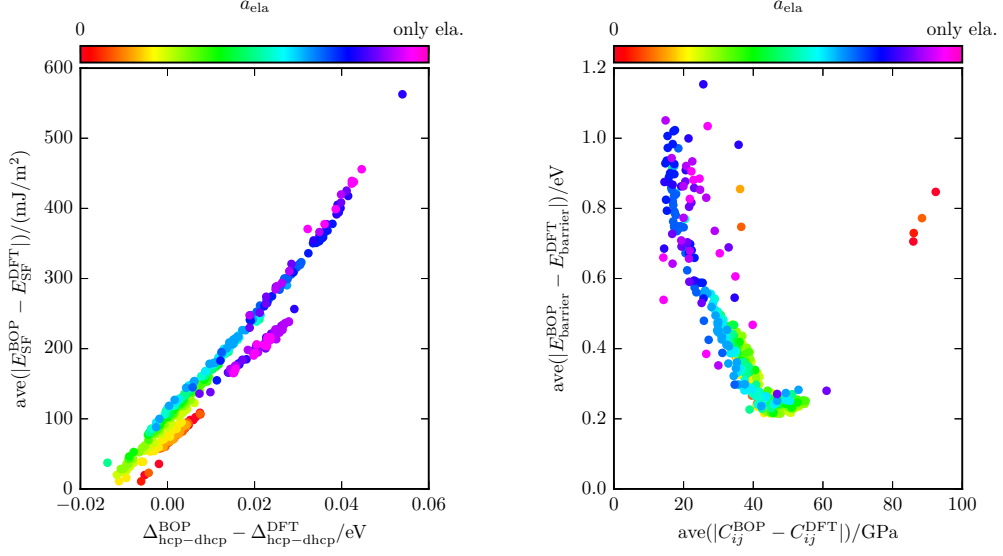


Figure 5.20.: Spearman's rank correlation coefficient ρ_S of the absolute values of the considered test quantities of the analytic BOPs of Fig. 5.12.

Spearman's rank correlation coefficient for their absolute values are plotted in Fig. 5.21. The points are coloured according to the value for a_{ela} . The Spearman's rank correlation coefficient is largest for the average error in the SF formation energies and the absolute value of the error in the energy difference of the hcp and dhcp structures at their equilibrium volume. This is in agreement with the fact that the ideal basal intrinsic SF has a local dhcp environment. The smallest negative Spearman's rank correlation coefficient is obtained for the average error in the elastic constants and the average error in the two considered energy barriers for the vacancy diffusion. The atomic environments of the elastic deformations are not related to the local atomic environments along the diffusion channel. Therefore, a large fraction of this correlation is caused by the change of the model parameters due to the different value of a_{ela} . It may be a surprise that the average absolute errors in the elastic constants and the bulk structures do not have a large value for the Spearman's rank correlation coefficient, even though these two quantities are related to the two cost functions for which the Pareto front was estimated. This is resolved by Figs. 5.13d, 5.13f, which show that the error in the elastic constants remains moderate in a regime with high errors in the energies of the elastic deformations and the c/a -ratio.



(a) Average absolute error in SF formation energies versus error in the hcp-dhcp energy difference at equilibrium volume.

(b) Average absolute error in vacancy diffusion barriers versus average absolute error in elastic constants.

Figure 5.21.: Individual errors in the two different test quantities with the largest positive and smallest negative value of ρ_S in Fig. 5.20.

5.6. Influence of Model Complexity

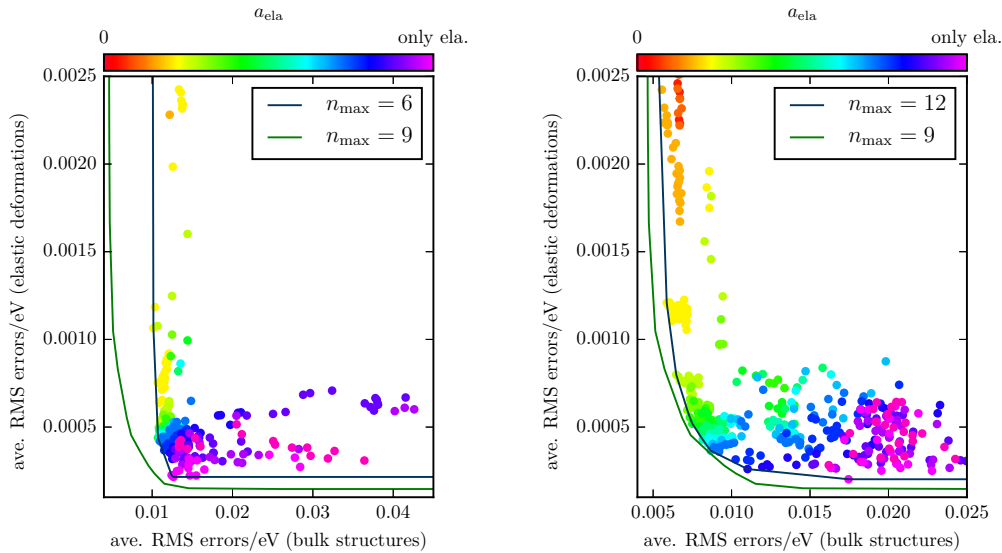
The results of Secs. 5.4, 5.5 show that the analytic BOPs with the used model complexity of nine exactly calculated moments with a very simple description of the pair repulsion (Eq. 5.8) and the approximation of an environment-independent atomic interaction can describe many quantities accurately but often compromises have to be made in order to describe different regimes at the same time. As discussed in Sec. 5.2.1, nine exactly calculated moments ($n_{\max} = 9$) have been found to be a good compromise between efficiency and accuracy. Therefore, this value was used to parametrize the Pareto-optimal analytic BOP for Re. It is straightforward to increase the model complexity by increasing the number of moments and depending on the application, the computational effort for a higher number of moments may be possible. A smaller number of moments may be attractive for computationally expensive calculations. Therefore, further initial models are parametrized with the parametrization protocol of Fig. 5.1 to investigate how accurate a parametrization with a smaller number of moments is and if it is worthwhile to increase the number of exactly calculated moments. Following the procedure of Sec. 5.4.3, systematic samplings of a_{ela} are obtained for $n_{\max} = 6$ and $n_{\max} = 12$ in Fig. 5.22.

The estimated Pareto front with $n_{\max} = 6$ is clearly at larger values of the

RMS error than that of $n_{\max} = 9$. Especially, the RMS error in the energies of the bulk structures is much higher. Therefore, none of the models with $n_{\max} = 6$ pass all tests of Fig. 5.14.

The estimated Pareto front for $n_{\max} = 12$ is close to that of $n_{\max} = 9$. However, the corresponding points of the RMS errors are all above the estimated Pareto front obtained for $n_{\max} = 9$. It may come as a surprise that a more complex form for the analytic BOPs does not necessarily lead to an increase in accuracy. However, many physical quantities do not converge at $n_{\max} = 12$ but still oscillate with respect to the number of exactly calculated moments [98, 121]. It is therefore possible that also the Pareto front oscillates with respect to n_{\max} . None of the models with $n_{\max} = 12$ pass all tests of Fig. 5.14, which shows that it is not beneficial to increase this part of the model complexity by using twelve exactly calculated moments.

The results indicate that a more transferable analytic BOP for Re cannot simply be obtained by increasing the number of exactly calculated moments to $n_{\max} = 12$. Significant improvement may be obtained by an environment-dependent description of the interatomic interaction or by an explicit treatment of the s -electrons, which have been replaced by the computationally effective embedding term (Eq. 2.224). It may also be possible that these approaches have to be conducted at the same time and that a higher number of exactly calculated moments may lead to a further improvement if the model complexity has been increased in an alternative way.



(a) RMS errors for models with $n_{\max} = 6$.

(b) RMS errors for models with $n_{\max} = 12$.

Figure 5.22.: Comparison of the estimated Pareto front obtained in Fig. 5.12 for an analytic BOP with nine exactly calculated moments ($n_{\max} = 9$) to those for six and twelve exactly calculated moments.

Conclusion

A computationally more effective description of the interatomic interaction than density-functional theory (DFT) is needed for simulations of large composition ranges and of representations of a material of more than a few hundred atoms. This is provided by analytic bond-order potentials (BOPs), which are obtained by a moments expansion from the tight-binding (TB) theory, which can be derived from DFT by a second-order approximation. However, analytic BOPs require a pairwise parametrization of the interatomic interaction, which has been found to be very time-consuming and which was conducted only for a few combinations of elements. This parametrization process is facilitated in this work to allow for a fast parametrization of accurate and transferable analytic BOPs. For this purpose, TB parametrizations across the periodic table and a map of local atomic environments are developed, which are both used in an automated parametrization strategy.

Non-orthogonal and orthogonal TB parametrizations for almost all combinations of elements from periods 1 to 6 and groups 3 to 18 of the periodic table are obtained by optimizing the projection of the DFT wave function for dimers in the Harris-Foulkes approximation onto a TB minimal basis. All 48048 inequivalent matrix elements are parametrized by a flexible functional form. The number of required parameters depends on the considered range of interatomic distances. The flexible functional form facilitates a further optimization of the TB matrix elements to reference data and shows systematic trends of the parameters across the periodic table. This validates the robustness of the parametrizations and allows for insight into the chemical diversity of interatomic interactions. The parametrizations are used to test TB parametrizations which assume specific trends across the periodic table and are compared to TB parametrizations obtained by other methods.

Moments-descriptors based on the local electronic density of states (DOS) are introduced, which describe the local atomic environment and determine the bond chemistry. The two lowest structure-dependent moments of the electronic DOS as obtained from canonical *sp*- and *d*-valent TB models are used to span a 2-D map of local atomic environments. The map of local atomic environments is used for the discussion of crystal structures. It is shown that structures with one or two atoms in the primitive cell are bound to specific regions of the map. By making use of the analytic BOP expansion, it is argued that the lowest energy structure for a specific material should be found

close to the boundaries of these regions. It is further shown that the energy difference between two structures depends on the distance between the structures in the map. This is numerically validated by extensive TB and DFT calculations. The intuitive insight into the space of local atomic environments and the bond chemistry is particularly useful to assess and optimize the transferability of local atomic environments.

This is employed in an optimization of analytic BOPs to DFT reference data, which is initialized by the TB parametrizations across the periodic table. In an automated parametrization strategy for *sd*-valent systems, the accuracy of analytic BOPs with respect to DFT reference data is optimized by minimizing a cost function with a local optimization algorithm. The TB parameters from the parametrizations across the periodic table are extended by a simple pair repulsion and the computational efficiency is increased by replacing the long ranged *s* orbitals by an embedding term. It is shown that the transferability of analytic BOPs can be systematically optimized by using reference data from a homogeneous sampling in the map of local atomic environments. Furthermore, a new analytic BOP for Re is parametrized, which requires the exact calculation of the first nine moments. The relevant reference data is rationalized with the map of local atomic environments. The automated parametrization strategy for *sd*-valent systems is applied to optimize the analytic BOP with respect to DFT reference data. The trade-off between the accuracy in the description of the elastic deformations of the ground state phases hcp and the transferability to other phases is controlled by a weight parameter. The variation of this parameter allows one to map out a Pareto. A Pareto-optimal analytic BOP for Re is selected by a combination of several tests for the transferability of the potential. It is further shown that a smaller number of exactly calculated moments is not sufficient to achieve the desired accuracy and a larger number of moments does not improve the accuracy further.

The results suggest that the automated parametrization strategy can be applied to parametrize analytic BOPs or TB models for all *sd*-valent systems. The TB parametrizations across the periodic table may be used together with the map of local atomic environments based on the canonical *sp*-valent TB model for the parametrization of *sp*-valent systems. Only small modifications of the automated parametrization protocol are necessary as an explicit treatment of the *s*-electrons may be required.

Outlook

The proposed automated parametrization strategy can be used to parametrize further analytic bond-order potential (BOP) models and parametrizations based on the proposed initialization will be published by other authors for the Ni-W-Re system to simulate Ni-base superalloys and for the W-Re-Os system to simulate plasma-facing materials for fusion applications (Ref. 172) as well as for the Ti-Ta system to simulate shape memory alloys (Ref. 224). An important continuation of this work is a high-throughput parametrization framework of analytic BOPs for all combinations of transition metals. Moreover, the developed parametrization strategy for *sd*-valent elements may be adapted to parametrize *sp*-valent elements and systems which consist of both *sp*- and *sd*-valent elements such that a high-throughput parametrizations across the periodic would become possible.

Another option to make use of the tight-binding (TB) parametrizations across the periodic table is to interpolate the trends of the model parameters with respect to the period number and group number to develop a qualitative multi-component TB model. This model could be further improved by extracting systematic scaling behaviours of the optimized TB matrix elements to reference data for bulk structures.

An alternative strategy to predict physical quantities from reference data is to replace a physical model like the analytic BOPs by statistical machine-learning methods. However, for an efficient use of these methods, descriptors have to be generated which encode the most important quantities of the underlying system. For this, the TB parametrizations across the periodic table and the map of local atomic environments can be applied. The obtained interatomic TB parameters provide a description of the chemical bonds, which may be used to derive chemistry informed descriptors for the interatomic interaction. The moments-descriptors used in the map of local atomic environments have been shown to capture a large fraction of the cohesive energy of the model and to provide a measure for the similarity of atomic environments. Therefore, the map of local atomic environments has been used in Ref. 194 to predict the cohesive energy by a supervised machine-learning method. In Ref. 225, the map was used to cluster the atomic environments in potential transparent conductors by an unsupervised machine-learning method and then the moments-descriptors have been used among others to construct features for a supervised prediction of the formation energy and band gap.

Moreover, the map may also be used to classify the individual atoms in atomistic simulations like, e.g., molecular-dynamics simulations, where typically a very large number of atom hinders manual analysis and requires tools for automated identification of processes like nucleation, phase transformation or dislocation movement.

Appendices

A

Trends of Homoatomic Dimers

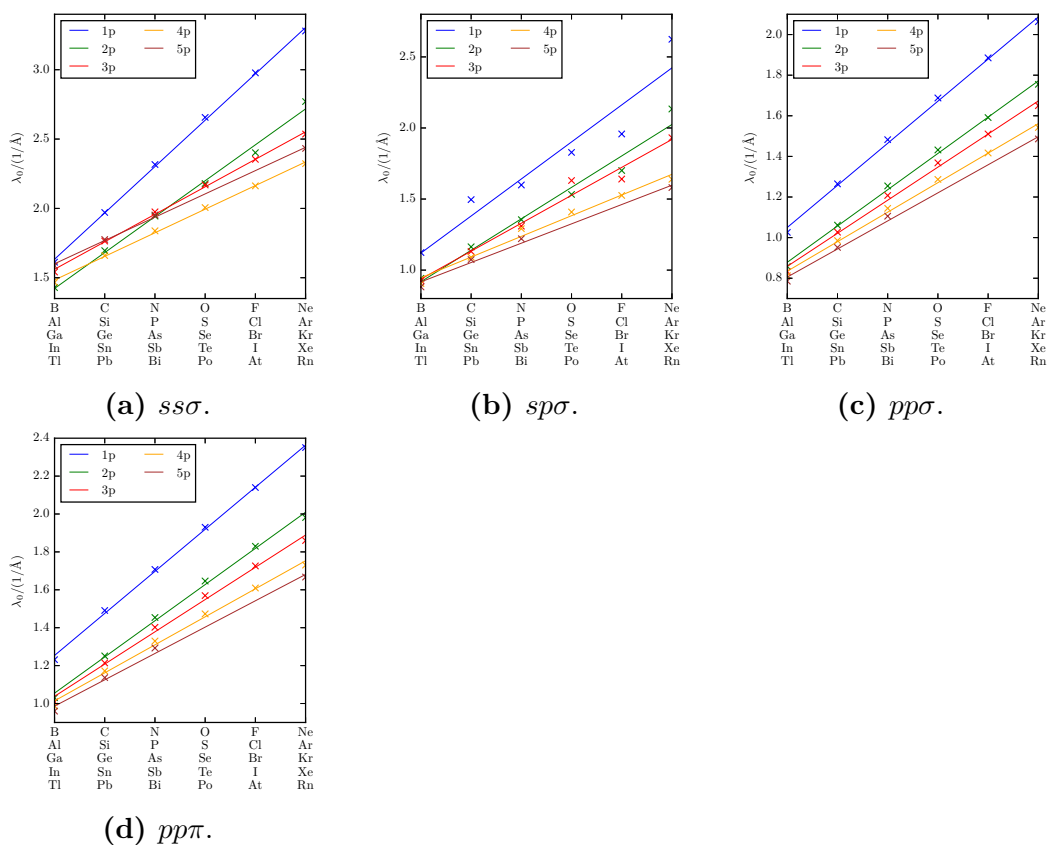


Figure A.1.: Trend of the decay parameter λ_0 of the interatomic matrix elements of H^{orth} across different periods of the sp -valent homoatomic dimers.

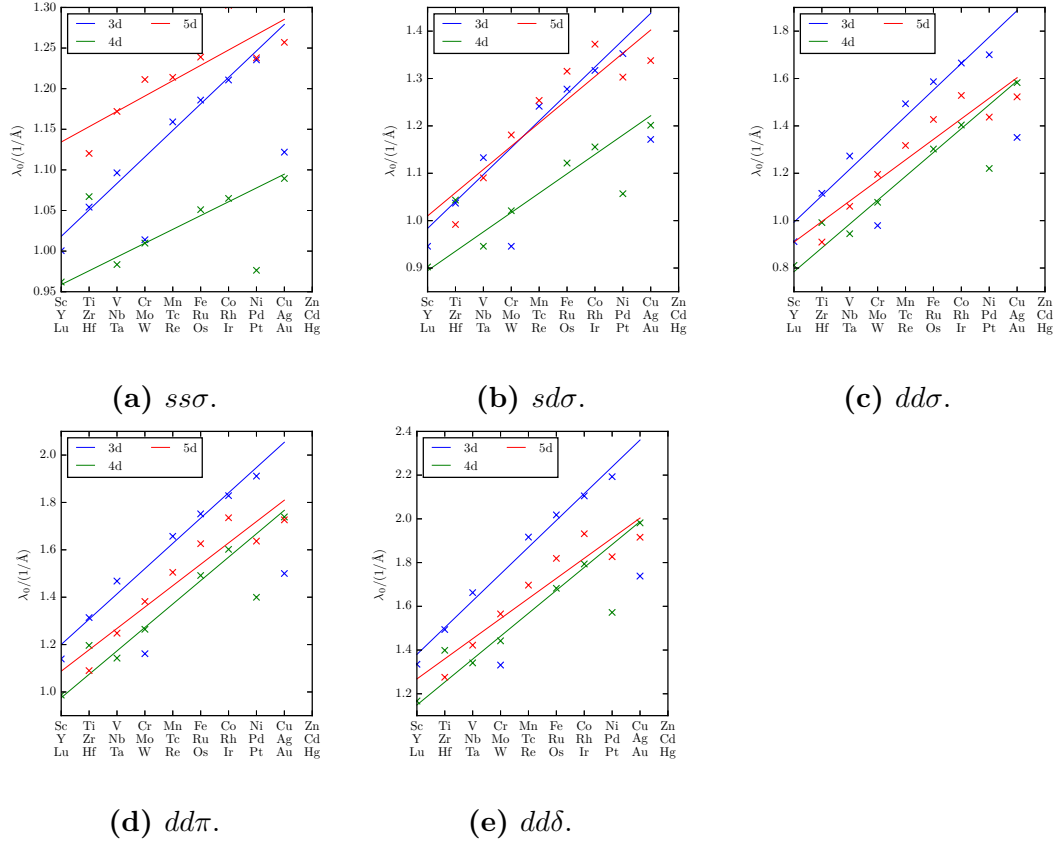


Figure A.2.: Trend of the decay parameter λ_0 of the interatomic matrix elements of H^{orth} across different periods of the sd -valent homoatomic dimers.

B

Trends of Heteroatomic Dimers

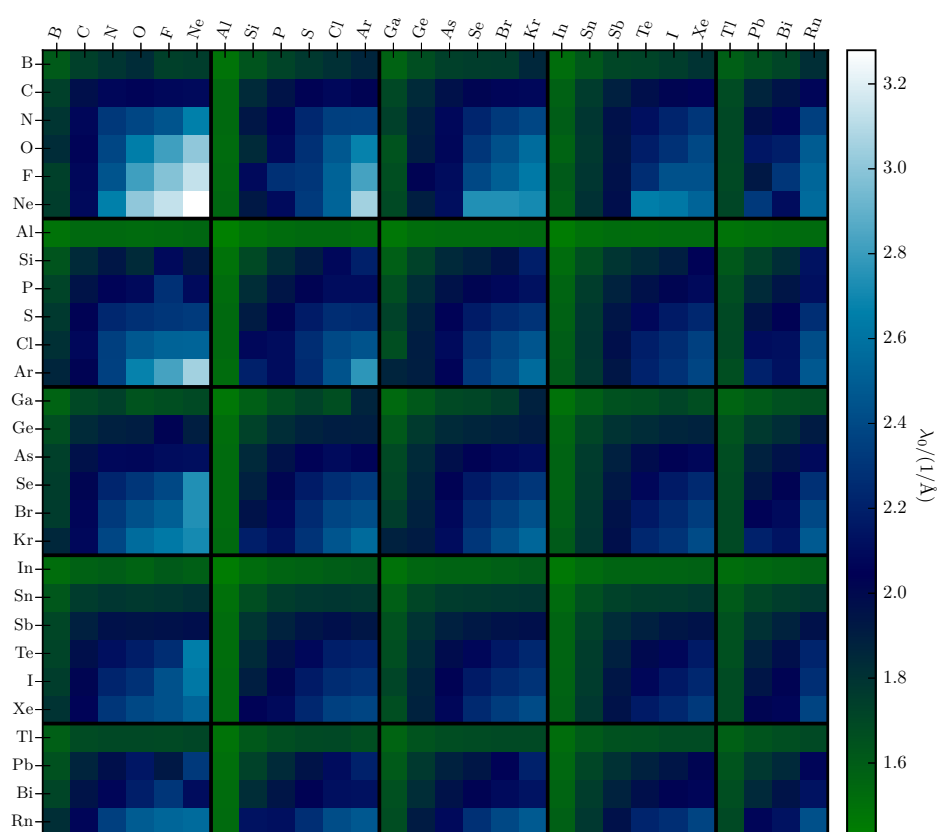


Figure B.1.: Trend of the decay parameter λ_0 of the interatomic matrix elements of $ss\sigma$ of H^{orth} of the heteroatomic sp -valent dimers.

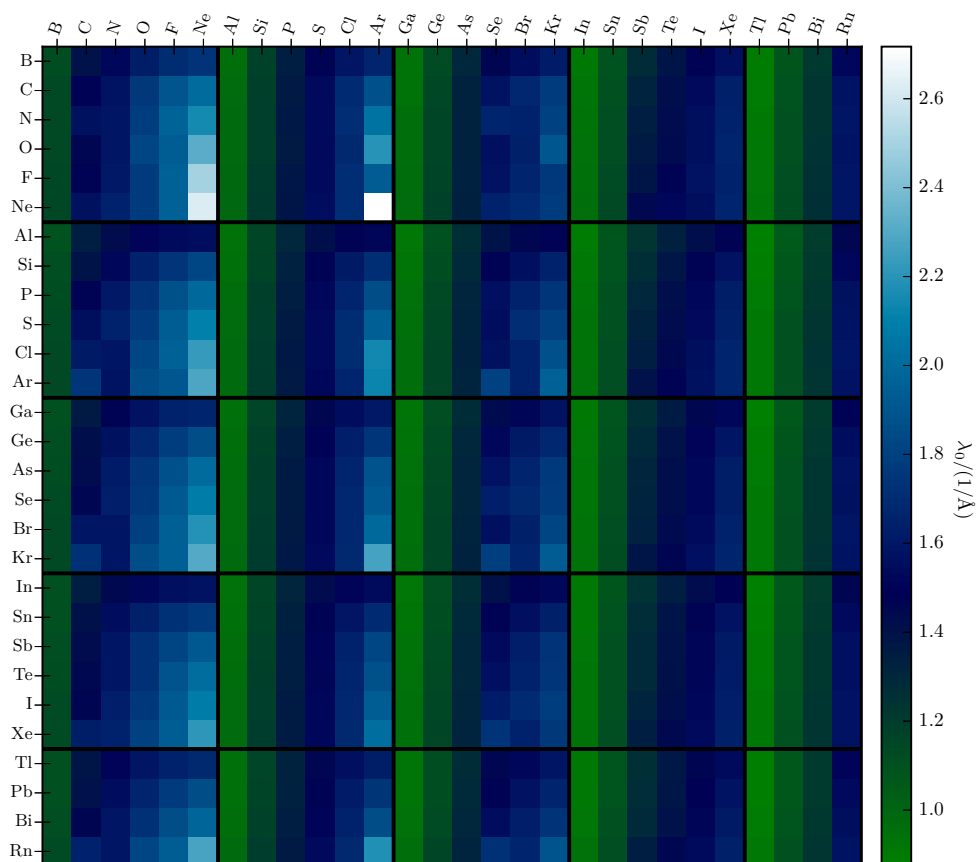


Figure B.2.: Trend of the decay parameter λ_0 of the interatomic matrix elements of $sp\sigma$ of H^{orth} of the heteroatomic sp -valent dimers. First element (contributing the s -orbital) is specified by the row, second element (contributing the d -orbital) by the column.

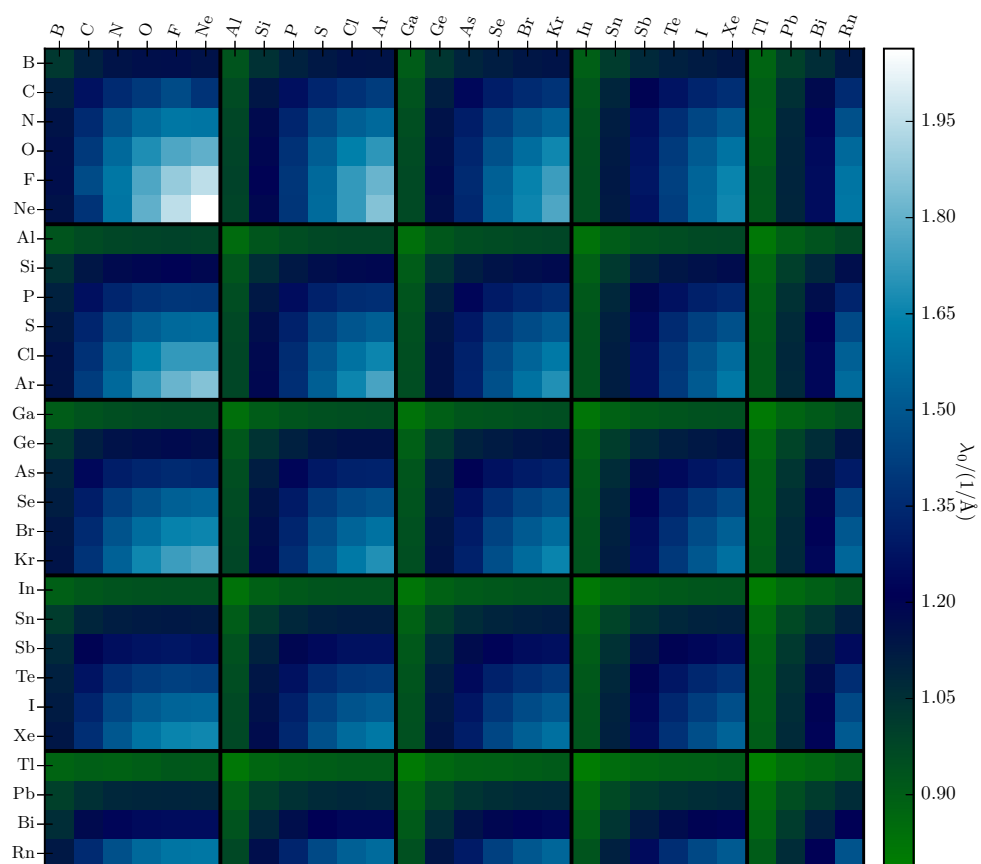


Figure B.3.: Trend of the decay parameter λ_0 of the interatomic matrix elements of $pp\sigma$ of H^{orth} of the heteroatomic sp -valent dimers.

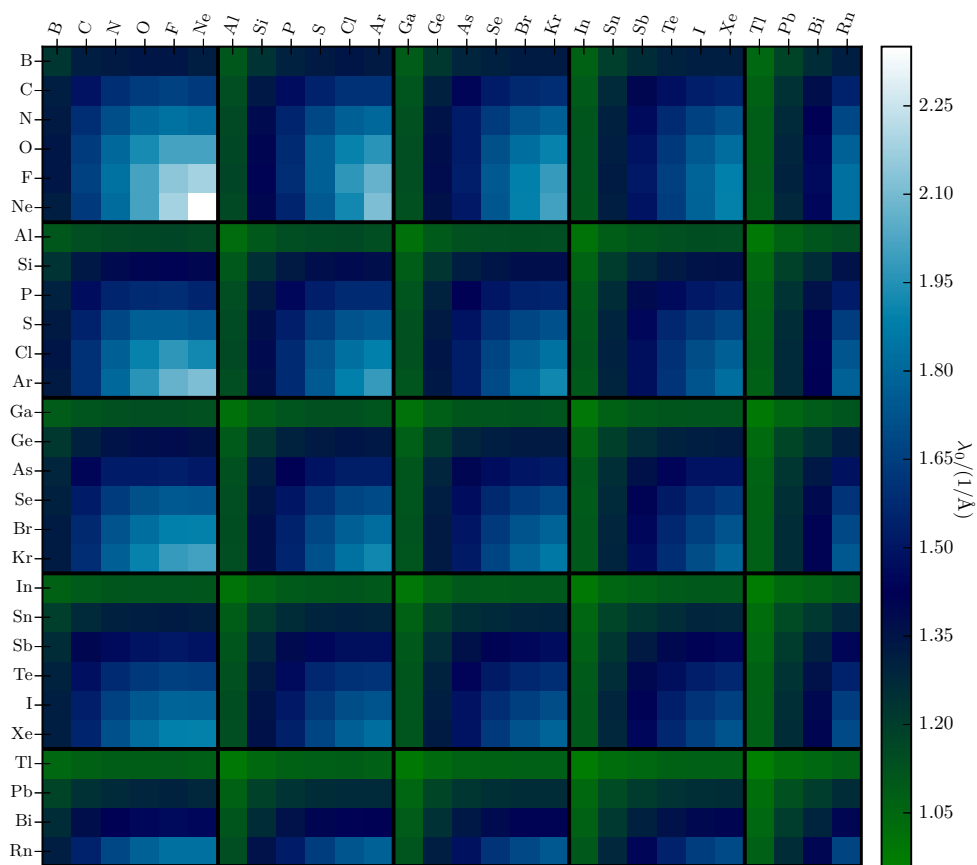


Figure B.4.: Trend of the decay parameter λ_0 of the interatomic matrix elements of $pp\pi$ of H^{orth} of the heteroatomic sp -valent dimers.

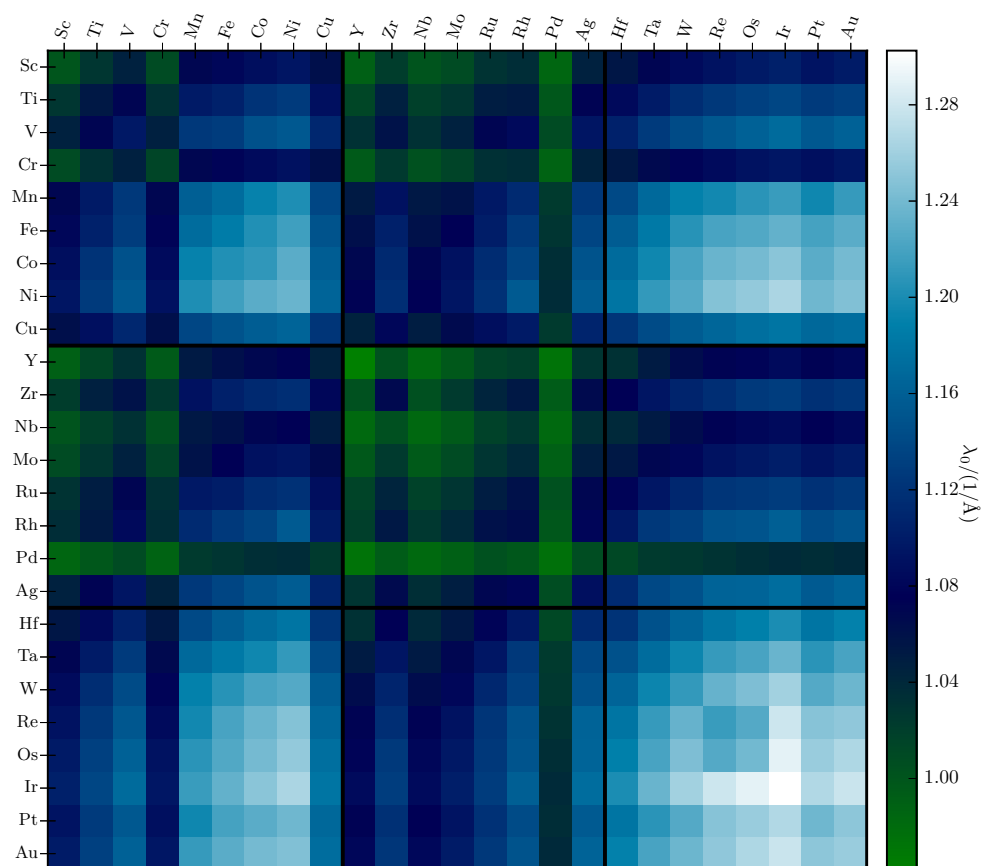


Figure B.5.: Trend of the decay parameter λ_0 of the interatomic matrix elements of $ss\sigma$ of H^{orth} of the heteroatomic sd -valent dimers.

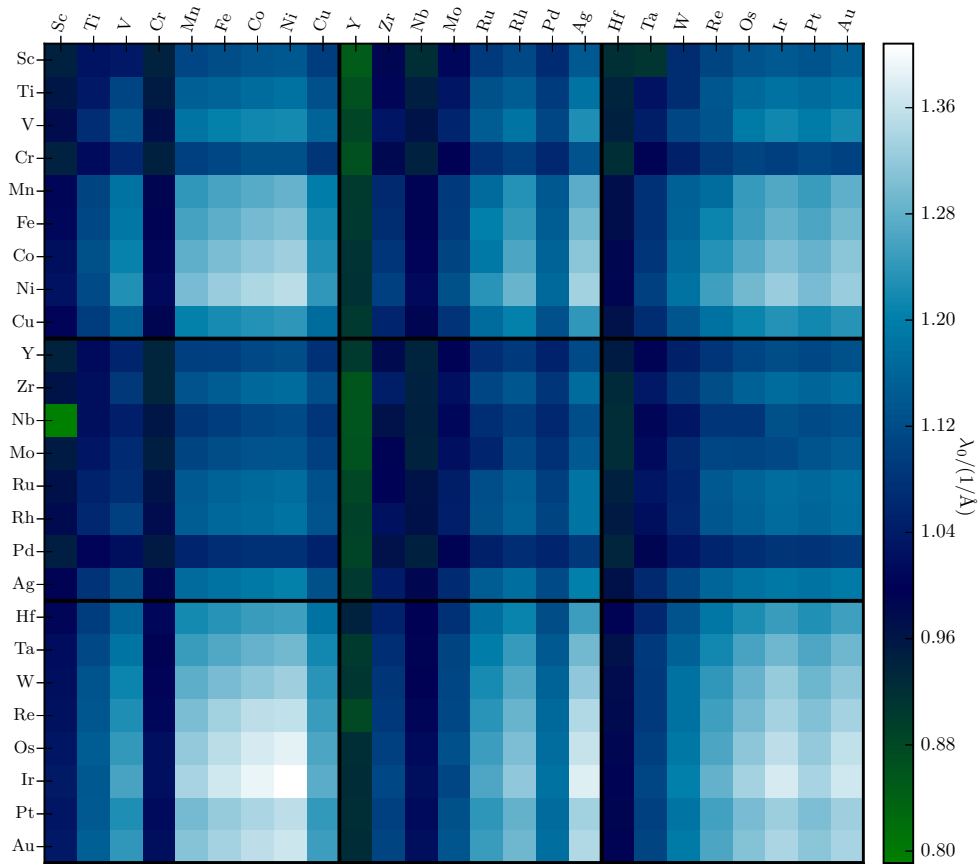


Figure B.6.: Trend of the decay parameter λ_0 of the interatomic matrix elements of $sd\sigma$ of H^{orth} of the heteroatomic sd -valent dimers. First element (contributing the s -orbital) is specified by the row, second element (contributing the d -orbital) by the column.

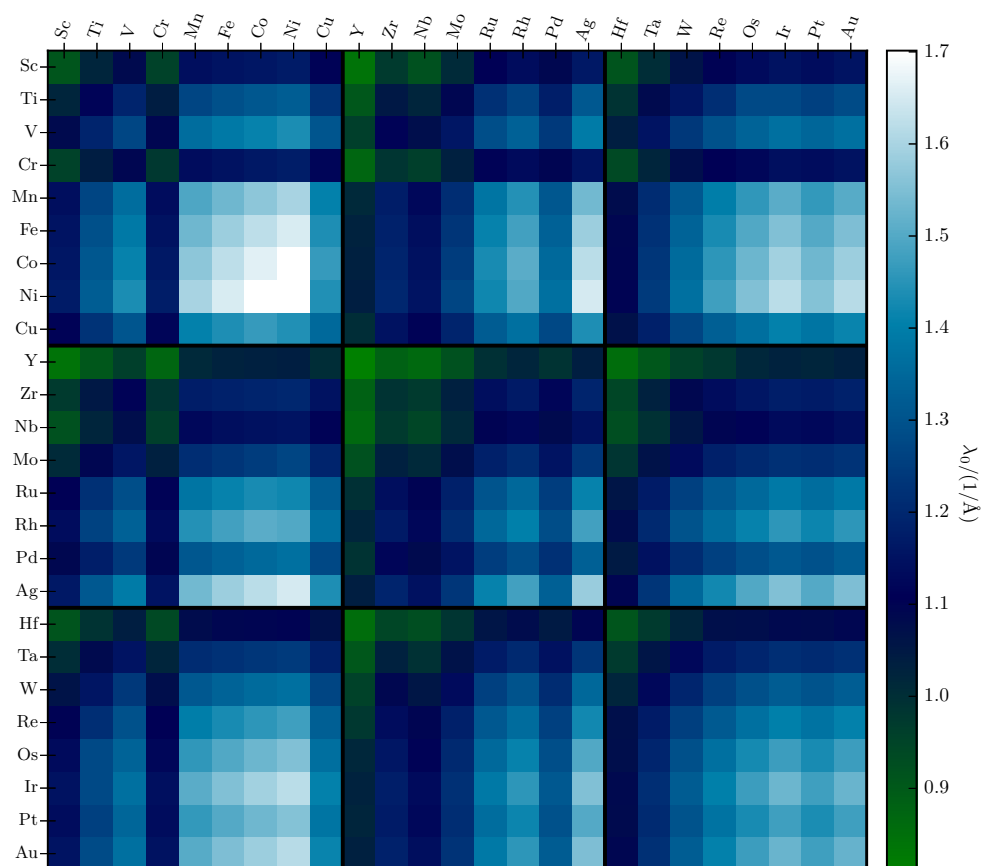


Figure B.7.: Trend of the decay parameter λ_0 of the interatomic matrix elements of $dd\sigma$ of H^{orth} of the heteroatomic dd -valent dimers.

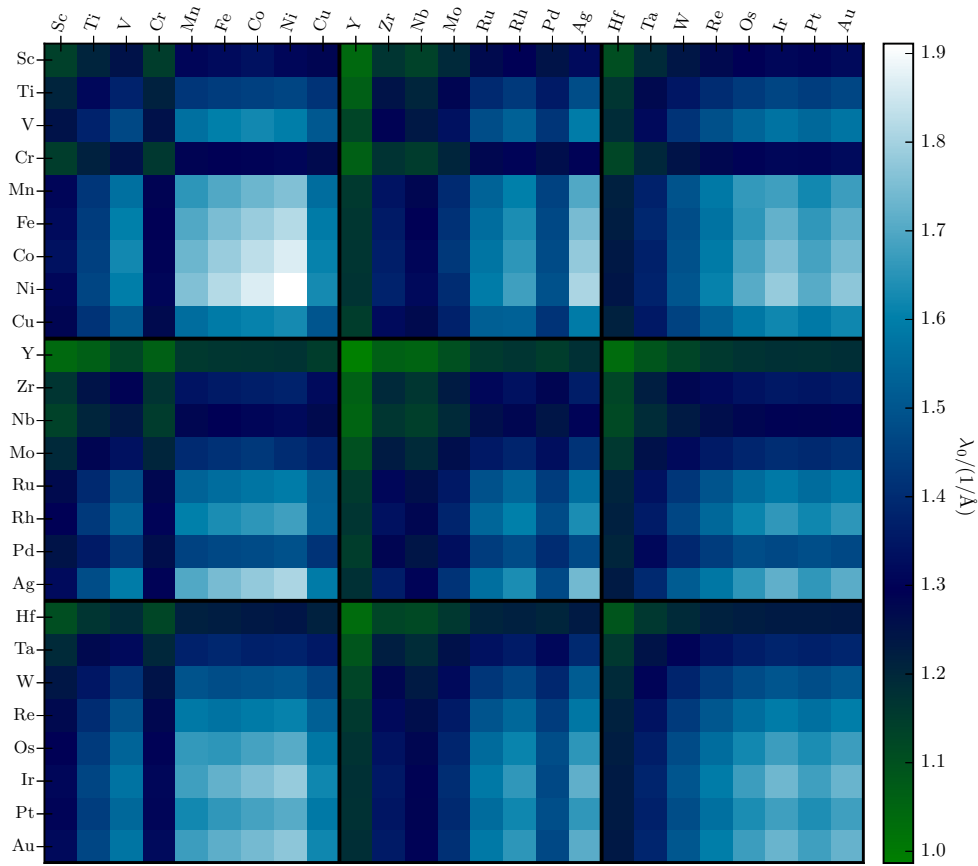


Figure B.8.: Trend of the decay parameter λ_0 of the interatomic matrix elements of $dd\pi$ of H^{orth} of the heteroatomic dd -valent dimers.

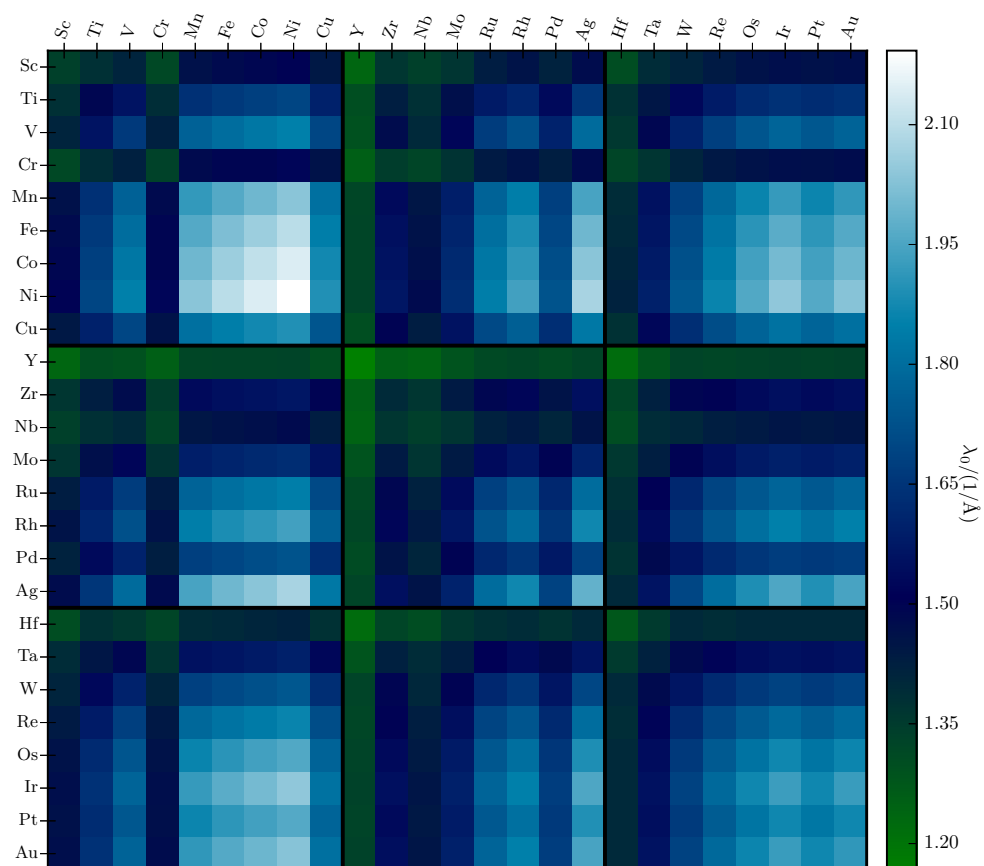


Figure B.9.: Trend of the decay parameter λ_0 of the interatomic matrix elements of $dd\delta$ of H^{orth} of the heteroatomic dd -valent dimers.

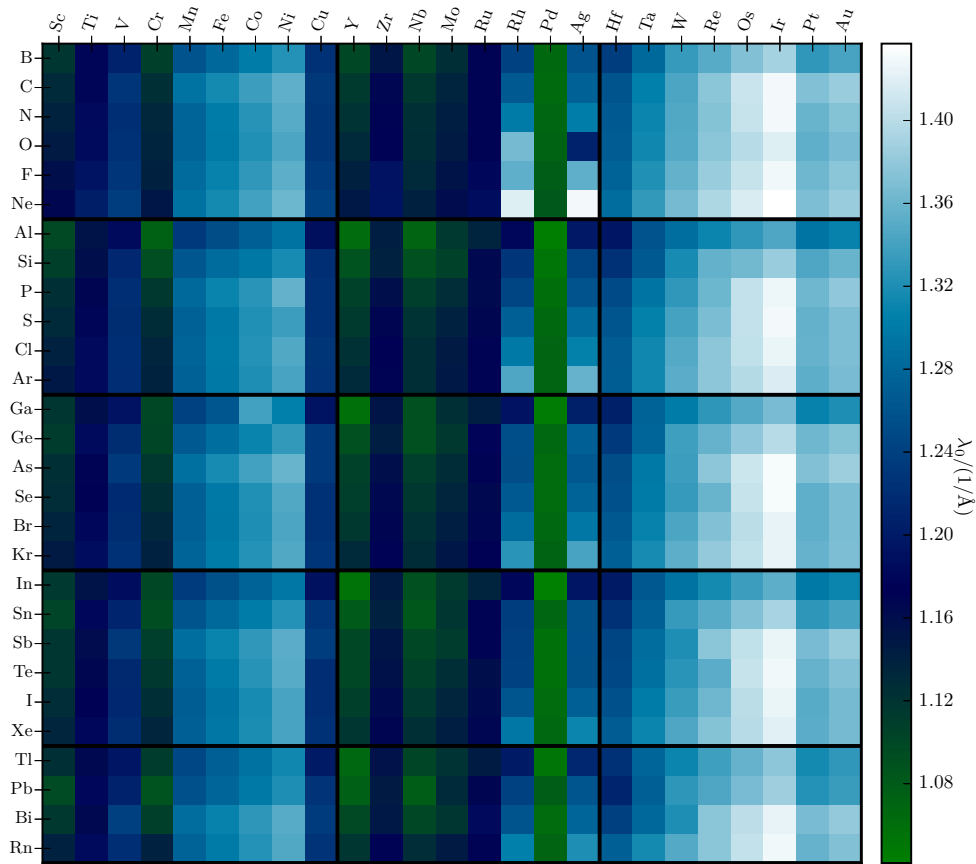


Figure B.10.: Trend of the decay parameter λ_0 of the interatomic matrix elements of $ss\sigma$ of H^{orth} of the heteroatomic dimers consisting of one sp -valent atom (row) and one sd -valent atom (column).

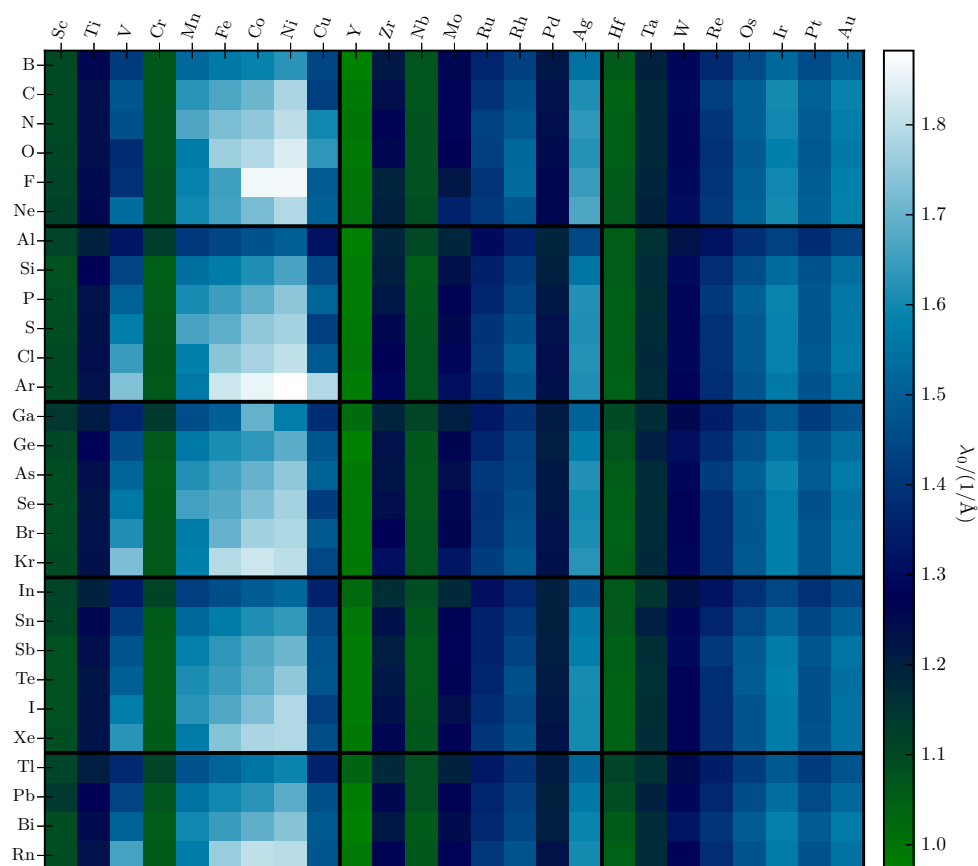


Figure B.11.: Trend of the decay parameter λ_0 of the interatomic matrix elements of $sd\sigma$ of H^{orth} of the heteroatomic dimers consisting of one sp -valent atom (row) and one sd -valent atom (column).

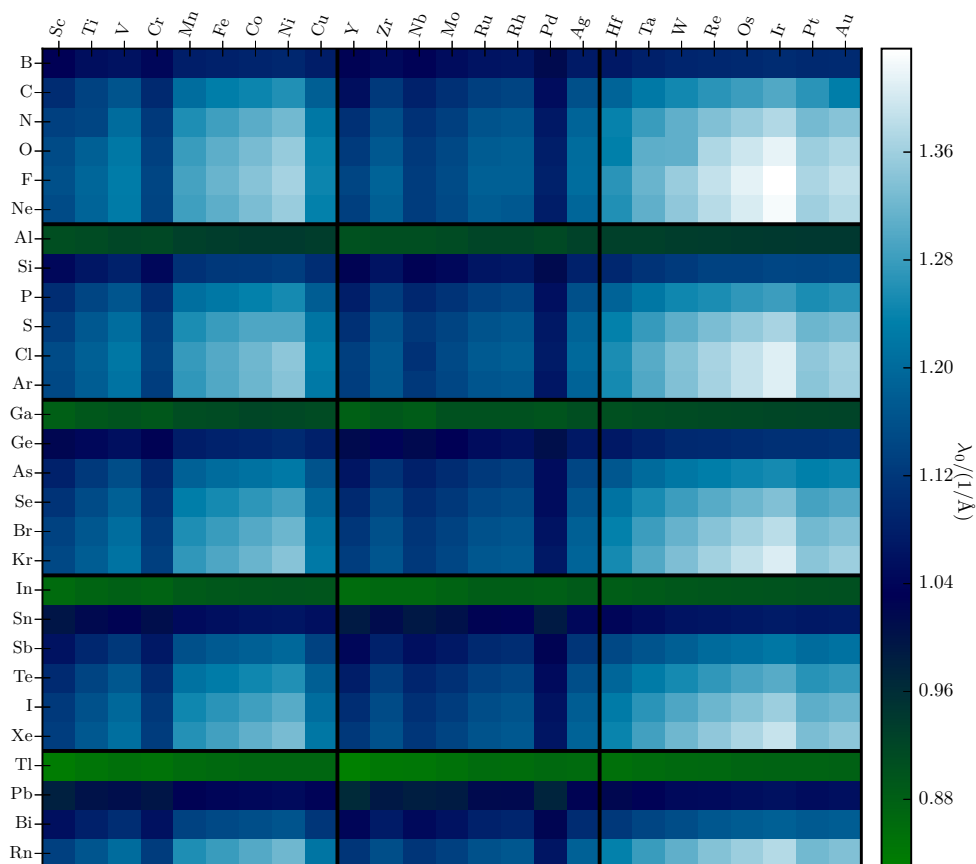


Figure B.12.: Trend of the decay parameter λ_0 of the interatomic matrix elements of $p\sigma$ of H^{orth} of the heteroatomic dimers consisting of one sp -valent atom (row) and one sd -valent atom (column).

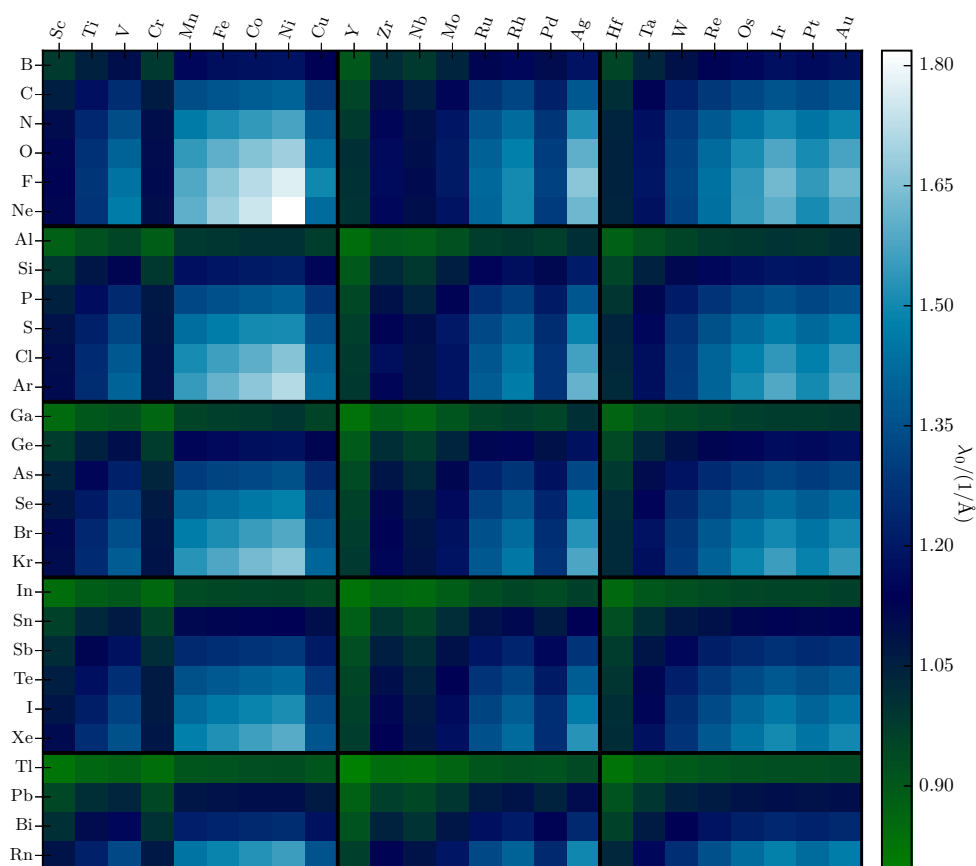


Figure B.13.: Trend of the decay parameter λ_0 of the interatomic matrix elements of $pd\sigma$ of H^{orth} of the heteroatomic dimers consisting of one sp -valent atom (row) and one sd -valent atom (column).

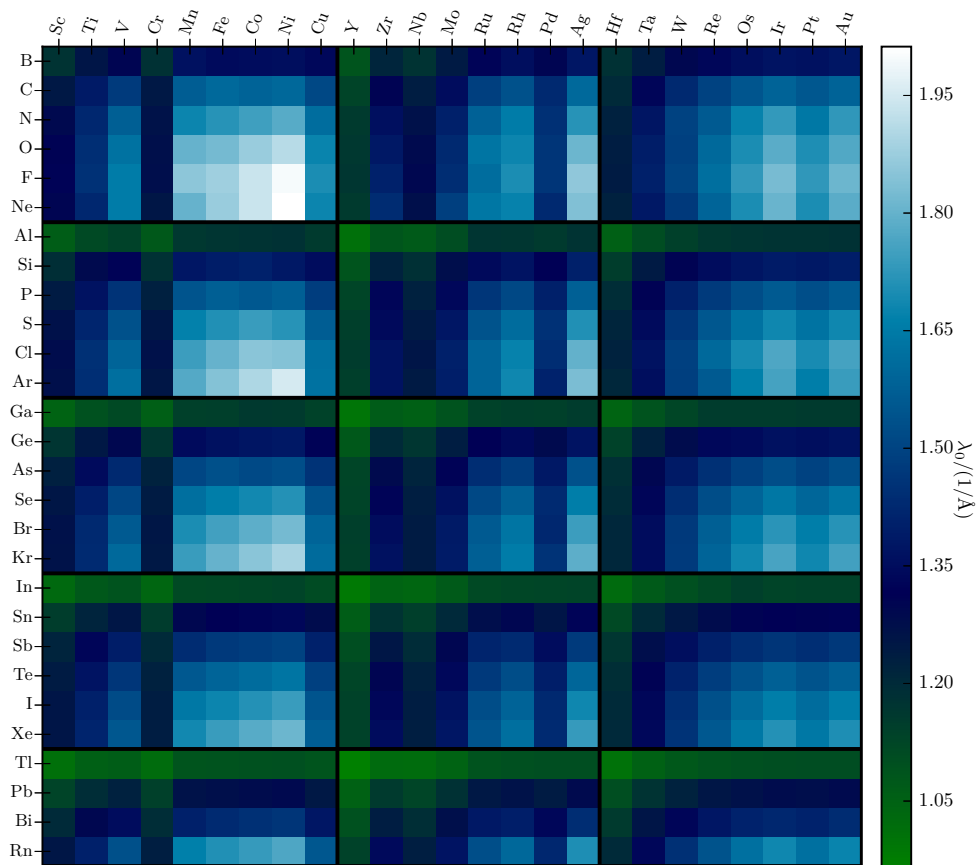


Figure B.14.: Trend of the decay parameter λ_0 of the interatomic matrix elements of $pd\pi$ of H^{orth} of the heteroatomic dimers consisting of one sp -valent atom (row) and one sd -valent atom (column).

C

Calculation of Elastic Constants for the Hexagonal Crystal Structure

The Lagrangian theory of elasticity of an anisotropic material is discussed e.g. in Refs. 220, 221. The elastic behaviour is determined by the stiffness tensor \mathbf{C} , which defines the relation between the Lagrangian stress $\boldsymbol{\tau}$ and the Lagrangian strain $\boldsymbol{\eta}$ by the generalized Hooke's law

$$\tau_{ij} = \sum_{k,l=1}^3 C_{ijkl} \eta_{kl}, \quad (\text{C.1})$$

where i, j, k and l are Cartesian indices. The elements of the stiffness tensor are referred to as elastic constants. The Lagrangian strain and the physical strain $\boldsymbol{\epsilon}$, which define the deformation of the unit cell, are related by

$$\boldsymbol{\eta} = \boldsymbol{\epsilon} + \frac{1}{2} \boldsymbol{\epsilon}^2. \quad (\text{C.2})$$

Equivalent pairs of Cartesian indices ij are enumerated in Voigt notation by the index α , according to

ij	11	22	33	23, 32	13, 31	12, 21
α	1	2	3	4	5	6.

A power series expansion of the total energy with respect to $\boldsymbol{\eta}$ is written in Voigt notation as

$$E(\boldsymbol{\eta}) = E^{(0)} + V^{(0)} \sum_{\alpha} \tau_{\alpha}^{(0)} \eta_{\alpha} + \frac{V^{(0)}}{2} \sum_{\alpha, \beta} C_{\alpha\beta} \eta_{\alpha} \eta_{\beta} + \dots, \quad (\text{C.3})$$

where $E^{(0)}$, $V^{(0)}$ and $\tau^{(0)}$ are the total energy, volume and stress of the reference structure.

The elastic constants are computed from energy calculations performed with DFT or with interatomic potentials by selecting the number of elastic deformations according to the number of independent elastic constants $C_{\alpha\beta}$ for the crystal structure under consideration. The cell is deformed with different strain values η for each elastic deformation. The corresponding total energies are computed and curves $E^{\text{fit}}(\eta)$ are fitted to the data. From the second derivatives of these curves, the elastic constants are computed by the solution of a system of linear equations. This method is implemented in the program code `ElaStic`, which is introduced in Ref. 221. The program code has been adapted to calculate elastic constants with `VASP` and `BOPfox` and was further modified in the choice of elastic deformations (see Tab. C.1).

The stiffness tensor of hexagonal crystal structures is given by

$$\mathbf{C}^{\text{hex.}} = \begin{pmatrix} C_{11} & C_{12} & C_{13} & 0 & 0 & 0 \\ C_{12} & C_{11} & C_{13} & 0 & 0 & 0 \\ C_{13} & C_{13} & C_{33} & 0 & 0 & 0 \\ 0 & 0 & 0 & C_{44} & 0 & 0 \\ 0 & 0 & 0 & 0 & C_{44} & 0 \\ 0 & 0 & 0 & 0 & 0 & (C_{11} - C_{12})/2 \end{pmatrix} \quad (\text{C.4})$$

and has five independent elastic constants. Therefore, five different elastic deformations are required to compute them from the total energy.

Voigt notation	Lagrangian strain	$E^{(2)}(\boldsymbol{\eta} = 0)$
(1, 0, 0, 0, 0, 0)	$\begin{pmatrix} \eta & 0 & 0 \\ 0 & 0 & 0 \\ 0 & 0 & 0 \end{pmatrix}$	$\frac{V^0}{2}C_{11}$
(0, 0, 1, 0, 0, 0)	$\begin{pmatrix} 0 & 0 & 0 \\ 0 & 0 & 0 \\ 0 & 0 & \eta \end{pmatrix}$	$\frac{V^0}{2}C_{33}$
(1, 1, 0, 0, 0, 0)	$\begin{pmatrix} \eta & 0 & 0 \\ 0 & \eta & 0 \\ 0 & 0 & 0 \end{pmatrix}$	$V^0(C_{11} + C_{12})$
(1, 0, 1, 0, 0, 0)	$\begin{pmatrix} \eta & 0 & 0 \\ 0 & 0 & 0 \\ 0 & 0 & \eta \end{pmatrix}$	$\frac{V^0}{2}(C_{11} + C_{33} + 2C_{13})$
(0, 0, 0, 1, 0, 0)	$\begin{pmatrix} 0 & 0 & 0 \\ 0 & 0 & \eta/2 \\ 0 & \eta/2 & 0 \end{pmatrix}$	$\frac{V^0}{2}C_{44}$

Table C.1.: Elastic deformations and their corresponding second derivative of the total energy used to calculate the elastic constants of the hcp crystal structure.

Bibliography

- [1] M. Finnis, *Interatomic Forces in Condensed Matter* (Oxford University Press, 2003).
- [2] R. M. Martin, *Electronic Structure: Basic Theory and Practical Methods* (Cambridge University Press, 2004).
- [3] H. Bruus and K. Flensberg, *Many-Body Quantum Theory in Condensed Matter Physics* (Oxford University Press, 2004).
- [4] D. Pettifor, *Bonding and Structure of Molecules and Solids*, Oxford science publications (Clarendon Press, 1995).
- [5] G. Czycholl, *Theoretische Festkörperphysik: Von den klassischen Modellen zu modernen Forschungsthemen*, Springer-Lehrbuch (Springer, 2007).
- [6] A. T. Paxton, “An Introduction to the Tight Binding approximation - Implementation by Diagonalisation,” in *NIC Series Volume 42: Multiscale Simulation Methods in Molecular Sciences, Lecture Notes, Johannes Grotendorst, Norbert Attig, Stefan Blügel, Dominik Marx*, NIC series, Vol. 42 (John von Neumann Institute for Computing, Jülich, 2009) pp. 145–176.
- [7] T. Hammerschmidt and R. Drautz, “Bond-Order Potentials for Bridging the Electronic to Atomistic Modelling Hierarchies,” in *NIC Series Volume 42: Multiscale Simulation Methods in Molecular Sciences, Lecture Notes, Johannes Grotendorst, Norbert Attig, Stefan Blügel, Dominik Marx*, NIC series, Vol. 42 (John von Neumann Institute for Computing, Jülich, 2009) pp. 229–246.
- [8] R. Drautz, *Quantum Mechanics in Materials Science* (Ruhr-Universität Bochum, Lecture notes, 2013).
- [9] R. Drautz, *Basics of the tight-binding approximation* (Ruhr-Universität Bochum, AMS seminar, Lecture notes, 2014).
- [10] M. Born and R. Oppenheimer, *Annalen der Physik* **389**, 457 (1927).
- [11] W. Pauli, *Zeitschrift für Physik* **31**, 765 (1925).
- [12] W. Ritz, *Journal für die reine und angewandte Mathematik* **135**, 1 (1909).

- [13] J. W. S. Rayleigh, *The London, Edinburgh, and Dublin Philosophical Magazine and Journal of Science* **22**, 225 (1911).
- [14] W. Kohn, *Rev. Mod. Phys.* **71**, 1253 (1999).
- [15] D. R. Hartree, *Mathematical Proceedings of the Cambridge Philosophical Society* **24**, 89 (1928).
- [16] V. Fock, *Zeitschrift für Physik* **61**, 126 (1930).
- [17] P. Hohenberg and W. Kohn, *Phys. Rev.* **136**, B864 (1964).
- [18] W. Kohn and L. J. Sham, *Phys. Rev.* **140**, A1133 (1965).
- [19] P. A. M. Dirac, *Mathematical Proceedings of the Cambridge Philosophical Society* **26**, 376 (1930).
- [20] E. Wigner, *Trans. Faraday Soc.* **34**, 678 (1938).
- [21] D. Ceperley, *Phys. Rev. B* **18**, 3126 (1978).
- [22] D. M. Ceperley and B. J. Alder, *Phys. Rev. Lett.* **45**, 566 (1980).
- [23] J. P. Perdew, *Phys. Rev. Lett.* **55**, 1665 (1985).
- [24] J. P. Perdew and Y. Wang, *Phys. Rev. B* **45**, 13244 (1992).
- [25] J. P. Perdew, K. Burke, and M. Ernzerhof, *Phys. Rev. Lett.* **77**, 3865 (1996).
- [26] J. P. Perdew, K. Burke, and M. Ernzerhof, *Phys. Rev. Lett.* **78**, 1396 (1997).
- [27] J. Tao, J. P. Perdew, V. N. Staroverov, and G. E. Scuseria, *Phys. Rev. Lett.* **91**, 146401 (2003).
- [28] A. D. Becke, *The Journal of Chemical Physics* **98**, 5648 (1993).
- [29] D. Rappoport, N. R. M. Crawford, F. Furche, and K. Burke, "Approximate Density Functionals: Which Should I Choose?" in *Encyclopedia of Inorganic Chemistry* (American Cancer Society, 2009).
- [30] F. Bloch, *Zeitschrift für Physik* **52**, 555 (1929).
- [31] E. Wigner and F. Seitz, *Phys. Rev.* **43**, 804 (1933).
- [32] G. Gilat and L. J. Raubenheimer, *Phys. Rev.* **144**, 390 (1966).
- [33] D. J. Chadi and M. L. Cohen, *Phys. Rev. B* **8**, 5747 (1973).
- [34] H. J. Monkhorst and J. D. Pack, *Phys. Rev. B* **13**, 5188 (1976).
- [35] M. Methfessel and A. T. Paxton, *Phys. Rev. B* **40**, 3616 (1989).
- [36] P. E. Blöchl, O. Jepsen, and O. K. Andersen, *Phys. Rev. B* **49**, 16223 (1994).

-
- [37] D. R. Hamann, M. Schlüter, and C. Chiang, *Phys. Rev. Lett.* **43**, 1494 (1979).
- [38] O. K. Andersen, *Phys. Rev. B* **12**, 3060 (1975).
- [39] P. E. Blöchl, *Phys. Rev. B* **50**, 17953 (1994).
- [40] PAW Setups 0.9.11271, <https://wiki.fysik.dtu.dk/gpaw/setups/setups.html> (Online: accessed 19-January-2018, released 27-May-2014).
- [41] J. Junquera, O. Paz, D. Sánchez-Portal, and E. Artacho, *Phys. Rev. B* **64**, 235111 (2001).
- [42] J. M. Soler, E. Artacho, J. D. Gale, A. García, J. Junquera, P. Ordejón, and D. Sánchez-Portal, *Journal of Physics: Condensed Matter* **14**, 2745 (2002).
- [43] A. H. Larsen, M. Vanin, J. J. Mortensen, K. S. Thygesen, and K. W. Jacobsen, *Phys. Rev. B* **80**, 195112 (2009).
- [44] E. Artacho, D. Sánchez-Portal, P. Ordejón, A. García, and J. M. Soler, *physica status solidi (b)* **215**, 809 (1999).
- [45] J. Enkovaara, C. Rostgaard, J. J. Mortensen, J. Chen, M. Dułak, L. Ferrighi, J. Gavnholt, C. Glinsvad, V. Haikola, H. A. Hansen, H. H. Kristoffersen, M. Kuisma, A. H. Larsen, L. Lehtovaara, M. Ljungberg, O. Lopez-Acevedo, P. G. Moses, J. Ojanen, T. Olsen, V. Petzold, N. A. Romero, J. Stausholm-Møller, M. Strange, G. A. Tritsarlis, M. Vanin, M. Walter, B. Hammer, H. Häkkinen, G. K. H. Madsen, R. M. Nieminen, J. K. Nørskov, M. Puska, T. T. Rantala, J. Schiøtz, K. S. Thygesen, and K. W. Jacobsen, *Journal of Physics: Condensed Matter* **22**, 253202 (2010).
- [46] K. Lejaeghere, G. Bihlmayer, T. Björkman, P. Blaha, S. Blügel, V. Blum, D. Caliste, I. E. Castelli, S. J. Clark, A. Dal Corso, S. de Gironcoli, T. Deutsch, J. K. Dewhurst, I. Di Marco, C. Draxl, M. Dułak, O. Eriksson, J. A. Flores-Livas, K. F. Garrity, L. Genovese, P. Giannozzi, M. Giantomassi, S. Goedecker, X. Gonze, O. Grånäs, E. K. U. Gross, A. Gulans, F. Gygi, D. R. Hamann, P. J. Hasnip, N. A. W. Holzwarth, D. Iuşan, D. B. Jochym, F. Jollet, D. Jones, G. Kresse, K. Koepnik, E. Küçükbenli, Y. O. Kvashnin, I. L. M. Locht, S. Lubeck, M. Marsman, N. Marzari, U. Nitzsche, L. Nordström, T. Ozaki, L. Paulatto, C. J. Pickard, W. Poelmans, M. I. J. Probert, K. Refson, M. Richter, G.-M. Rignanese, S. Saha, M. Scheffler, M. Schlipf, K. Schwarz, S. Sharma, F. Tavazza, P. Thunström, A. Tkatchenko, M. Torrent, D. Vanderbilt, M. J. van Setten, V. Van Speybroeck, J. M. Wills, J. R. Yates, G.-X. Zhang, and S. Cottenier, *Science* **351** (2016).
- [47] J. J. Mortensen, L. B. Hansen, and K. W. Jacobsen, *Phys. Rev. B* **71**, 035109 (2005).
- [48] G. Kresse and J. Hafner, *Phys. Rev. B* **47**, 558 (1993).

- [49] G. Kresse and J. Hafner, *Phys. Rev. B* **49**, 14251 (1994).
- [50] G. Kresse and J. Furthmüller, *Computational Materials Science* **6**, 15 (1996).
- [51] G. Kresse and J. Furthmüller, *Phys. Rev. B* **54**, 11169 (1996).
- [52] G. Kresse and D. Joubert, *Phys. Rev. B* **59**, 1758 (1999).
- [53] L. E. Ballentine and M. Kolar, *Journal of Physics C: Solid State Physics* **19**, 981 (1986).
- [54] J. Harris, *Phys. Rev. B* **31**, 1770 (1985).
- [55] W. M. C. Foulkes and R. Haydock, *Phys. Rev. B* **39**, 12520 (1989).
- [56] R. P. Sherman and R. Grinter, *Journal of Molecular Structure: THEOCHEM* **135**, 127 (1986).
- [57] J. C. Slater and G. F. Koster, *Phys. Rev.* **94**, 1498 (1954).
- [58] R. R. Sharma, *Phys. Rev. B* **19**, 2813 (1979).
- [59] http://openmopac.net/manual/rotate_atomic_orbitals.html (Online: accessed 22-March-2018).
- [60] A. P. Sutton, M. W. Finnis, D. G. Pettifor, and Y. Ohta, *Journal of Physics C: Solid State Physics* **21**, 35 (1988).
- [61] A. P. Horsfield, A. M. Bratkovsky, M. Fearn, D. G. Pettifor, and M. Aoki, *Phys. Rev. B* **53**, 12694 (1996).
- [62] R. Drautz and D. G. Pettifor, *Phys. Rev. B* **74**, 174117 (2006).
- [63] N. Hatcher, G. K. H. Madsen, and R. Drautz, *Phys. Rev. B* **86**, 155115 (2012).
- [64] D. J. Chadi, *Phys. Rev. Lett.* **41**, 1062 (1978).
- [65] D. J. Chadi, *Phys. Rev. B* **19**, 2074 (1979).
- [66] R. Drautz, D. A. Murdick, D. Nguyen-Manh, X. Zhou, H. N. G. Wadley, and D. G. Pettifor, *Phys. Rev. B* **72**, 144105 (2005).
- [67] J. Friedel, *Advances in Physics* **3**, 446 (1954).
- [68] J. Hubbard, *Proceedings of the Royal Society of London A: Mathematical, Physical and Engineering Sciences* **276**, 238 (1963).
- [69] P.-O. Löwdin, *Advances in Physics* **5**, 1 (1956).
- [70] R. Drautz, T. Hammerschmidt, M. Čák, and D. G. Pettifor, *Modelling and Simulation in Materials Science and Engineering* **23**, 074004 (2015).

-
- [71] E. R. Margine and D. G. Pettifor, *Phys. Rev. B* **89**, 235134 (2014).
- [72] H. Hellmann, *Einführung in die Quantenchemie* (Springer Spektrum, 1937).
- [73] R. P. Feynman, *Phys. Rev.* **56**, 340 (1939).
- [74] G. K. H. Madsen, E. J. McEniry, and R. Drautz, *Phys. Rev. B* **83**, 184119 (2011).
- [75] A. Urban, M. Reese, M. Mrovec, C. Elsässer, and B. Meyer, *Phys. Rev. B* **84**, 155119 (2011).
- [76] E. J. McEniry, G. K. H. Madsen, J. F. Drain, and R. Drautz, *Journal of Physics: Condensed Matter* **23**, 276004 (2011).
- [77] E. J. McEniry, R. Drautz, and G. K. H. Madsen, *Journal of Physics: Condensed Matter* **25**, 115502 (2013).
- [78] A. Katre and G. K. H. Madsen, *Phys. Rev. B* **93**, 155203 (2016).
- [79] A. Ladines, R. Drautz, and T. Hammerschmidt, *Journal of Alloys and Compounds* **693**, 1315 (2017).
- [80] J. Shohat, *Biometrika* **21**, 361 (1929).
- [81] F. Cyrot-Lackmann, *Advances in Physics* **16**, 393 (1967).
- [82] F. Cyrot-Lackmann, *Journal of Physics and Chemistry of Solids* **29**, 1235 (1968).
- [83] R. Haydock, V. Heine, and M. J. Kelly, *Journal of Physics C: Solid State Physics* **5**, 2845 (1972).
- [84] R. Haydock, *Solid State Physics* **35**, 215 (1980).
- [85] C. Lanczos, *Journal of Research of the National Bureau of Standards* **45**, 255 (1950).
- [86] A. Horsfield, *Materials Science and Engineering: B* **37**, 219 (1996).
- [87] D. G. Pettifor, *Phys. Rev. Lett.* **63**, 2480 (1989).
- [88] M. Aoki and D. G. Pettifor, *International Journal of Modern Physics B* **07**, 299 (1993).
- [89] M. Aoki, *Phys. Rev. Lett.* **71**, 3842 (1993).
- [90] M. Aoki, D. Nguyen-Manh, D. Pettifor, and V. Vitek, *Progress in Materials Science* **52**, 154 (2007).
- [91] D. G. Pettifor and I. I. Oleinik, *Phys. Rev. B* **59**, 8487 (1999).
- [92] I. I. Oleinik and D. G. Pettifor, *Phys. Rev. B* **59**, 8500 (1999).

- [93] D. G. Pettifor and I. I. Oleinik, *Phys. Rev. Lett.* **84**, 4124 (2000).
- [94] I. Bronštejn, H. Mühlig, K. Semendjajew, and G. Musiol, *Taschenbuch der Mathematik*, Edition Harri Deutsch (Europa Lehrmittel Verlag, 2016).
- [95] B. Seiser, D. G. Pettifor, and R. Drautz, *Phys. Rev. B* **87**, 094105 (2013).
- [96] N. Beer and D. G. Pettifor, “The recursion method and the estimation of local densities of states,” in *The Electronic Structure of Complex Systems*, edited by W. M. Phariseau, P. and Temmerman (Springer US, Boston, MA, 1984) pp. 769–777.
- [97] R. Haydock and R. L. Johannes, *Journal of Physics F: Metal Physics* **5**, 2055 (1975).
- [98] M. E. Ford, R. Drautz, T. Hammerschmidt, and D. G. Pettifor, *Modelling and Simulation in Materials Science and Engineering* **22**, 034005 (2014).
- [99] S. Gerschgorin, *Bulletin de l’Académie des Sciences de l’URSS* **6**, 749 (1931).
- [100] P. Turchi, F. Ducastelle, and G. Treglia, *Journal of Physics C: Solid State Physics* **15**, 2891 (1982).
- [101] A. Weiße, G. Wellein, A. Alvermann, and H. Fehske, *Rev. Mod. Phys.* **78**, 275 (2006).
- [102] R. Drautz and D. G. Pettifor, *Phys. Rev. B* **84**, 214114 (2011).
- [103] OpenKIM Knowledgebase of Interatomic Models, <https://openkim.org/> (Online: accessed 27-March-2018).
- [104] G. J. Ackland, M. W. Finnis, and V. Vitek, *Journal of Physics F: Metal Physics* **18**, L153 (1988).
- [105] M. W. Finnis and J. E. Sinclair, *Philosophical Magazine A* **50**, 45 (1984).
- [106] G. Allan and M. Lannoo, *Journal of Physics and Chemistry of Solids* **37**, 699 (1976).
- [107] K. Masuda and A. Sato, *Philosophical Magazine A* **44**, 799 (1981).
- [108] M. S. Daw and M. I. Baskes, *Phys. Rev. B* **29**, 6443 (1984).
- [109] M. S. Daw and M. I. Baskes, *Phys. Rev. Lett.* **50**, 1285 (1983).
- [110] F. Ercolessi, E. Tosatti, and M. Parrinello, *Phys. Rev. Lett.* **57**, 719 (1986).
- [111] A. E. Carlsson and N. W. Ashcroft, *Phys. Rev. B* **27**, 2101 (1983).
- [112] A. Carlsson, *Solid State Physics* **43**, 1 (1990).
- [113] A. E. Carlsson, *Phys. Rev. B* **44**, 6590 (1991).

-
- [114] S. M. Foiles, *Phys. Rev. B* **48**, 4287 (1993).
- [115] J. Tersoff, *Phys. Rev. Lett.* **56**, 632 (1986).
- [116] J. Tersoff, *Phys. Rev. B* **37**, 6991 (1988).
- [117] J. Tersoff, *Phys. Rev. B* **38**, 9902 (1988).
- [118] P. Alinaghian, P. Gumbsch, A. J. Skinner, and D. G. Pettifor, *Journal of Physics: Condensed Matter* **5**, 5795 (1993).
- [119] D. G. Pettifor and M. Aoki, *Philosophical Transactions of the Royal Society of London A: Mathematical, Physical and Engineering Sciences* **334**, 439 (1991).
- [120] N. Hatcher, G. K. H. Madsen, and R. Drautz, *Journal of Physics: Condensed Matter* **26**, 145502 (2014).
- [121] J. F. Drain, R. Drautz, and D. G. Pettifor, *Phys. Rev. B* **89**, 134102 (2014).
- [122] M. W. Finnis, A. B. Walker, and P. Gumbsch, *Journal of Physics: Condensed Matter* **10**, 7983 (1998).
- [123] T. Hammerschmidt, B. Seiser, M. Ford, A. Ladines, S. Schreiber, N. Wang, J. Jenke, Y. Lysogorskiy, C. Teijeiro, M. Mrovec, M. Cak, E. Margine, D. Pettifor, and R. Drautz, *Computer Physics Communications* (2018).
- [124] C. Teijeiro, T. Hammerschmidt, B. Seiser, R. Drautz, and G. Sutmann, *Modelling and Simulation in Materials Science and Engineering* **24**, 025008 (2016).
- [125] C. Teijeiro, T. Hammerschmidt, R. Drautz, and G. Sutmann, *Computer Physics Communications* **204**, 64 (2016).
- [126] C. Teijeiro, T. Hammerschmidt, R. Drautz, and G. Sutmann, *The International Journal of High Performance Computing Applications* **1-15** (2017).
- [127] D. G. Pettifor, *Journal of Physics C: Solid State Physics* **19**, 285 (1986).
- [128] B. Seiser, T. Hammerschmidt, A. N. Kolmogorov, R. Drautz, and D. G. Pettifor, *Phys. Rev. B* **83**, 224116 (2011).
- [129] P. Turchi and F. Ducastelle, “Continued fractions and perturbation theory: Application to tight binding systems,” in *The Recursion Method and Its Applications: Proceedings of the Conference, Imperial College, London, England September 13–14, 1984*, edited by D. G. Pettifor and D. L. Weaire (Springer Berlin Heidelberg, 1987) pp. 104–119.
- [130] J. C. Cressoni and D. G. Pettifor, *Journal of Physics: Condensed Matter* **3**, 495 (1991).
- [131] J. L. Mercer and M. Y. Chou, *Phys. Rev. B* **49**, 8506 (1994).

- [132] J. Gehrmann, D. G. Pettifor, A. N. Kolmogorov, M. Reese, M. Mrovec, C. Elsässer, and R. Drautz, *Phys. Rev. B* **91**, 054109 (2015).
- [133] D. Pettifor, M. Finnis, D. Nguyen-Manh, D. Murdick, X. Zhou, and H. Wadley, *Materials Science and Engineering: A* **365**, 2 (2004).
- [134] J. Koringa, *Physica* **13**, 392 (1947).
- [135] W. Kohn and N. Rostoker, *Phys. Rev.* **94**, 1111 (1954).
- [136] O. K. Andersen, W. Klose, and H. Nohl, *Phys. Rev. B* **17**, 1209 (1978).
- [137] O. K. Andersen, O. Jepsen, and M. Sob, “Linearized band structure methods,” in *Electronic Band Structure and Its Applications*, edited by M. Yussouff (Springer Berlin Heidelberg, 1987) pp. 1–57.
- [138] W. Harrison, *Electronic Structure and the Properties of Solids: The Physics of the Chemical Bond*, Dover Books on Physics (Dover Publications, 2012).
- [139] W. A. Harrison, “The physics of solid state chemistry,” in *Festkörperprobleme: Plenary lectures of the Divisions Semiconductor Physics, Metal Physics, Low Temperature Physics, Thermodynamics and Statistical Physics, Crystallography, Magnetism, Surface Physics, of the German Physical Society, Münster, March 7-12, 1977*, edited by J. Treusch (Springer Berlin Heidelberg, 1977) pp. 135–155.
- [140] D. J. Chadi and M. L. Cohen, *physica status solidi (b)* **68**, 405 (1975).
- [141] G. S. Painter, D. E. Ellis, and A. R. Lubinsky, *Phys. Rev. B* **4**, 3610 (1971).
- [142] F. Herman and S. Skillman, *Atomic Structure Calculations*, Materials science and technology (Prentice-Hall, 1963).
- [143] S. Froyen and W. A. Harrison, *Phys. Rev. B* **20**, 2420 (1979).
- [144] W. A. Harrison and S. Froyen, *Phys. Rev. B* **21**, 3214 (1980).
- [145] L. Shi and D. A. Papaconstantopoulos, *Phys. Rev. B* **70**, 205101 (2004).
- [146] D. Pettifor, *Solid State Physics* **40**, 43 (1987).
- [147] D. Pettifor, “Electron theory of metals,” in *Physical Metallurgy*, Vol. 1 (Elsevier Science, 1996) pp. 47–134.
- [148] M. J. Mehl and D. A. Papaconstantopoulos, *Phys. Rev. B* **54**, 4519 (1996).
- [149] D. A. Papaconstantopoulos *et al.*, *Handbook of the band structure of elemental solids* (Springer, 1986).
- [150] D. A. Papaconstantopoulos and M. J. Mehl, *Journal of Physics: Condensed Matter* **15**, R413 (2003).

-
- [151] I. Schnell, M. D. Jones, S. P. Rudin, and R. C. Albers, *Phys. Rev. B* **74**, 054104 (2006).
- [152] D. Porezag, T. Frauenheim, T. Köhler, G. Seifert, and R. Kaschner, *Phys. Rev. B* **51**, 12947 (1995).
- [153] M. Elstner, D. Porezag, G. Jungnickel, J. Elsner, M. Haugk, T. Frauenheim, S. Suhai, and G. Seifert, *Phys. Rev. B* **58**, 7260 (1998).
- [154] M. Wahiduzzaman, A. F. Oliveira, P. Philippsen, L. Zhechkov, E. van Lenthe, H. A. Witek, and T. Heine, *Journal of Chemical Theory and Computation* **9**, 4006 (2013).
- [155] S. Grimme, C. Bannwarth, and P. Shushkov, *Journal of Chemical Theory and Computation* **13**, 1989 (2017).
- [156] D. Nguyen-Manh, D. G. Pettifor, and V. Vitek, *Phys. Rev. Lett.* **85**, 4136 (2000).
- [157] R. Drautz, X. Zhou, D. Murdick, B. Gillespie, H. Wadley, and D. Pettifor, *Progress in Materials Science* **52**, 196 (2007).
- [158] J. Frenzel, A. F. Oliveira, N. Jardillier, T. Heine, and G. Seifert, TU-Dresden 2004-2009, <https://www.dftb.org/parameters> (Online: accessed 29-May-2018).
- [159] S. Markov, B. Aradi, C. Y. Yam, H. Xie, T. Frauenheim, and G. Chen, *IEEE Transactions on Electron Devices* **62**, 696 (2015).
- [160] S. Markov, G. Penazzi, Y. Kwok, A. Pecchia, B. Aradi, T. Frauenheim, and G. Chen, *IEEE Electron Device Letters* **36**, 1076 (2015).
- [161] D. A. Papaconstantopoulos, M. J. Mehl, S. C. Erwin, and M. R. Pederson, *MRS Proceedings* **491**, 221 (1997).
- [162] J. A. Moriarty, *Phys. Rev. B* **38**, 3199 (1988).
- [163] M. Čák, T. Hammerschmidt, J. Rogal, V. Vitek, and R. Drautz, *Journal of Physics: Condensed Matter* **26**, 195501 (2014).
- [164] Y.-S. Lin, M. Mrovec, and V. Vitek, *Phys. Rev. B* **93**, 214107 (2016).
- [165] V. Paidar, L. G. Wang, M. Sob, and V. Vitek, *Modelling and Simulation in Materials Science and Engineering* **7**, 369 (1999).
- [166] Y.-S. Lin, M. Mrovec, and V. Vitek, *Modelling and Simulation in Materials Science and Engineering* **22**, 034002 (2014).
- [167] E. C. Bain and N. Dunkirk, *trans. AIME* **70**, 25 (1924).
- [168] W. Luo, D. Roundy, M. L. Cohen, and J. W. Morris, *Phys. Rev. B* **66**, 094110 (2002).

- [169] M. Friák and M. Šob, *Phys. Rev. B* **77**, 174117 (2008).
- [170] A. K. Sinha, *Progress in Materials Science* **15**, 81 (1972).
- [171] T. Hammerschmidt, A. N. Ladines, J. Koßmann, and R. Drautz, *Crystals* **6**, 18 (2016).
- [172] A. P. A. Subramanyam, Ph.D. thesis, Ruhr-Universität-Bochum, Fakultät für Physik und Astronomie, Bochum (to be published).
- [173] J. Foadi and G. Evans, *Acta Crystallographica Section A* **67**, 93 (2011).
- [174] P. J. Steinhardt, D. R. Nelson, and M. Ronchetti, *Phys. Rev. B* **28**, 784 (1983).
- [175] W. Lechner and C. Dellago, *The Journal of Chemical Physics* **129**, 114707 (2008).
- [176] A. P. Bartók, M. C. Payne, R. Kondor, and G. Csányi, *Phys. Rev. Lett.* **104**, 136403 (2010).
- [177] A. P. Bartók, R. Kondor, and G. Csányi, *Phys. Rev. B* **87**, 184115 (2013).
- [178] J. Behler, *The Journal of Chemical Physics* **134**, 074106 (2011).
- [179] N. Artrith, T. Morawietz, and J. Behler, *Phys. Rev. B* **83**, 153101 (2011).
- [180] S. Hajinazar, J. Shao, and A. N. Kolmogorov, *Phys. Rev. B* **95**, 014114 (2017).
- [181] M. Rupp, A. Tkatchenko, K.-R. Müller, and O. A. von Lilienfeld, *Phys. Rev. Lett.* **108**, 058301 (2012).
- [182] O. A. von Lilienfeld, R. Ramakrishnan, M. Rupp, and A. Knoll, *International Journal of Quantum Chemistry* **115**, 1084 (2015).
- [183] K. Hansen, F. Biegler, R. Ramakrishnan, W. Pronobis, O. A. von Lilienfeld, K.-R. Müller, and A. Tkatchenko, *The Journal of Physical Chemistry Letters* **6**, 2326 (2015).
- [184] A. F. Bialon, T. Hammerschmidt, and R. Drautz, *Chemistry of Materials* **28**, 2550 (2016).
- [185] L. M. Ghiringhelli, J. Vybiral, S. V. Levchenko, C. Draxl, and M. Scheffler, *Phys. Rev. Lett.* **114**, 105503 (2015).
- [186] Y. Saad, D. Gao, T. Ngo, S. Bobbitt, J. R. Chelikowsky, and W. Andreoni, *Phys. Rev. B* **85**, 104104 (2012).
- [187] K. T. Schütt, H. Glawe, F. Brockherde, A. Sanna, K. R. Müller, and E. K. U. Gross, *Phys. Rev. B* **89**, 205118 (2014).

-
- [188] O. Isayev, D. Fourches, E. N. Muratov, C. Oses, K. Rasch, A. Tropsha, and S. Curtarolo, *Chemistry of Materials* **27**, 735 (2015).
- [189] T. Hammerschmidt, A. F. Bialon, D. G. Pettifor, and R. Drautz, *New Journal of Physics* **15**, 115016 (2013).
- [190] T. Hammerschmidt, B. Seiser, R. Drautz, and D. G. Pettifor, “Modelling topologically close-packed phases in superalloys: Valence-dependent bond-order potentials based on ab-initio calculations,” in *Superalloys* (The Metals, Minerals and Materials Society, Warrendale, PA, 2008) pp. 847–853.
- [191] A. Bartók-Pártay, *The Gaussian Approximation Potential: An Interatomic Potential Derived from First Principles Quantum Mechanics*, Springer Theses (Springer Berlin Heidelberg, 2010).
- [192] D. S. Karls, *Transferability of Empirical Potentials and the Knowledgebase of Interatomic Models (KIM)*, Ph.D. thesis, University of Minnesota, Faculty of the graduate school, Bochum (2016).
- [193] T. C. Hales, *Annals of mathematics* **162**, 1065 (2005).
- [194] M. Densow, *Assessing Descriptors for Transferability Using High-Throughput Calculations*, Master’s thesis, Ruhr-Universität-Bochum, Fakultät für Physik und Astronomie, Bochum (2018).
- [195] F. Ercolessi and J. B. Adams, *EPL (Europhysics Letters)* **26**, 583 (1994).
- [196] K. Levenberg, *Quarterly of Applied Mathematics* **2**, 164 (1944).
- [197] D. W. Marquardt, *Journal of the Society for Industrial and Applied Mathematics* **11**, 431 (1963).
- [198] J. J. Moré, B. S. Garbow, and K. E. Hillstrom, *User guide for MINPACK-1*, Tech. Rep. ANL-80-74 (Argonne Nat. Lab., Argonne, IL, 1980).
- [199] P. Brommer and F. Gähler, *Modelling and Simulation in Materials Science and Engineering* **15**, 295 (2007).
- [200] A. Jaramillo-Botero, S. Naserifar, and W. A. Goddard, *Journal of Chemical Theory and Computation* **10**, 1426 (2014).
- [201] A. I. Duff, M. Finnis, P. Maugis, B. J. Thijsse, and M. H. Sluiter, *Computer Physics Communications* **196**, 439 (2015).
- [202] N. Artrith and A. Urban, *Computational Materials Science* **114**, 135 (2016).
- [203] C. D. Barrett and R. L. Carino, *Integrating Materials and Manufacturing Innovation*, 9 (2016).
- [204] A. Stukowski, E. Fransson, M. Mock, and P. Erhart, *Modelling and Simulation in Materials Science and Engineering* **25**, 055003 (2017).

- [205] C.-P. Chou, Y. Nishimura, C.-C. Fan, G. Mazur, S. Irle, and H. A. Witek, *Journal of Chemical Theory and Computation* **12**, 53 (2016).
- [206] A. N. Ladines, (in preparation).
- [207] J. Behler and M. Parrinello, *Phys. Rev. Lett.* **98**, 146401 (2007).
- [208] M. F. Horstemeyer, J. M. Hughes, N. Sukhija, W. B. Lawrimore, S. Kim, R. Carino, and M. I. Baskes, *JOM* **67**, 143 (2015).
- [209] M. D. Jones and R. C. Albers, *Phys. Rev. B* **66**, 134105 (2002).
- [210] M. J. Cawkwell, D. Nguyen-Manh, D. G. Pettifor, and V. Vitek, *Phys. Rev. B* **73**, 064104 (2006).
- [211] D. Nguyen-Manh, D. Pettifor, S. Znam, and V. Vitek, “Negative cauchy pressure within the tight-binding approximation,” in *Tight-binding Approach to Computational Materials Science*, edited by P. Turchi, A. Gonis, and L. Colombo (Materials Research Society, 1998) pp. 353–358.
- [212] M. Aoki and T. Kurokawa, *Journal of Physics: Condensed Matter* **19**, 236228 (2007).
- [213] C. Rae and R. Reed, *Acta Materialia* **49**, 4113 (2001).
- [214] O. Levy, M. Jahnátek, R. V. Chepulskii, G. L. W. Hart, and S. Curtarolo, *Journal of the American Chemical Society* **133**, 158 (2011).
- [215] W. Setyawan, N. Gao, and R. J. Kurtz, *Journal of Applied Physics* **123**, 205102 (2018).
- [216] D. Hull and D. Bacon, *Introduction to Dislocations*, Materials Science and Technology (Elsevier Science, 2011).
- [217] G. Henkelman, B. P. Uberuaga, and H. Jónsson, *The Journal of Chemical Physics* **113**, 9901 (2000).
- [218] G. Henkelman and H. Jónsson, *The Journal of Chemical Physics* **113**, 9978 (2000).
- [219] B. Yin, Z. Wu, and W. Curtin, *Acta Materialia* **123**, 223 (2017).
- [220] D. C. Wallace, *Thermodynamics of Crystals* (Dover Publications, Inc., 1998).
- [221] R. Golezorkhtabar, P. Pavone, J. Spitaler, P. Puschnig, and C. Draxl, *Computer Physics Communications* **184**, 1861 (2013).
- [222] A. Togo and I. Tanaka, *Scripta Materialia* **108**, 1 (2015).
- [223] M. Papageorgiou, M. Leibold, and M. Buss, *Optimierung: Statische, dynamische, stochastische Verfahren für die Anwendung* (Springer Berlin Heidelberg, 2015).

- [224] A. Ferrari, Ph.D. thesis, Ruhr-Universität-Bochum, Fakultät für Physik und Astronomie, Bochum (to be published).
- [225] C. Sutton, L. M. Ghiringhelli, T. Yamamoto, Y. Lysogorskiy, L. Blumenthal, T. Hammerschmidt, J. Golebiowski, X. Liu, A. Ziletti, and M. Scheffler, (in prepration).

Curriculum Vitae

Name : Jan Jenke
Geburtsdatum : 6. Januar 1990
Geburtsort : Gladbeck

AUSBILDUNG

Sep. 2000 - Aug. 2009 : Abitur, Riesener-Gymnasium Gladbeck
Sep. 2009 - Aug. 2012 : B.Sc in Physik, Ruhr-Universität Bochum,
*Numerische Methoden der Statistischen Physik -
Thermodynamische Phasenübergänge des Ising Modells*
Sep. 2012 - Aug. 2014 : M.Sc in Physik, Ruhr-Universität Bochum,
*Comparison of Classical and Quantum Monte Carlo
Methods in the Context of the Ising Spin Glas Model*
seit Sep. 2014 : Promotion in Physik, Ruhr-Universität Bochum

AKTIVITÄTEN

Aug. 2014 : Summer School on Quantum Monte Carlo and the CASINO
program IX
(Vallico Sotto, Italien)
Jan. 2015/16 : Teaching assistant: Introduction to modelling in materials science
(Oxford, Großbritannien)
Okt. 2015 : CECAM DFTB Workshop and Tutorial
Poster: *Tight-binding parameterizations across the periodic table*
(Bremen, Deutschland)
Mär. 2016 : DPG-Frühjahrstagung der Sektion Kondensierte Materie
Vortrag: *Tight-binding parameterizations across the periodic table*
(Regensburg, Deutschland)
Mai 2016 : Materials Chain International Conference
Poster: *Tight-binding parameterizations across the periodic table*
(Bochum, Deutschland)
Jun. 2016 : Computational Materials Science Workshop (Vortrag)
(Domburg, Niederlande)
Mär. 2017 : DPG-Frühjahrstagung der Sektion Kondensierte Materie
Vortrag: *Quantification of different atomic environments by a 2d
structure map*
(Dresden, Deutschland)
Mär. 2018 : DPG-Frühjahrstagung der Sektion Kondensierte Materie
Vortrag: *Data-driven approach to accelerate the development of
bond-order potentials*
(Berlin, Deutschland)
Jun. 2018 : 10 years ICAMS - International symposium
Vortrag: *Construction of structure and chemistry descriptors
for machine-learning material properties*
(Bochum, Deutschland)

VERÖFFENTLICHUNGEN

1. J. Jenke, A. P. A. Subramanyam, M. Densow, T. Hammerschmidt, D. G. Pettifor and R. Drautz, *Electronic structure based descriptor for characterizing local atomic environments*, Phys. Rev. B 98, 144102 (2018)
2. T. Hammerschmidt, B. Seiser, M. E. Ford, A. N. Ladines, N. Wang, J. Jenke, Y. Lysogorskiy, C. Teijeiro, M. Mrovec, M. Čák, E. R. Margine, D. G. Pettifor and R. Drautz, *BOPfox program for tight-binding and analytic bond-order potential calculations*, Computer Physics Communications (2018)